UNIVERSIDAD COMPLUTENSE DE MADRID

FACULTAD DE CIENCIAS FÍSICAS
Departamento de Física de la Tierra, Astronomía y Astrofísica I
(Geofísica y Meteorología) (Astronomía y Geodesia)

TESIS DOCTORAL

Radiation fog, gravity waves and their interactions with turbulence in the atmospheric boundary layer

(Nieblas radiactivas, ondas de gravedad y sus interacciones con la turbulencia en la capa límite atmosférica)

MEMORIA PARA OPTAR AL GRADO DE DOCTOR

PRESENTADA POR

Carlos Román Cascón

Director
Carlos Yagüe Anguís

Madrid, 2016

RADIATION FOG, GRAVITY WAVES AND THEIR INTERACTIONS WITH TURBULENCE IN THE ATMOSPHERIC BOUNDARY LAYER

(NIEBLAS RADIATIVAS, ONDAS DE GRAVEDAD Y SUS INTERACCIONES CON LA TURBULENCIA EN LA CAPA LÍMITE ATMOSFÉRICA)

CARLOS ROMÁN CASCÓN

Memoria de tesis para optar al grado de doctor

Departamento de Física de la Tierra, Astronomía y Astrofísica I
Facultad de Ciencias Físicas
Universidad Complutense de Madrid

Director:
Carlos Yagüe Anguís (UCM)

Octubre 2015
Madrid

Carlos Román Cascón: *Radiation fog, gravity waves and their interactions with turbulence in the atmospheric boundary layer.* Memoria de tesis para optar al grado de doctor. © *Final Version* as of October 16, 2015.

Cover picture (printed version) corresponds to the life cycle of an idealised radiation-fog event. The fog forms during stable nighttime conditions (with gravity waves appearance). Then, the fog evolves to its mature stage (turbulent mixing generated by the fog itself) and finally, the fog dissipates from surface after the sunrise. Picture by Lourdes Román Cascón.

"A mis padres"

ACKNOWLEDGEMENTS (AGRADECIMIENTOS)

Por fin lo más leído de la tesis.

Es curioso, en la parte que concluye esta tesis he escrito lo siguiente: *"las cosas en la vida son normalmente oscilantes y a veces brumosas. Ambas pueden ser disipadas añadiendo más turbulencia (energía)"*, en lo que pretendía ser una adaptación (acorde a la tesis) del dicho de mi padre: *"al toro se le agarra por los cuernos"*. Lo cierto es que los casi 5 años de mi doctorado no han sido ni oscilantes ni brumosos. No sé qué me deparará el futuro, pero siempre recordaré este periodo como uno de los más bonitos que he vivido y en el que creo que he aprendido mucho en todos los aspectos. Sin embargo, todo ello lo debo a la acción conjunta de las personas que me han rodeado.

Hace casi 5 años ya que Carlos Yagüe me dio esta oportunidad y progresivamente he ido dándome cuenta de que dudo que alguna vez en mi vida vuelva a tener un jefe como él. Carlos me ha escuchado siempre, me ha enseñado, me ha contagiado su interés por las pequeñas cosas de la meteorología. He tenido el director de tesis que todos quieren tener, muy grande en lo profesional y más aún en lo personal. Carlos, muchas gracias por la oportunidad que me diste, por preocuparte por mi siempre, por tu ayuda, por tu amistad y por haberme transmitido tantos conocimientos. Claro que aún nos queda mucho que trabajar juntos y esto no es una despedida. :-)

Pero no sólo Carlos me ha ayudado y se ha convertido en mi amigo estos años en la UCM. Gracias a Belén por su lucha y preocupación constante por nuestro futuro, nuestros contratos, proyectos, por ser tan amiga de todos y por estar siempre al lado de los doctorandos. Gracias por tan buenas conversaciones a mi vecina Ana N., gracias a Elsa, Maurizio, Luís D. 1, Luís D. 2, Fátima, V. Carlos, Encarna, y a todo el personal del departamento con el que he coincidido estos años, sin olvidar por supuesto a Lucía y a Salva. Gracias a Saioa y a Rosa por haber compartido con ellas mi experiencia docente. Por supuesto, gracias a Goyo por su compañía en los viajes al CIBA y a Francia. Y gracias a los compañeros del *otro departamento*.

El hecho de tener ganas de venir al trabajo no tiene precio. Esto lo han conseguido todos mis compañeros, gracias a los buenos momentos y a las constantes risas compartidas. Esta tesis me ha ido dando esos magníficos compis y amigos desde el principio: Blanca (mi maestra en MatLab), Teresa, Álvaro, Marta A., Javi B., Javi P., Marta M., Jesús, Antonio, Cristina, Ade, Ibrahima, er Rober y Julián, mi amigo y compañero de cafés y confidencias.

Gracias a todos ellos y a mis compis del laboratorio 203, dignos competidores del concurso bolita-palmera: Georgetown, Iñigol, Jon y Mariano, con el que he pasado tantos inolvidables momentos en congresos por todo el mundo y en la campaña BLLAST. Gracias también a Francisco S. por iniciarme al WRF y a Samuel V. por dejarnos el camino tan bien allanado a los micrometeorólogos. Gracias a Gema M. de AEMET por estar siempre dispuesta a colaborar científicamente. Y gracias al equipo más laureado del paraninfo, EMOTAMZOR, especialmente a Edgar, su atemporal capitán.

A great part of my work has been possible thanks to the help of Gert-Jan S. I would like to say you thanks for giving me the opportunity of working with you in Wageningen and for all your help there. I also hope to keep on collaborating with you in the future. Thanks also to the friendly people in Wageningen: Eduardo, Daniëlle, Mihau, Marina, Anneke, Folmer, Marie, Henk, Natalie, Jordi, Oscar, Arnold, Bert and Kees. Thanks also to Eric P. for letting me participate in the MATERHORN-X Fog field campaign in Salt Lake City and for being so friendly. Thanks to all the people there, especially to Derek, Chao, Alexei and Sebastian H. for nice IOPs in Heber Valley! Thanks to all the people involved in BLLAST, especially to Marie L., who is always taking care of us, David P., Joan C., Dani, Clara and Estel. Thanks also to Larry M. for pleasant conversations about gravity waves and dogs.

Ahora que he agradecido a las personas de mi ámbito laboral (aunque muchas son ya verdaderos amigos), me gustaría dar las gracias a todos mis amigos de Sanlúcar por estar siempre ahí diciendo tonterías, tan necesarias en la vida. A *Los Caramierdas*: gracias *Nariz*, *Chato*, Manolo, Colóm, Evaristo, *Mazi*, Cristobita, *Hoffman*, *Negro*, Guille, *Joseman*, Ballén, Gorka, Rafa y mis compares Dani y Luismi, compañeros malasañeros de mis primeros años en Madrín. Gracias a todos mis amigos de Madrid y a sus respectivas por no haber tenido reparo en mirar las ruedas y cambiarle el aceite al coche para asistir a grandes barbacoas en Colmenarejo o Galapagar. :-)

Gracias a mis abuelos por haberme enseñado a amar la naturaleza, el mar, los animales y la vida en general, que descansen en paz, yo mientras los seguiré recordando. Gracias a mis tías Mari Carmen y Miriam y a mi casitía Maria del Pilar por criarme desde pequeño; también a mi tía Vicky por acogerme tan bien durante mis días en Dallas. Y gracias por tantos buenos años juntos a mis primos Christopher y David.

Esta etapa en Madrid no hubiera sido igual sin el cuidado de una persona muy especial. Ella me acogió, me alimentó, me arropó, me cuidó como una madre y me contagió unas virtudes que siempre llevaba encendidas: la fuerza, la anti-pereza, la positividad, el buen humor y las ganas de hacer cosas, algo que tanto me ha ayudado para terminar esta tesis. Manoli, aunque no me puedas leer, gracias por todo ello. Me hubiera gustado decirte lo que me alegra que mis hijos lleven una parte de ti. Descansa en paz. Y muchas

gracias también a Martín, por su ayuda constante y por hacerme catador de sus exquisitos guisos, a Inmaculada y a Marta.

Y llega el momento de dar las gracias a mi compañera de vida, Nuria. Nos arrejuntamos al principio de mi doctorado y tú has estado ahí siempre. Al principio gastábamos nuestro tiempo libre sembrando semillas y cultivando lechugas, tomates o coliflores. Hoy en día cosechamos sonrisas, risas y miradas entre las tres (cuatro) personitas que forman nuestra familia* y que cada vez se unen más y más. *Honimonkia*, muchas gracias por esa bonita sonrisa diaria que has compartido conmigo durante estos años, gracias por quererme de esa forma, tal y como soy, gracias por animarme siempre, por aguantar estos meses de fin-de-tesis y por ser la maravillosa madre que tienen y tendrán mis hijos. Este *Te todo* aquí escrito no expresa ni una centésima parte de lo que me gustaría transmitirte y agradecerte.

Mi Zamu. En España no es muy típico tener un hijo mientras haces un doctorado, pero no sé si lo hubiera conseguido de esta forma sin él. En mi caso, Samuel me espabiló desde que me enteré que venía a la Tierra y la verdad es que no sé lo que estaría haciendo ahora mismo si él no estuviera en la cama dormido (que por fin me ha dejado un rato libre para escribir estos agradecimientos mientras me tomo una cerveza). Él embellece la primera ley de la termodinámica y transforma toda mi energía en felicidad. Con tan solo dos años y tanto que agradecerte. :-) Para cuando puedas leerlo, gracias Samu. Y gracias también al nuevo bebesio que llegará en unos meses (probablemente Adrián) por convertirse en una nueva ilusión.

Y en este último párrafo me gustaría dar las gracias a mi familia por haberme hecho como me gusta ser. Gracias a mi hermana mayor Elisa por su bondad conmigo, su compañía y por su cuidado desde que era *el enano* (y gracias a mi sobrinito Martín por ser tan bonito). Muchísimas gracias a mi increíble hermana chica Lourdes, en la que siempre me veo reflejado, pero en versión femenina y 11 años después, mi MOZOM, gracias por ser como eres**. Y para terminar, cómo no, gracias a mis padres por haberme diferenciado siempre el rumbo verdadero del rumbo de aguja. Ahora más que nunca valoro vuestro esfuerzo a lo largo de tantos años. Mamá y papá, gracias por haberme educado como lo habéis hecho, creo que este pequeño logro os lo debo principalmente a vosotros, por eso os quiero dedicar esta tesis con todas mis ganas. :-)

---

* Nuestra familia no estaría completa sin nuestra perra Pimienta. Me gustaría dejar aquí escrito la alegría y tranquilidad que me produce su compañía, siempre moviéndome el rabo y mirándome de la misma forma. Mis días son mucho mejores cuando he paseado con ella.

** Gracias también por haber hecho la mejor portada del mundo posible para mi tesis. :-)

FINANCIAL SUPPORT AND OTHERS

This PhD has been funded by the MINECO grant BES-2013-064585 (*Ayudas para contratos predoctorales para la formación de doctores*), belonging to the National MINECO Project CGL2012-37416-C04-02 and through research contracts within the MINECO projects CGL2009-12797-C03-03, CGL2011-13477-E (BLLAST campaign) and the UCM-Santander Bank projects of the group of *Micrometeorología y Variabilidad Climática* (References: GR 35/10-A and GR 3/14). Also thanks to the Wageningen Institute for Environment and Climate Research (WIMEK) research fellowship for supporting a 5-month scientific stay in Wageningen (The Netherlands). Thanks to all the funding institutions of the BLLAST field campaign.

Thanks also to Dr. F. Bosveld and KNMI for making CESAR data available and Dr. J. Peláez and Prof. J.L. Casanova for access to CIBA facilities.

Thanks to ECMWF and NCEP for providing data used for WRF initialization and to NASA Land Processes Distributed Active Archive Center (LP DAAC) for Routine ASTER Global Digital Elevation Model data. Thanks to the Satellite Receiving Station from Dundee University for providing a high-resolution satellite image.

CONTENTS

Note that hyperlinks (in pdf version) to references, thesis sections and URLs are indicated along the text with green, blue and purple colours respectively.

ABSTRACT

INTRODUCTION AND OBJECTIVES

This thesis deals with the study of two atmospheric phenomena that normally appear in the stable boundary layer (SBL): radiation fog and gravity waves (GWs), processes that are still not well understood. Therefore, their representation in the numerical weather prediction (NWP) models is one of the current challenges for the meteorological modelling. Thus, the main objective of this thesis is to gain knowledge about these phenomena, with especial emphasis to their interactions with turbulence in the SBL.

The work starts with sensitivity experiments of the WRF (Weather Research and Forecasting) mesoscale model, in order to determine the most appropriate physical options for the simulation of fog. Subsequently, radiation-fog forecasting is addressed through two different approaches: numerical modelling (WRF) and statistical methods (M14, Menut et al. (2014)). These two methods are evaluated and compared at two contrasting experimental sites. Finally, new methods for the fog-top height estimation are presented. This variable is usually unknown or subjected to expensive or not-always accessible data. The estimation offered in this thesis is based on turbulent surface measurements (friction velocity and heat flux).

Regarding GWs, on the one hand, a comprehensive observational analysis of near-monochromatic GWs propagated in a duct layer is presented, being difficult to have the chance of analysing a case like this in the real atmosphere. On the other hand, the physical mechanisms governing smaller-scale GWs and drainage flows are elucidated, analysing in detail the interactions of these phenomena with the turbulence in the SBL, which is one of the main current challenges in micrometeorological studies.

METHODOLOGY

The research strategy is based on the analysis of observational data from three experimental sites: the Cabauw Experimental Site for Atmospheric Research (CESAR), the Research Centre for the Lower Atmosphere (CIBA) and the BLLAST (Boundary-Layer Late Afternoon and Sunset Turbulence) field campaign. These data are studied through time series analyses, spatial comparison, statistics, etc. Furthermore, high-resolution surface pressure data from microbarometers have been employed for the analysis of GWs, using wavelet transforms and phase differences analyses. Multi-resolution flux de-

composition methods have also been used for the analysis of high-frequency data from sonic anemometers. Finally, radiation-fog forecasting is evaluated with the mesoscale model WRF and its skill is analysed under different physical parameterizations.

RESULTS

Planetary boundary layer (PBL) parameterizations as MYNN and QNSE offer the best results for radiation-fog forecasting, as well as the use of the gravity-settling option or sophisticated microphysics schemes. The statistical method M14 has been evaluated at CESAR and CIBA, offering satisfactory results, which are also obtained with the use of new predictor variables, such as the friction velocity. However, the combination of this method with output from the WRF model worsened the results. Regarding the simulation of liquid water content (LWC) from the model, it normally offers satisfactory simulations of fog when configured with high resolution and computationally-expensive physical options, although considerably better results are obtained when using long and adequate spin-up times.

On the other hand, fog-top height shows a high linear correlation with the friction velocity and less with the heat flux (for convectively-active fog). The estimation of fog thickness through temperature measurements in the vertical is not possible for shallow or very deep fog.

Regarding GWs, clear and sinusoidal oscillations detected in the surface pressure records during the BLLAST campaign have been associated with GWs formed as consequence of downdraughts located at the wake-low part of a mesoscale convective system (MCS). These GWs were ducted in a layer from surface up to 2000 m above ground level and propagated horizontally in the same direction of the MCS. With respect to the smaller-scale GWs associated with drainage flows, the results show how the turbulent parameters and surface fluxes highly depend on the height and specific location where the measurements are taken when these phenomena are present in the SBL, as well as the necessity of the determination of the spectral gap.

CONCLUSIONS

The numerical forecasting of radiation fog is improved through the specific selection of physical parameterizations. Radiation-fog forecasting through statistical methods is also a valid alternative, specially for nowcasting with observations, results that are especially useful for NWP modellers and operational forecasters. Furthermore, the climatological analysis shows differ-

ences between radiation fog at CESAR and CIBA, mainly caused by their differences in humidity and geographical location.

The fog-top height can be estimated attending to surface values of turbulent measurements, which opens a new way for the estimation of this variable with a unique sonic anemometer deployed at surface and could be operationally implemented.

Regarding the observational analysis of two case studies of GWs, in one of them it has been shown how the ducting mechanism controls the horizontal propagation and features of the GWs, while their formation was linked to downdraughts at the wake low located at the rear part of a MCS. The other case study showed how drainage flows of different scales and GWs govern the turbulence and structure/evolution of the SBL during the evening transition at the BLLAST site. The descriptions provided in this thesis serve to improve the representation of these processes in NWP models. These structures are clearly separated from smaller-scale ones (turbulence) by a spectral gap, which should be taken into account when computing turbulent fluxes. However, there is an open question about the diffusive or non-diffusive character of structures linked to GWs, whose time scales are lower than the GWs ones but higher than those of the turbulent motions.

RESUMEN (SPANISH)

INTRODUCCIÓN Y OBJETIVOS

Esta tesis aborda el estudio de dos fenómenos atmosféricos que aparecen normalmente en la capa límite estable (SBL): nieblas radiativas y ondas de gravedad (GWs). Estos procesos no están bien comprendidos y por lo tanto su representación en los modelos numéricos es uno de los desafíos a los que se enfrenta la modelización meteorológica futura. De esta forma, el principal objetivo de esta tesis es ampliar el conocimiento sobre estos fenómenos, con un enfoque especial a sus interacciones con la turbulencia en la SBL.

El trabajo comienza con experimentos de sensibilidad del modelo WRF (*Weather Research and Forecasting*) para la determinación de las opciones físicas más apropiadas para la predicción de nieblas. Posteriormente, se aborda la predicción de nieblas a través de dos enfoques diferentes: modelización numérica directa (WRF) y métodos estadísticos (M14, Menut et al. (2014)). Estos dos métodos son evaluados y comparados en dos centros experimentales diferentes. Por otro lado, se presenta una climatología estadística robusta con el objetivo de señalar las diferencias más importantes entre las nieblas radiativas en ambos sitios. Finalmente, se ofrecen nuevos métodos para la estimación de la altura del tope de la niebla. Esta variable es normalmente desconocida o está sujeta a la disponibilidad de datos de difícil adquisición. La estimación que se ofrece en esta tesis se basa en medidas superficiales de turbulencia (velocidad de fricción y flujo de calor).

Con respecto a las GWs, por un lado se presenta un análisis observacional único de GWs casi monocromáticas propagadas en un canal, siendo difícil tener la oportunidad de analizar observacionalmente un caso como éste. Por otro lado, se muestran los mecanismos físicos que gobiernan GWs de menor escala y flujos de drenaje, analizando en detalle las interacciones de estos fenómenos con la turbulencia en la SBL, tema que es uno de los actuales desafíos de los estudios micrometeorológicos.

METODOLOGÍA

La estrategia de investigación se basa en el análisis de datos observacionales de tres áreas experimentales: *the Cabauw Experimental Site for Atmospheric Research* (CESAR), el Centro de Investigación de la Baja Atmósfera (CIBA) y la campaña experimental *Boundary-Layer Late Afternoon and Sunset Turbu-*

lence (BLLAST). Estos datos se estudian mediante análisis de series temporales, comparaciones espaciales, estadística, etc. Además, se han empleado datos de presión de alta resolución de microbarómetros para el análisis de GWs usando la transformada wavelet y análisis de diferencias de fase, así como métodos multi-resolución de descomposición de flujos (MRFD) para el análisis de datos de alta frecuencia de anemómetros sónicos. Finalmente, la predicción de nieblas radiativas es evaluada con el modelo WRF y se analiza su comportamiento ante el uso de diferentes parametrizaciones físicas.

RESULTADOS

Esquemas de capa límite planetaria (PBL) como MYNN o QNSE ofrecen mejores resultados para la predicción de nieblas, así como el uso de la opción de caída gravitacional de gotitas o esquemas complejos de microfísica. El método estadístico M14 ha sido evaluado en CESAR y CIBA, ofreciendo resultados satisfactorios, que se obtienen también mediante el uso de nuevas variables predictoras, como la velocidad de fricción. Sin embargo, la combinación de este método con salidas numéricas del modelo WRF ofrece peores resultados. Atendiendo a la simulación de contenido líquido acuoso (LWC) del modelo, éste ofrece predicciones satisfactorias de nieblas cuando se configura con opciones de alta exigencia computacional, aunque se obtienen resultados considerablemente mejores usando *spin-up* largos y apropiados.

Por otro lado, la altura del tope de la niebla muestra una alta correlación lineal con la velocidad de fricción y algo menor para el flujo de calor (para nieblas activas convectivamente). Su estimación mediante medidas de temperatura en la vertical no es posible para nieblas someras o muy profundas.

Respecto a las GWs, oscilaciones claras y sinusoidales en los registros de presión durante la campaña BLLAST se han asociado a GWs formadas por corrientes descendentes en la *wake low* de un sistema convectivo de mesoescala (MCS). Estas GWs se canalizaron en una capa desde superficie hasta unos 2000 m sobre el nivel del suelo y se propagaron horizontalmente en la misma dirección que el MCS. Atendiendo a GWs de menor escala relacionadas con flujos de drenaje, los resultados muestran cómo los flujos y parámetros turbulentos dependen de la altura y la localización específica donde se tomen las medidas cuando estos fenómenos están presentes en la SBL, así como también es necesario determinar el *gap* espectral.

CONCLUSIONES

La predicción numérica de nieblas radiativas se ve mejorada mediante la selección apropiada de parametrizaciones físicas. El método estadístico M14 es

también una alternativa válida, sobre todo para la predicción inmediata de nieblas radiativas mediante observaciones, resultados que son especialmente útiles para modelizadores y predictores. Por otro lado, la climatología señala diferencias entre las nieblas radiativas en CESAR y CIBA, relacionadas con las diferencias en humedad y localización geográfica.

La altura del tope de la niebla puede ser estimada atendiendo a valores superficiales de medidas turbulentas, resultado que abre una nueva vía para la estimación de esta variable con un anemómetro sónico en superficie, lo cual podría ser aplicado operacionalmente.

Atendiendo al análisis observacional de dos casos de estudio de GWs, en uno de ellos se ha mostrado cómo el mecanismo de canalización controla la propagación horizontal y las características de las GWs, mientras que su formación se asoció a corrientes descendentes de la *wake low* de un MCS. El otro caso de estudio muestra cómo los flujos de drenaje de distintas escalas y las GWs gobiernan la turbulencia y la estructura/evolución de la SBL durante la transición nocturna en el área de BLLAST. La descripción ofrecida en esta tesis puede servir para mejorar la representación de estos procesos en los modelos numéricos. Estas estructuras están separadas de escalas menores (turbulencia) mediante un *gap* espectral, hecho que deber ser tenido en cuenta a la hora de calcular flujos turbulentos. Sin embargo, aún queda una pregunta abierta sobre el carácter difusivo o no de las estructuras asociadas a GWs, cuyas escalas son menores que las de las propias GWs pero mayores que las de los movimientos turbulentos.

INTRODUCING THE THESIS

Best decisions do not need a deep thinking to start. This is questionable in science.

1

INTRODUCTION AND OBJECTIVES

This thesis deals with two important and relevant atmospheric phenomena (radiation fog and gravity waves) and their interactions with turbulence and other processes of the atmospheric boundary layer. These processes and their respective state-of-the-art are introduced in this chapter, as well as some basic notions needed to understand the planetary boundary layer and, specially, the difficulties and complexity of stable boundary layers. However, each chapter of results includes a more specific introduction to the particular problem addressed.

The last section of this introductory chapter resumes the outline and the main objectives of the thesis.

1.1 PLANETARY BOUNDARY LAYER

The *planetary boundary layer** (PBL) is the region of the troposphere formed as consequence of the interactions between the atmosphere and the underlying surface (land or water) (Arya, 2001) and where human beings live (Figure 1.1). Numerous atmospheric processes are found in this layer, such as fog, low clouds, sea/mountain breezes, microclimates, low-level jets, drainage flows or some types of gravity waves.

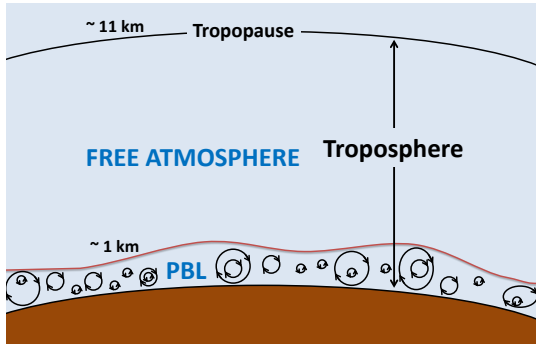

Figure 1.1: Schematic representation of the PBL within the troposphere. Adapted from Fig 1.1 of Stull (1988).

The air motions in the PBL are mainly chaotic and produced by two main mechanisms: wind shear or buoyancy. The result of both processes is to form irregular and chaotic motions of air at different scales (*eddies*), whose addition defines the so-called *turbulence* in the PBL. This turbulence or turbulent mixing in the PBL is characterized by a high diffusivity, i.e., it can effectively spread and redistribute momentum, heat or scalars like moisture or pollutants (for example CO_2). However, turbulence is not only important for their redistribution in the atmosphere; it is also crucial for the exchange of momentum, heat, humidity or CO_2 between the surface and the atmosphere, best-known as *momentum*, *sensible heat*, *latent heat* or CO_2 *fluxes*.

The thickness of the PBL is associated with the size of the eddies; it varies from one place to another and especially due to the diurnal cycle. The typical PBL in mid-latitudes is called *convective boundary layer* (CBL) during a great part of the daytime when the Sun is heating the surface. Soon after sunrise, the heated bubbles of air located close to the surface rise due to their lower density (buoyancy) and form the CBL, which reaches its maximum

* Also known as *atmospheric boundary layer* (ABL) or *boundary layer* (BL).

depth during the afternoon (~ 1-2 km). Some minutes (or a few hours) before sunset, the CBL is totally transformed from the ground into a different layer, known as the *stable boundary layer* (SBL). The decrease in the incoming energy from the Sun causes a negative energy balance at surface and, consequently, a net radiative cooling that hampers the convective vertical motions (positive buoyancy), since now the air is colder and denser near the ground (Van de Wiel et al., 2012). Thus, the turbulence in the SBL is mainly produced by wind shear (variations of wind with height), which makes the SBL be shallower than the CBL (Stull, 1988). Besides this, the turbulence in the SBL acquires an intermittent nature (Van de Wiel et al., 2003; Vindel et al., 2008), often produced by several complex and sometimes unknown mechanisms. However, a remaining and somehow decoupled mixed layer usually persists above the stable boundary layer during the nighttime. This layer is known as the *residual layer* and can influence the growing of the PBL during the next day (Lothon et al., 2014). Figure 1.2 shows a picture of an idealised evolution of the PBL during the diurnal cycle, adapted from a classic figure of Stull (1988).

Smoke from low chimneys usually moves horizontally quite close to the surface under stable stratification.

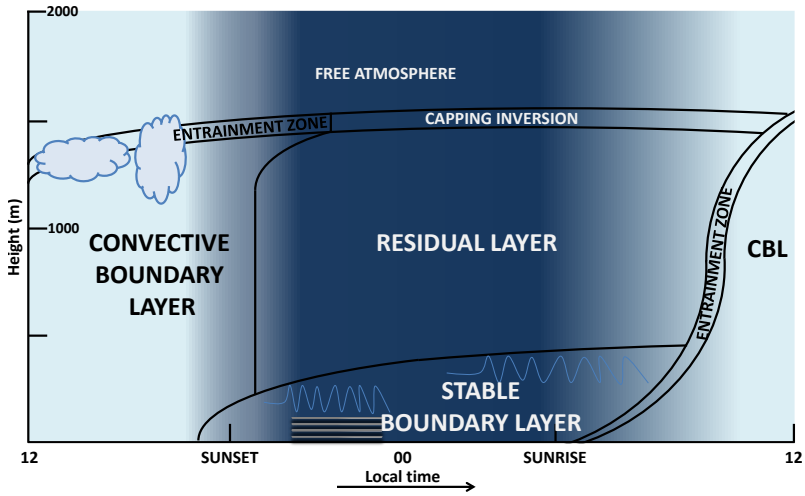

Figure 1.2: Schematic and idealised representation of the typical PBL evolution during the diurnal cycle over fair-weather zones in mid-latitudes. The two processes addressed in this thesis (gravity waves and fog) are included in the SBL. Adapted from Fig 1.7 of Stull (1988).

Although most SBLs are formed by the radiative cooling at surface, they are not limited to nighttime conditions. They are found in typical long-lasting stable situations of polar regions during persistent nighttime conditions, specially in winter, when the radiation from the Sun is greatly reduced (Yagüe and Redondo, 1995). They can also be formed as the result of warm

advections over colder coast waters (Smedman et al., 1993) or over irrigated regions (Steeneveld, 2014).

These differences between CBL and SBL are traduced into different vertical profiles of temperature. In the first case, the potential temperature*(θ) is nearly constant in the whole CBL (near neutral stratification or even unstable close to the surface), since the layer is well-mixed due to the intense turbulence and heating of the surface. However, in the SBL the stratification is stable (the potential temperature increases with height) due to the radiative cooling of the surface. In many occasions, even a surface-based thermal inversion forms from the surface, where the temperature (not potential) also increases with height. Figure 1.3 is a representative case of the temperature cycle close to the surface during a clear day and its relation with the incoming short-wave radiation from the Sun and surface heat flux.

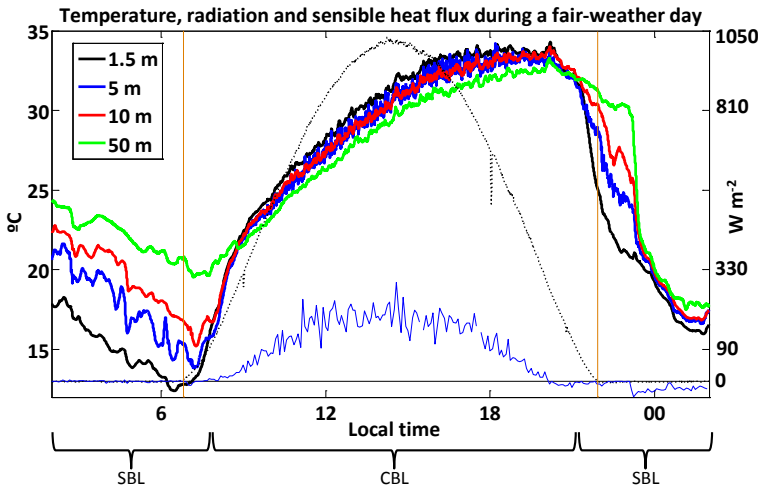

Figure 1.3: Temperature (°C) during a fair-weather day (28 June 2015) at the Research Centre for the Lower Atmosphere (CIBA) at different heights (1.5 m (black line), 5 m (blue line), 10 m (red line) and 50 m (green line)). The incoming short-wave radiation (W m^{-2}, black thin dashed line) shows a well-defined "bell shape", according to the clear-sky conditions. Sensible heat flux (W m^{-2}) is shown with blue thin line; its shape indicates the buoyancy (convection) soon after the sunrise until some time before the sunset. The heat flux is negative (around 0 W m^{-2}) when the SBL is established. Orange vertical lines indicate the sunrise and the sunset.

* Potential temperature is the temperature that an air parcel located at some height would have if it were adiabatically descended into a reference level (usually 1000 hPa). It is very useful for the comparison of temperatures of air parcels at different heights.

The physical processes in the CBL are in general better understood than those produced in the SBL (Fernando and Weil, 2010). This is consequence of the larger-scale motions found in CBLs, which make their observation easier, as well as their representation in numerical models. On the other hand, SBLs are dominated by smaller scales, which are more difficult to detect with instruments and definitely harder to be numerically represented. Thus, numerical weather prediction (NWP) models have problems representing SBLs (Holtslag et al., 2013; Steeneveld, 2014), for example related to PBL evening transitions (Sastre et al., 2012; Lapworth, 2014), minimum temperatures (Blay-Carreras et al., 2015), low-level winds (Cuxart, 2008; Storm et al., 2009) or sporadic turbulence (Steeneveld, 2014). One of the reasons of these failures is the existence of many interrelated physical processes and features affecting the formation and evolution of SBLs at the same time, among which are:

1. *Net radiation* –> Mainly controlled by the long-wave radiation. The surface cools at different rates depending on its temperature, which at the same time depends on the soil type, land use, wind, cloud cover, etc. Besides this, each atmospheric layer emits a different amount of radiation according to its temperature (radiation flux divergence), gas concentration, etc.; therefore, the degree of stratification becomes very important (Hoch, 2006; Steeneveld et al., 2010).

2. *Turbulence* –> It is mainly generated by the wind shear among different layers and it also appears sporadically as the result of other complex processes. Stably stratified layers prevent the vertical motions and reduce the turbulence. The turbulence is thus governed by the wind and temperature at different levels. These variables can be quite different between relatively closer layers. For a complete understanding of turbulence in SBLs and in PBLs in general, the readers are referred to the following text books: Stull (1988), Sorbjan (1989), Garratt (1994), Arya (2001) or more specifically to Wyngaard (2010).

3. *Surface fluxes* –> In ideal land-atmosphere coupled systems, the surface-fluxes sum should be equal to the net radiation, but the energy balance closure problem (Foken, 2008) remains unsolved. Sensible heat flux is determined by the differences in temperature between the ground and the air above and by the wind speed. It is normally small and negative (downward heat flux) in SBLs, which means that the heat is transferred from above (warmer) to below (colder). Latent heat flux is determined by the differences in moisture between the ground and the underlying air and by the wind. The larger it is, the lower the sensible heat flux

is. Ground heat flux is determined by the differences in temperature between the different layers within the ground. For more information about surface fluxes, see Stull (1988), Arya (2001) or Vilà-Guerau de Arellano et al. (2015).

4. *Type of soil, land use, vegetation and surface water availability* –> These characteristics, whose parameters are usually tabulated in tables in NWP models, affect the capacity of heat and humidity storage of the ground and the surface fluxes (Pan and Mahrt, 1987). See Moene and van Dam (2014) or Vilà-Guerau de Arellano et al. (2015) for a state-of-the-art review of these topics.

5. *Low-level jets* –> The air at some height above the SBL becomes frictionless and speeds up usually until supergeostrophic values. These winds can also transport scalars effectively into large distances. See Sisterson and Frenzen (1978), Cuxart (2008), Storm et al. (2009) or Van de Wiel et al. (2010) for more information.

All of these SBL processes are at the same time influenced by the local topography and heterogeneities of the surface.

6. *Sea breezes* –> They form as the result of the different heat capacity of the land and the sea. They blow from sea to land during the day and vice versa during the night (SBL) and can be responsible of significant humidity and temperature variations. See Miller et al. (2003) for a broad review.

7. *Drainage flows* –> They appear under low-synoptic forcing in mountain regions or even in slightly sloped terrains as a consequence of the differential radiative cooling between more elevated and lower areas (Whiteman, 2000). When they appear, they can also change the structure of the SBLs through the generation of turbulent mixing at some heights, topic that is analysed in Chapter 7.

8. *Dew deposition* –> Small droplets of water condensate over certain surfaces, which are normally colder than the air. It represents a loss of water content of the air and a moistening of the ground (Agam and Berliner, 2006). It also affects the radiative cooling rate and consequently the surface fluxes.

9. *Submeso motions* –> Complex structures of scales ranging between turbulent eddies and the smallest mesoscale motions (~ 2 km). They include microfront-like structures, horizontal modes, solitons, ramp structures, gravity waves, etc. See Mahrt (2007) or Mahrt (2014) for more information and deeper descriptions.

10. *Fog* –> Boundary-layer clouds that appear at the surface and affect significantly the evolution of the PBL. Section 1.2 includes a complete description of this phenomenon.

11. *Gravity waves* –> Oscillations of air parcels at different scales. In SBLs they are usually associated with the microscale, although the effect of other larger-scale waves can influence the SBL properties. They can transport momentum and energy and their representation in numerical models is challenging. See Section 1.3 for a deeper explanation.

With this myriad of processes connected among them, it is not strange to state that a theoretical understanding of SBLs is still and unachieved goal (Mahrt, 2014) and a challenging task for the improvement of NWP models (Van de Wiel et al., 2003; Baklanov et al., 2011; Seaman et al., 2012; Holtslag et al., 2013; Davy and Esau, 2014; Fernando et al., 2015). This will lead to better weather forecasts, which are specially important for wind energy resources (Sisterson and Frenzen, 1978; De Rooy and Kok, 2004; Storm et al., 2009), agriculture (Snyder and Melo-Abreu, 2005; Prabha and Hoogenboom, 2008) and fog (Van der Velde et al., 2010) or air-quality (Andrén, 1990; Baklanov et al., 2009) forecasts among others.

In this thesis, two of these processes are deeply addressed: radiation fog and gravity waves*. Accordingly, these two phenomena are more specifically introduced in the two next sections.

* Gravity waves are not exclusive phenomena of SBLs, since they can appear in upper stable layers. However, this thesis focuses on the effects of them on the SBL.

1.2 RADIATION FOG

The capacity of the air for storing water vapour decreases exponentially with decreasing temperature. That is, the colder the air is, the less water vapour it can contain. Thus, when the temperature decreases, the relative humidity (RH) increases progressively following Equation 1.1:

$$RH\ (\%) = \frac{e}{e_w(T)} \times 100, \tag{1.1}$$

where e is the *actual water vapour pressure* of the air and $e_w(T)$ is the *saturated water vapour pressure** or the maximum water vapour pressure possible for that air mass at the same ambient temperature. Therefore, RH can vary by changing the amount of water vapour content (e) or the temperature (and therefore e_w) of the air mass. In all the cases, if the conditions are appropriate, small droplets of water (or ice) can appear suspended in the air if the relative humidity increases up to values near 100%. *Fog* is then defined when these small water droplets (or ice crystals) reduce the horizontal visibility close to the surface to less than 1 km (DOC/NOAA, 1995), while *mist* is defined when the visibility oscillates between 1 and 5 km (WMO, 1967).

However, most variations of RH in the PBL are caused by changes in temperature, where this variable strongly depends on the diurnal cycle (Betts, 2001). Some minutes (or a few hours) before the sunset, the surface starts to cool radiatively and the adjacent air layer above also cools by contact with this surface. This cooling is extended upwards by turbulence and consequently, the relative humidity of the air increases gradually until, in some cases, it reaches saturation values. When this happens, condensation is observed first over the ground and over some surfaces, since they are generally colder than the air. If conditions are appropriate and the relative humidity is high enough, condensation occurs in the air over small particles called cloud condensation nuclei (CCN) and fog starts to form. The explained phenomena corresponds to the initial formation mechanism of the most common type of fog, known as *radiation fog* (Roach et al., 1976; Guedalia and Bergot, 1994). Although there are other very important and interesting types of fog (Tardif and Rasmussen, 2007), the physical processes involved in their formation and evolution are different and they will not be analysed in the present thesis.

Water droplets or ice crystals in fog have a typical diameter between 5 to 50 μm.

* This amount is tabulated in tables and can be calculated using empirical formulas (e.g. Tetens formula) or the temperature-water vapour curve.

Radiation fog in mid-latitudes usually forms over land some time after sunset under clear-sky and low-wind conditions, usually associated with weak synoptic forcing related to low horizontal pressure gradients. No-clouds conditions are needed to allow an effective radiative cooling at the surface and to form a stably stratified boundary layer, while low-wind conditions prevent from the turbulent mixing caused by wind shear. Nevertheless, other factors play a determinant role in the formation of radiation fog (Figure 1.4).

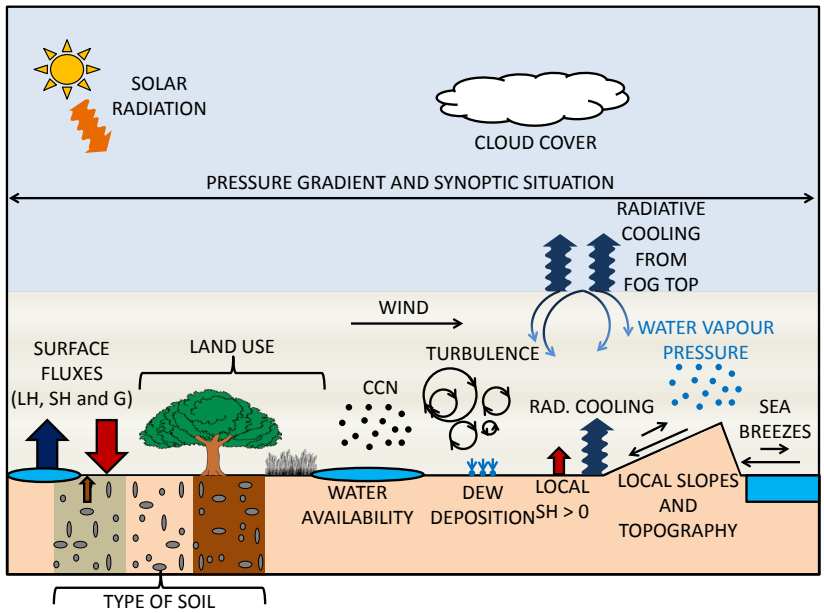

Figure 1.4: Schematic representation of some of the particularities and physical processes affecting the formation and life cycle of radiation fog.

Radiation fog takes its name from the RADIATIVE cooling needed at surface to cause the condensation. However, many other processes play a determinant role.

One of the most important is the availability of water vapour content in the PBL. That is, if this amount is too low, RH will hardly increase until saturation values. On the other hand, if the terrain is very dry and absorptive, it will rapidly absorb the water droplets condensed over the ground, preventing the formation of fog through the reduction of water vapour in the lowest meters of the SBL. Thus, the land use, the soil type or the snow coverage (Figure 1.5) are important factors for fog formation. Another crucial requirement for the formation of fog is the availability of enough CCN, suggested long time ago by Mensbrugghe (1892) and later by Willett (1928). The number of CCN is at the same time determined by the proximity of urban areas (anthropogenic contaminants), sea (salt), arid or plow regions (dust) and previous wind conditions (Twonisvi and Wojciechowski, 1969; Andreae and Rosenfeld, 2008).

The complexity of the terrain is also very important for the development of radiation fog (Müller et al., 2010); it prevails in flat areas, where the absence of slopes favours the radiative cooling. Otherwise, down-slope winds can form and the fog formation hampered in the slopes and favoured in valleys or cool pools (Martínez et al., 2010) (so-called valley fog), or oppositely, favoured in the slopes within upslope flows (anabatic winds, upslope fog). As stated in Müller et al. (2010), these mechanisms can favour the correct forecast of fog if the topography is well represented in the model rather than difficult it. Additionally, sea breezes and even the sea surface temperature can significantly influence the formation or dissipation of fog through modifications in humidity and temperature (Bari et al., 2015).

Figure 1.5: Fog dissipation stage (after sunrise) at Heber Valley (Utah, USA) on 16th January 2015 at 09:59 UTC during the MATERHORN-X Fog field campaign (note the tethered balloon in the background). Frozen conditions add complexity to the simulation of fog (Van der Velde et al., 2010).

No less important is the role of the turbulence on radiation-fog formation. While some authors (Welch and Wielicki, 1986) support the theory that turbulence acts favouring the formation of fog, others (Roach et al., 1976) established that turbulence acts favouring the dissipation. It seems that there exists a threshold on the relation between turbulence and fog development (Zhou and Ferrier, 2008), since a minimum turbulence is needed to start developing the fog in the vertical. Otherwise, the fog will not be formed and the small droplets will be finally deposited on the ground in the form of dew.

Once the fog is formed, other factors become more important for its development, such as the downward turbulent motions generated by the radiative cooling at the top of the fog (Nakanishi, 2000; Porson et al., 2011; Price, 2011). These downward motions generate enough turbulence to change the vertical profile of the fog and mix the whole fog layer. Besides, other processes as local heating of the surface (generating positive sensible heat fluxes) and gravity-waves (Duynkerke, 1991) breaking can also help generating turbulence inside the fog. However, the incoming solar radiation after sunrise is the more common source of energy affecting the dissipation of fog, although in some particular persistent cases, the incoming short-wave radiation acts extending the fog in the vertical rather than dissipating it, as it will be seen in a case study analysed in Chapter 5. This dissipation is normally produced first over the outer edges of the fog, due to the circulation generated by the differential heating of the surface beyond and beneath the fog (Gurka, 1978).

It is very difficult or almost impossible to handle with all the phenomena involved in this myriad of processes (Figure 1.4) at the same time. This thesis focuses mainly on the relation between turbulence and fog, either the turbulence associated with the formation of radiation fog or the turbulence generated by the fog itself when it is well-mixed. Nevertheless, other micrometeorological and non-turbulent parameters are also taken into account along the thesis for the statistical and numerical forecasting of radiation fog.

The scientific interest in fog understanding has been present for years because of its effects on the daily life of humans. Gultepe et al. (2007) present a review of fog history since Aristotle's times. Nowadays, the societal problems associated with the poor visibility conditions caused by fog are well known, specifically those related to aerial (Fabbian et al., 2007), maritime (Fu et al., 2010) and terrestrial (Bartok et al., 2012) transportation. Regarding the aerial transportation, fog can cause cancellations, delays or deviation to other airports (Stolaki et al., 2012). This fact results in substantial losses for airlines and airports, comparable to the costs related to tornadoes destruction (Gultepe et al., 2007). Gaseous air pollutant levels can also be modified during foggy conditions and affect the number of asthma cases over certain regions (Tanaka et al., 1998). However, the effect of these boundary-layer clouds is not always negative, since in many sites of the world they are used as a water source for humans through the use of fog collectors (Schemenauer and Cereceda, 1994; Klemm et al., 2012). Fog also serves as an additional source of nutrients (within CCN in droplets) and water for trees (Azevedo and Morgan, 1974; Gultepe et al., 2007) through the natural collection of water by leaves and roots from the water drips at the ground (Dawson, 1998). Finally, it is reasonable to take into account among the influences, those related to the fog impacts over the evolution of the SBL and the CBL of the

next day. Fog modifies significantly the values of temperature close to the surface; once formed it prevents from the additional radiative cooling during night (increasing the minimum temperature) and if it persists during the daytime, it can reduce the maximum surface temperature reached, with all the implications that this fact can have over the logistics of human activities. Therefore, a correct prediction of fog and its duration is specially important for an accurate prediction of the surface temperature.

Despite the numerous influences of fog on daily life of humans and ecosystems, it is still poorly forecasted by NWP models (Bergot et al., 2007; Müller et al., 2010; Price et al., 2015; Steeneveld et al., 2015). One of the causes of the unsuccessful prediction of fog is the interaction of some of the processes previously commented (Gultepe et al., 2009), which are difficult to capture by models: radiative cooling during fog formation and heating during fog dissipation, pre-fog turbulence intensity, turbulence generated by fog itself (Cuxart and Jiménez, 2012), concentration of cloud condensation nuclei (CCN), surface water availability, particular features of the area influencing local winds, nearby advections, local positive heat fluxes during fog, etc.

Thus, many studies analyse the sensitivity of NWP models to different technical configurations or physical parameterizations that try to capture these processes (Bergot and Guedalia, 1994; Pagowski et al., 2004; Van der Velde et al., 2010, or the sensitivity analyses presented in Chapter 3). Some of the cited fog-modelling problems have been investigated with the Weather Research and Forecasting (WRF) model, which allows the use of different combinations of physical options, domain configuration or the application of data assimilation. Müller et al. (2010) evaluated WRF for a fog case in the Swiss midland and found particular sensitivity to the microphysics scheme, as well as high liquid water content (LWC) in the early fog stage using Ferrier microphysics scheme, which were avoided by an enhanced representation of droplet sedimentation, as also found in Katata et al. (2010) and in Katata et al. (2011). Kim et al. (2014) also focused on microphysics schemes (for ice fog) and found how the newly implemented homogeneous freezing process generates a greater concentration of ice crystals than the original Thompson scheme. Moreover, Steeneveld et al. (2015) found how the onset of the modelled fog was more sensitive to the PBL scheme used and the dissipation, instead, to the microphysics parameterization. On the other hand, Payra and Mohan (2014) and Ryerson and Hacker (2014) obtained warm temperature and negative relative humidity biases during fog periods and stated that LWC is not an useful direct model output for fog-forecasting, as Van der Velde et al. (2010), who showed how the WRF model was able to provide correct values of temperature and mixing ratio, but had problems reproducing LWC. There is also a continuous effort by the modelling community to

improve fog forecasting through the incorporation of new physical parameterizations (e.g. Katata et al., 2011) or increasing resolutions (Boutle et al.). In this context, the first main objective of this thesis (see Section 1.4 for a complete list of objectives) is to test the ability of the WRF model simulating radiation fog under different parameterizations, which is the main content of Chapter 3.

However, NWP models also have fog-forecasting issues associated with the role of initial conditions (Rémy et al., 2012; Bari et al., 2015) and the use of appropriate vertical (Tardif, 2007) and horizontal (Tang et al., 2009) resolutions. Hence, statistical models and observation-based techniques are also valid options for short-term forecasting and nowcasting* of fog (Bocchieri et al., 1974; Pasini et al., 2001; Fabbian et al., 2007). Against this background, Menut et al. (2014) (hereinafter M14) have recently published a method based on threshold values of key variables for radiation-fog formation (pre-fog periods) around the SIRTA area in Paris (Haeffelin et al., 2005, 2010). They used this method with observations and with output from a NWP model. Their results showed how 87% of radiation-fog events were detected using observations and 74% using output from the WRF model in analysis mode. Thus, the second main objective of this thesis is to extend M14 method through an evaluation of its robustness in forecasting radiation fog at two sites with different conditions: the Research Centre for the Lower Atmosphere (CIBA) in Spain and the Cabauw Experimental Site for Atmospheric Research (CESAR) in the Netherlands (Chapter 4). Besides, an evaluation and discussion of the ability of the WRF model simulating directly radiation fog (in terms of LWC output) at these sites is also presented and compared to the previously commented statistical method (M14), corresponding to the third objective of the thesis.

Since these sites are contrasting in terms of geographical situation, humidity, altitude and climate zone (Cfb for CESAR and Csb for CIBA, Köppen-Geiger climate classification**), a climatology of radiation-fog events at CESAR and CIBA through robust 6-year statistics is also provided in Chapter 4. As stated in Gultepe et al. (2007), reliable fog statistics (e.g. Syed et al., 2012; Scherrer and Appenzeller, 2014) are necessary and useful tools to better understand the nature of fog and improve its predictability. Therefore, the fourth objective of this thesis is to detect and establish climatological differences on radiation fog at these two contrasting sites.

---

* Nowcasting is defined as a weather forecast for the next 6 hours.

** Cfb corresponds to *Oceanic climate* and Csb to *Warm-summer Mediterranean climate*.

During the comparison of forecasted fog with observed ones in this thesis, it has become aware the importance of having good estimations of fog-top height for validation of model simulations. In addition, numerical models have problems simulating the fog vertical extension (e.g. Guedalia and Bergot, 1994; Shi et al., 2012, or the case presented in Chapter 3), in part due to the vertical resolution of models. Comparisons between observed and simulated fog thickness cannot be done in many cases due to the lack of fog-top observational data. On the other hand, there is no doubt about the importance of an accurate information of fog thickness for data assimilation of NWP models, due to the significant impact of fog thickness on the radiation budget close to the surface (Rémy and Bergot, 2009). This parameter is also crucial to help with the nowcasting of fog dissipation, since the clearing of deeper radiation fog requires more time than for shallower fog. Finally, the knowledge of the fog-top height can be a quite meaningful information for aircraft pilots when they are landing in foggy conditions, specially in potential emergency cases without Instrument Landing System (ILS). Most airports have regulatory meteorological instrumentation composed by surface visibilimeters, a ceilometer (measuring cloud base and cloud cover) and standard meteorological instrumentation, but all these data are not enough to provide information about fog-top height.

Despite the numerous potential applications of this variable, its knowledge or estimation is not always clear. Many studies cannot provide information about observed fog-top height due to the lack of measurements in the vertical. In many cases, temperature and humidity data from atmospheric soundings are used to estimate it (e.g. Koračin et al., 2001; Liu et al., 2011; Boers et al., 2013; Bari et al., 2015). However, these soundings are not always available or their temporal frequency is not sufficient to cover the whole fog cycle. In other cases, reflectivity-based instruments are used to estimate the fog top. Dabas et al. (2012) studied the ability of using reflectivity measurements from SODAR to estimate fog-top height, while Boers et al. (2013) derived visibility from radar reflectivity for a case study of radiation fog. Ceilometers detect cloud-base height of low clouds (e.g. Dupont et al., 2012), but they are not useful to provide information about fog-top height. All these instruments are usually expensive and sometimes their vertical resolution is not appropriate compared to the fog thickness.

On the other hand, data or products from satellite have been widely used to detect fog or low clouds in numerous fog analyses (e.g. Reudenbach and Bendix, 1998; Van der Velde et al., 2010). In these cases, difficulties appear when trying to differentiate between fog and low clouds. Thus, Ellrod (1995) developed a technique to approximate fog thickness from brightness differences of two IR channels. Thereafter, Brenguier et al. (2000) related cloud

thickness with liquid-water path from remote sensing using an adiabatic model, assuming liquid water content increasing from cloud base to the cloud top. Bendix et al. (2005) proposed the determination of low stratus thickness and top height of clouds (fog) from MODIS daytime data in order to differentiate between low clouds and fog. Alternatively, Cermak and Bendix (2011) developed a method for the determination of low-stratus thickness from MSG-SEVIRI data. However, most of these methods have to estimate liquid water path from satellite, and in some cases they do not offer the high vertical resolution required for fog studies. Besides, thin cirrus can also obstruct the detection of fog and the availability of the data needed for these approaches can be limited in some cases. In any case, fog is defined as a visibility threshold, but unfortunately, only a few works have the opportunity of using visibilimeters deployed at different heights to determine the fog top (e.g. Guedalia and Bergot, 1994). These problems are addressed in Chapter 5, where an indirect method for the estimation of the fog-top height is presented. This method is based on the relation found between fog thickness and surface turbulence (friction velocity or buoyancy flux) and corresponds to the results of the fifth main objective of the present thesis. The relation is statistically calculated by using data from numerous radiation-fog events at CESAR and CIBA. A potential applicability of this method could provide a continuous estimation of fog-top height during radiation-fog events with the deployment of a unique sonic anemometer at the surface.

Finally and connected with the physical processes of the last method, an evaluation of the estimation of fog thickness trough temperature measurements in the vertical is presented in Chapter 5 (sixth thesis' main objective). The homogenization within well-mixed fog (Nakanishi, 2000; Porson et al., 2011; Price, 2011) causes temperature convergence at the levels where the fog is present. Price (2011) suggested that the temperature convergence did not occur for shallow fog, although he was not able to show this issue, since its statistical observational study did not include fog-thickness data. In this thesis, a comparison between real observed fog thickness (through visibility measurements at different heights) with estimations of fog-top height based on differences between temperature measured at several heights is provided.

1.3 GRAVITY WAVES

Waves in fluids are manifested by oscillations of fluid particles moving with a slight phase difference between them and their neighbouring particles (Nappo, 2012). They are named gravity waves (GWs) when the restoring force of gravity (buoyancy) acts to recover the equilibrium state after the destabilization caused by some trigger mechanism (e.g. the orography) in a stable stratified fluid or at the interface between two media of different densities. In the atmosphere, air parcels acquire a vertical component of motion after this destabilization and tend to oscillate while trying to recover their initial state. Although GWs are common phenomena in the atmosphere, they are one of worst understood physical processes (Nappo, 2012), partly due to the fact that they are (normally) not visible to the human eye.

An analogy of atmospheric GWs is possible with sea waves (wind waves); the latter form at the interface of two fluids with contrasting densities, where the water (below) is considerably denser than the air (above). That is, oceanic waves also form in stable environments, but logically, the contrast in density is much higher than the density gradient in the atmosphere (Figure 1.6).

Although GWs in the ocean are called surface waves, they also extend within the water up to some depth and interact with the sea-bottom close to the shoreline.

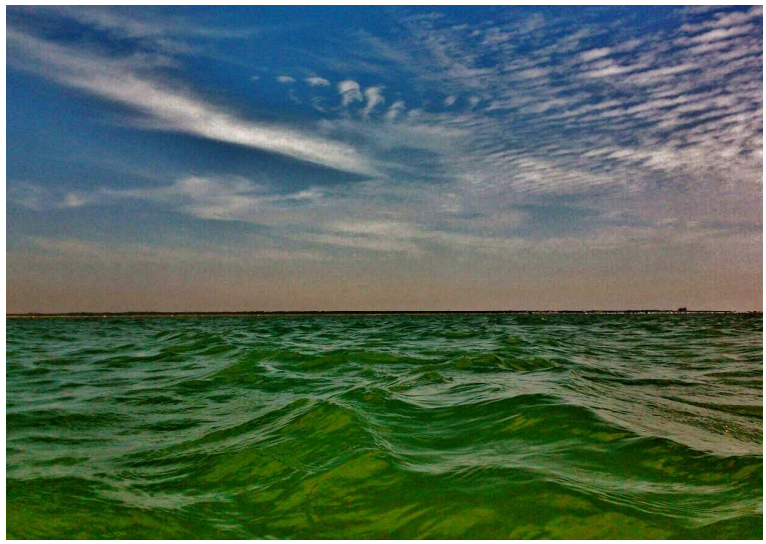

Figure 1.6: Gravity waves at the sea surface forming sea waves and at the mid-upper levels of the troposphere forming wave-like clouds. The formation of both types of waves requires stable environments and density decreasing with height; this contrast in density is logically much higher at the interface between the sea and the atmosphere. Picture taken at La Jara beach, Sanlúcar de Barrameda (Cádiz, Spain) on 11 August 2015 at 11:15 UTC.

Most waves in the ocean are formed by wind stress*, which causes an important shear between these two different fluids (the air is moving much faster than the water). However, GWs in the atmosphere can be initiated by air displacements (buoyancy-forced GWs, Sun et al. (2015a)) or by shear instabilities (vorticity waves, Carpenter et al. (2013), see also Figure 1.7). These two mechanisms can be triggered by several processes. Although these processes are varied, complex and many times difficult to detect in the real atmosphere, several of them have been proposed in the literature:

1. Geostrophic adjustment (e.g. Luo and Fritts, 1993).
2. Topography (e.g. Nastrom and Fritts, 1992).
3. Jet streams (e.g. Fritts and Nastrom, 1992).
4. Wind shear (e.g. Merrill and Grant, 1979).
5. Convective currents (e.g. Lane and Reeder, 2001).
6. Downdraughts (e.g. Jewett et al., 2003, or the GWs analysed in Chapter 6).
7. Density currents (e.g. Viana et al., 2010, or the GWs analysed in Chapter 7).

The main requirement of an atmospheric layer to allow the formation of GWs states that the frequency of a specific wave (N_{wave}) must be lower than the Brunt-Väisälä frequency (N_{BV}, Equation 1.2) in a determined layer of the atmosphere, where N_{BV} is:

$$N_{BV} = \sqrt{\frac{g}{\theta_0}\frac{\partial\theta}{\partial z}} \quad , \tag{1.2}$$

mainly determined by the vertical profile of potential temperature ($\partial\theta/\partial z$) and with units of s^{-1} if SI units are used. Here, g is the acceleration due to gravity and θ_0 is the potential temperature at the base level. With the exception of the PBL, the atmosphere is nearly always stably stratified ($N^2_{BV}>0$). Therefore, GWs can frequently occur in the atmosphere with a wide variety of characteristics (Nappo, 2012) and scales. Large-scale inertia GWs (between

* Waves in oceans are also associated with tides and, less commonly, with earthquakes (tsunamis).

hundreds and a few thousands of kilometres) are important for climatological studies (e.g. Holton, 1983) and for middle and upper troposphere analyses (e.g. Fritts and Alexander, 2003; Serafimovich et al., 2005). Mesoscale GWs (tens to hundreds of kilometers) are usually associated with convective currents (e.g. Uccelini, 1975; Chagnon and Gray, 2008), thunderstorms (e.g. Balachandran, 1980; Gupta and Sunil, 2001; Viana et al., 2009, or the case analysed in Chapter 6) or cold fronts (e.g. Knupp, 2006). Finally, smaller-scale GWs are usually observed within the SBL (e.g. Viana et al., 2010; Sun et al., 2015a, or the case analysed in Chapter 7).

Gravity waves effects are not always invisible to the human eye. In some cases, they form wave-like clouds that can appear at different heights.

Figure 1.7: Kelvin-Helmholtz clouds formed by the action of gravity waves. Picture taken from Peñalara mountain (Madrid, Spain) on 15 May 2015 at 07:00 UTC.

When the atmospheric conditions are appropriate, the waves propagate towards some directions (preferably in the main wind direction); then they weaken in time and finally they transfer their energy to the main flow (Nappo, 2012) or dissipate through turbulence (Einaudi and Finnigan, 1993; Smedman et al., 1995). In fact, GWs have frequently been associated with intermittent turbulence during night-time in the PBL (Chimonas, 1999).

Once the wave is formed, an additional mechanism is needed for its maintenance and propagation. In some cases, the trigger mechanism is continuous and provides enough energy to continue generating GWs, for example in cumulonimbus clouds, where convection is strong and persistent (Lindzen and Tung, 1976). In other cases, the thermal and/or dynamic profiles of the atmosphere may favour the horizontal propagation of the GWs in a layer known as the wave duct. This mechanism is somehow similar to the use

of the Scorer parameter* ($l^2(z)$) to study trapped orographically generated GWs (mountain or lee waves), which has been traditionally employed in mountain-wave studies (e.g. Doyle and Durran, 2002). Thus, a duct layer or wave guide is formed for certain GWs when the Scorer parameter is larger than the horizontal wavenumber of the wave concerned. Normally, the wave is trapped between the surface and some atmospheric reflecting layer, although the ducting can also be favoured in elevated layers. This mechanism was studied by Lindzen and Tung (1976) and has been identified in several observational studies (e.g. Ralph et al., 1993, 1997; Monserrat and Thorpe, 1996; Doyle and Durran, 2002; Viana et al., 2009, or the case analysed in Chapter 6).

Scientific interest in atmospheric GWs has increased remarkably during the last years (Fritts and Alexander, 2003; Nappo, 2012). On the one hand, GWs are an important source of energy and momentum transport (Sukoriansky et al., 2009; Fernando and Weil, 2010) in the atmosphere and need an accurate parametrization in NWP models (Fritts and Alexander, 2003; Kim and Hong, 2009; Belušić and Mahrt, 2012; Nappo, 2012; Sun et al., 2015b), since most GWs are not directly resolved by global or mesoscale models. Thus, a better understanding of the physics behind these phenomena will undoubtedly help to the development of these parameterizations.

On the other hand, GWs seem to influence the formation and evolution of convective systems (e.g. Uccelini, 1975; Balachandran, 1980; Nicholls and Pielke, 2000). They can also produce widespread damage due to their associated wind gusts, which represent a potential threat for aviation during landing and take-off manoeuvres (Fujita and Caracena, 1977; Manasseh and Middleton, 1995; Miller, 1999, 2000). In some cases, GWs associated with wake low zones of mesoscale convective systems (MCSs) (figure 1 in Houze et al. (1989)) can also produce dangerous wind gusts at the surface in regions of the MCS where no severe winds are expected (Loehrer and Johnson, 1995; Bernardet and Cotton, 1998; Coleman and Knupp, 2009). In this context, near monochromatic GWs associated with the wake low zone of a MCS are deeply analysed in Chapter 6, with the aim of a better physical understanding of such type of events (seventh objective of the thesis).

As commented before, GWs have been observationally analysed using different approaches, nevertheless, detailed analyses of the impact of GWs on

* $l^2(z) = N_{BV}^2/U^2 - (\partial^2 U/\partial z^2)/U$, where U is the horizontal wind and z the height. It describes the flow over a mountain from temperature and wind vertical profiles and is used to indicate when trapped lee waves can be expected at the leeward side of a mountain range with specific shape and size.

turbulent fluxes have received little attention in the literature (Viana et al., 2009; Sun et al., 2015b). In some cases, they have been shown to be structures that are effective at generating intermittent turbulence, as in Einaudi and Finnigan (1993), Smedman et al. (1995) or in the case presented in Chapter 6. However, other studies highlight the important turbulence-suppressing effect that they can cause (Viana et al., 2009). In any case, the ubiquity of GWs in the SBL over a wide variety of scales (Belušić and Mahrt, 2012) and the presence of other turbulent and non-turbulent motions (sub-meso motions) make the study of these wave-turbulence interactions very complex (Belušić and Mahrt, 2008; Mahrt, 2009). As stated in Sun et al. (2015b), complete understanding of wave-turbulence interactions is an important challenge that remains elusive yet.

GWs in SBLs are usually associated with wave-like oscillations of several meteorological parameters, such as surface pressure, wind speed, wind direction or temperature. They change the vertical and horizontal gradients of these magnitudes and affect directly to the turbulent fluxes close to the surface. Hence, Chapter 7 focuses on the interactions between GWs detected during a fair-weather day, drainage flows and turbulence in the SBL, in order to gain knowledge about these complex interactions (eighth objective of the thesis).

The mathematical frame used to address the study of GWs is generally described by a set of relatively simple equations composing the *linear theory*. These formulations are based on the *Taylor-Goldstein* equation and they establish linear polarization relations (Nappo, 2012) between different atmospheric variables (pressure, wind or temperature). Unfortunately, the simplicity of this theory leads to a hard application in the real atmosphere. This is caused by the non-monochromaticity character of GWs in the real atmosphere, which are normally interacting with other waves, other structures (sub-meso motions) and with turbulent motions. In any case, at least for the purposes of this thesis, the most appropriate variable for the analysis of GWs in the PBL is the surface pressure. This variable includes the effects of the whole column of air above the barometer and is less sensitive to temperature/wind changes caused by local heterogeneities. That is, normally the GWs are detected in a clearer way in surface pressure records than in temperature or wind. In this context, the use of an array of microbarometers* is advised, since wave parameters (wavelength, phase speed, direction of propagation) can be calculated through cross-correlation (Terradellas et al., 2001;

* Microbarometers are sophisticated barometers able to measure surface pressure with a high accuracy and resolution.

Viana et al., 2009) or phase differences analyses (Li and Nozaki, 1997). One of the advantages of the case studies analysed in Chapter 6 and Chapter 7 was the availability of these instruments during the Boundary-Layer Late Afternoon and Sunset Turbulence (BLLAST) campaign, which moreover was extensively instrumented with other useful meteorological devices.

This thesis deals with two types of GWs: one related to a mesoscale convective system (presented in Chapter 6) and the other more related to the microscale, associated with the SBL formation and surface drainage flows (presented in Chapter 7). However, both cases influenced directly the characteristics of the SBL by alterations in surface fluxes and temperature and wind vertical gradients.

1.4 THESIS OUTLINE AND MAIN OBJECTIVES

The general purpose of the present thesis is to gain knowledge about two common and important processes that usually appear in the stable boundary layer: radiation fog and gravity waves. The necessity of a better understanding and forecasting of these processes has been revealed in the previous subsections. Thus, these phenomena are here addressed through different approaches: the observational analysis of high-quality data from three research centres and from numerical simulations. Although GWs can also coexist within radiation fog and influence its life-cycle, this thesis studies both processes separately. The first part deals with the study of radiation fog and has been divided in three main chapters, while the second part of the thesis focuses on the observational analysis of two different cases of GWs:

Part I - Radiation fog

A. Chapter 3. Several radiation-fog events are simulated with the WRF model with the aim of evaluating its skill for fog forecasting. Different parameterizations are tested in order to establish the best configuration needed to simulate adequately radiation fog with WRF. The obtained results are partially applied over the next chapter.

B. Chapter 4. In this chapter, two different approaches are compared for the forecasting of radiation fog at two contrasting sites: statistical (M14 method) and numerical (WRF) methods. A statistical comparison between the climatology of radiation fog at these two sites is also presented.

C. Chapter 5. This chapter tries to solve a technical problem found during the completion of the two previous chapters, as well as in other fog studies: the lack of information about fog thickness. Thus, surface turbulence parameters are proposed as potential indicators of fog-top height. Additionally, the fog-top height estimation based on the temperature homogenisation within well-mixed fog is also evaluated.

Part II - Gravity waves

A. Chapter 6. GWs associated with the wake-low part of a mesoscale convective system are here analysed through the observational analysis of data from several instruments deployed during the BLLAST campaign.

B. Chapter 7. A different case study is presented in this chapter. In this case, the detected GWs were associated with drainage flows and the study focuses on wave-turbulence interactions.

Finally, the conclusions and the desirable future-work points are presented in the last chapter (Chapter 8).

Within the two main parts of this thesis, the order of the chapters has been established following the writing of the associated publications in scientific journals. Besides, every new chapter tries to solve issues or is motivated by findings of the previous one, as shown in conceptual Figure 1.8.

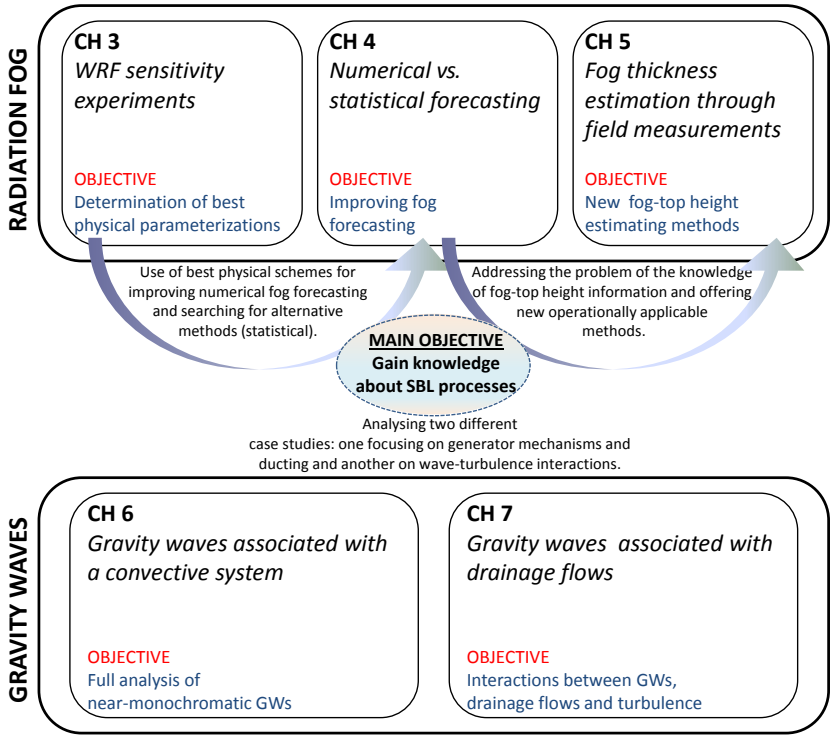

Figure 1.8: Research strategy scheme.

Thus, the main objectives of this thesis are briefly summarised below:

——— RADIATION FOG

1. To determine the ability of the WRF model simulating radiation fog under different physical options (Chapter 3).
2. To evaluate and extend a statistical fog-forecasting method (M14) at two contrasting sites using pre-fog observations and WRF numerical output as predictors (Chapter 4).
3. To evaluate and discuss the ability of the WRF model simulating radiation fog (attending to LWC output) at these sites (Chapter 4).
4. To develop a robust statistical 6-year climatology for the studied sites (Chapter 4).
5. To provide new methods for the estimation of fog thickness (fog-top height) through surface turbulent measurements (Chapter 5).
6. To evaluate the skill of the estimation of fog-top height through vertical profiles of temperature (Chapter 5).

——— GRAVITY WAVES

7. To analyse observationally near-monochromatic oscillations detected in surface pressure records (Chapter 6).
8. To analyse in detail the interactions between evening transition processes (gravity waves and drainage flows) and turbulence in the SBL (Chapter 7).

2

DATA AND METHODOLOGY

This thesis analyses boundary-layer processes through two different approaches. On the one hand, it uses observational data from meteorological instruments deployed at three different sites to investigate the most interesting features of these phenomena. Data-analysis techniques such as wavelet and multi-resolution flux decomposition are employed to carry out this goal. Additionally, the Weather Research and Forecasting (WRF) model is used to complement the observational analysis and to evaluate the ability of this mesoscale model simulating radiation fog at two experimental sites (CESAR and CIBA) under different physical options. Therefore, this chapter presents the experimental sites, explains the commented methods and introduces the WRF model and some of its principal physical options.

2.1 OBSERVATIONAL SITES

Observational data from different meteorological instruments deployed at three experimental sites have been employed in order to achieve the main objectives of this thesis:

1. CIBA (Research Centre for the Lower Atmosphere), located in Valladolid, Spain.
2. CESAR (Cabauw Experimental Site for Atmospheric Research), situated in Cabauw, the Netherlands.
3. BLLAST (Boundary-Layer Late Afternoon and Sunset Turbulence) field campaign, which took place in Lannemezan, France.

The climatology and statistical fog-forecasting analyses of radiation fog have been performed using data from CIBA and CESAR. On the contrary, gravity waves analyses have been carried out using data from the BLLAST field campaign. Figure 2.1 shows the location of these sites.

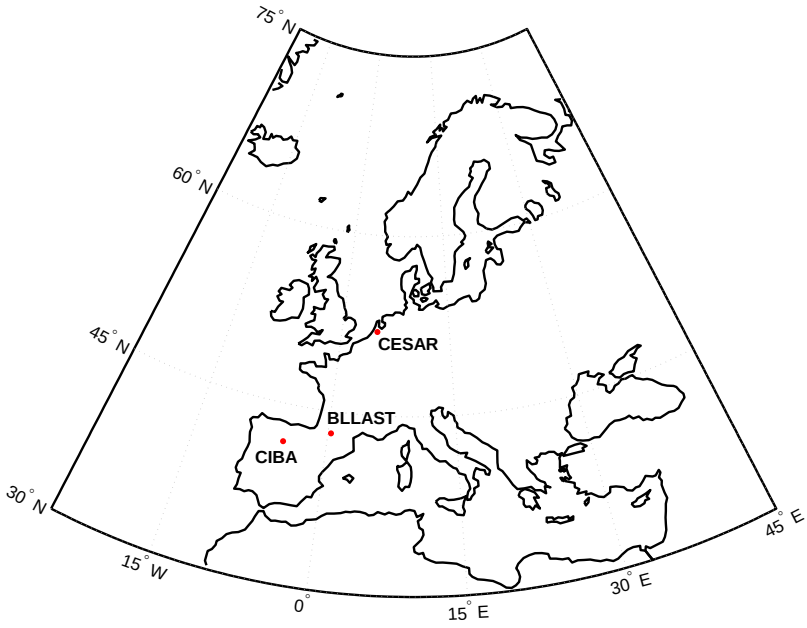

Figure 2.1: Location of the three experimental sites used in this thesis.

Specific descriptions about the main features and facilities of these three sites are presented hereinafter.

2.1.1 *CIBA*

The Research Centre for the Lower Atmosphere (CIBA, *Centro de Investigación de la Baja Atmósfera* in Spanish, Cuxart et al. (2000)) is situated over the Spanish Northern Plateau (41°48.92'N, 4°55.92'W, 840 m above sea level (asl)). It is located over *Los Montes Torozos*, which is a very homogeneous and extensive plateau (800 km²) over the high basin of the Duero river. It is 24 km NW from the city of Valladolid and 13 km NNW from Valladolid airport (LEVD). CIBA area is characterised by a quite dry terrain surrounded by pasture, cropland and shrubland, far from highly populated areas. The sea and the mountains are also far away (180 km and 120 km respectively). The average precipitation is 435 mm $year^{-1}$ (with maxima in spring and autumn). Figure 2.2 shows an aerial view of CIBA site from the top of the main mast.

CIBA site is located close to the village of Villanubla, which can be translated as "foggy town" from spanish.

Figure 2.2: Aerial view of CIBA area from the top of the 100-m tower.

Numerous meteorological devices have been deployed at CIBA by different institutions since 1980. The most remarkable facility of this centre is the 100-m tower instrumented at different heights (San José et al., 1985; Yagüe and Cano, 1994; Yagüe et al., 2009; Sastre et al., 2015). Besides, additional instrumentation deployed at surface and at another instrumented tower of 10 m height have been employed for the completion of this thesis, as well as METAR reports from the nearby LEVD airport. Since the instrumentation used for fog analyses have changed during the development of this thesis, every fog-related chapter includes specific descriptions of the instrumentation used in each case (see Table 4.1 and Figure 5.1).

2.1.2 *CESAR*

The Cabauw Experimental Site for Atmospheric Research (CESAR, Beljaars and Bosveld (1997); Boers et al. (2013)) is situated over central Netherlands (51°58.22'N, 4°55.57'E, -0.7 m asl). It is 18 km SW from the city of Utrecht and 40 km SSE from Amsterdam airport Schiphol (AMS), which is one of the most important airports in Europe. CESAR area is characterised by a quite humid terrain surrounded by grass, water canals and pasture. It is over the flat terrain characterising the Netherlands, 40 km away from the North Sea and very close to the moderately-high populated area of Utrecht-Amsterdam. The closeness to urban areas and sea influences radiation fog formation mechanisms through the modification of the availability of CCN, as explained in Chapter 1. Besides, nearby urban areas may also alter the temperature and wind in their downwind areas and consequently influence the fog cycle too. The yearly precipitation at Cabauw is about 800 mm, homogeneously distributed along the year, although water tables are artificially maintained close to the field level to avoid oxidation of the peat soil.

The 200-m tower of CESAR started measuring in 1972.

Figure 2.3: Aerial view of CESAR with the 200-m tower.

A 200-m mast stands at CESAR (Figure 2.3), with many meteorological instruments from different institutes. However, only a few of them were necessary for the analyses presented in this thesis. Table 4.1 and Figure 5.1 include a detailed list of instruments used in each corresponding chapter.

2.1.3 *BLLAST*

The BLLAST field campaign (Lothon et al., 2014) took place in Lannemezan (43°07'N, 0°21'E, 600 m asl) and its surroundings from 14 June to 8 July 2011. The main goal of the BLLAST campaign was to study the PBL processes governing the late-afternoon transition. During the transition, atmospheric forcings are weak and the turbulence decays. This leads to a stratification of the boundary layer and to the end of the mixed stage. This transition remains poorly understood, though it may have significant impacts on trace gas transport and scale interaction. Thus, a large amount of instrumentation were deployed over the area (specially near the Centre for Atmospheric Research (CRA, *Centre de Recherches Atmosphériques* in French)) in order to obtain accurate and reliable measurements during this transition. The site is located on the plateau of Lannemezan, approximately 45 km North from the Pyrenees highest peaks of the Spanish-French border, in a quite heterogeneous area (hilly with different land uses).

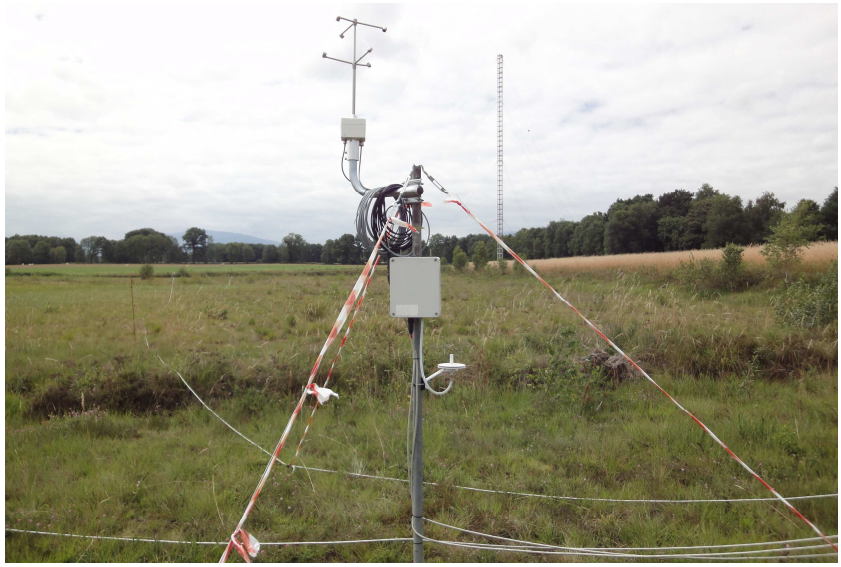

BLLAST project was possible thanks to the effort of numerous international researchers. The UCM group contributed with three microbarometers and a sonic anemometer.

Figure 2.4: One of the microbarometers and the sonic anemometer deployed by the UCM group during BLLAST, with the 60-m tower in the background.

One of the objectives of the BLLAST campaign was to learn more about gravity waves that could develop during the transition and posterior SBL. To study these processes, an array of three microbarometers (PAROSCIENTIFIC model 6000-16B (Cuxart et al., 2002)) were deployed by the UCM group (Figure 2.4). However, data from numerous devices were also used for GWs analyses, which are deeply explained in Chapter 6 and Chapter 7.

2.2 METHODOLOGY

The methodology of this thesis is based on two different but complementary research tools: the analysis of observational data from experimental sites and the 3-D numerical modelling with the WRF mesoscale model.

2.2.1 *Observational data analysis methods*

While most data from CESAR were used from previously validated and quality-controlled datasets, the pre-processing and quality control processes of BLLAST and CIBA data was performed by our research group, including the installation of meteorological instruments. Subsequently, the data were studied by means of time-series analysis, comparison between different variables, statistical analyses, etc. However, other more complex multi-scale techniques have also been employed and are introduced thereafter:

a) Wavelet analysis / phase differences analysis

Wavelet transform (WT) is a useful spectra tool for the analysis of time series, widely used in many scientific disciplines, but specially in geophysics. In the context of micrometeorology, wavelet analysis has been previously used in numerous works (e.g. Meyers et al., 1993; Torrence and Compo, 1998; Terradellas et al., 2001; van den Kroonenberg and Bange, 2007; Viana et al., 2009, 2010; Soler et al., 2014), normally with the objective of distinguishing structures with a determined scale (such as GWs), since it provides a visual picture of the energy density per time associated to each scale. It is also a rather useful technique to detect isolated signals that are not constant in time, such as those related to intermittent turbulence in the SBL.

Complete mathematical descriptions of WTs are numerous in the literature (e.g. Daubechies, 1992; Torrence and Compo, 1998); therefore, only a short development will be included in the present thesis. The method is based on the local Fourier decomposition, where the WT coefficients for a determined space and temporal scale ($F_{s,\tau}$, Equation 2.1) of a specific time series *f(t)* are defined as:

$$F_{s,\tau} = \int_{-\infty}^{+\infty} f(t)\psi^*_{s,\tau}(t)dt \ , \tag{2.1}$$

where $\psi^*_{s,\tau}(t)$ is the complex conjugated of the "daughter" wavelet (Equation 2.2), generated from a "mother" wavelet ($\psi(t)$), moving it along the time series and extending or comprising its shape such as:

$$\psi_{s,\tau}(t) = \frac{1}{\sqrt{|s|}}\psi\left(\frac{t-\tau}{s}\right) \quad . \tag{2.2}$$

Equation 2.1 could be interpreted as a measure of the similarity between the signal of the time series and a determined wavelet (for some specific scale). In order to choose the mother wavelet, its function has to fulfil some criteria:

1. The admissibility criterion: its average in time should be null, as well as its transform for the frequency equal to zero.

2. It should have a well-defined location in time and in scales: ideally its shape should be similar to the shape of the events of the time series that the researcher is trying to detect. Thus, the WT coefficients for a determined space and temporal scale ($F_{s,\tau}$, Equation 2.1) will be high where the spectral components are similar to those of the daughter wavelets (for specific scale (period) and time intervals).

In this thesis the Morlet function (Equation 2.3) has been used as the mother wavelet, a complex function consisting of a plane wave modulated by a Gaussian function, traditionally used in the literature for the analysis of time series with oscillatory behaviour (Torrence and Compo, 1998; Cuxart et al., 2002; Serafimovich et al., 2005; Viana et al., 2009):

$$\psi(t) = e^{i\omega_0 t}e^{-t^2/2} \quad , \tag{2.3}$$

where ω_0 is the is the base frequency, equal to 6 in the calculations of this work, which ensures the admissibility criterion (Viana, 2011).

In this thesis, wavelet analyses were mainly applied over filtered surface pressure data with the objective of detecting energy peaks, which can indicate the presence of gravity waves or coherent structures when the energy signal remains high and almost constant for a determined range of periods and during a relatively long time interval. These pressure data came from three microbarometers PAROSCIENTIFIC 6000-16B (Cuxart et al., 2002) deployed during the BLLAST field campaign in the CRA area. These devices were installed at 1 m agl forming a triangle (Figure 2.5) with a well known position between them (~ 150 m, Table 2.1). They were configured to provide measurements with a frequency of 2 Hz, allowing a resolution of 0.002 hPa (compromise between enough temporal resolution and accurate pressure

measurements). In order to avoid the contamination of the pressure measurements from the dynamic perturbation of the wind, static pressure ports (GILL 230-61002) were connected to the microbarometers. Subsequently, the WT is applied over time series of surface pressure after using a Butterworth high-pass filter to remove periods higher than 45 minutes. Thus, the diurnal cycle (barometric tide) and other pressure tendencies of lower frequencies are not taken into account.

Figure 2.5: Location of three microbarometers during the BLLAST campaign at the CRA area.

Table 2.1: Universal Transverse Mercator (UTM) coordinates for each microbarometer during the BLLAST campaign.

		X (m)	Y (m)	Z (m agl)
Micro A	31 T	285494E	4777972N	606
Micro B	31 T	285630E	4777939N	606
Micro C	31 T	285540E	4777827N	605

Since the Morlet wavelet (Equation 2.3) is a complex wavelet, it allows the analysis of phase differences between several signals (Viana, 2011), which is

used for the calculation of wave parameters (wavelength, phase speed and direction of propagation) (Terradellas et al., 2001; Viana et al., 2009). This method is based on the time differences observed in the wavelet spectral energy peaks of time series of an atmospheric variable measured at least at three different sites at the surface, knowing the exact position of each instrument. These differences are calculated for a determined time period and attending to different wave periods. Thus, for selected ranges of time and wave periods, specific ranges of wave parameters are obtained. The shorter this range of values is (for example for wavelength), the closer to be monochromatic a wave is.

The phase of the oscillatory signal is calculated for each time and period through the WT coefficients (Equation 2.1). This signal is measured at different points (in this case at the well-known locations of the three microbarometers) for each time. Thus, the phase (φ, Equation 2.4) of these coefficients will provide information about the coherent structures at each position:

$$\varphi_i = k_x x_i + k_y y_i - \omega t \ , \tag{2.4}$$

where x_i and y_i represent the position of each instrument (i) and k_x, k_y are the components of the horizontal wavenumber vector ($\vec{k}$). Hence, the system formed by these phases at three different points (Equation 2.5 and Equation 2.6) can be solved:

$$\varphi_2 - \varphi_1 = k_x(x_2 - x_1) + k_y(y_2 - y_1) \tag{2.5}$$
$$\varphi_3 - \varphi_1 = k_x(x_3 - x_1) + k_y(y_3 - y_1) \ , \tag{2.6}$$

from where k_x and k_y are obtained and the rest of the wave parameters are calculated (wavelength (λ, Equation 2.7), direction of propagation (d, Equation 2.8) and phase speed (c, Equation 2.9)):

$$\lambda = 2\pi / |\vec{k}| \tag{2.7}$$
$$d = tan^{-1}(k_y/k_x) \tag{2.8}$$
$$c = \lambda/T \ . \tag{2.9}$$

This procedure is an alternative to other methods for the estimation of wave parameters, such as the cross-correlation method (Rees and Mobbs, 1988; Einaudi et al., 1989; Li and Nozaki, 1997; Viana et al., 2010), which offers a unique solution for the whole window.

b) Multi-resolution flux decomposition

Multi-resolution flux decomposition (MRFD) method has been mainly used for the analysis of turbulent parameters and surface fluxes obtained from high-frequency (20 Hz) measurements of sonic anemometers.

MRFD is a multi-variate and multi-scale statistical tool based on the Haar transform (Haar, 1910). It represents a simple orthogonal decomposition whose spectra satisfies Reynolds averaging at every scale. It has been shown to be a powerful tool for studies of atmospheric turbulence (Howell and Mahrt, 1997; Vickers and Mahrt, 2003), since it allows the separation of turbulent eddies from possible non-turbulent motions of larger scales when a spectral gap (or minimum of energy of the spectrum) is well-defined (van den Kroonenberg and Bange, 2007; Viana et al., 2009, 2010; Nilsson et al., 2014). The contributions to the total flux from different temporal scales are well distinguished with MRFD, specially for high frequencies. MRFD is calculated through the differences between cumulative multi-resolution fluxes for different scales, which is somehow similar to ogive plots. These differences are calculated to obtain the contribution of every range of scales instead of cumulative fluxes. The difference between ogives and the multi-resolution method (cumulative) is that ogives are calculated using the spectral decomposition of Fourier (sin and cos) and multi-resolution is calculated using the spectral decomposition of Haar basis set.

MRFD is an alternative to the widely used eddy-covariance method for the study of turbulent parameters or surface fluxes. It can be applied over time series of any variable; in this thesis it has been used for the analysis of the friction velocity (u_*, Equation 2.10):

$$u_* = [(-\overline{u'w'})^2 + (-\overline{v'w'})^2]^{0.25} \quad , \tag{2.10}$$

and the kinematic buoyancy flux ($\overline{w'\theta'_v}$), where u′, v′ and w′ are the fluctuations of the two horizontal and vertical components of the wind and θ'_v is the fluctuation of the virtual potential temperature*.

MRFD calculations carried out in this thesis are based on the algorithm developed in Viana et al. (2009) (see example for kinematic heat flux in Figure 2.6). It departs from two simultaneous time series of two atmospheric variables (for example vertical velocity and virtual potential temperature)

* Temperature from a sonic anemometer is derived from air density and, in fact, it corresponds to the virtual potential temperature, since the effect of the humidity content of the air is implicitly included in the density measurement.

measured each 0.05 seconds (corresponding to the 20 Hz frequency of the sonic anemometers measurements used in this thesis).

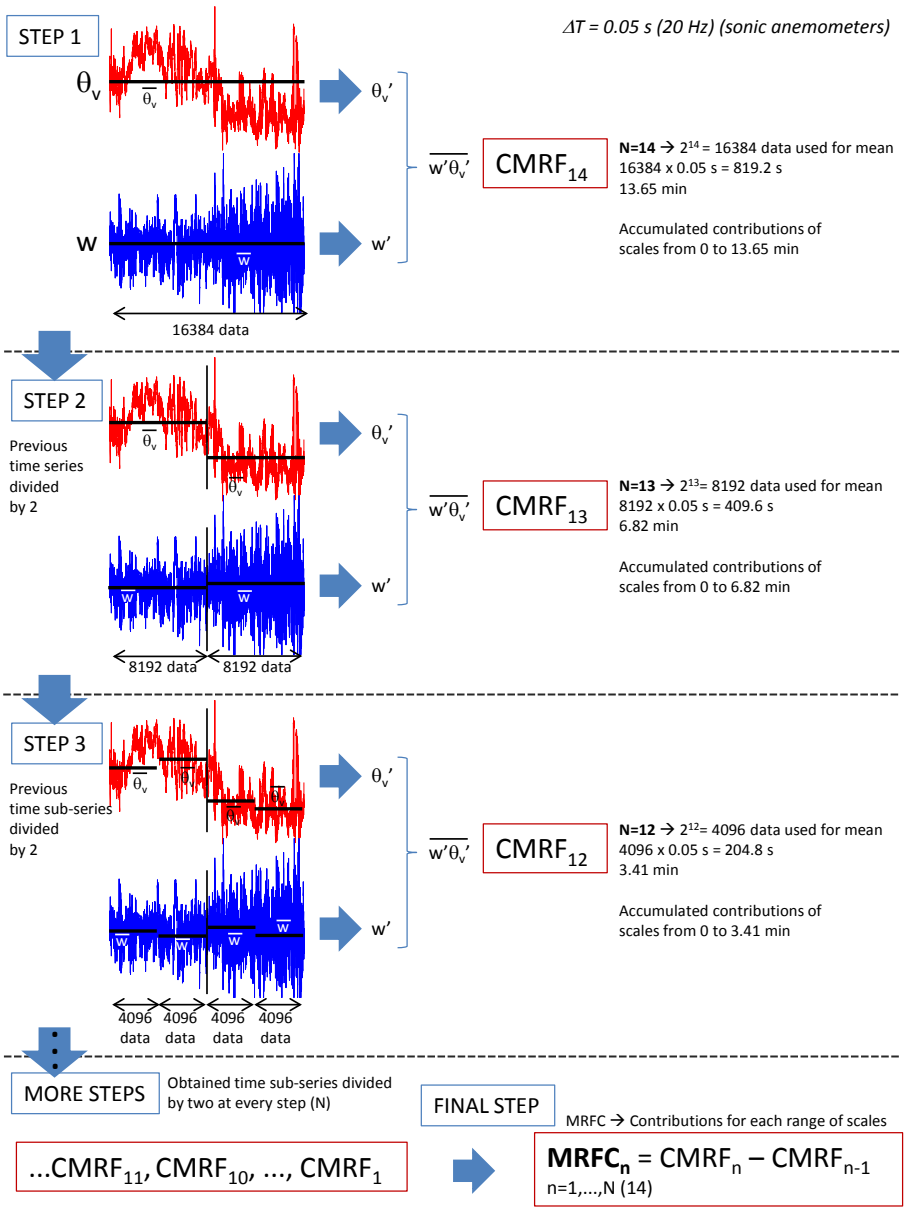

Figure 2.6: Procedure for the MRFD method used in this thesis (example for the kinematic heat flux), based on the algorithm developed in Viana et al. (2009). Note how the CMRF obtained every step is equivalent to the flux calculated with eddy covariance using the averaging window corresponding to each N.

The average of each variable in the selected interval is subtracted to each time series and the mean covariance is calculated (e.g. $\overline{w'\theta'_v}$), obtaining the cumulative multi-resolution flux ($CMRF_N$) for the time scale $2^N\Delta T$ (in seconds). In this thesis, N is equal to 14, meaning that the length of this first averaging window uses 2^{14} measurements; since ΔT is 0.05 s, $2^N\Delta T$ is equivalent to 819.2 seconds (13.65 minutes), which is the first averaging window. This would be equal to the kinematic vertical heat flux calculated through eddy covariance methods using this averaging window of 13.65 minutes. Subsequently, both time series are divided by two (step 2 in Figure 2.6), the average of each new time sub-series is subtracted to every time series and the covariance of both variables is calculated again. The result is the CMRF for the temporal scale $2^{N-1}\Delta T$ ($CMRF_{N-1}$), which is equal to the eddy covariance flux using an averaging window of half length than in the previous step. Then, each time sub-series is divided again by two (step 3 in Figure 2.6) and the same procedure is applied. The following steps are applied dividing each time sub-series by two until reaching N = 1, equal to 0.1 s, which is the minimum analysable scale when using 20 Hz measurements. The multi-resolution coefficients at every step of the sequence are interpreted as contributions to the total flux from the structures of time scales from 0 s to the time scale of each step. The final step of the MRFD method calculates the contribution of the different ranges of temporal scales, so-called multi-resolution flux coespectra ($MRFC_n$), knowing that $MRFC_0 = 0$ for the calculation of $MRFC_1$. In this thesis, this method is applied every minute and figures like the ones shown in Chapter 6 and Chapter 7 are obtained, where a 3-minutes running mean is additionally applied over the values in order to smooth the final figures.

2.2.2 *WRF modelling*

The Weather Research and Forecasting (WRF) model have been used in this thesis to evaluate the ability of this state-of-the-art numerical model simulating fog events, to perform sensitivity experiments for fog forecasting under different parameterizations and to complement the observational analysis of some atmospheric processes when no observational data were available. Numerous studies have employed this model to evaluate its ability forecasting fog (e.g. Van der Velde et al., 2010; Steeneveld et al., 2015) or to simulate GWs associated to density currents (e.g. Udina et al., 2013; Soler et al., 2014).

The WRF model (Skamarock et al., 2008) is a mesoscale NWP model used for research and operational purposes. It is a non-hydrostatic model that considers a fully compressible atmosphere and uses terrain-following verti-

cal coordinates. It uses equations based on the Reynolds-averaged Navier-Stokes method to describe the evolution of the state of the atmosphere. The downscaling performed by the model requires original data input from a global model. In this thesis, these boundary data come from the *Global Forecast System (GFS)* from the *National Centre for Environmental Prediction (NCEP) Final (FNL)* data or from the *European Centre for Medium-Range Weather Forecasts (ECMWF)* operational analysis. The horizontal resolution of the model is configured by the user (grid size) and nested domains are possible, where the inner domain can have higher resolution than the outer ones. Processes of smaller spatial scales than the grid size are not explicitly resolved by the governing equations, but parameterized with physical schemes.

The WRF model was designed as the successor to the Fifth-Generation Penn State/NCAR Mesoscale Model (MM5).

The model is used worldwide for many different applications, which helps to fix problems and to develop new physical schemes under different tested conditions. Thus, improved versions of the model appear from time to time, as well as corrected and new physical schemes. Therefore, the WRF version and the physical options selected for the simulations used in this thesis have been changing during the completion of the PhD*. Hence, specific model configurations are defined in each corresponding chapter. Nonetheless, a brief explanation of the most used parameterizations or model options is presented hereinafter**:

1. *PBL parameterizations*

   PBL parameterizations resolve the turbulent fluxes of scales below the grid size. In this thesis, TKE-closure schemes have been used preferentially, since it has been demonstrated that they perform better under stable conditions, and it was expected to deal mainly with stable stratification during the analysed periods.

   - *Yonsei University (YSU)* (Hong et al., 2006): It is a first-order closure and non-local scheme with a counter-gradient term.
   - *Mellor Yamada Janjic (MYJ)* (Mellor and Yamada, 1982; Janjić, 2002): It is the Eta operational scheme. It has a one-dimensional prognostic TKE scheme with local vertical mixing (1.5 order).

* However, model version and configuration are respected when performing sensitivity experiments in order to obtain comparable results.

** Further descriptions and references to the parameterizations can be found in Skamarock et al. (2008). Technical issues of the model can be found in one of the WRF user's guides (e.g. Wang et al., 2011).

- *Quasi-Normal Scale Elimination (QNSE)* (Sukoriansky et al., 2005): It is an extended version of MYJ based on its code. It uses a TKE-prediction option with a theory for stably stratified regions (considering anisotropy for diffusivity as well as the effect of internal gravity waves). It was designed to improve the results in stably stratified conditions.
- *Mellor-Yamada-Nakanishi-Niino Level 2.5 (MYNN)* (Nakanishi and Niino, 2004): It predicts a more realistic entrainment at the top of the PBL (moreover it forecasts other second order moments besides TKE). It has a new equation for the master mixing length and parametrises the buoyancy effects on the pressure covariances. It also includes a new condensation physics with respect to the older MYJ (NCEP, 2011).

2. *Surface-layer parameterizations*

   Surface-layer schemes determine the friction velocity and the exchange coefficients for surface fluxes. Their use is restricted depending on the selected PBL scheme. For example, MYNN allows the use of three different surface layer (SL) parameterizations, which were also compared in Chapter 3.

   - *Eta*: It was used in Eta model and it is based on Monin and Obukhov (1954) with Zilitinkevich (1995) thermal roughness length and standard similarity functions from look-up tables (NCEP, 2011).
   - *MM5*: It is based on Monin and Obukhov (1954) with Carlson and Boland (1978) viscous sub-layer and similarity functions from look-up tables.
   - *MYNN*: It is the Nakanishi and Niino (2004) PBL's surface layer scheme and it uses Monin and Obukhov (1954) to calculate the surface layer length scale.

3. *Land-surface schemes*

   They provide heat and moisture fluxes over the different points at the surface, which are subsequently used as lower boundary conditions by the PBL parameterizations.

   - *Noah* (Chen and Dudhia, 2001): It is a 4-layer (starting at 0, 10, 40 and 100 cm) soil temperature and moisture model with canopy moisture. It predicts snow cover and soil ice and it has an improved urban treatment.

- *Rapid Update Cycle (RUC)* (Smirnova et al., 1997, 2000): It has one canopy layer and a soil model of six layers (at 0, 5, 20, 40, 160 and 300 cm). It takes into account phase changes of soil water.

4. *Microphysics schemes*

   These schemes include the processes associated with water vapour, cloud and precipitation. They range from simplified to sophisticated schemes with mixed-phase processes.

   - *WRF Single Moment 3-class (WSM3)* (Hong et al., 2004; Hong and Lim, 2006): It is a simple, efficient scheme with ice and snow processes.
   - *WRF Double Moment 6-class (WDM6)*: Similar to WRF Single Moment 6-class, but with double-moment rain and cloud and CCN for warm processes (Skamarock et al., 2008).
   - *Lin et al.* (Lin et al., 1983): It is a sophisticated scheme that has ice, snow and graupel processes, indicated for high-resolution simulations.
   - *Goddard* (Tao and Simpson, 1983): It is a modified version of the previous, also indicated for high-resolution simulations.

5. *Radiation schemes*

   One-dimensional schemes for longwave and shortwave radiation. They provide the atmospheric heating and the downward longwave and shortwave radiation for the ground heat flux.

   Dudhia (1989) was the longwave radiation scheme chosen in all the studies of this thesis, while the Rapid Radiative Transfer Model (RRTM) (Mlawer et al., 1997) was used as the shortwave radiation scheme.

6. *Land-use / soil-type datasets*

   They are not physical schemes but specifications of soil and surface parameters. They define these parameters depending on the soil and land use at each point. Two options are initially available in WRF, with different land-use and soil categories.

   - *USGS*: 24 land-use and 16 soil categories. Data from the United States Geological Survey (USGS), see Wang et al. (2011).
   - *IGBP-modified MODIS*: 20 land-use and 16 soil categories. Data from Moderate Resolution Imaging Spectroradiometer (MODIS), see Wang et al. (2011).

As previously commented, a common configuration has not been used for the whole thesis and some of the physical options selected have been changed during the completion of the PhD. Therefore, the configuration of the model for each work is specified in its corresponding chapter. Additionally, all the information concerning the model version, horizontal resolution, vertical levels, time step, nesting, spin-up time, etc. will be commented for each case.

The model has been employed in Chapter 3 to perform sensitivity experiments of fog simulation under different physical parameterizations. It has also been used to evaluate the ability of the model simulating fog in terms of liquid water content (LWC) output of the model (Chapter 3 and Chapter 4). WRF fields are also employed in Chapter 4 to assess the skill of other output as pre-fog variables for the statistical forecasting of fog (using M14 method). Finally, the model is used in Chapter 7 as a complement to determine the origin and characteristics of the wind observationally detected during the analysis of GWs.

PART I - RADIATION FOG

Little foggy morning, great walking afternoon.
(Spanish folk saying)

3

WRF SENSITIVITY EXPERIMENTS FOR FOG FORECASTING - PBL AND OTHER MODEL OPTIONS

In this chapter, observational analyses of three different periods with fog at the Spanish Northern Plateau have been carried out. These periods have also been simulated with the WRF numerical model and their results have been compared to observations. The study includes a comparison of the skill of different PBL parameterizations, surface layer schemes and a test of the gravitational settling of cloud/fog droplets option. A statistical analysis of this comparison has been evaluated in order to study differences between periods and between physical parameterizations. The model results were different depending on the studied period, due to differences in the features of each fog. This fact made it difficult to obtain generalized conclusions, but allowed to determinate which scheme performed better for each case. In general, judging on the models results of LWC, none of the PBL schemes was able to correctly simulate fog, being Mellor-Yamada Nakanishi and Niino (MYNN) 2.5 level PBL scheme the best one in most of the cases. This conclusion is also supported by the Root Mean Square Error (RMSE) calculated for different meteorological variables. Additionally, other physical options of the model have been tested (microphysics schemes, land-surface schemes and land-use/soil type datasets) for a different period.

The main part of this chapter has been published in:

ROMÁN-CASCÓN, C., YAGÜE, C., SASTRE, M., MAQUEDA, G., SALAMANCA, F. & VIANA, S. (2012): Observations and WRF simulations of fog events at the Spanish Northern Plateau. *Adv. Sci. Res.*, **8(1)**, 11-18.
http://www.adv-sci-res.net/8/11/2012/asr-8-11-2012.html

3.1 INTRODUCTION

The use of numerical models can be very useful to investigate the relation between turbulence and fog formation/dissipation. The chosen PBL scheme is very important to obtain appropriate simulations of fog. Several studies comparing different PBL schemes for WRF model have been carried out in the last years (concerning fog or not). Shin and Hong (2011) did an intercomparison of various PBL parameterizations for a single day and found differences between unstable and stable conditions. Several recent studies have been also carried out investigating how NWP models simulate fog under different conditions. Van der Velde et al. (2010) studied the ability of the High-Resolution Limited-Area Model (HIRLAM) and WRF model simulating a case of fog under frost conditions and they compared different microphysics and PBL options.

In this chapter, three different periods with fog at the Spanish Northern Plateau have been observationally analysed. These periods have also been simulated with the WRF model and their results have been compared to observations. The effect of turbulence on fog is studied through the use of different PBL parameterizations, as well as three surface layer (SL) parameterizations. Additionally, an option of gravitational settling of cloud/fog droplets has been tested. Differences between simulated and observed values (bias) and RMSE (root mean square error) for different meteorological variables have been calculated for each period and for each model option, in order to study differences among the periods and among the parameterizations. The results for each PBL parameterization were different depending on the period, due to differences on the features of the fog.

Additionally, this chapter presents other sensitivity experiments comparing additional physical options, such as microphysics or land-surface schemes and the two land-use and soil-type datasets available for the WRF model. These experiments have been performed for a relatively long period characterized by radiation-fog events in January 2015 at CIBA.

3.2 DATA AND METHODOLOGY

3.2.1 *Data collection*

This study uses data from CIBA. The main instrumentation used for this study was installed on two towers (10 and 100 m). The 10-m tower was equipped with two METEK USA-1 fast-response (20 Hz) sonic anemometers at 1.5 and 10 m agl and with conventional cup anemometers, vanes

thermometers and hygrometers at 1.5 and 10 m agl. The 100-m tower was equipped with standard anemometers and thermometers at 10, 20, 35 and 97 m agl, and with hygrometers at heights of 10 and 97 m agl among other instrumentation. Section 2.1.1 or Yagüe et al. (2009) can be consulted for further information about this experimental site and the commented towers, while Table 4.1 for specific characteristics of instruments at CIBA.

Unfortunately, no visibility measurements were available at CIBA during the studied periods. Therefore, visibility information from METAR reports of the Valladolid-Villanubla Airport (LEVD) were used to support the existence of fog. This airport is located 14.5 km SE from CIBA, but since the terrain is very homogeneous, it was supposed that the conditions in both places were approximately the same. However, sometimes there exists a doubt in the possible local nature of the fog. For this reason, in this chapter, fog is considered when the relative humidity is higher than 95% at CIBA and the visibility at the LEVD airport is lower than 1000 m. Note that reports from METAR consider fog when the visibility is below 1000 m and mist when it is between 1000 and 5000 m.

LWC output from WRF model at different heights are compared to observed fog thickness in Section 3.3.2. Fog thickness in these cases is estimated using relative humidity measurements at 10 and 97 meters and temperature measurements at different heights of the tower (10, 20, 35 and 97 m). Thus, fog is supposed to be present at the highest level when the fog is reported at the lowest one by METAR reports and when the relative humidity is higher than 95% at 97 m. The temperature measurements at the intermediate levels are used to estimate the fog presence at the corresponding level when the temperature convergence is observed (i.e., when the temperature at certain level equals the temperature at the lowest level). The performance of this method and its optimisation are presented in Chapter 5.

3.2.2 *WRF Model*

The WRF-ARW v.3.3 model (Section 2.2.2) has been employed in this study in order to evaluate the ability of this model simulating these fog events. In this work, three TKE PBL parameterizations were chosen: Mellor-Yamada-Janjic (MYJ), Quasi-Normal Scale Elimination (QNSE) and Mellor-Yamada-Nakanishi-Niino Level 2.5 (MYNN). These PBL parameterizations have been chosen among others because it has been demonstrated that TKE closure schemes are better simulating cases dominated by stable conditions, and it was expected to deal with stable cases during these periods, at least before the fog onset.

In this chapter, four two-way nested domains with a horizontal resolution of 27, 9, 3 and 1 km, and fifty vertical levels were used (28 levels below 1000 m agl and 8 levels below 100 m agl). The boundary conditions were taken from NCEP (1° resolution, each 6 h). A time step of 90 s and a spin-up of 12 hours were used. Dudhia was the shortwave radiation scheme chosen, Rapid Radiative Transfer Model (RRTM) the longwave radiation one and WRF Single-Moment 3-class scheme (WSM3) the microphysics package. A first comparison of three PBLs parameterizations was done using MYJ, QNSE and MYNN schemes. Then a comparison of three surface layer (Eta, MM5 and MYNN) parameterizations was done using MYNN PBL scheme. Finally, the gravitational settling of clouds/fog droplets option was tested. Since observations LWC are not available for the studied site, a comparison of the LWC simulated by WRF for the different parameterizations will be shown together with the observed relative humidity.

The reader is referred to Section 2.2.2 for more information about these and more schemes available in the WRF model.

Additionally, other sensitivity experiments are presented in this chapter for a different period. In this case, the MYNN PBL parameterization is fixed and three microphysics schemes are evaluated (WSM3, Lin et al. and Goddard). Then, two land-surface schemes are compared (Noah and RUC). Finally, the effects of using two different land-use and soil-type datasets (USGS and IGBP-modified MODIS) are also tested.

3.3 RESULTS

3.3.1 *PBL sensitivity experiments*

a) Observational analysis

Three different periods with radiation fog have been studied. Each period is composed of 3 days (72 hours), but the number of fog hours was different for each period. Most of the periods were characterised by favourable synoptic situations (not shown*) for the development of radiation fog, i.e. high pressure systems with low pressure gradient and clear skies, allowing the nocturnal radiative cooling required to saturate the air. However, in some cases it is difficult to conclude that they are purely radiation fog. Differences between periods are in Table 3.1, which shows mean values of different variables for the periods. Mean values for strictly fog moments are also shown

* To see maps with the synoptic situation of these periods, the reader is referred to the supplemental material 1 of the paper associated with this chapter: http://www.adv-sci-res.net/8/11/2012/asr-8-11-2012-supplement.zip

in the same table in brackets. It should be underlined the different degree of turbulence (evaluated from the friction velocity) which is present for the fog moments.

Table 3.1: Mean observed values for different variables for complete periods (3 days) and during strictly fog moments (in brackets).

	10-11-12 NOVEMBER 2009	10-11-12 DECEMBER 2009	4-5-6 NOVEMBER 2010
Total hours of fog (72 hours)	13	44	29
1.5 m Relative Humidity (%)	81,16 (96,38)	87,96 (96,3)	88,76 (97,39)
1.5 m Temperature (°C)	9,56 (6,91)	3,62 (1,75)	9,78 (6,96)
1.5 m Mixing Ratio (g kg^{-1})	6,56 (6,58)	4,74 (4,59)	7,32 (6,71)
10 m Wind Speed (m s^{-1})	4,17 (3,5)	2,05 (1,15)	1,82 (1,6)
Sensible Heat Flux (W m^{-2})	10,35 (1,36)	12,9 (11,92)	20,78 (29,35)
Friction Velocity (m s^{-1})	0,76 (0,57)	0,25 (0,09)	0,14 (0,15)

The first period corresponds to 10-11-12 November 2009. It is composed by a total of 13 hours of fog, characterised by short morning fog (Figure 3.1 (a)). Fog was present from 07:00 UTC to 10:30 UTC approx. on 10 November 2009. The main feature of this day was the relatively moderate wind speed (not shown), remaining around 2.5 m s^{-1} before the fog onset and increasing from 3 to 4 m s^{-1} when the fog was present. Probably, this increase in wind contributed to the evaporation of the previously condensed dew over the surface during the night and allowed the fog formation. Later, the wind continued increasing and contributed to the fog dissipation. It can be observed how during this day, there is one moment from 06:00 UTC to 07:00 UTC when the relative humidity at 97 m agl was greater than at 10 m agl. The mixing ratio at the height of 97 m agl was higher (5.5 g kg^{-1}) than at 10 m agl (4 g kg^{-1}) (not shown). This increase in mixing ratio at 97 m agl was caused by a change in wind direction from southwest to south at this height during these times (which can represent a source of vapour at 97 m agl). During the second day (day 11), the fog was present from 03:00 to 09:30 UTC; and from 02:00 UTC to 06:00 UTC on day 12, in accordance with the relative humidity records. METAR information support this fog schedule except for the day 12, when the fog could have a patchy behaviour, being difficult to affirm that a relative humidity higher than 95% could indicate fog formation on this day. Relative humidity at 97 m agl shows how the fog progressed upwards and reached this level during days 10 and 11, but not on day 12.

The second period corresponds to 10-11-12 December 2009. It is composed by a total of 44 hours of fog and can be divided in two fog events (Figure 3.2). The first one is an event of dense fog with visibilities around 100 m (infor-

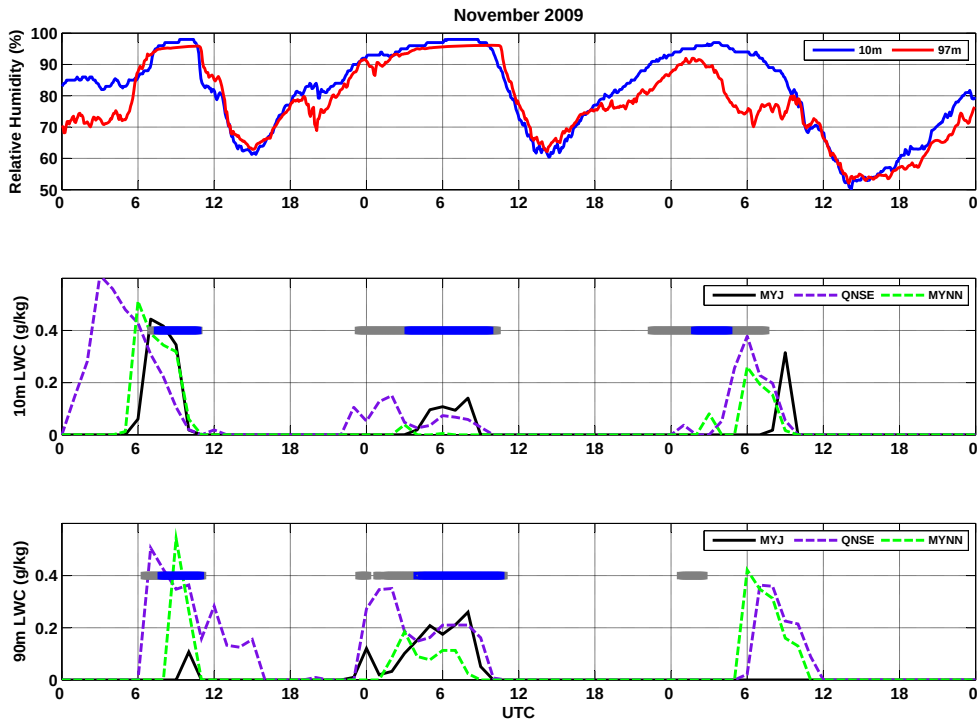

Figure 3.1: Analysis for 10, 11 and 12 November 2009. a) Observed relative humidity at 10 m agl (blue line) and 97 m agl (red line). b) Simulated LWC at 10 m agl using MYJ (black line), QNSE (dashed purple line) and MYNN (dashed green line). Blue and grey rectangles indicate observed relative humidity at 10 m agl larger than 95% and larger than 90%, respectively. c) Same as in (b) for 90 m agl. Blue and grey rectangles indicate the same as in (b) but for 97 m agl.

mation from METAR reports, not shown). The onset was around 00:00 UTC on day 10 and the dissipation at 11:00 UTC approximately. The second event was a case of a very persistent fog without dissipation during the daytime, established approximately at 00:00 UTC on day 11 and dissipated the next day (12 December at 12:00 UTC), i.e., remaining for at least 36 hours. Relatively low values of friction velocity and wind (not shown) contributed to the persistence of this fog.

The third case corresponds to the period 4-5-6 November 2010, with a total of 29 hours of fog. It is a clear case of pure radiation fog developed during the early hours in the night and dissipated at the afternoon (Figure 3.3). Fog was established at 05:00 UTC and dissipated at 09:00 UTC on day 4, with a possible progressive transformation into low clouds (decrease in relative humidity at 10 m agl and increase at 97 m agl). Day 5 was characterised by fog formed at 01:00 UTC approximately and dissipated at 12:00 UTC,

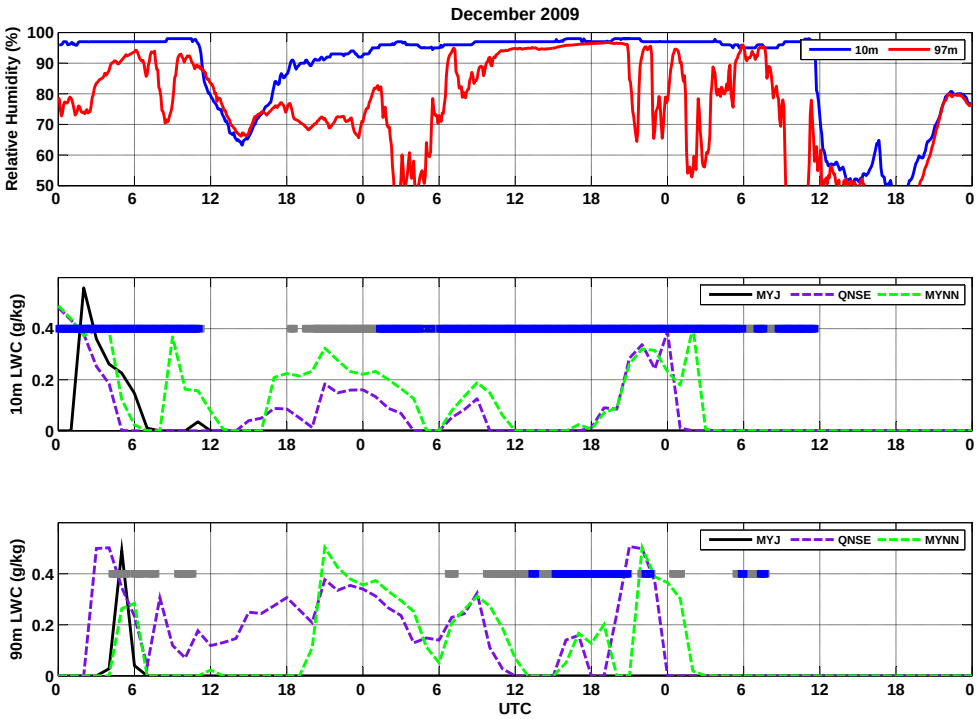

Figure 3.2: As in Figure 3.1, but for 10, 11 and 12 December 2009.

with a higher relative humidity at 97 m agl during the last 3 hours of the event (from 09:00 UTC to 12:00 UTC). On day 6, the fog was developed around 23:00 UTC of the previous day and dissipated at 13:30 UTC of day 6, possibly reaching the height of 97 m agl from 09:00 to 13:30 UTC, as relative humidity records indicate.

b) WRF analysis

The studied periods were simulated with the WRF model using the three PBL parameterizations previously commented. Figure 3.1 (b and c) shows simulated LWC at 10 and 90 m agl respectively using different PBL parameterizations for the first studied period (November 2009). This can be compared with observed relative humidity at 10 and 97 m agl. For the first day (day 10), the three PBL parameterizations simulated relatively well the fog, but with an earlier dissipation and an earlier formation for QNSE, giving also a wrong transformation of the fog into low clouds (see LWC at 90 m agl). MYJ predicted a correct fog at 10 m agl but not at 90 m agl. MYNN seems to be the best parameterization simulating LWC at 10 and 90 m agl.

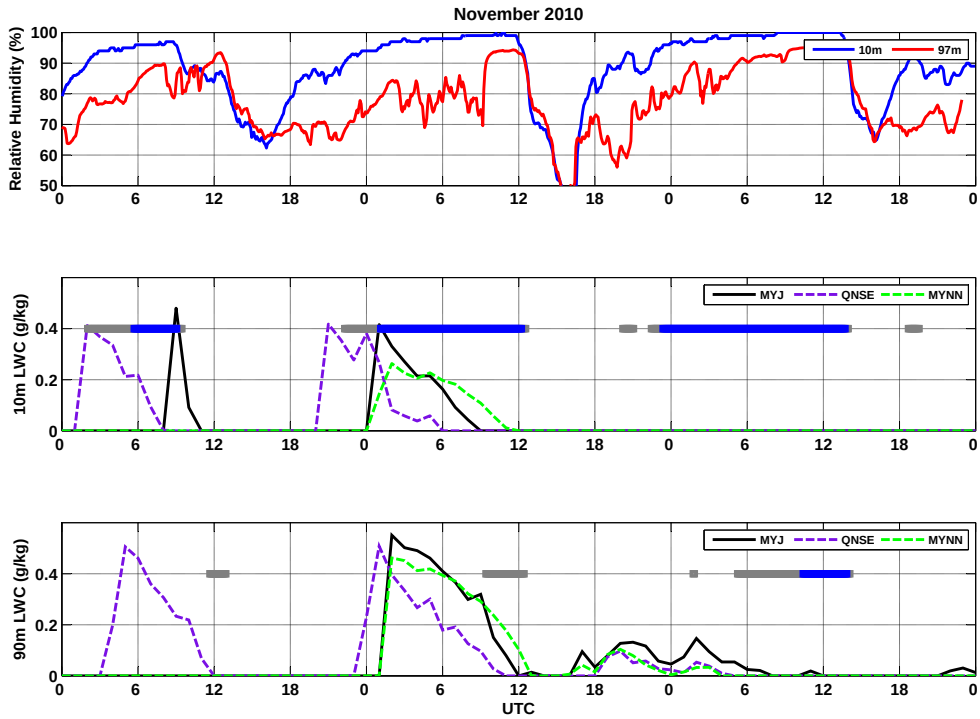

Figure 3.3: As in Figure 3.1, but for 4, 5 and 6 November 2010.

For day 11, MYJ was the best PBL scheme simulating the fog at both levels, while for day 12, QNSE and MYNN obtained more realistic results, but slightly delayed on time.

Regarding the simulation of the second period (December 2009, Figure 3.2 (b and c)), it is shown how MYJ was able to simulate the fog during some hours for the fog event 1 but it was not able to simulate the persistent fog event. MYNN was probably the best PBL scheme simulating the fog during the first event and also during the second fog event, but it was not able to remain the fog during the daytime. QNSE gave a similar behaviour of MYNN. The thickness of the fog was not correctly simulated by any of the parameterizations during this period.

Finally, for the third period (November 2010, Figure 3.3 (b and c)), MYJ and QNSE predicted morning fog on day 4, but not MYNN. In any case, the predicted fog was not totally correct on time. QNSE seems to fail in the thickness of the fog, as can be seen looking at LWC simulated at 97 m agl. Fog on day 5 was relatively well simulated by the three parameterizations; MYNN was the best one, while QNSE and MYJ failed on the onset and dissipation of the fog. Regarding relative humidity at 97 m agl, all of them

overestimate the thickness of the fog. For the third day (day 6), none of the PBL parameterizations was able to simulate LWC at 10 m agl, while in the reality the fog was present for more than 12 hours and reached 97 m agl during the last hours of the fog event.

Additionally, a similar comparison but for the different SL parameterizations was performed (not shown*). From this comparison is deduced that no important differences can be found using different SL schemes, only small differences. Finally, a testing of the gravitational settling (GS) option have been also performed (figures not shown*). The effect of using this option was mainly to produce more realistic results in these cases, with less LWC at high levels (producing a shallower fog and closer to the ground). For November 2009 period, the effect was to produce no LWC at 90 m agl on the first day. During days 11 and 12 November 2009, the effect of using this option did not change significantly the results. For December 2009 period, the effect of using the GS option was to obtain more realistic results at 90 m agl, consequence of producing a shallower fog and closer to the ground. For November 2010 period, the effect of using the GS option was to obtain better results for LWC for day 6, with a more correct simulated fog at 10 m agl, but mistakenly simulated at 90 m agl.

c) WRF statistics

In the previous section it has been shown how depending on the different fog event analysed, sometimes a PBL parameterization is better than other. In order to have an overall view, a statistical analysis comparing simulated to observational results has been carried out. A total of 216 hours were analysed and simulated (72 hours for each period). For this purpose, RMSE and bias were calculated for each PBL parameterization. The model produced instant values for each hour, but a comparison with the observed averaged values was done after checking that the temporal variability of the model in the different studied variables was not very high. Table 3.2 indicates RMSE and bias for temperature, relative humidity and wind speed for all the periods.

* Figures from these experiments are not included in the present thesis for space reasons, but the reader can find them in the supplemental material 2 of the paper associated with this chapter: http://www.adv-sci-res.net/8/11/2012/asr-8-11-2012-supplement.zip

Table 3.2: RMSE and bias calculated for each period (3 days) and during fog moments (indicated by "fog") for different variables and for different PBL parameterizations, MYJ (Mellor-Yamada Janjic), QNSE (Quasi-Normal Scale Elimination) and MYNN Eta (Mellor Yamada Nakanishi and Niino 2.5 level). Lowest values are indicated in bold.

10-11-12 NOV 2009	**MYJ**		**QNSE**		**MYNN Eta**	
	RMSE	Bias	RMSE	Bias	RMSE	Bias
2 m Temperature (°C)	**3,03**	**-1,51**	3,24	-2,13	**3,03**	-1,69
10 m Relative Humidity (%)	**13**	**9,6**	15,33	12,85	14,21	10,74
10 m Wind Speed (m s^{-1})	2,55	0,97	**2,37**	**0,59**	2,54	1,19
NOV 2009 (fog)						
2 m Temperature (°C)	2,22	0,77	2,08	**0,38**	**1,89**	0,74
10 m Relative Humidity (%)	**2,55**	2,09	3,02	2,88	2,8	**1,92**
10 m Wind Speed (m s^{-1})	3,42	2,34	**3,08**	**2,2**	3,82	2,94
10-11-12 DEC 2009	**MYJ**		**QNSE**		**MYNN Eta**	
	RMSE	Bias	RMSE	Bias	RMSE	Bias
2 m Temperature (°C)	2,87	1,87	2,73	-1,01	**2,38**	**-0,89**
10 m Relative Humidity (%)	19,03	-12,38	10,49	4,78	**8,08**	**3,94**
10 m Wind Speed (m s^{-1})	1,08	0,28	**0,92**	**0,17**	0,94	**0,17**
DEC 2009 (fog)						
2 m Temperature (°C)	3,54	3,18	**1,32**	0,36	1,35	**0,25**
10 m Relative Humidity (%)	23,61	-18,93	4,5	**0,11**	**4,34**	0,78
10 m Wind Speed (m s^{-1})	0,79	0,45	0,66	0,33	0,66	**0,21**
4-5-6 NOV 2010	**MYJ**		**QNSE**		**MYNN Eta**	
	RMSE	Bias	RMSE	Bias	RMSE	Bias
2 m Temperature (°C)	3,28	0,42	3,75	-1,15	**3,2**	**0,1**
10 m Relative Humidity (%)	**10,08**	0,2	10,61	4,56	10,91	**0,08**
10 m Wind Speed (m s^{-1})	**1,06**	**0,29**	1,09	0,51	1,35	0,87
NOV 2010 (fog)						
2 m Temperature (°C)	2,98	2,13	**2,58**	**1,57**	2,77	1,68
10 m Relative Humidity (%)	5,85	-3,62	**5,08**	**-3,05**	5,91	-3,29
10 m Wind Speed (m s^{-1})	1,15	0,53	**0,91**	**0,55**	1,47	1,23

These statistical values* have also been calculated only for those moments with determined observed fog and are labelled in the tables as *fog*.

According to the November 2009 period, lower values for RMSE and bias are observed during fog times, except for wind speed, although it should be taken into account the lower number of fog hours (only 13 hours). MYNN obtained slightly better results and QNSE for the wind speed prediction. Nevertheless, there were not too many differences between the 3 parameterizations.

For December 2009 case, MYJ produced unsatisfactory results. MYNN was the best scheme with the lowest values of RMSE and bias (absolute value) and QNSE provided the lowest values for wind speed. The model overestimated the temperature during this period because it was not able to predict the persistent fog during the daytime.

For November 2010, QNSE obtained the lowest values for bias (absolute value) and RMSE during fog times. Despite of this, the results for the three PBL parameterizations used were quite similar.

During fog moments, all of the parameterizations overestimate the temperature, and this could be one of the reasons because the model did not predict the fog, not allowing the relative humidity to increase sufficient to produce condensation. In general, these temperature biases were positive during the whole period because the model did not predict the fog, and a higher temperature was simulated during daytime, consequence of a higher downward short wave radiation at surface than in the reality. These results agree with Shin and Hong (2011), who found how the PBL parameterizations in WRF tended to underestimate the surface cooling rate during nighttime (in this case before fog onset).

The predicted wind can be also an important factor affecting the fog forecasting, with positive bias values. This overestimation of wind speed could give an earlier dissipation of fog by the model. The first problem is that a comparison done with only 72 hours is not sufficient to obtain reliable results. It has also been deduced that a complete statistics (using the three periods together) cannot be done, since the studied periods and their statistical values are different from each other, depending on the period.

The fact of analysing different types of radiation fog (with different features, for example related to their thickness) and try to use them as the same type may affect the results of the simulation with different PBL parameter-

* A complete statistical analysis (including variables as friction velocity, mixing ratio and sensible heat flux) can be found in Supplemental material 3 of the paper associated with this chapter: http://www.adv-sci-res.net/8/11/2012/asr-8-11-2012-supplement.zip

izations. The evolution and the type of fog are mainly driven by the phase changes of the fog water and its microphysics, radiation budget, advection, turbulence and effects of the terrain (Cuxart and Jiménez, 2012). That is, the relative importance of the turbulence on fog would not be the same depending on the other factors and on the type of the fog event. For instance, it would not be the same a case of persistent, dense and deep fog than a case of short, not very dense and shallow fog. A classification of different types of radiation-fog events has to be done in order to correctly calculate this type of statistics using different PBL parameterizations. Despite of these uncertainties, MYNN scheme seems to be the most appropriate PBL parameterization for most cases, with the minimum RMSE values. Also the use of the gravitational settling option produced slightly better results. The discrepancies in the formation and dissipation of fog by MYJ PBL scheme (see Nakanishi and Niino (2004)) are well known, and the improvements added in MYNN and QNSE (see Section 2.2.2) seem to work during some of these cases. Anyway, these improvements are not sufficient in some cases, as for the case of persistent fog in December 2009 period and the radiation fog observed on 6 November 2010.

3.3.2 *Additional sensitivity experiments*

In this section, additional sensitivity experiments have been performed over a different period at CIBA. The studied period (3-15 January 2012) was characterised by high pressure systems over the western of Europe, which led to more than 10 consecutive foggy days at CIBA with different features (thickness, persistence during the daytime, vertical extension, freezing temperature values, etc., see Figure 3.4 (a)). As in the cases analysed in the previous section, MYNN and QNSE performed better for radiation fog. Thus, the QNSE parameterization has been fixed as the PBL parameterization. Firstly, three different microphysics parameterizations are compared (Figure 3.4 (b)): WSM3, Lin et al. and Goddard (see Section 2.2.2). In general, the vertical extension of the simulated fog tended to be overestimated until 200-300 m agl (see red and green line in Figure 3.4 (b)) and persistent fog was not correctly simulated, since most fog events were dissipated by the model around midday (for example days 5, 9 or 10).

As a general behaviour of the model, the surface minimum temperature is usually overestimated a few degrees (Figure 3.4 (c,2)). However, the mixing ratio is also overestimated by the model a few g kg^{-1} (Figure 3.4 (c,3)). This combination of errors led sometimes to a correct prediction of the relative humidity (Figure 3.4 (c,1)) and thus the fog was reproduced in some of the

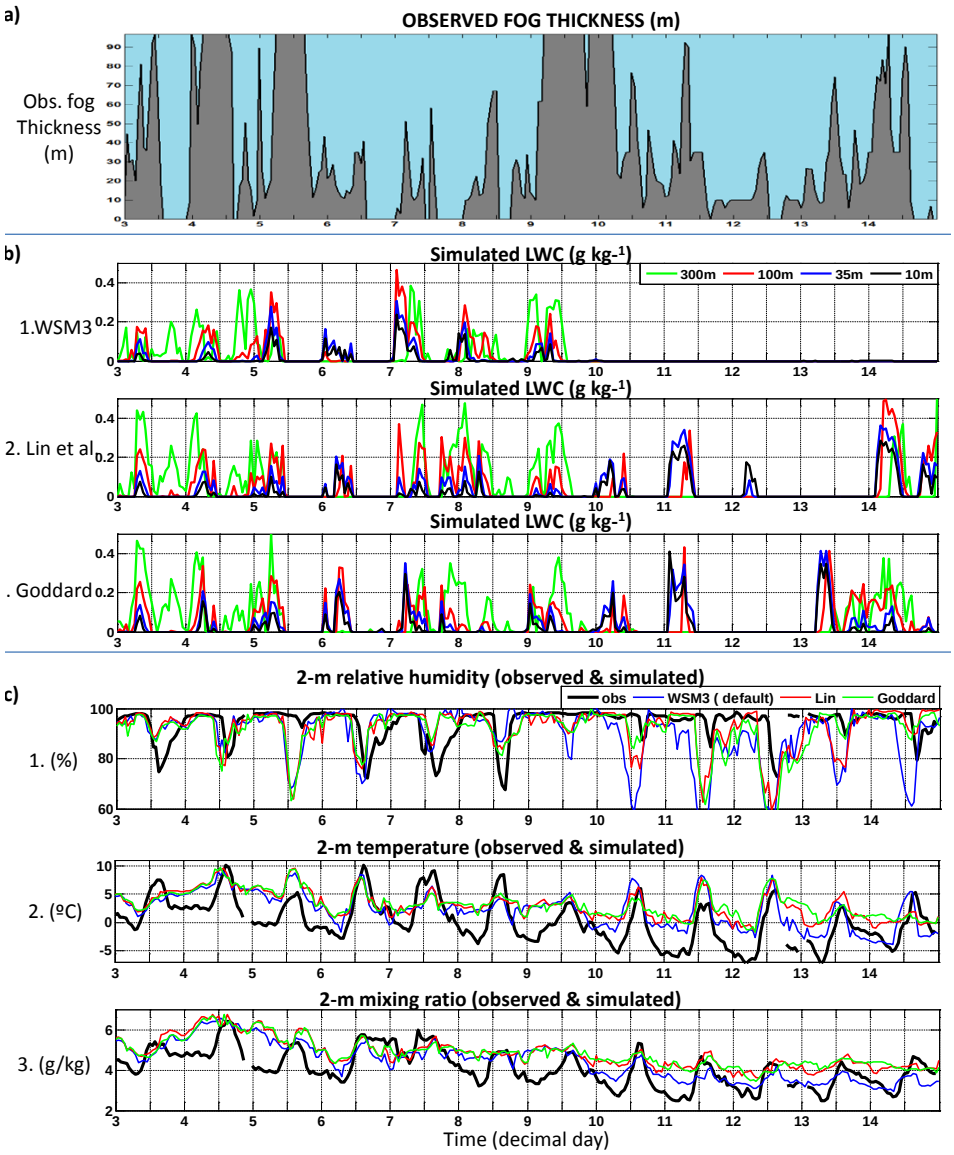

Figure 3.4: a) Observed fog thickness (m) (approximation). b) LWC simulated by WRF model at 10 m (black), 35 m (blue), 100 m (red) and 300 m (green) agl for 3 different microphysical schemes: 1=WSM3, 2=Lin et al., 3=Goddard scheme. c) Relative humidity (1), temperature (2) and mixing ratio (3) at 2 m agl: observed (black) and simulated for 3 different microphysics options: WSM3 (blue), Lin et al. (red) and Goddard (green).

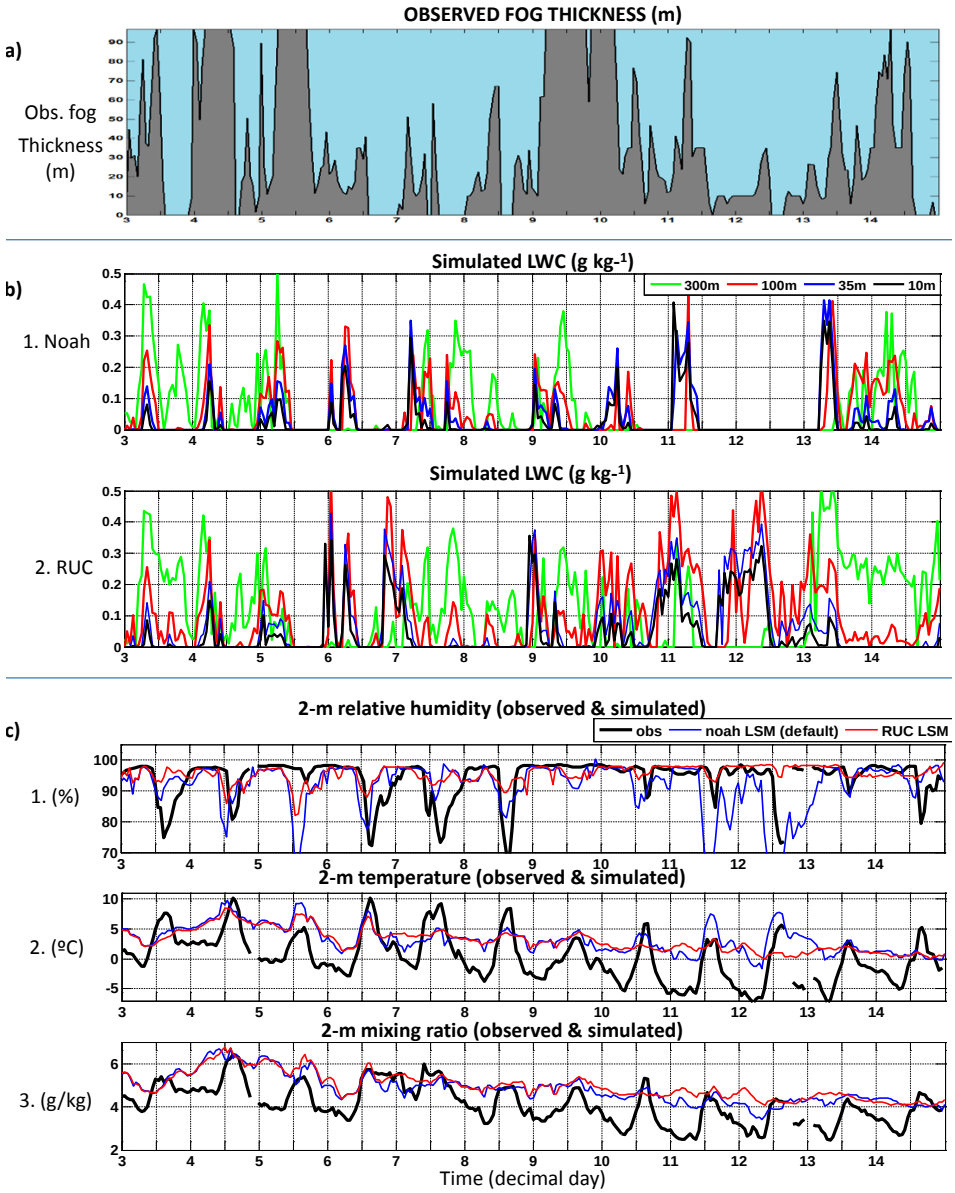

Figure 3.5: a) Observed fog thickness (m) (approximation). b) LWC simulated by WRF model at 10 m (black), 35 m (blue), 100 m (red) and 300 m (green) agl for 2 different land-surface schemes: 1=NOAH, 2=RUC. c) Relative humidity (1), temperature (2) and mixing ratio (3) at 2 m agl: observed (black) and simulated for 2 different land-surface parameterizations: NOAH (blue) and RUC (red).

cases. In any case, the use of more complex schemes for the microphysics representation improves considerably the results (reproducing the fog of days 10, 11 and 14; also day 12 in the case of Lin et al. and day 13 with Goddard scheme, which were days characterised by strong thermal inversions). Subsequently, a sensitivity experiment to different land-surface schemes was performed: Noah and RUC (see Section 2.2.2). Both simulations were similar (Figure 3.5 (b)), but RUC was able to simulate the shallow fog of day 12. However, again, this result was a consequence of an overestimation of surface temperature (Figure 3.5 (c,2)) and a more intense overestimation of mixing ratio (Figure 3.5 (c,2)).

Finally, an experiment has been performed comparing the sensitivity of the model to the two available land-use/soil-type datasets in WRF (USGS and IGBP-modified MODIS, see Section 2.2.2). As observed in Figure 3.6, there exist some differences between land characteristics definition at CIBA area between USGS and IGBP-modified MODIS, with more homogeneity in USGS data set. CIBA site is over a very homogeneous area composed mainly by cropland and shrubland (see Figure 3.6 (c) or Figure 2.2). However, no remarkable differences (not shown) were found when simulating the foggy period previously commented using USGS or IGBP-modified MODIS datasets.

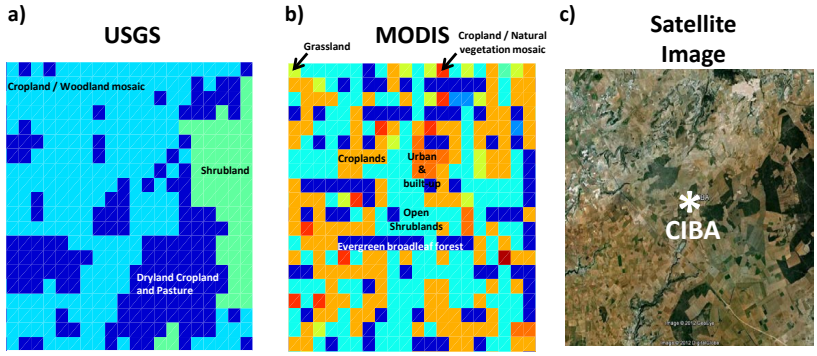

Figure 3.6: USGS (a) and MODIS (b) land-use at CIBA site (20 x 20 km). c) Satellite image of CIBA site (20 x 20 km) (from Google earth).

3.4 SUMMARY AND CONCLUSIONS

Three periods with fog at the Spanish Northern Plateau were analysed and simulated with the WRF model. The features of the fog events were different for each period. Consequently, the results of the simulations depended on the period more than on the different physical options used. This fact made it difficult to obtain generalised conclusions from this study. However, MYNN provided slightly better results simulating LWC during fog moments. The surface layer scheme used was not very sensitive in terms of LWC simulated by the model, with only local differences between the different schemes. Additional gravity settling of clouds/fog droplets produced less LWC at high levels, a shallower fog, and it usually improved the simulation. The relative importance of the different physical processes affecting the fog, turbulence among them, depends on the features and the type of the radiation fog (specially concerning shallow or deep fog events). Thus, some distinction between shallow and deeper radiation-fog events is needed (issue addressed in Chapter 5) to compare statistically the differences between observations and simulated values with different PBLs parameterizations. Despite the improvement obtained using MYNN and QNSE parameterizations, it has been shown how they also have several uncertainties during specific events.

On the other hand, additional sensitivity experiments have been performed for other physical options of the model (microphysics parameterizations, land-surface schemes and land-use/soil type datasets) for a different period with consecutive and persistent fog events at CIBA. More complex microphysics schemes (Lin et al. and Goddard) improved the fog forecasting (specially during days with shallow fog and strong thermal inversion), although through a combination of errors (overestimation of temperature and mixing ratio). Regarding land-surface schemes, RUC (specially designed for inversions and frost conditions) predicted the fog for day 12 (shallow fog, strong inversion and frost-conditions day), but it was not able to predict correctly the surface temperature. No important differences in LWC were observed between USGS and MODIS land-use data sets, although they presented differences in the definition of the land use at the CIBA area.

4

FORECASTING RADIATION FOG AT CLIMATOLOGICALLY CONTRASTING SITES: EVALUATION OF STATISTICAL METHODS AND WRF

A 6-year climatology of radiation fog has been compiled at CIBA and CESAR. These sites are contrasting in terms of geographical situation, climate zone, altitude, humidity and soil water availability. Therefore, several climatological differences in fog abundance, onset, dissipation and duration have been quantified between both sites. The more humid site (CESAR) is characterised by relatively short radiation-fog events distributed throughout the year. However, radiation fog at the drier site (CIBA) is more persistent and appears during late-autumn/winter months. In general, its formation requires more time after sunset (∼ 2 h more), since further cooling is required to reach saturation. The forecast of these fog events has been evaluated through two different approaches. On the one hand, the statistical method presented by Menut et al. (2014) (M14) is extended. This method uses statistics to define threshold values on key variables for fog formation (pre-fog) and verifies its predictability using observations and numerical model output. Some of the most appropriate threshold values for the forecasting of pre-fog periods at both sites are presented, which differ from those provided in M14 and depend on the optimisation of the hit-rate or the false-alarm rate. Additionally, other variables are suggested to be included as potential predictors for fog formation (friction velocity and visibility tendency). Finally, the chapter is focused on the fog simulation by the WRF model in terms of LWC. This model was able to simulate radiation fog when configured with sophisticated physical options and high resolution. However it failed simulating the onset, dissipation and vertical extension of fog (overestimated). Moreover, the model results were extremely sensitive to the spin-up time.

The content of this chapter is *under revision* in *Quarterly Journal of the Royal Meteorological Society* in the following article:

ROMÁN-CASCÓN, C., STEENEVELD, G. J., YAGÜE, C., SASTRE, M., ARRILLAGA, J. A. & MAQUEDA, G. (2015): Forecasting radiation fog at climatologically contrasting sites: evaluation of statistical methods and WRF. Under revision in *Q. J. R. Meteorol. Soc.*. QJ-15-0176.

4.1 INTRODUCTION

The problems associated with the numerical forecasting of radiation fog were commented in the introduction of this thesis (Chapter 1). Therefore, other alternatives have appeared in the literature recently, such as some statistical methods. In this chapter, the method presented by Menut et al. (2014) (M14) is extended through an evaluation of its robustness in forecasting radiation fog at two sites with different conditions: CIBA and CESAR. These sites are contrasting in terms of geographical situation, humidity, altitude and climate zone. CESAR is located over a relatively humid area in The Netherlands and CIBA is located over a drier area at the Spanish Northern Plateau. In this chapter, an analysis of the frequency distributions of the key variables for fog formation is provided for both sites (comparing pre-fog and *all data* conditions). These distributions are compared with the ones presented in M14 for the Paris area. The M14 method is also extended suggesting other variables as potential predictors for fog formation (friction velocity and visibility tendency). The most appropriate combinations of threshold values of the key variables for fog formation are provided for both sites taking into account the use of different performance indicators (as hit-rate, false-alarm rate or Gilbert skill score). Additionally, this study also focuses on LWC output of the WRF model during one month with frequent radiation-fog events at both sites. To carry out all these analyses, firstly, a climatology of radiation-fog events is performed at CESAR and CIBA through robust 6-year statistics. The differences between sites are elucidated taking into account the time of onset, time of dissipation, duration and fog occurrence seasonality.

Therefore, the main objectives of this work are: a) To develop robust statistics able to highlight the climatological differences between radiation fog at CESAR and CIBA. b) To evaluate and extend a statistical fog-forecasting method (M14) at two contrasting sites using pre-fog observations and WRF numerical output as predictors. c) To evaluate and discuss the ability of the WRF model to simulate directly (LWC output) radiation fog at both sites.

The chapter is organised as follows: Section 4.2 describes each experimental site, the M14 method and the WRF model configuration. In Section 4.3, the main features of radiation-fog events and pre-fog conditions are presented through statistical analyses of observations, as well as the M14 method is evaluated using observations and WRF model output of key variables for fog formation as predictors. The section of results also includes the analysis of the ability of the WRF model simulating radiation fog directly (LWC output). Finally, a short discussion and the main conclusions are provided in Section 4.4.

4.2 DATA AND METHODOLOGY

4.2.1 *Research sites*

Six-year (from Jan 2008 to Dec 2013) data from several meteorological instruments deployed at CESAR and CIBA have been used to identify, analyse, perform statistics and compare radiation-fog characteristics at both sites. Table 4.1 shows information about measurements used to carry out this study. CESAR and CIBA are affected by numerous low-visibility events throughout the year. The main weather patterns affecting these two areas are considerably different due to their geographical situation. CESAR is more frequently influenced by low-pressure weather patterns and associated westerlies while CIBA is normally influenced by the persistence of high-pressure systems over the area, especially in winter. Apart from this, the main differences between both sites are the atmospheric humidity and soil water availability.

Table 4.1: Information about the measurements and instrumentation used in this study at CESAR and CIBA. For further information, see Beljaars and Bosveld (1997) (CESAR) and Cuxart et al. (2000) (CIBA). * means that the data are only available for the period from 24th December 2014 to 28th February 2015. ** LEVD indicates the Valladolid-Villanubla airport.

Parameter	Height (m agl)	Instrument
	CESAR	
Temperature	2	E&E pt1000 - pt500 thermocoup.
Dew point temperature	2	E&E - Vaisala HMP243
Wind speed	10	Gill propeller vane 8002DX
Visibility	2-10-20-40-70-140-200	BIRAL 100 SWS
Rain	Surface	Rain gauge
Friction velocity	3	Sonic anemometer GILL R3
Long wave radiation (up and down)	Surface	Eppley Pyrgeometer
Height cloud base	Surface	Ceilometer LD40 and CT75
	CIBA	
Temperature	2-10.5-20.5-35.5-96.6	pt500 - pt100 RISØ
Humidity	10, 97	T. Friedrichs 3030 - Vaisala HMP45A
Wind speed	10	T. Friedrichs Wind vane 4035
Visibility*	2	BIRAL 100 SWS
LEVD** visibility (x3)	2	Vaisala FD12
LEVD** cloud cover	Surface	Vaisala CL31
Rain	Surface	Rain gauge
Friction velocity	1,5	Sonic METEK USA-1
Long wave radiation (up and down)*	1,5	Pyrg. Hukseflux NR01/RA01

4.2.2 *Fog classification procedure*

In this section, the procedure employed to identify radiation-fog events from 10-min data is described for both sites (4 criteria, Figure 4.1). Since the available instrumentation was different at both sites, the procedure employed to select radiation-fog events slightly differs between them.

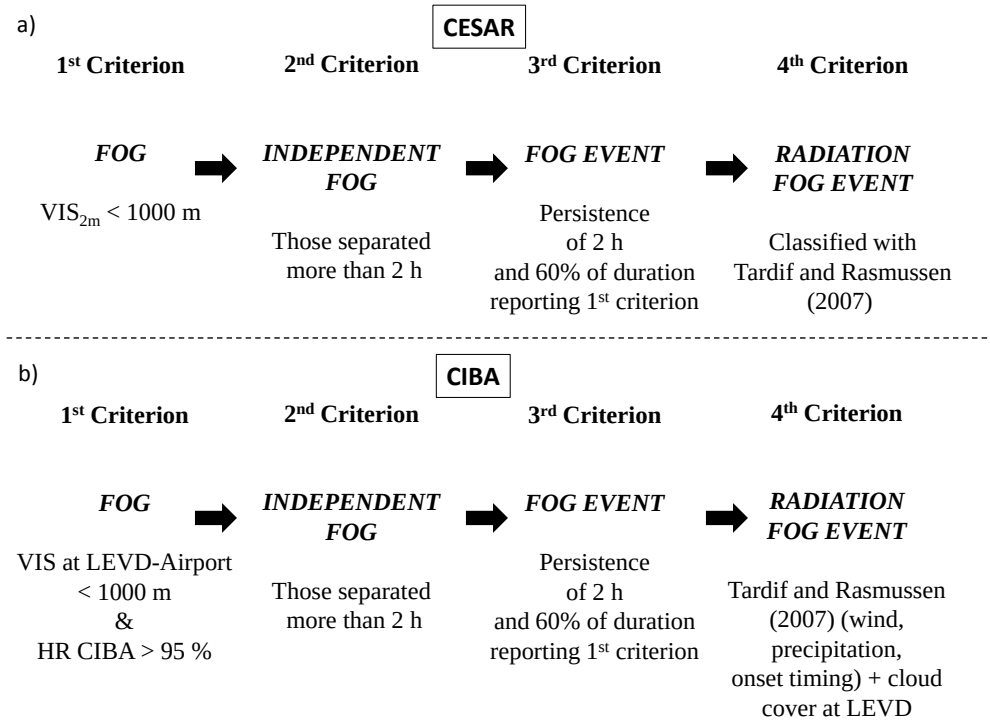

Figure 4.1: Criteria for the determination of radiation-fog events at CESAR (a) and CIBA (b) sites from 10-minutes observational data.

At CESAR, surface visibility measurements are available for the whole period. Therefore, *fog* is defined when the 2-m visibility is less than 1000 m (1st criterion, (DOC/NOAA, 1995)). Two fogs are considered as independent ones when they are separated more than two hours, i.e. when more than two hours between them report no-fog conditions (2nd criterion). By doing this, two fogs are considered different when a radiation-fog event is transformed into low clouds during the afternoon and appears again some hours later because of the lowering of these low clouds. In addition, these independent fogs are restricted to persist for at least two hours with 60% of the observed time slots (10-min data) from the onset to the dissipation period reporting fog. With this restriction (3rd criterion), *fog events* are defined while excluding

short-lived, patchy and non-well established fog events. The latter would reduce the robustness of the statistical analysis and should be avoided. Finally, the Tardif and Rasmussen (2007) fog classification is employed to select only radiation fog (*radiation-fog events*, 4th criterion). This classification is based on the fog formation mechanisms and distinguishes fog archetypes in radiation fog, advection fog, precipitation fog and cloud-base lowering (cbl) fog. The classification tree uses measurements of wind speed, visibility, temperature, dew-point temperature, ceiling height and precipitation*.

At CIBA, the procedure employed to select radiation-fog events slightly differs, since no direct visibility measurements were available for the 6-year period. Therefore, visibility measurements from 3 visibilimeters deployed at Villanubla-Valladolid airport (LEVD, ICAO code) have been used as fog indicators. This airport is located only 13 km SSE from CIBA. The visibilimeters cover a distance of almost 3 km along the airport airstrip, which is also situated over *Los Montes Torozos*. Thus, fog is defined at CIBA when the visibility from all three visibilimeters at LEVD is less than 1000 m (indicating fog homogeneous conditions).

The agreement between the existence of radiation fog at CIBA and LEVD has been verified for 24th December 2014 to 28th February 2015. During this period, visibility measurements at 2, 30, 70 and 100 m agl were also available at CIBA. Eighteen fog events were detected during this period (seven of them pure radiation-fog events, nine cbl fog events and three advection/-precipitation fog events). Among the radiation-fog events, only in one case the difference between onset at CIBA and LEVD was higher than 2 hours. For all other cases the difference between the onset at CIBA and LEVD had a mean of $\pm$ 55 minutes. However, an additional condition is imposed: the relative humidity at CIBA should be higher than 95%, since almost all visibilities less than 1000 m at CIBA (98% of cases) are associated with relative humidity higher than this limit. Therefore, these considerations based on visibility at LEVD and relative humidity at CIBA are reliable proxies for fog events detection at CIBA. After this definition of fog at CIBA, 2nd and 3rd criteria (Figure 4.1) are applied in the same manner as at CESAR. However, Tardif and Rasmussen (2007) classification of fog at CIBA was only partially applied due to the unavailability of ceiling height measurements. Therefore, radiation-fog events at this location (4th criterion) were defined using only

* The reader is referred to Figure 4 or Table II of Tardif and Rasmussen (2007) for more information. It should be noted that advection fog was discarded in this study by the thresholds included in this classification: no precipitation was observed during the hour prior to the fog onset and the wind speed at 10 m agl was lower than 2.5 m s^{-1}.

the thresholds for wind speed (wind speed lower than 2.5 m s^{-1} during the fog onset), precipitation (no precipitation during pre-fog period) and onset time relative to sunset and sunrise given in Tardif and Rasmussen (2007) (fog onset between one hour before sunset and sunrise in some cases when the fog has not been classified before). To avoid the misclassification of a radiation fog when is actually a cbl fog at CIBA, only fog events preceded by cloud cover lower than six oktas were considered, based on cloud cover data at LEVD. A total of 322 fog events were considered at CESAR, from which 61% were classified as radiation fog (197 events) and 20% as advection or precipitation fog (65 events, not used in this work). From all radiation-fog events at CESAR, 85 events (43%) included precipitation during the 24 hours preceding the fog onset (but not during the hour prior to the fog onset). These events are usually shallow radiation fog formed soon after sunset, as the result of the decrease in temperature and the high availability of humidity after afternoon convective rain. On the other hand, at CIBA, a total of 135 fog events were detected, from which 60% were classified as radiation fog (80 events) and 31% as advection or precipitation fog (42 events). Note that at both places, more advection, precipitation or radiation-fog events could be observed, but the 3rd criterion excludes all fog events that do not persist for more than 2 hours.

4.2.3 *Statistical fog forecasting method*

The point of departure is the M14 study. With their method, they were able to detect a high percentage of observed radiation-fog events, quantifying threshold values of key variables involved on fog formation from the comparison between pre-fog and *all data* frequency histograms. Note that as pre-fog periods they considered the time interval between 6 hours before fog onset and fog onset. For the calculation of these thresholds, M14 used a dataset of two winters (2010-2011 and 2011-2012) from the Paris area (Haeffelin et al., 2005, 2010). From this dataset, they selected radiation-fog events and defined threshold values for four key variables involved in fog formation: 2-m relative humidity (RH_{2m}), 2-m temperature tendency ($\triangle T_{2m}$), 10-m wind speed (U_{10m}) and net infrared radiation (F_{IR}). $\triangle T_{2m}$ was defined as the difference between the temperature at a certain moment and 3 hours earlier while F_{IR} is the difference between the incoming and outgoing longwave radiation. They defined the following thresholds as favourable pre-fog conditions:

A. $RH_{2m} > 90\%$.

B. $\triangle T_{2m} < -0.5$ °C.

C. $U_{10m} < 3$ m s^{-1}.

D. $F_{IR} < -10$ W m^{-2}.

Then, they verified the skill of these threshold values as predictors for radiation-fog formation using observations during one month (November 2011). On the other hand, they evaluated the ability of WRF simulating these pre-fog conditions for the same month. They checked how this methodology led to the detection of 87% of pre-fog periods of radiation fog using observations and 74% in the case of model output (in terms of hit rate).

In the present study, this method is applied to CESAR and CIBA in order to evaluate its robustness at sites with different conditions. To do this, the frequency histograms of each variable are composed for all data and pre-fog periods of radiation-fog events. Additionally, friction velocity (u_*) and 2-m visibility tendency in one hour ($\triangle VIS_{2m}$) are included as potential predictors of radiation fog. These frequency histograms are presented in Section 4.3.1.

The verification procedure (Figure 4.2) has been maintained as similar as possible to the one presented in M14 in order to obtain comparable results. However, in the present work, in order to perform independent verifications, the periods employed (Table 4.2) for the verification of the M14 method using observations (Section 4.3.2) are different to those used for the calculation of frequency histograms of key variables for fog formation (Section 4.3.1). The verification has been performed over two years (2012 and 2013) at CESAR and over more than two months (from 24 December 2014 to 28 February 2015) at CIBA for the observation-based M14 forecast (Section 4.3.2). For this specific period at CIBA, visibility and radiation measurements were available, and therefore, a reliable verification could be performed. Hence, four years (2008, 2009, 2010 and 2011) of a total of six have been used for the analysis of frequency histograms at CESAR and six years (from 2008 to 2013) at CIBA (Table 4.2).

Table 4.2: Periods used for each part of the study. * Frequency histograms and threshold values of F_{IR}, u_* and $\triangle VIS_{2m}$ at CIBA (Figure 4.5 (d - f)) have been calculated from data of the period comprising from 24th December 2014 to 28th February 2015.

	CESAR	**CIBA**
Fog features statistics	2008 - 2013	2008 - 2013
Frequency histograms & threshold values	2008 - 2011	2008 - 2013 *
M14 observation-based verification	2012 - 2013	24th Dec. 2014 - 28th Feb. 2015
M14 WRF-based verification	Nov. 2011	Jan. 2012
WRF numerical forecast (LWC)	Nov. 2011	Jan. 2012

For the observation-based fog forecast (M14), the observations of the key variables on fog formation are compared with the thresholds provided in

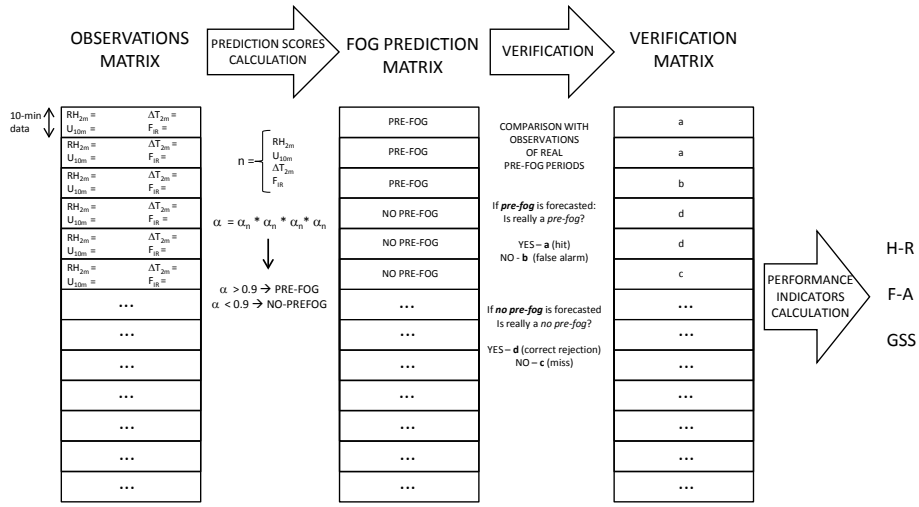

Figure 4.2: Verification process performed to obtain forecast scores and performance indicators for the evaluation of the M14 method at CESAR and CIBA.

M14. Additionally, these thresholds are obtained taking into account the pre-fog frequency histograms at CESAR and CIBA. Finally, different combinations of threshold values are calculated based on improvements of each performance indicator. As in M14, a prediction score α_n is calculated for each variable (n), being 1 when the value is equal or lower than the threshold value (Equation 4.1) (equal or larger for the case of relative humidity). When this condition is not fulfilled, the prediction score is between 0 and 1, following a Gaussian distribution (depending on the distance to the threshold value, Equation 4.1).

$$\alpha_n = \begin{cases} 1 & \text{if} \quad n <= n_{th} \\ \exp[-\dfrac{(n-n_{th})^2}{2\sigma_n}] & \text{if} \quad n > n_{th} \end{cases} \tag{4.1}$$

Where n is each predictor variable (e.g. RH_{2m}, $\triangle T_{2m}$, etc.). Therefore, α_n and σ_n are the prediction score and the standard deviation for each corresponding variable and the subscript *th* indicates the use of the threshold value. After the calculation of α_n for each variable, the total prediction score (α) is obtained through the multiplication of all of them.

As in M14, a pre-fog is defined if $\alpha > 0.9$, i.e. a fog will be forecasted for the following 0-6 hours. Subsequently, performance indicators are calculated using classical forecast score parameters (see contingency table, Table 4.3)

obtained through the comparison of the prediction matrix (pre-fog and no pre-fog) with the real observations (see Figure 4.2). In this case, the hit rate (H-R, Equation 4.2), false alarm rate (F-A, Equation 4.3, Barnes et al., 2009) and Gilbert Skill Score (GSS, Equation 4.4) are shown:

$$\text{H-R}\ (\%) = \frac{a}{a+c} \times 100 \ , \tag{4.2}$$

$$\text{F-A}\ (\%) = \frac{b}{b+d} \times 100 \ , \tag{4.3}$$

$$\text{GSS} = \frac{a - a_r}{a+b+c-a_r} \ . \tag{4.4}$$

Where a, b, c and d are defined in Table 4.3 and a_r (Equation 4.5) is:

$$a_r = \frac{(a+b)(a+c)}{a+b+c+d} \ . \tag{4.5}$$

Table 4.3: Classical forecast score parameters.

	Observed YES	**Observed NO**
Forecasted YES	a (hit)	b (false alarm)
Forecasted NO	c (miss)	d (correct rejection)

While H-R only focuses on the percentage of well forecasted radiation-fog events with respect to all observed ones, F-A only focuses on the percentage of incorrect forecasted events among all non-observed ones. Therefore, the GSS is included, since it combines aspects of H-R and F-A, being a more balanced score. In addition, GSS does not tend to give poorer scores for rare events (as radiation-fog events during datasets of several years). The minimum GSS value is near 0 (although it can be less than 0 for abundant events) and the maximum is 1 (perfect forecast). GSS is commonly known as the Equitable Threat Score (ETS), but in this work, it is called Gilbert Skill Score (GSS) following the recommendations of Hogan et al. (2010), where it is demonstrated how ETS is only equitable for infinite sample sizes. In any case, this measure of verification has been included and assumed as the more appropriate performance indicator for this work.

The same procedure is maintained for the verification of M14 using WRF results as predictors, but comparing model output (instead of observations) against threshold values. In this case, one month has been simulated at each site (November 2011 at CESAR and January 2012 at CIBA, see Table 4.2). These months have been chosen because they include several radiation-fog events.

4.2.4 *Numerical fog forecasting (WRF)*

On the one hand, the mesoscale WRF-ARW 3.5.1 model (see Section 2.2.2) has been employed to study the ability of a NWP model simulating the conditions leading to the onset of radiation fog (pre-fog periods based on RH_{2m}, $\triangle T_{2m}$, U_{10m} and F_{IR}). On the other hand, it has also been used to evaluate its skill forecasting radiation fog directly (taking into account the LWC model output and comparing to observations). WRF is a NWP model widely used for research and operational purposes (Skamarock et al., 2008) and employed for fog-forecasting in several studies (Van der Velde et al., 2010; Steeneveld et al., 2015, or the analysis presented in Chapter 3).

In this case, the simulations were initialised with 0.25° resolution data from the ECMWF operational analysis, defined on 24 pressure levels. The model was run with only one domain (300 x 300 points) centred at each site. Previous studies have shown that using a single domain provides better results than nested domains (Warner et al., 1997; Leduc and Laprise, 2009; Leduc et al., 2011; Steeneveld et al., 2015). A quite-high horizontal resolution of 2.5 km has been used, which is one of the necessary conditions to obtain satisfactory simulations of fog (Tang et al., 2009). This horizontal resolution matches the state-of-the-art operational model resolution, as for example used in the AROME configuration (Seity et al., 2011). 51 vertical levels have been set, with 28 levels below the lowest 1000 m, 8 levels below the lowest 100 m and the first level at 10 m agl approximately. The time-step used in the simulations was 15 s, following the recommendation of 6 times the horizontal resolution (in km). For the microphysics scheme, the WDM6 was used. The MYNN 2.5 level parameterization (Nakanishi and Niino, 2004) was used for the PBL and surface layer schemes, which has also been proved to perform adequately for fog conditions (see results from previous chapter (Chapter 3). RRTM (Mlawer et al., 1997) and Dudhia (1989) parameterizations were used for shortwave and longwave radiation respectively. Data for the land use are taken from the USGS land use dataset and the Noah model was selected as the land-surface scheme.

A set of 30 simulations of 54 hours (6 h + 2 days) was carried out at each site starting at 12:00 UTC, where the first 6 hours are strictly employed as spin-up time. From these simulations, two different monthly compositions were performed:

- S1 - The *first-forecasted-day composition*, which corresponds to 0 h to 24 h from model initialization + 6 h of spin-up.
- S2 - The *second-forecasted-day composition*, which corresponds to 24 h to 48 h from model initialization + 6 h of spin-up.

These two different compositions are compared due to the detection of many cases in which the model simulates more correctly radiation-fog events for the second forecasted day than for the first one. This fact is due to the high sensitivity of the model to the spin-up and will be analysed in Section 4.3.3. The corresponding simulated months are November 2011 at CESAR and January 2012 (1^{st} to 30^{th}) at CIBA. These months were selected because they were characterized by stable situations with long night-times. A total of 10 and 17 radiation-fog events were observed at CESAR and CIBA respectively.

In Section 4.3.3, the vertical extension of simulated fog by WRF (LWC) and the thickness of observed fog have been compared. The latter were estimated at CESAR using visibilimeter data available at 2, 10, 20, 40, 70, 140 and 200 m agl. Since visibilimeters at different heights were not available at CIBA, fog thickness has been estimated using relative humidity at 10 and 97 m agl and temperature data at 2, 10, 35, 70 and 97 m agl from the 100-m tower deployed at CIBA. This estimation is based on the turbulent mixing caused by the fog itself, making the temperature approximately converge to the value at the surface (mixing within the fog layer). Although this method is not perfect, it offers an approximation of fog thickness to be compared with the fog vertical extension provided by the model.

4.3 RESULTS

4.3.1 *Fog statistics (observations)*

a) Climatological analysis

Significant climatological differences have been found between the features of radiation-fog events at CESAR and CIBA sites (Figure 4.3). The monthly distribution of radiation-fog events is different at both sites (Figure 4.3 (a,b)).

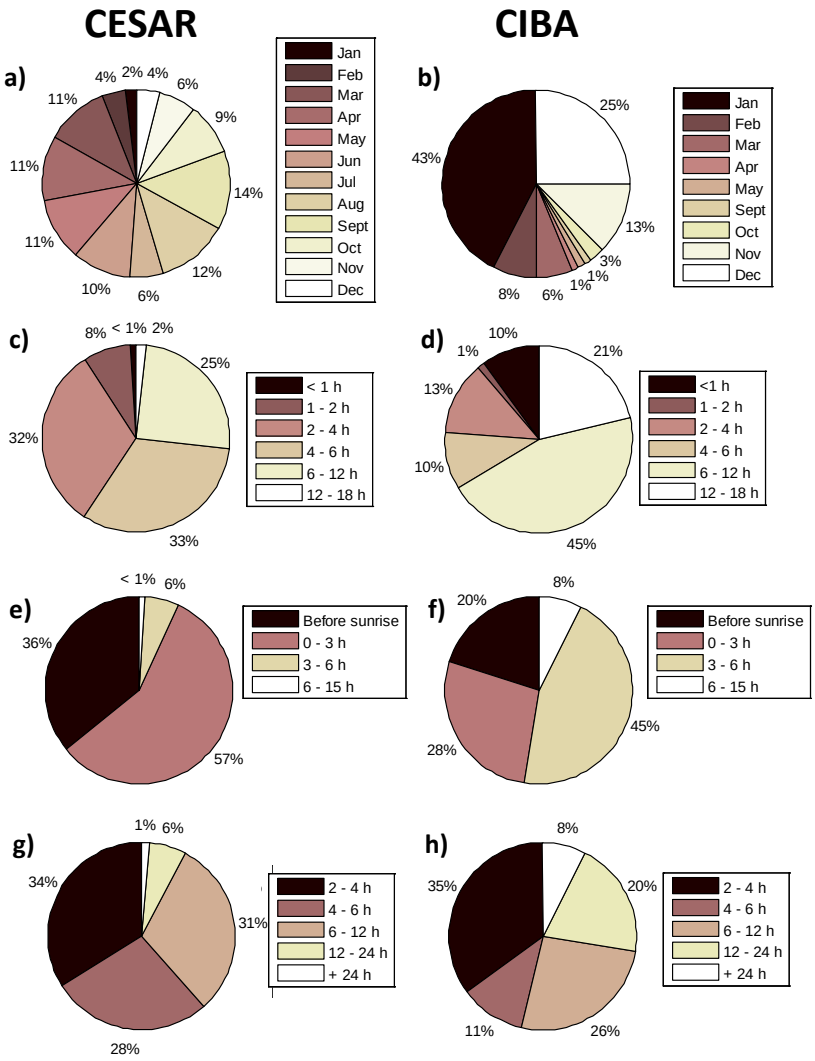

Figure 4.3: Radiation-fog features at CESAR (left) and CIBA (right) from observational data. a,b) Monthly distribution. c,d) Onset time relative to sunset. e,f) Dissipation time relative to sunrise. g,h) Fog event duration.

At CESAR, fog occurrence is almost equally distributed throughout the year, with fewer cases from November to February (only 16%). However, at CIBA, more than 75% of radiation-fog events occur during these colder months. The geographical location of both sites is crucial for such differences. The Spanish Northern Plateau is rather frequently affected by high pressure systems in winter, which can persist for several days and be responsible of strong nocturnal stability periods, leading to radiation-fog formation. However, the proximity of The Netherlands to the polar jet stream makes the

CESAR area be more frequently influenced by low-pressure perturbation systems than the CIBA area. Anticyclones usually persist shorter than over The Iberian Peninsula, especially in winter.

Moreover, the humidity and water availability differences between both experimental sites are also local causes of these differences: the cooling needed at CIBA to reach air saturation is higher than that required at CESAR. For this reason, radiation fog appears at CIBA preferably during cold months with long nights. At CESAR, water availability is higher and only a low decrease in surface temperature is required to reach condensation. This fact also makes the fog to develop sooner (relative to sunset) at CESAR than at CIBA (Figure 4.3 (c,d)). Note that almost 75% of radiation fog form during the first 6 hours after sunset (only 34% at CIBA). Moreover, spring and summer radiation fog at CESAR commonly occurs after night-time/afternoon convective rains, which lead to high values of relative humidity. Therefore, only a small decrease in near surface temperature is needed to produce condensation and fog. These radiation-fog events at CESAR are typically shallow ones and their dissipation (Figure 4.3 (e,f)) is quicker than at CIBA (almost all fog events at CESAR dissipate before sunrise or within the 3 hours after sunrise, while more than 50% of fog events persist more than 3 hours after sunrise at CIBA). Radiation fog is usually associated with previous strong surface cooling and well-established stable conditions at CIBA. This leads to more dense and, consequently, more persistent fog (Figure 4.3 (g,h)) at CIBA, since more energy is required for their dissipation. Thus, 28% of radiation-fog events at CIBA persist more than 12 hours (Figure 4.3 (h)), phenomena rarely observed at CESAR (only 7% of radiation-fog events).

b) Pre-fog conditions

The previous section revealed that the climatological features of radiation fog are different at CESAR and CIBA. Therefore, an analysis of the conditions leading to the formation of radiation fog at both sites is now presented (Figure 4.4 at CESAR and Figure 4.5 at CIBA) in the form of frequency histograms. As in M14, four key variables for fog formation have been analysed: RH_{2m} (RH_{10m} at CIBA for data availability reasons), $\triangle T_{2m}$, U_{10m} and F_{IR} (see Section 4.2). Additionally, the analyses for friction velocity (u_*) and 1h-visibility tendency at 2 meters ($\triangle VIS_{2m}$) are also included, as potential key variables for fog formation.

It should be noted that frequency histograms of F_{IR}, u_* and $\triangle VIS_{2m}$ at CIBA (Figure 4.5 (d-f)) have been calculated from data of the period comprising from 24th December 2014 to 28th February 2015 at CIBA (Table 4.2). Frequency distributions from data of pre-fog periods are compared to the

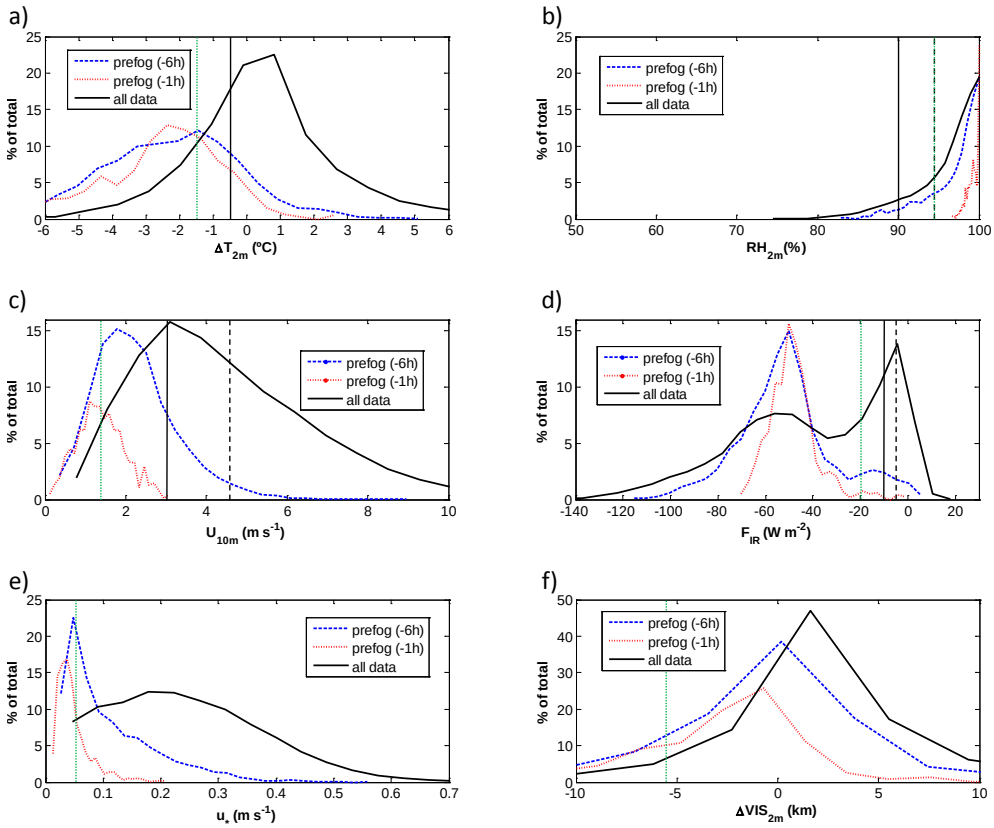

Figure 4.4: Distribution of key variables for radiation-fog formation using 4 years of data (black line) and for 6-h and 1-h pre-fog conditions (dashed blue and dotted red lines respectively) at CESAR. a) $\triangle T_{2m}$ (°C). b) RH_{2m} (%). c) U_{10m} (m s^{-1}). d) F_{IR} (W m^{-2}). e) u_* (m s^{-1}). f) $\triangle VIS_{2m}$ (km). Vertical lines indicate threshold values used: M14 values (solid black line), CESAR values (dashed black line), optimum value for GSS (dotted green line). Note that solid black line is overlapping dashed black line in figure a and dashed black line is overlapping dotted green line in figure b.

ones obtained using all data. That is, solid black lines in Figure 4.4 and Figure 4.5 show the frequency distributions of each variable for all data. Red dotted lines indicate the conditions immediately prior to fog formation (1 hour before), while blue dashed lines indicate the conditions observed during the 6 hours previous to the onset of all considered radiation-fog events. The comparison between dashed blue line and red dotted line highlights the evolution of the variables as the fog onset gets closer. The distribution is always centred to more extreme values for 1-h pre-fog periods, which indi-

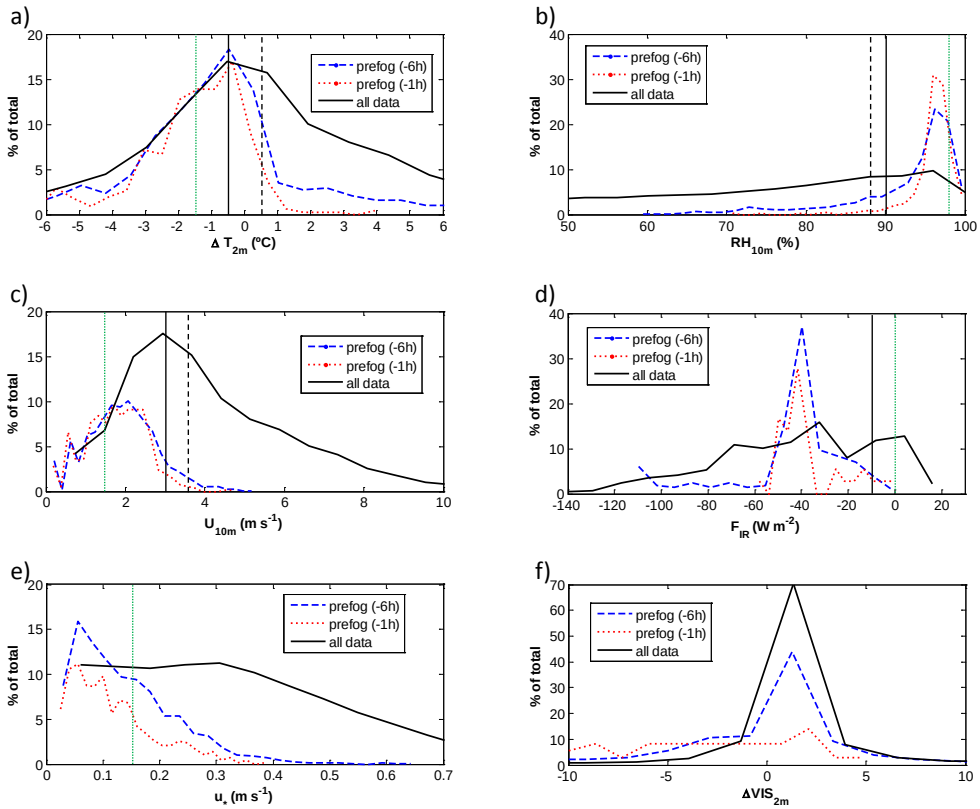

Figure 4.5: Distribution of key variables for radiation-fog formation using 6 years of data (black line) and for 6-h and 1-h pre-fog conditions (dashed blue and dotted red lines respectively) at CIBA. a) $\triangle T_{2m}$ (°C). b) RH_{10m} (%). c) U_{10m} (m s^{-1}). d) F_{IR} (W m^{-2}). e) u_* (m s^{-1}). f) a) $\triangle VIS_{2m}$ (km). Vertical lines indicate threshold values used: M14 values (solid black line), CIBA values (dashed black line), optimum value for GSS (dotted green line). Note that solid black line is overlapping dashed black line in figure d. F_{IR}, u_* and $\triangle VIS_{2m}$ figures were calculated from data of period from 24th December 2014 to 28th February 2015.

cates an enhancement of their skill as fog predictors when the fog onset is closer.

Pre-fog frequency distributions for $\triangle T_{2m}$ at CESAR (Figure 4.4 (a)) is clearly shifted to negative values. Although this distribution is also shifted to negative values at CIBA (Figure 4.5 (a)), it includes some positive values, meaning that increasing temperatures can be found within the 6 hours before fog formation. Many of the cases where $\triangle T_{2m} > 2$ K at CIBA are consequence of several radiation-fog events formed during the afternoon (10% of fog events formed within 1 hour after sunset (see Figure 4.3 (d)) in persistent anticyclonic situations. That is, many cases at CIBA in which fog is

dissipated during the day, it is transformed into low clouds, while in other cases just adds its humidity to the air. In both cases, the humidity available in the PBL after one foggy day is high enough to form fog the next day quite early in the evening. These cases are commonly observed at CIBA during persistent anticyclonic situations. The result is that $\triangle T_{2m}$ is positive within the 6-h pre-fog time interval of these fog events, since it also comprises daytime with increasing temperatures. However, many of the cases of 0 K < $\triangle T_{2m}$ < 2 K are also observed during nighttime or soon after sunrise and could correspond to other small-scale processes, such as moistening, wind speed dropping or quick mixing at the surface after sunrise.

In the case of RH_{2m}, pre-fog distributions are more shifted to high values at CESAR (Figure 4.4 (b)) than at CIBA (Figure 4.5 (b)). The difference between the shape of the frequency distribution for all the data and for the pre-fog periods is sharper at CIBA than at CESAR, meaning that at CESAR RH_{2m} is not a recommended predictor of fog formation, because the relative humidity is almost always very high.

In general, the values found for U_{10m} at CESAR (Figure 4.4 (c)) and CIBA (Figure 4.5 (c)) are higher than for the Paris area in M14, which could be due to local differences and heterogeneities between sites. In any case, the pre-fog frequency distributions are clearly shifted to lower values compared to the ones obtained for all the data (black lines).

The case of F_{IR} is also representative of conditions leading to radiative fog formation (Figure 4.4 (d) and Figure 4.5 (d)), with pre-fog frequency distributions centred in clearly negative values (clear-sky conditions). Frequency distribution for all data has two maxima, one of them centred around 0 W m^{-2}, indicating cloudy conditions. This centre is more pronounced at CESAR than at CIBA, because it is a site usually more affected by cloudy conditions.

On the other hand, the same frequency histograms have been determined for the friction velocity (u_*) (Figure 4.4 (e) and Figure 4.5 (e)) and 1h visibility tendency at 2 m ($\triangle VIS_{2m}$) (Figure 4.4 (f) and Figure 4.5 (f)) in order to analyse the skill of these variables as predictors for fog detection. The pre-fog distribution of u_* is considerably shifted with respect to the distribution for all the data at both sites (even more than for U_{10m}), which suggests that this variable can be useful for fog prediction. The skill of the M14 method for fog forecasting including u_* instead of U_{10m} is analysed in Section 4.3.2. Although this variable is not operationally available at most routine weather stations, this analysis is useful to determine if instruments measuring turbulence (sonic anemometers) could be useful for fog forecasting. The usefulness of $\triangle VIS_{2m}$ is also discussed in Section 4.3.2.

Determination of thresholds values

The threshold values for these variables are determined in M14 from the analysis of the 6-h pre-fog frequency histograms. However, M14 do not define an objective way for the definition of these thresholds, but after a careful inspection of their Figure 4 (in Menut et al. (2014)), it can be determined that they selected the threshold values after discarding approximately 20%, 25%, 5% and 3% of the 6-h pre-fog line distribution for RH_{2m}, $\triangle T_{2m}$, U_{10m} and F_{IR} respectively. Thus, an evaluation of the usefulness of these percentages at other sites (CESAR and CIBA) is performed in this work. Thus, these approximate percentages are used, as well as the 6-h pre-fog distribution at CESAR and CIBA (Figure 4.4 and Figure 4.5, blue dashed line), determining a second combination of threshold values for fog formation at CESAR and CIBA:

A. RH_{2m} must be > 94% at CESAR and RH_{10m} > 88% at CIBA (> 90% in M14).

B. $\triangle T_{2m}$ must be < -0.5 °C at CESAR and < 0.5 °C at CIBA (< -0.5 °C in M14).

C. U_{10m} must be < 4.5 m s^{-1} at CESAR and < 3.6 m s^{-1} at CIBA (< 3 m s^{-1} in M14).

D. F_{IR} must be < -5 W m^{-2} at CESAR and CIBA (< -10 W m^{-2} in M14).

These values and their comparison with the threshold values defined for the Paris area in M14 are included in Figure 4.4 and Figure 4.5 in form of vertical lines (solid line for M14 values and dashed black line for calculated values based on M14 percentages and frequency histograms at CESAR and CIBA). The largest difference between threshold values is found for U_{10m}, which can be due to local characteristics of the sites, as the proximity of Paris city (larger roughness length) to SIRTA site, influencing in turbulence and causing dissipation of fog with lower wind speed. The skill of these two different combinations of threshold values is compared in the next section (Section 4.3.2), where the M14 method is also calibrated to provide some of the most appropriate combinations of threshold values for H-R, F-A and GSS. Note that vertical green dotted lines in Figure 4.4 and Figure 4.5 indicate the values obtained in the combination which offers the optimum GSS for each site.

4.3.2 *Radiation-fog forecasting (M14 method)*

In this section, the skill of the M14 method in forecasting radiation fog at CESAR and CIBA is evaluated through the calculation of performance indicators using the threshold values offered in M14 and the ones calculated taking into account the pre-fog distributions of CESAR and CIBA. Additionally, the values needed to improve each performance indicator are investigated (H-R, F-A and GSS). This is carried out testing possible combinations of reasonable threshold values used for the fog forecasting and calculating their associated performance indicators. From all these tests, those that provide high values of H-R and GSS and low values for F-A are selected.

On the one hand, the method is employed using only observations, i.e. the use of threshold values for key-parameters as radiation-fog predictors is evaluated using observations. On the other hand, the method is employed using WRF output of these variables, i.e. the ability of the model simulating these favourable conditions for radiation-fog formation (pre-fog) is evaluated.

a) Verification using only observations as predictors

1. CESAR.

Two-years of data (2012 and 2013) (see Table 4.2) are used for the evaluation at CESAR. Firstly, the threshold values given in M14 (for Paris) are used (combination 1 in Table 4.4). With this M14 threshold values, 86.7% of radiation-fog events are detected with 21% of F-A. These results are slightly better than those obtained in M14 for the Paris site, since F-A is considerably reduced (21.7%) compared to the 39% found in M14 for Paris. Secondly, the same performance indicators are calculated, but taking into account the pre-fog frequency distribution at CESAR (combination 2, based on percentages of frequency distributions used for determination of thresholds in M14). The results for H-R, F-A and GSS are in general slightly better if the values given in M14 are used. This means that the use of the approximate percentages included in pre-fog distributions in M14 applied to the 6-h pre-fog frequency distributions obtained at CESAR (Figure 4.4) is not worth (other percentages of the distributions should be used).

Hence, some of the best combinations of threshold values for each performance indicator are explored (H-R, F-A and GSS, combinations 3, 4 and 5 respectively in Table 4.4). These combinations of values differ depending on the performance indicator considered to evaluate the skill of the method and in an operational use they will depend on the purposes of the forecaster. It is observed how it is possible to obtain a 95.5% of well predicted pre-fog

Table 4.4: Performance indicators for the M14 method using only observations at CESAR: Hit Rate (H-R), False Alarm (F-A) and Gilbert Skill Score (GSS) for different combinations of threshold values. Note that combination 2 (C2) is based on pre-fog frequency histograms at CESAR (Figure 4.4) and on approximate percentages used in M14. The threshold values for key-parameters on fog formation used for each combination are also provided. Note that *** indicates that this parameter is not included as predictor in the corresponding combination.

CESAR	H-R/F-A/GSS	U_{10m} (m s^{-1})	RH_{2m} (%)	F_{IR} (W m^{-2})	$\triangle T_{2m}$ (°C)	u_* (m s^{-1})	$\triangle$VIS (m)
M14 thresholds (C1)	86.7/21.7/0.049	3	90	-10	-0.5	***	***
CESAR thresholds (C2)	82.1/30.6/0.029	4.5	94	-5	-0.5	***	***
Optimum H-R (C3)	95.5/38.9/0.025	4	88	5	0.0	***	***
Optimum F-A (C4)	29.8/2,0/0.131	1.5	98	-20	-1.5	***	***
Optimum GSS (C5)	40.4/3.1/0.136	1.5	95	-20	-1.5	***	***
- RH_{2m} (C6)	43.1/3.7/0.128	1.5	***	-20	-1.5	***	***
-RH_{2m}-U_{10m}+u_* (C7)	70.4/12.2/0.074	***	***	-20	-0.5	0.05	***
-RH_{2m}+$\triangle VIS_{2m}$ (C8)	33.0/1.9/0.150	1.5	***	-20	-1.5	***	-5500

periods, but at the expense of a quite high F-A (38.9%) and vice versa (2% of F-A but only 29.8% of H-R). If the GSS is considered as the most appropriate performance indicator, then the threshold values obtained are 95%, -1.5 °C, 1.5 m s^{-1} and -20 W m^{-2} for RH_{2m}, $\triangle T_{2m}$, U_{10m} and F_{IR} respectively. By using these thresholds, it could be able to forecast (nowcast) 40.4% of radiation-fog events with only 3.1% of false alarm predictions between 6 and 0 hours before the fog onset at CESAR.

On the other hand, analysing the frequency histograms given in Figure 4.4 (b), RH_{2m} does not seem an appropriate predictor in the case of CESAR, since the humidity is almost always very high (including no pre-fog periods). In fact, if this variable is removed as a key-variable for fog formation (combination 6 in Table 4.4), the results obtained to evaluate the method are similar than if it is included (combination 5 in Table 4.4). The H-R improves slightly at the expense of an increase in the F-A. Furthermore, the use of additional variables as pre-fog indicators have been tested. If U_{10m} is changed by friction velocity (u_*) and RH_{2m} is removed (combination 7), up to 70.4% of radiation fog could be forecasted, with only 12.2% of F-A (GSS = 0.074). In the case of the use of visibility tendency ($\triangle VIS_{2m}$, combination 8), the results improve for the F-A and GSS when a threshold of $\triangle VIS_{2m}$ < -5500 m is used (visibility decreasing during pre-fog periods).

2. CIBA.

These results are also provided for the fog forecast evaluation at CIBA (Table 4.5). It should be remembered that in this case, the period comprising 24th December 2014 to 28th February 2015 is used, since radiation (F_{IR}) and visibility data at CIBA were only available for this period, allowing a more accurate verification. From 24 December 2014 to 12 January 2015, persistent anticyclonic systems were present over the Iberian Peninsula, which is a typical situation in late-autumn/winter. This led to the formation of many radiation and cbl fog events. In fact, the complete period includes 18 fog events. However, only 6 of them were considered as radiation-fog events, since many of the cases were cbl fogs (9). Many of these cbl fog events are also associated with similar pre-fog conditions of radiation fog, but their inclusion for the verification is inappropriate, since for example the F_{IR} is quite high during the hours prior to the onset of these type of fogs, and it would led to unsuccessful forecasts.

Table 4.5: Performance indicators for the M14 method using only observations at CIBA: Hit Rate (H-R), False Alarm rate (F-A) and Gilbert Skill Score (GSS) for different combinations of threshold values. Note that Comb 2 is based on pre-fog frequency histograms at CIBA (Figure 4.5) and on percentages used in M14. The threshold values for key-parameters on fog formation used for each combination are also provided. Note that *** indicates that this parameter is not included as predictor in the corresponding combination.

CIBA	**H-R/F-A/GSS**	**U_{10m}** (m s^{-1})	**RH_{10m}** (%)	**F_{IR}** (W m^{-2})	**$\triangle T_{2m}$** (°C)	**u_*** (m s^{-1})
M14 thresholds (C1)	64.3/14.0/0.064	3.0	90	-10	-0.5	***
CIBA thresholds (C2)	73.9/22.3/0.044	3.6	88	-10	0.5	***
Optimum H-R (C3)	80.9/21.0/0.053	1.8	80	5	1.5	***
Optimum F-A (C4)	32.5/0.4/0.265	1.5	98	0	-1.5	***
Optimum GSS (C5)	41.4/0.7/0.303	1.5	98	0	-1.5	***
-U_{10m}+u_* (C6)	40.8/0.6/0.309	***	98	0	0	0.15

In this case, the use of M14 thresholds provides worse values for H-R (64.3%) compared to CESAR and Paris site (86.7% and 87% respectively), although the F-A is lower at CIBA (14%). On the other hand, thresholds calculated from CIBA frequency histograms (combination 2) improve H-R with respect to the M14 thresholds, but worsening F-A and GSS. H-R can be enhanced up to 80.9%, and it is possible to reduce the F-A to very low values (combinations 3 and 4, Table 4.5). In any case, the results are possibly affected by the evaluation of a period with only 6 radiation-fog events. In this case, it is not advisable to remove RH_{10m} as a predictor, since its fre-

quency histogram is quite shifted for pre-fog periods comparing to all-data (Figure 4.5 (b)). The inclusion of a new additional criterion ($u_* < 0.15$ m s^{-1}) instead of using U_{10m} slightly reduce the F-A (combination 6, Table 4.5). Again, the determination of the best combination of values to use as thresholds depends on the performance indicator used. Therefore, the selection of threshold values will depend on the desired balance between H-R and F-A of specific nowcasting.

b) Verification using only WRF output as predictors

For each site, one month has been simulated with the WRF model using the configuration detailed in Section 4.2. Here, the ability of this model to simulate the meteorological conditions leading to radiation-fog formation (pre-fog conditions) is evaluated, rather than looking at LWC directly (Section 4.3.3). Table 4.6 shows the performance indicators obtained from the fog-forecasting evaluation at CESAR and CIBA. A comparison between results using the 1st or the 2nd-forecasted-day composition (S1 and S2) is also provided.

1. CESAR.

At CESAR, November 2011 has been simulated, containing 11 fog events in total. However, only 5 of them were pure radiation-fog events according to the Tardif and Rasmussen (2007) classification. The remaining events were classified as advection fog (4 cases), precipitation fog (1 case) or *not classified* (1 event).

The performance indicators obtained are expressed in Table 4.6, using M14 thresholds (combination 1) and using the best possible combination for GSS and H-R (combinations 5 and 3 respectively) obtained in the observation-based M14 prediction (Table 4.4). The results for M14 thresholds are better than those for combination 5. This occurs as a result of the threshold values used. By using GSS thresholds (combination 5), the model is forced to find values for $U_{10m} < 1.5$ m s^{-1} and $\triangle T_{2m} < -1.5$ °C. With these restrictions, the model only finds 79 and 117 data from a total of 720 (30 days x 24 hours) satisfying $\alpha_n > 0.9$ for U_{10m} and $\triangle T_{2m}$ respectively. Therefore, the forecasted cases are fewer and H-R and F-A are quite small. This is because the model generally overestimates the wind speed during stable situations and underestimates the temperature amplitude of the diurnal cycle (Betts, 2006; Holtslag et al., 2013; Kleczek et al., 2014). However, the results improve using the M14 thresholds. This is directly caused by the smoothing of the criteria (increasing $\triangle T_{2m}$ and U_{10m} thresholds). The result is an increase in the H-R and GSS (although there is also an increase in F-A). In any case, the

Table 4.6: Performance indicators for the M14 method using WRF output at CESAR and CIBA: Hit Rate (H-R), False Alarm rate (F-A) and Gilbert Skill Score (GSS). Threshold values for Combinations 1, 5 and 3 are expressed in Table 4.4 and Table 4.5 for CESAR and CIBA respectively. The total number of data that fulfil the criterion $\alpha_n > 0.9$ is expressed for each variable. Note that total number of data is 740 (30 days x 24 hours).

	H-R	F-A	GSS	n°α_n> 0.9	n°α_n> 0.9	n°α_n> 0.9	n°α_n> 0.9
CESAR				$\mathbf{F_{IR}}$	**RH**	$\mathbf{\triangle T_{2m}}$	$\mathbf{U_{10m}}$
1st forecasted day							
Comb 1 (M14)	33.3	12.2	0.067	351	643	426	276
Comb 5 (GSS)	3.3	0.8	0.022	304	475	117	79
Comb 3 (H-R)	73.3	34.7	0.053	657	720	536	427
2nd forecasted day							
Comb 1 (M14)	20.0	10.5	0.034	351	653	402	249
Comb 5 (GSS)	10.0	0.4	0.086	304	489	161	50
Comb 3 (H-R)	86.7	37.4	0.066	657	720	557	428
CIBA							
1st forecasted day							
Comb 1 (M14)	33.7	16.0	0.093	429	532	474	505
Comb 5 (GSS)	17.4	7.6	0.063	705	290	474	321
Comb 3 (H-R)	47.8	31.9	0.060	718	632	662	331
2nd forecasted day							
Comb 1 (M14)	34.8	17.3	0.089	429	578	479	522
Comb 5 (GSS)	31.5	12.8	0.106	705	391	479	325
Comb 3 (H-R)	59.8	35.7	0.086	718	660	674	325

results are not totally satisfactory, mainly because of the wrong agreement between observed and simulated onset of fog events. That is, the model predicts fog events with their pre-fog periods, but these do not agree in time with the real observed ones. As expected, the H-R increases when using combination 3 (thresholds defined in Table 4.4 for the observation-based M14 fog forecast which offered the highest values for H-R within a reasonable range of threshold values). In this case, it is possible to detect up to 86.7% of radiation-fog events when using the 2nd-forecasted-day composition (S2). These results are better than those obtained for S1 (73.3% for H-R).

2. CIBA.

The results for CIBA are also expressed in Table 4.6. In this case, January 2012 was simulated. Eighteen radiation-fog events were observed during this month at CIBA, resulting from the persistence of anticyclonic systems

over the area. The results are in general worse when they are compared to those obtained at CESAR, especially for the H-R, which does not exceed 60% (using combination 3 and output from S2) and at the expense of 35.7% of F-A. However, GSS values are maximised until 0.106 in the case of combination 3 and using output from 2nd forecasted day, resulting from small values of F-A (12.8%) and 31.5% of H-R. At CIBA, the same problem is found as in CESAR for combination 5, i.e. the restrictions forced by using these threshold values (RH_{10m} > 98%, U_{10m} < 1.75 m s^{-1} and $\triangle T_{2m}$ < -0.5 °C) lead to few data satisfying the criteria. Additionally, the consecutive character of radiation-fog events at CIBA during January 2012 added complexity to this period (more discrepancies between onset and dissipation of radiation fog, and therefore, worse performance indicators). In any case, it is observed how the use of the output from S2 improves the result in general, which is due to the better simulation of fog (and pre-fog) periods. This subject will be discussed in Section 4.3.3.

4.3.3 *Radiation-fog forecasting (WRF output (LWC))*

In this section, the ability of the WRF model simulating radiation fog directly (via the model output of LWC) is evaluated, rather than using statistical methods as in previous sections. The objective of this section is to determine whether a mesoscale model with the employed configuration is able to provide successful fog forecasts. To carry out this analysis, daily simulations of 54 hours each have been conducted. The same months as in the previous section have been simulated: November 2011 at CESAR (Figure 4.6) and January 2012 (1st to 30th) at CIBA (Figure 4.7). In these figures, comparisons between estimated fog thickness and simulated LWC by WRF are provided. Additionally, for each site, we include a comparison between results from the 1st-forecasted day composition (S1) (daily simulations of 0-24 h from model initialization plus 6 h of spin-up) and the 2nd-forecasted day composition (S2) (daily simulations of 24-48 h from model initialization plus 6 h of spin-up). The objective of this sensitivity experiment is to analyse the dependence of the results on the total spin-up (note that the total spin-up for S2 is equivalent to 30 h while is 6 h for S1).

At CESAR, almost all fog events are simulated, except the shallow fog of day 6 (Figure 4.6). The fog of day 28 is also incorrectly simulated. S2 normally simulated a more vertically developed fog (Figure 4.6 (b)). The contrary happens for S1 (Figure 4.6 (a)), for example during the case of the persistent fog formed the afternoon of day 19 and lasting until day 22, where fog grows from the surface every new simulated day. This indicates

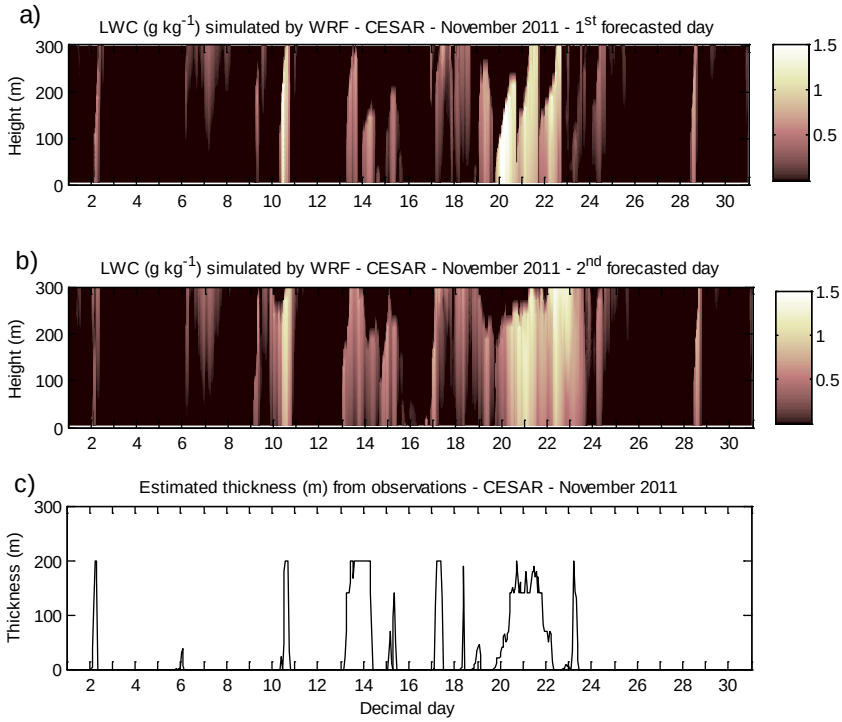

Figure 4.6: CESAR, November 2011. a) Composition of LWC (g kg^{-1}) simulated by WRF model each day, using 1st forecasted day (0-24 h from model initialization + 6 h spin-up) (S1). b) Idem, but using 2nd forecasted day (24-48 h from model initialization + 6 h spin-up) (S2). c) Estimated fog thickness from observations for the same period. Note that minimum contours (black) of figures a and b correspond to an approximate visibility of more than 1000 m, following Kunkel (1984) formula to convert LWC in visibility.

that initial conditions did not include the well-formed fog at the beginning of the simulation and the model needs to develop the fog in the vertical after the model initialization. This result demonstrates the critical role of initial conditions in fog forecasting (Rémy and Bergot, 2010). Besides, the LWC simulated by WRF for both compositions is usually overestimated and too much extended in the vertical.

Almost all fog events are also simulated at CIBA (Figure 4.7), although in this case the results are substantially affected by the spin-up time and they show significant differences between S1 and S2. It should be noted the complexity of the simulated month due to the existence of many consecutive and short-time-separated fog events. Using S1 (Figure 4.7 (a)), the model was not able to simulate correctly the shallow and consecutive fog events of the

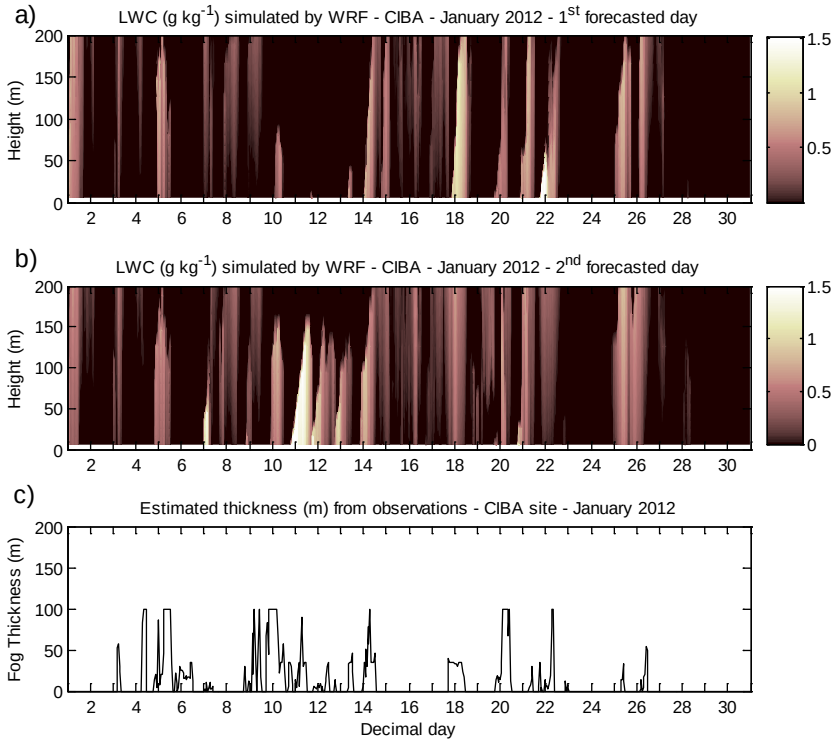

Figure 4.7: As in Figure 7.6 but for CIBA site, January 2012.

period from day 5 to 15. However, for S2 (Figure 4.7 (b)), the model was able to simulate the fog events for these days. This fact is mainly related to the spin-up time and initial conditions; therefore, it will be subsequently investigated.

As indicated in Table 4.7, S2 simulations reproduce more fog hours than S1 at both sites (simulated fog hours, 46% more at CESAR and 54% more at CIBA). This is traduced on an improvement of the correctly simulated fog hours, specially at CIBA (134/201 for S2 vs 96/201 for S1), although it also deteriorates the false-alarm rate (incorrectly simulated no-fog hours). These results are consequence of the ability of the model to produce higher values of relative humidity for S2 comparing to S1, since the decrease in the surface temperature during the late afternoon is more correctly simulated for S2, specially at CIBA. Thus, at CIBA, the temperature bias for S2 is +0.8 °C and -0.2 °C for S1 during the time interval from 17:00 UTC (approximate sunset time) to 00:00 UTC for the whole month, while the mean relative humidity simulated for this time period is 92.9% for S1 and 95.3% for S2 (Table 4.7). At CESAR, these differences in temperature and relative humidity simulations

between S1 and S2 are not as important as at CIBA. For these reasons, the results for S1 and S2 are similar in this case. In the next paragraphs, the analysis is focused on some specific days at CIBA, in order to analyse with more detail the previously commented findings.

Table 4.7: Comparison between S1 and S2 radiation-fog simulations of WRF (LWC at the lowest level) at CESAR and CIBA.

CESAR	**S1**	**S2**
OBSERVED fog hours	163/720	163/720
SIMULATED fog hours	162/720	237/720
Correctly SIMULATED fog hours (hit)	43/163	50/163
Incorrectly SIMULATED fog hours (miss)	120/163	113/163
Correctly SIMULATED no-fog hours (correct rejection)	438/557	370/557
Incorrectly SIMULATED no-fog hours (false alarm)	119/557	187/557
T_{2m} bias (from 15:00 UTC to 00:00 UTC)	-0.8 °C	-1.1 °C
Mean relative humidity (from 15:00 UTC to 00:00 UTC)	95.5%	95.9%

CIBA	**S1**	**S2**
OBSERVED fog hours	201/720	201/720
SIMULATED fog hours	183/720	281/720
Correctly SIMULATED fog hours (hit)	96/201	134/201
Incorrectly SIMULATED fog hours (miss)	105/201	67/201
Correctly SIMULATED no-fog hours (correct rejection)	432/519	372/519
Incorrectly SIMULATED no-fog hours (false alarm)	87/519	147/519
T_{2m} bias (from 16:00 UTC to 00:00 UTC)	+0.8 °C	-0.2 °C
Mean relative humidity (from 16:00 UTC to 00:00 UTC)	92.9%	95.3%

The very shallow fog formed during the late-afternoon/evening of day 11 and lasting until midday of day 12 was reproduced by the model taking into account S2 (Figure 4.8 (a)), although its vertical extension was significantly overestimated. However, the model failed simulating this fog when using S1 (Figure 4.8 (b)). These results are directly related to the underestimation of relative humidity (Figure 4.8 (d)) (bias of -9% from 18:00 UTC of day 11 to 18:00 UTC of day 12 for S1 and +5% for S2) and overestimation of temperature attending to S1 (Figure 4.8 (f)) (bias of +3.03 °C for S1 and +0.57 °C for S2 for this period). This overestimation in temperature by S1 is due to the inability of the model to forecast the strong nocturnal cooling of day 11 from 15:00 UTC onwards (Figure 4.8 (f), see black ellipse). However, the decrease in temperature was more intense (and more real) for S2 (Figure 4.8 (e), see black ellipse), which led to higher values of relative humidity (Figure 4.8 (c)) (overestimation of 5% for the analysed period for S2).

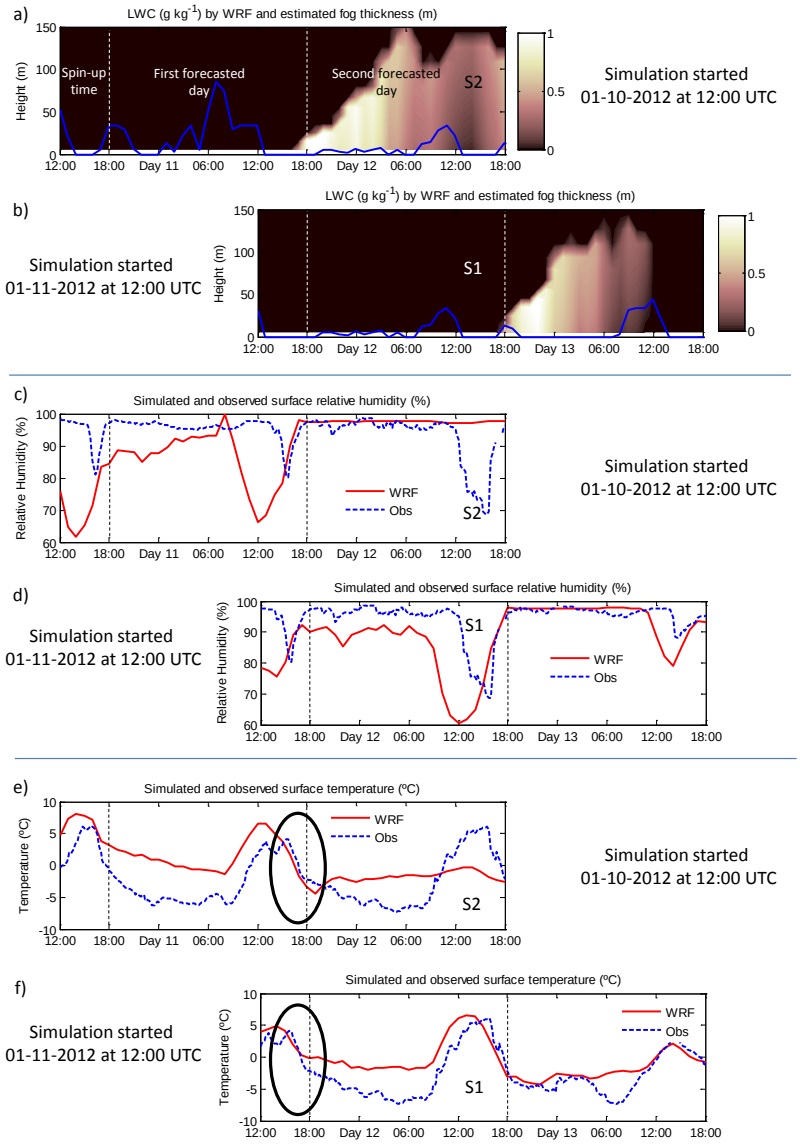

Figure 4.8: CIBA site. a,b) Estimated fog thickness (m) from observations (blue solid line) and LWC (g kg^{-1}) simulated by WRF (contours) for the simulation initialized on 01-10-2012 at 12:00 UTC (a) and on 01-11-2012 at 12:00 UTC (b). c,d) Observed (blue dashed line) and simulated (red solid line) relative humidity (%) for the simulation initialized on 01-10-2012 at 12:00 UTC and on 01-11-2012 at 12:00 UTC (d). e,f) Observed (blue dashed line) and simulated (red solid line) temperature (°C) for the simulation initialized on 01-10-2012 at 12:00 UTC (e) and on 01-11-2012 at 12:00 UTC (f). Note that vertical dashed lines separate spin-up time (6 h), first simulated day and second simulated day, as indicated in figure a.

Therefore this was traduced on the simulation of fog (Figure 4.8 (a)). Although it is not shown, similar results are found for the rest of the days of this period and this example can be extrapolated to the other days with shallow fog at CIBA.

The inability of the model to produce enough surface cooling at the beginning of the simulation is due to the stabilization period of the model, which produces spurious waves to get the model in balance with the provided boundary conditions (Figure 4.9).

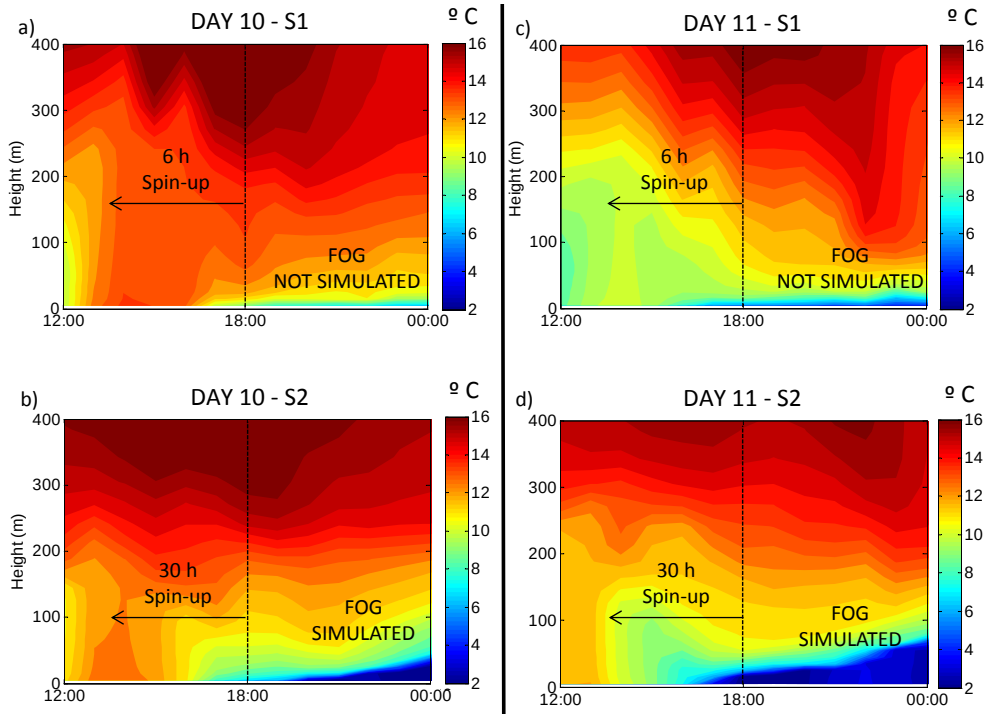

Figure 4.9: CIBA site. Potential temperature (°C) simulated by WRF for the afternoon of day 10 (a and b) and for the afternoon of day 11 (c and d). Upper figures correspond to S1 (simulation started 6 hours before the vertical dashed line) and lower figures correspond to S2 (simulation started 30 hours before the vertical dashed line). Note how fog developed after 18:00 UTC were not simulated by the upper figures.

This figure compares the potential temperature simulated by the model from the lowest level up to 400 m agl for S1 and S2 during the period comprising from 12:00 UTC to 00:00 UTC for two different days. As shown in Figure 4.8, the surface cooling is more effective for S2 (Figure 4.9 (b and d)), while it is weaker for S1 (Figure 4.9 (a and c)), since some oscillations appear above 200 m agl soon after the model initialization (upper figures, Figure 4.9 (a and c)). One of the consequences of these apparently spurious waves is

the prevention of the efficient cooling of the lower layers (and therefore the inability of the model simulating high values of relative humidity and fog). However, these oscillations are not observed attending to S2 (Figure 4.9 (b and d)) and the cooling is more efficient at the lower layers. Thus, it is shown how the model needs more time to start reproducing correctly the conditions leading to fog onset (enough surface cooling) and to develop fog in the vertical, so longer spin-up times are required to obtain satisfactory simulations of radiation fog. On the other hand, this result also suggests that the dynamical downscaling using a physical configuration for the higher-resolution model more consistent with the global and lower-resolution model could be more convenient (for example using the same definition for vertical levels), since this could prevent the formation of the spurious waves formed to get the mesoscale model in balance with the input provided. This experiment is out of the scope of the present study, although it is encouraged for future numerical works.

4.4 SUMMARY AND CONCLUSIONS

Six-year data from two contrasting sites (CESAR and CIBA) were used to perform a robust statistical 6-year climatology of radiation fog and to highlight differences in the life cycle of radiation fog at both experimental sites. At CESAR, radiation-fog events are distributed throughout the whole year. Almost 75% of them are formed less than 6 hours after sunset, they persist a few hours (more than 50% less than 6 hours) and dissipate around sunrise. These features are determined by the high availability of humidity at CESAR, helping the formation of radiation fog, especially in spring and summer after afternoon convective rains. Fog at CESAR is usually quite shallow and easy to dissipate around sunrise. However, radiation-fog events at CIBA occur mainly during late-autumn/winter (the coldest months), when persistent anticyclones cause clear skies and low-wind conditions. The relatively lower humidity at CIBA makes radiation fog form later in the night in general, after strong nocturnal surface cooling. These radiation-fog events are usually more persistent than at CESAR.

Two different radiation-fog forecasting approaches have been evaluated at both sites. The first one is a statistical method based on the work presented by Menut et al. (2014) (M14). This method is based on the use of threshold values for different key variables during 6 h preceding fog formation (RH_{2m}, $\triangle T_{2m}$, U_{10m}, F_{IR}). Here, the skill of this method for forecasting radiation fog at CESAR and CIBA has been evaluated, in order to analyse its robustness at different sites. In general, the results obtained at CESAR and

CIBA were quite satisfactory. Firstly, the same threshold values obtained at the Paris area in M14 are used. Then, the frequency histograms of these variables during pre-fog conditions at CESAR and CIBA are used to calculate other combinations of threshold values. The threshold values given in M14 (based on evaluation in Paris area) produced in general better performance indicators than those thresholds calculated taking into account the local climatology of both sites, although at CIBA the Hit Rate (H-R) is improved using its specific thresholds. Accordingly, a calibration of this method is offered by providing some of the combinations of threshold values needed to obtain the best fog-forecasting results in terms of H-R, False Alarm (F-A) rate and Gilbert Skill Score (GSS) at each site within a reasonable range of threshold values. With this calibration, 95.5% (F-A of 38.9%) of radiation-fog events are detected at CESAR and 80.9% (F-A of 21%) at CIBA. In the case of CESAR, the use of RH_{2m} is not necessary, since the humidity is almost always very high. The use of additional variables (u_* and $\triangle VIS_{2m}$) can be useful for fog prediction. However, the use of $\triangle VIS_{2m}$ is not recommended at CIBA, since radiation fog is usually observed during relatively long periods with many consecutive events, and pre-fog conditions can coincide with post-fog conditions of previous events (increasing visibility).

The use of WRF model output as predictor for the M14 method does not provide satisfactory performance indicators, since the timing of fog is usually not correctly predicted by the model. The H-R is higher at CESAR (up to 86.7% of predicted pre-fog periods), although at the expense of a quite high F-A (37.4%). The use of too limiting thresholds for some variables as U_{10m} and $\triangle T_{2m}$ leads to a limited prediction of fog events, since the model fails in simulating low-wind and strong cooling conditions. At CIBA, this approach is even more complicated, since radiation-fog events are usually separated by short-time intervals (dissipation of a fog event and onset a few hours later again). This causes a worsening of the performance indicators due to the difficulties of the model simulating the onset (Steeneveld et al., 2015) and the persistence of fog (see results from previous chapter, Chapter 3). These considerations lead to the conclusion that fog-forecasting at both sites using the M14 method is satisfactory, but it is highly influenced by the selection of threshold values. In general, the use of too high values for some variables (for example $\triangle T_{2m}$ and U_{10m}) led to unsatisfactory H-R, specially in the case of the M14 method with model output.

Finally, the simulation of fog in terms of LWC has also been evaluated for one month at each site. In general the WRF model was able to correctly simulate most radiation-fog events at the expense of sophisticated physical options and a high resolution (one domain with 300 x 300 points and 2.5 km of horizontal resolution). A comparison between the 1st (6 h of spin-up + 0

to 24 hours from model initialization) and the 2nd (6 h of spin-up + 24 to 48 hours from model initialization, equivalent to 30 h of spin-up) forecasted day is also performed. The 2nd forecasted day (S2) usually offered the best simulation of radiation fog, since in some cases, some spurious waves produced after the model initialization avoided the surface cooling necessary to provide high values of relative humidity. These results evidence the high sensitivity of the model to the spin-up time and initial conditions during foggy periods and manifest the necessity of using long and adequate spin-up times. The findings also contraindicate the downscaling from a coarser resolution model for fog forecasting and encourage the use of data assimilation. On the other hand, this also suggests the use of higher and lower resolution models with similar physics and dynamics to avoid the spurious waves formed during the spin-up.

To conclude, on the one hand the statistical analysis of long datasets allows for improving fog forecasting through the use of statistical methods (e.g. the M14 method). On the other hand, quality and reliable observations are needed to improve NWP data assimilation and initial conditions of numerical models. Therefore, it is necessary to preserve the important research facilities as CIBA and CESAR. This will lead to better forecasts of fog events.

5

ESTIMATING FOG-TOP HEIGHT THROUGH NEAR-SURFACE MICROMETEOROLOGICAL MEASUREMENTS

Fog-top height (fog thickness) is very useful information for aircraft manoeuvres, data assimilation/validation of Numerical Weather Prediction models or nowcasting of fog dissipation. This variable is usually difficult to determine, since the fog-layer top cannot be observed from the surface. In some cases, satellite data, ground remote-sensing instruments or atmospheric soundings are used to provide approximations of fog-top height. These instruments are expensive and their data not always available. In this work, two different methods for the estimation of fog-top height from field measurements are evaluated from the statistical analysis of several radiation-fog events at two research facilities. Firstly, surface friction velocity and buoyancy flux are here presented as potential indicators of fog thickness, since a linear correlation between fog thickness and surface turbulence is found at both sites. An operational application of this method can provide a continuous estimation of fog-top height with the deployment of a unique sonic anemometer at surface. Secondly, the fog-top height estimation based on the turbulent homogenisation within well-mixed fog events (an adiabatic temperature profile) is evaluated. The latter method provides a high percentage of correctly-estimated fog-top heights for well-mixed radiation fog events, considering the temperature difference between different levels of the fog. However, it is not valid for shallow fog (~ less than 50 m depth), since in these cases, the weaker turbulence within fog is not able to erode the surface-based temperature inversion and to homogenise the fog layer.

The content of this chapter is under review in *Atmospheric Research* journal in the following article:

ROMÁN-CASCÓN, C., YAGÜE, C., STEENEVELD, G. J., SASTRE, M., ARRILLAGA, J. A. & MAQUEDA, G. (2015): Estimating fog-top height through near-surface micrometeorological measurements. Under review in *Atm. Res.*. ATMOSRES-D-15-00532.

5.1 INTRODUCTION

As it could be appreciated in the previous chapters (Chapter 3 and Chapter 4), it is important to have reliable estimations of observed fog-top height for comparison with numerical simulations from models, as well as for other important purposes commented in the introduction of this thesis (Chapter 1). However, this variable is not always accessible and its knowledge is usually subjected to data from expensive or not-accessible instruments.

In this chapter, on the one hand, a clear linear correlation between surface turbulence and fog-top height is found. Thus, regression equations are calculated relating friction velocity and buoyancy flux at surface with fog thickness data. These relations are statistically calculated by using data from numerous radiation fog events at CESAR and CIBA. A potential applicability of this method could provide a continuous estimation of fog-top height during radiation-fog events with the deployment of a unique sonic anemometer close to the surface, which are cheaper instruments than those usually employed for this purpose.

On the other hand, the estimation of fog thickness using temperature measurements in the vertical is evaluated. This variable normally converge to the same value at the levels where the fog is present when the fog is sufficiently well-mixed (Nakanishi, 2000; Porson et al., 2011; Price, 2011). Therefore, observed fog thickness (through visibility measurements at several heights) are compared to estimated values based on differences between temperature measured at several levels, in order to check if the temperature convergence does not occur for shallow fog, as suggested by Price (2011). It is shown how the performance of the method strongly depends on the fog thickness and it is not valid for shallow fog. However its application is also limited for deeper fog ($\sim$ 200 m depth).

To conclude, a long-lasting event of radiation fog at CESAR is analysed, with the objective of determining the applicability and skill of these methods during a complete fog cycle.

The chapter is organised as follows: Section 5.2 specifies detailed information about the data used from the experimental sites. Section 5.3 shows the results for both methods and their evaluation for a case-study occurred at CESAR. Finally, a short discussion and conclusions are presented in Section 5.4.

5.2 DATA AND METHODOLOGY

This chapter uses data from CESAR, where a 200-m mast stands (Figure 5.1) with many meteorological instruments from different institutes. However, only a few of them (indicated in Figure 5.1) were necessary for this study. On the other hand, it also uses data from CIBA. The height of the mast at CIBA is 100 m, instrumented at different levels (see also the details in Figure 5.1). Note how the heights where the instruments were deployed differ between these two sites.

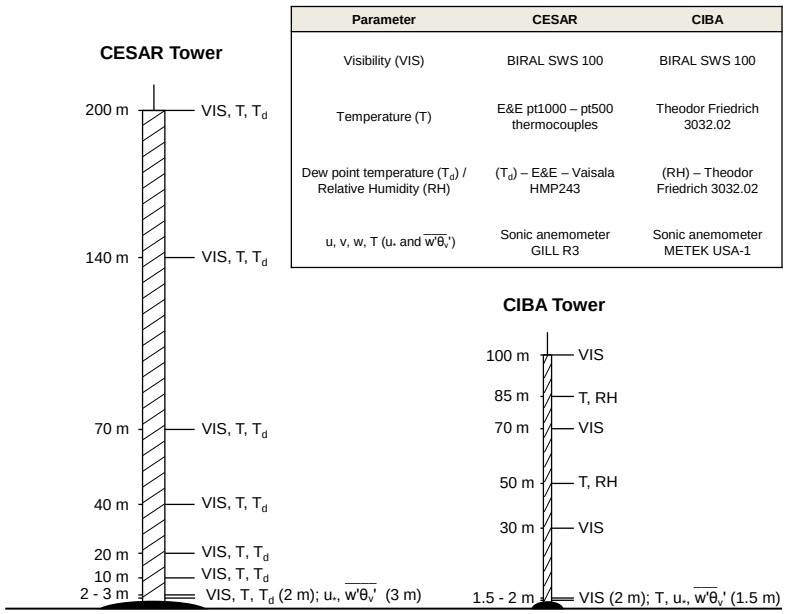

Parameter	CESAR	CIBA
Visibility (VIS)	BIRAL SWS 100	BIRAL SWS 100
Temperature (T)	E&E pt1000 – pt500 thermocouples	Theodor Friedrich 3032.02
Dew point temperature (T_d) / Relative Humidity (RH)	(T_d) – E&E – Vaisala HMP243	(RH) – Theodor Friedrich 3032.02
u, v, w, T (u. and $\overline{w'\theta_v'}$)	Sonic anemometer GILL R3	Sonic anemometer METEK USA-1

Figure 5.1: Graphical representation of CESAR and CIBA towers with measurements taken at each height. Information about the instruments is provided in the upper table.

Due to the necessity of visibility measurements at several heights to perform this study, data from fog events within the period from April 2011 to December 2013 and from 24 December 2014 to 14 January 2015 were analysed at CESAR and CIBA respectively. The starting date of the periods coincides with the implementation of these visibility measurements at each site. Since the mechanisms governing the different types of fog events differ, only radiation fog or cloud-base lowering (cbl) fog were analysed here, which were classified according to Tardif and Rasmussen (2007) classification, as done in the previous chapter. Therefore, advection or precipitation fog events have not been included in this study, since the physical mechanisms involved in their formation are different than those for radiation and cbl fog.

5.3 RESULTS

5.3.1 *Fog thickness estimation from surface turbulent measurements*

In this section, it is shown how surface turbulent parameters calculated from sonic anemometer measurements can provide satisfactory estimations of the fog-top height.

a) Estimation from friction velocity

Firstly, surface friction velocity (u_*, Equation 2.10) values are calculated from high frequency measurements of sonic anemometers at both sites. Subsequently, u_* values are averaged into 10-min data and compared with their associated values of fog thickness for all considered fog events at each site. It has not been considered only the mature stage of each event but the whole fog cycle, due to the observed high correlation between the value of this turbulent parameter and the growing or decaying of the fog layer. Note that only data when the visibility < 1000 m at 2 m agl are included, i.e., when fog is reported at the lowest level. Fog thickness was estimated from visibility measurements at different heights at each site (see Figure 5.1 for differences between sites) and it is assigned to the midpoint between the maximum height where the visibility is < 1000 m and the height of the next visibilimeter up in the tower (where visibility is > 1000 m). In the case of visibility < 1000 m at the highest level with availability of visibility measurements (200 m agl at CESAR and 100 m agl at CIBA), fog thickness is estimated to be equal to the corresponding level at each site, since there is no more information above these heights, although this can represent an underestimation.

Figure 5.2 shows the mean friction velocity calculated for each fog thickness value (discrete values). Vertical dotted blue lines indicate the uncertainty in the fog thickness, given by the height differences between adjacent visibilimeters. Horizontal dotted blue lines show the standard deviation of the set of friction velocity measurements for each fog-top height.

Afterwards, linear adjustments for fog-top height (Z_{f-t}) and u_* were calculated for each site and are expressed with red dashed lines in both figures, corresponding to Equation 5.1 at CESAR and Equation 5.2 at CIBA:

$$Z_{f-t} = 1369\ u_* - 28 \tag{5.1}$$

$$Z_{f-t} = 1029\ u_* - 30, \tag{5.2}$$

where Z_{f-t} is obtained in meters if u_* is provided in m s^{-1}. The coefficient of determination (R^2) is substantially high for both sites (0.974 at CESAR

and 0.982 at CIBA), which highlight the linear relation between these two parameters.

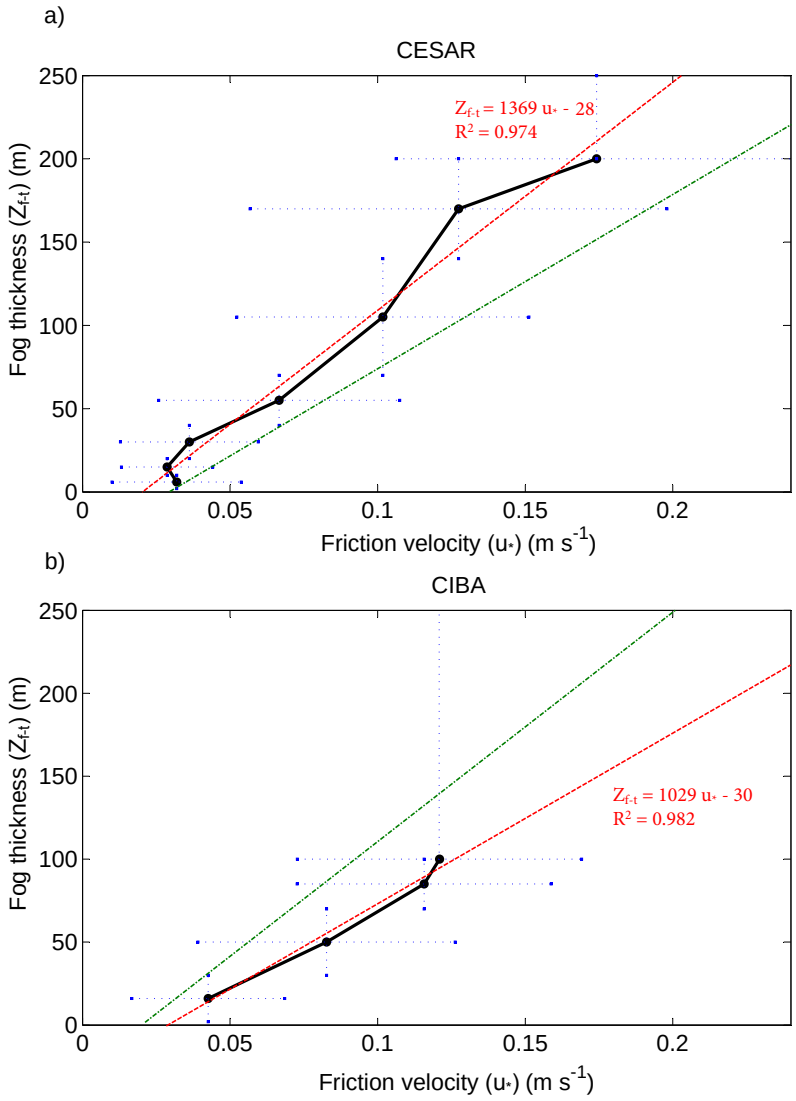

Figure 5.2: a) CESAR. b) CIBA. Mean friction velocity (u_*) (m s^{-1}) associated to each discrete value of fog thickness (m) (black solid line). The green dotted-dashed line indicates the linear regression obtained at the other experimental site (e.g. the green line above (CESAR) corresponds to the red line below (at CIBA)). Horizontal dotted lines indicate the error bars of u_* (standard deviation). Vertical dotted lines indicates the error bars for each fog thickness, determined by the distance between adjacent visibilimeters in the towers

The trend is statistically significant in both cases (T-student significance test with 95% of confidence). Nevertheless, the relatively extensive length of horizontal error bars should be noted, specially for deeper fog events, which indicates the spreading over a wide range of values. However, the fluctuating nature of a turbulent parameter as u_* and the use of 10-minutes data in this study make the use of u_* mean values appropriate for the linear regression.

The intercepts -28 and -30 in Equation 5.1 and Equation 5.2 (the point where the lines cross the x-axis of Figure 5.2 (a and b)) indicate that a minimum turbulence is needed to form radiation fog at CESAR and CIBA respectively. These values are quite similar at both sites (around 0.025 m s^{-1} at CESAR and 0.03 m s^{-1} at CIBA). Hence, according to the linear regression, no fog will be formed below these thresholds and these are the minimum turbulence values required to start forming a (very shallow) fog at each site. Oppositely, u_* maxima values for deep fog provide an indication of the turbulence required to dissipate the fog, since no fog is observed above these limits. Although u_* outliers can appear during fog events, values larger than 0.2 m s^{-1} at CESAR and 0.15 m s^{-1} at CIBA are rarely observed and they can be related to the transformation of fog into low clouds (dissipation at surface).

Green dotted-dashed lines in Figure 5.2 (a and b) show the regression line for the other site for a clearer comparison. In the case of CESAR, most analysed fog events in this study have less thickness than 200 m, and this height is normally exceeded by fog only for short time intervals. Therefore, the mean u_* value obtained for 200-m fog should not correspond to fog much deeper than 200 m. However, at CIBA many fog events exceeds the 100-m level and therefore the mean u_* associated with 100-m fog events could not correspond to fog events with thickness of 100-m, but some tens of meters more. Consequently, if this could have been considered, the slope of the line obtained at CIBA (green dotted-dashed line in Figure 5.2 (a) or red dashed line in Figure 5.2 (b)) would become more similar to the CESAR one (red dashed line in Figure 5.2 (a) or green dotted-dashed line in Figure 5.2 (b)). In any case, lower values of turbulence are found within radiation fog at CESAR compared to CIBA values, which can be due to differences between sonic instruments (GILL-R3 at CESAR and METEK-USA1 at CIBA), or to the height where they were installed (3 m agl at CESAR and 1.5 m agl at CIBA). Besides this, the results could also be affected by a possible site-dependence, such as differences on local heterogeneities, surface humidity affecting the strength of turbulence (Sastre et al., 2015), etc. Therefore, future comparisons with other sites with different surface and local characteristics are specially encouraged.

Figure 5.3 and Figure 5.4 show the frequency histograms of friction velocity measured for each fog-top height at CESAR and CIBA respectively. Vertical blue lines indicate the mean of these values (used in Figure 5.2 for the linear regression), which are relatively close to median values.

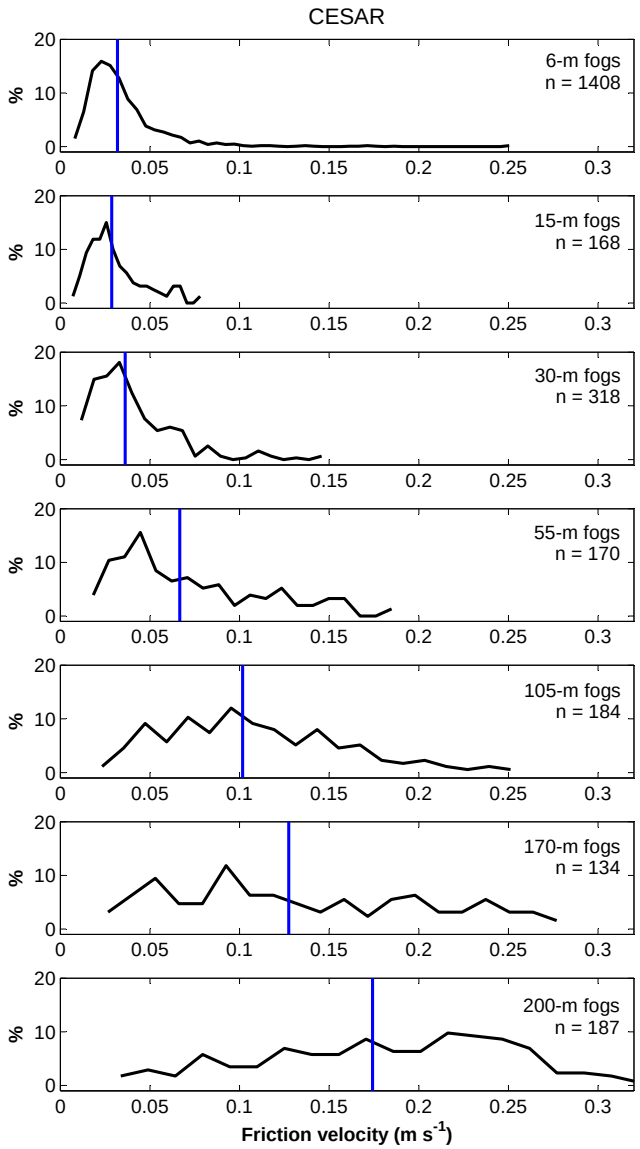

Figure 5.3: CESAR - Frequency distribution plots for friction velocity measurements (m s^{-1}) associated to each fog thickness (6, 15, 30, 55, 105, 170, 200 m fog -from top to bottom-). The blue vertical line indicates the mean value (used in Figure 5.2 (a) in black solid line), while n indicates the number of data for each fog thickness.

The number of considered data for each fog thickness is indicated with n, which is considerably larger for 6-m fog at CESAR (n = 1408) (note that 6-m fog are defined as those fog events observed at the level of 2 m agl but not at 10 m agl). This indicates that most fog events at CESAR (formed in spring and summer after convective rains) are very shallow. Since this number is quite high, the frequency distribution for 6-m fog at CESAR includes more outliers and therefore it has a relatively long tail towards larger values of friction velocity, compared to fog events with other thickness.

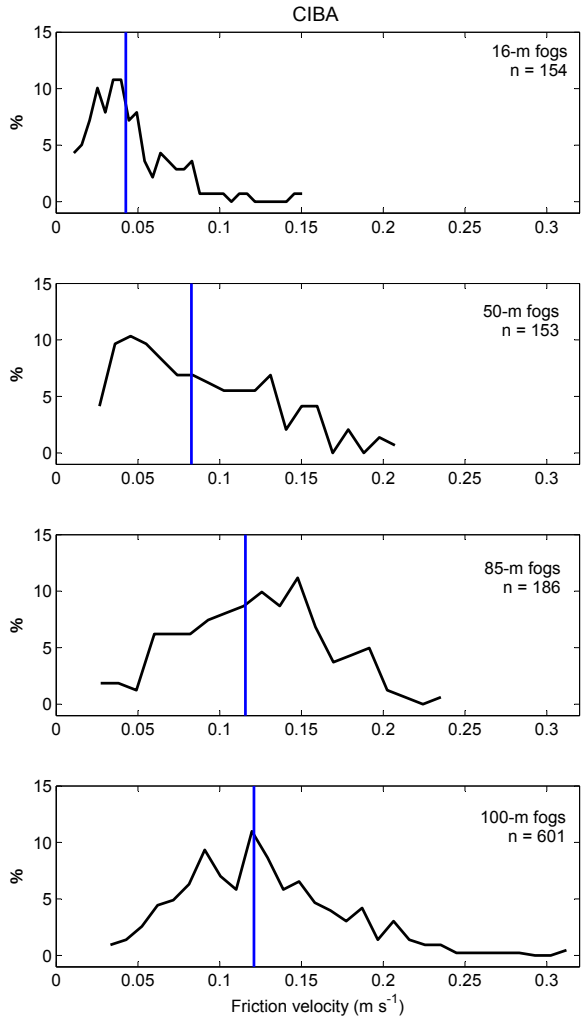

Figure 5.4: CIBA - Frequency distribution plots for friction velocity measurements (m s^{-1}) associated to each fog thickness (16, 50, 85, 100 m fog -from top to bottom-). The blue vertical line indicates the mean value (used in Figure 5.2 (b) in black solid line), while n indicates the number of data for each fog thickness.

Many of these relatively higher values of turbulence (the tail to the right of the frequency distribution of 6-m fog) are observed during the quick dissipation stage of these shallow fog events. Therefore, the mean value of friction velocity for 6-m fog is slightly larger than the obtained for 15-m fog events (as seen in black solid line of Figure 5.2 (a)). For deeper fog, the frequency distributions are shifted to larger friction velocity values at both sites, as also observed in Figure 5.2.

Note how n is larger for 100-m fog at CIBA (Figure 5.4) than for fog with other thickness. Therefore, its associated frequency distribution is widened in comparison with frequency histograms of fog events with other thickness, as happened with 6-m fog at CESAR. Besides, although 10-min data are used, u_* is a very fluctuating parameter and it is recommended to average its value over larger averaging times (around 1 h) for the calculation of continuous fog thickness in an operational use.

b) Estimation from buoyancy flux

On the other hand, and as it will be shown later, fog events with the top above certain height are convectively active and can be considered as well-mixed fogs. Therefore, the thickness of these fog events is supposed to be more influenced by the buoyancy generated by the fog itself (mainly due to the mixing caused by the radiative cooling at the fog top) than by turbulence near surface. Thus, some scaling parameter more related to the convection within the fog could become a more appropriate scale to link with the fog thickness, specially for deep fog. However, for an operational use, the scaling variable should not use information about the height of these buoyancy-related motions (similar to thermals), which is an usual parameter used for scaling convective boundary layers. Therefore, parameters as the convective velocity scale (Stull, 1988) cannot be used since only information about the buoyancy flux can be obtained from a surface sonic anemometer and no information about the height of the thermals (the height of the convective boundary layer or, in this case, the thickness of the fog) will be available. Hence, buoyancy flux values ($\overline{w'\theta'_v}$) have been linked to their associated fog thickness. Note that $\overline{w'\theta'_v}$ is calculated from vertical velocity and temperature measurements from a sonic anemometer (which is indeed the virtual temperature, since it is calculated from the density of the air).

Figure 5.5 (a and b) show the relation between the buoyancy flux and fog thickness at CESAR and CIBA respectively, calculated following the same procedure as with u_* in Figure 5.2. However, in this case the frequency distributions for this variable for each fog thickness (as in Figure 5.3 and Figure 5.4, but for $\overline{w'\theta'_v}$) show a more asymmetric distribution and more

dispersed to extreme values (not shown). Therefore, the use of mean values is not appropriate and median values for each fog thickness have been used to plot the curves shown in Figure 5.5 (mean values differ significantly from median values in this case and the linear regression is worse). The horizontal errors bars range from percentile 25 to percentile 75, indicating the position of the central 50% of the data. These error bars are significantly larger than in the case of friction velocity (Figure 5.2), even when standard deviations (which include approximately the 67% of the data with respect to the mean) are shown in Figure 5.2.

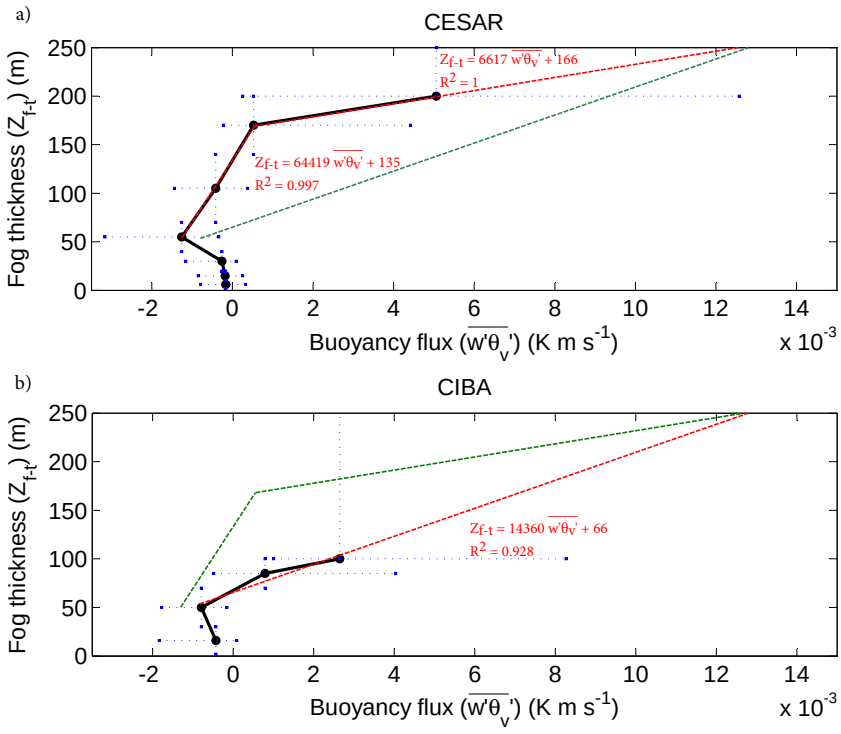

Figure 5.5: a) CESAR. b) CIBA. Buoyancy flux ($\overline{w'\theta'_v}$) (K m s^{-1}) median values associated to each discrete value of fog thickness (m) (black solid line). Red dashed lines represent the linear regressions for points considering fog thickness higher than 55-m at CESAR and 50-m at CIBA (corresponding to the equations written in red). Horizontal dotted blue lines indicate the error bars of $\overline{w'\theta'_v}$, determined by percentiles 25 and 75 of the set of measurements for each fog thickness. Vertical dotted blue lines indicates the error bars for each fog thickness.

Small values of buoyancy flux (and mainly negative) are associated with shallow fog (Figure 5.5), related to the weak convection and to the stable conditions within them. Therefore, it is difficult to associate $\overline{w'\theta'_v}$ values with fog thickness of shallow fog. However, it should be noted that the most

negative buoyancy flux is found for fog events of around 50-m depth at both sites. The explanation to this issue is more difficult and it could be related to the fact that most of these fog events (around 50-m fog) are in their initial stage and the negative buoyant motions from the fog-top prevail over positive motions. This issue could also be related to the fact that 50-m fog (approximately) is associated with larger values of turbulence than shallower fog, as observed in Figure 5.2. Thus, this turbulence could help to the enhancement of the negative buoyancy flux.

However, for deeper, more mixed and mature fog, this descendent motions do not seem to dominate but positive ones. This fact seems to indicate that the cooling at the fog top is more important during the development of the fog than during the mature stage, when the buoyancy flux has a wider range of values and more shifted to positive (ascending) ones. Besides, many of these deep fog events are usually persistent during daytime and their larger and positive values of $\overline{w'\theta'_v}$ are also associated with the heating of the surface caused by the fraction of the solar radiation able to cross the fog layer and heat the ground. Nevertheless, a near-linear relation is found for deep fog events (Equation 5.3 at CESAR and Equation 5.4 at CIBA and red text in Figure 5.5). Two slopes can be differentiated at CESAR: the first one has been calculated using median values of $\overline{w'\theta'_v}$ of 55-m, 105-m and 170-m fog events while the second one has been calculated with 170-m and 200-m fog (Equation 5.3). It is somehow logical that the slope of the line linking the upper points (170-m and 200-m fog) is lower, since the fog top is further from the ground and variations in the buoyancy flux at surface are somehow less linked to the conditions at that heights. At CIBA, only a linear regression (Equation 5.4) is calculated (using 50-m, 70-m and 100-m fog), due to the lack of data above 100 m.

For fog with $u_* < 0.061$ m s^{-1} (~ 55-m fog from Equation 5.1) at CESAR and $u_* < 0.077$ m s^{-1} (~ 50-m fog from Equation 5.2) at CIBA, Equation 5.1 and Equation 5.2 should be used, since they will be shallow fog events with no substantial buoyancy fluxes. Therefore, for fog exceeding a height threshold (~ 50 m), the following equations are proposed. At CESAR, if $u_* \geqslant 0.061$ m s^{-1} (~ 55-m fog from Equation 5.1), then:

$$Z_{f-t} = \begin{cases} 64419\,\overline{w'\theta'_v} + 135 & \text{if} \quad \overline{w'\theta'_v} \leqslant 5 \times 10^{-4} \text{ K m s}^{-1} \\ \\ 6617\,\overline{w'\theta'_v} + 166 & \text{if} \quad \overline{w'\theta'_v} > 5 \times 10^{-4} \text{ K m s}^{-1} \end{cases} . \tag{5.3}$$

At CIBA, if $u_* \geqslant 0.077$ m s^{-1} (~ 50-m fog from Equation 5.2), then

$$Z_{f-t} = 14360\,\overline{w'\theta'_v} + 66 . \tag{5.4}$$

Note that Z_{f-t} is obtained in meters if $\overline{w'\theta'_v}$ is provided in K m s^{-1}. In any case, in this case, the linear regression between $\overline{w'\theta'_v}$ and Z_{f-t} is statistically not significant with a confidence level of 95%, mainly due to the few points used to calculate it. Besides, this variable is highly oscillating (more than friction velocity) and an operational use of these equations for the estimation of fog thickness could be less appropriate than using u_* alone. R^2 values are lower than those for the friction velocity and the differences between sites are larger. In addition, the range of the buoyancy flux values varies from negative to positive values, and therefore, neither mean values nor absolute values can be used, since the positive buoyancy fluxes are usually larger than the negative ones.

In brief, the statistic presented in this section suggests the possibility of using data from sonic anemometers (using u_* or using u_* for shallow fog and $\overline{w'\theta'_v}$ for deep fog above certain threshold) deployed at surface to provide near-real-time estimations of fog thickness (fog-top height). Nevertheless, further calibrations are required at other sites to detect site and instrument dependences. This simple and clear method opens a new (as far as the authors know) manner of estimation of fog-top height with cheaper instruments than usually used. An evaluation of these methods during a representative case study at CESAR is presented in Section 5.3.3

5.3.2 *Fog thickness estimation through temperature convergence (TC method)*

The turbulent mixing within fog causes the homogenization of the layer where the fog is present. The main mechanism proposed in the literature for such turbulent mixing is the radiative cooling at the top of the fog (Nakanishi, 2000; Porson et al., 2011; Price, 2011), causing dense bubbles of air to fall and mix the fog layer. However, the heating of the lower levels by condensation processes, heat fluxes from different surfaces and intermittent turbulence (e.g. gravity waves breaking (Duynkerke, 1991)) can also be involved. The mixing causes the convergence of temperatures at different heights to approximately the same value. Thus, many studies evaluate the fog thickness through the vertical profile of temperature (e.g., Koračin et al., 2001; Liu et al., 2011; Boers et al., 2013; Bari et al., 2015), estimating it in the layer where the thermal profile is near neutral or unstable or through the detection of the capping inversion. Although this method (hereinafter temperature convergence method or TC method) has less applicability than the turbulent methods presented in the previous section, it is commonly used in sites with availability of temperature measurements at different heights or

with atmospheric soundings (ideally at short time intervals within the fog cycle, as usual in field campaigns).

However, the temperature convergence is not observed in all fog events and some of them remain with stable stratification during an important part of their fog cycle or even for the whole life of the fog. Therefore, an evaluation of the real applicability or skill of this method should be done. Price (2011) detected 18 fog events with temperature convergence from a total of 38 cases. He suggested that the non-converging fog events were shallow ones, but he could not test this statement due to the unavailability of real fog thickness data.

In this section, real fog thickness (obtained from visibility measurements at different heights) is compared with the estimated thickness from temperature measurements. That is, for the estimated fog thickness, the fog is considered to be present at a certain height when the difference in potential temperature with the surface level (2 m agl) is less than 1.2 °C ($|\theta_{2m} - \theta_z| = |\Delta\theta| < 1.2$ °C), where the subscript z indicates the height with available measurements. Thus, the fog thickness is estimated to be equal to the maximum height where this condition is fulfilled. With the use of the potential temperature, height-related differences are avoided. One can consider that the use of saturated virtual potential temperature is more appropriate, since it includes the effect of the water vapour and liquid water content on the temperature. However, non-substantial differences were detected between using potential temperature and saturated virtual potential temperature (not shown). Therefore, this work is focused on the use of potential temperature, since only temperature measurements are needed for its calculation, while humidity and LWC information (for example from visibility) are required to compute saturated virtual potential temperature. Moreover, this method would lose applicability if saturated virtual potential temperature was needed.

A potential temperature difference ($|\Delta\theta|$) of 1.2 °C has been selected to determine fog presence since it is the value that offers the best estimations of fog-top height (Table 5.1).

Instrument-related uncertainty of temperature measurements is 0.3 °C, therefore, the uncertainty between two temperature measurements is 0.6 °C. However, with a $|\Delta\theta| = 1.2$ °C, small differences in temperature between layers and small differences caused by humidity and water content of the air at different heights are allowed. This strategy was also followed by Price (2011), who allowed for a difference in temperature between fog layers of 0.8 °C. In any case, several test were done (Table 5.1) changing this value and the best results were obtained for $|\Delta\theta| = 1$ or 1.2 °C. Although some improvements are observed using other thresholds for certain fog thickness estimations, it is always at the expense of a worsening of the results for other fog thickness,

Table 5.1: Percentage of correctly estimated fogs at CESAR using the temperature-convergence (TC) method for several values of differences in potential temperature ($|\Delta\theta|$) for fogs with different thickness and for all fog events (last column).

	Hit (%)							
$\|\Delta\theta\|$ (°C)	6-m fogs	15-fogs	30-m fogs	55-m fogs	105-m fogs	170-m fogs	200-m fogs	All fogs
0,6	97,7	2,4	8,9	32,9	50	62,2	12,2	**64,7**
0,8	96,1	4,1	12,2	39,2	58,9	68,6	33,8	**67,3**
1	93,7	6,1	15,4	46,8	64,8	75,3	45,6	**68,6**
1,2	89,9	8,5	18,5	48,1	70	82,9	54,9	**68,6**
1,4	84	11,4	23,6	51,9	71,9	83,9	61,2	**67,1**
1,6	75,8	14,2	26,4	54,4	71,9	84,3	64,4	**63,6**

while on average $|\Delta\theta| = 1.2$ °C offers the best hit rate for all fog events (69.8% of correctly estimated fog thickness) and better values than $|\Delta\theta| = 1$ °C for deeper fog (see Table 5.1).

Focusing on $|\Delta\theta| = 1.2$ °C, percentages of success for each fog thickness have been calculated after the comparison of real fog thickness and estimated fog thickness using the temperature convergence method (Figure 5.6). That is, an evaluation of the percentage of times of correctly-estimated fog thickness is performed, by using only potential temperature at different heights.

This evaluation has been done over a total of 95 fog events (radiation and cloud-base lowering fog) at CESAR and using 10-min data, which makes a total of 2569 data points evaluated. The number of data points evaluated for each fog thickness is the same than those shown in Figure 5.3 with n. Therefore, 6-m fog was the most predominant, with a total of 1408 data. This evaluation has not been performed at CIBA due to the differences in heights between visibility sensors and thermometers (see Figure 5.1).

Figure 5.6 shows how using this method, the fog-top height of 89.9% of 6-m fog is well estimated, and only the remaining percentage is overestimated. This high value of success is determined by the fact that this is the lowest considered level. 6-m fog is associated with strong surface-based thermal inversions and the potential temperature at 10 m agl is considerably higher than at 2 m agl. Hence, the method considers no-well mixed fog at 10 m agl and estimates the fog to be between the first level (2 m) and the second one (10 m), but not above this (i.e., 6 ± 4 m), since it considers that the fog is not established at the second level (10 m). However, the percent-

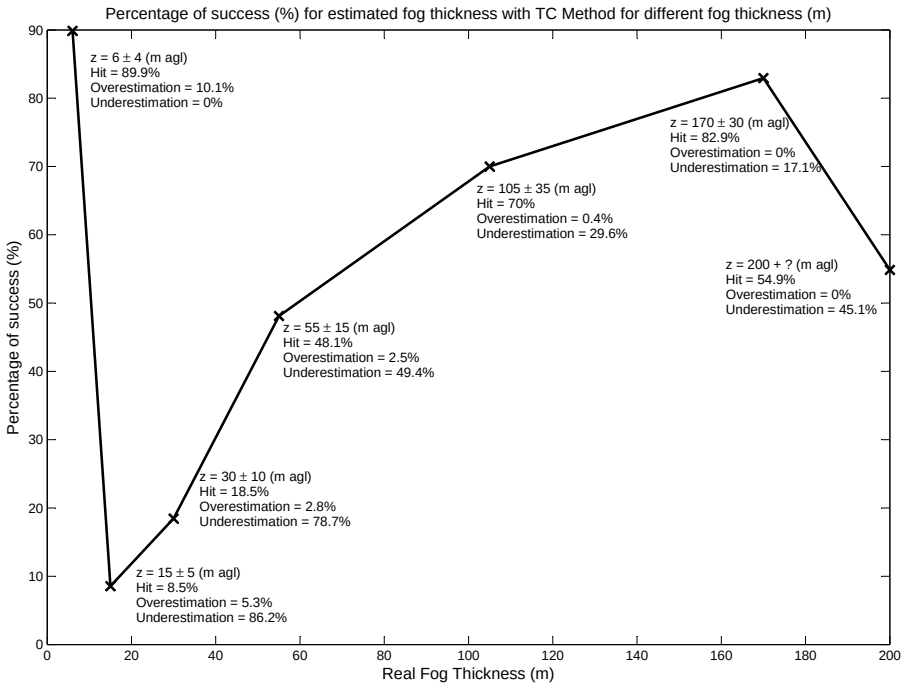

Figure 5.6: Percentage of success when estimating fog thickness with the TC method for each real observed fog thickness at CESAR. Text around points indicate the percentage of overestimated and underestimated values.

age of success for 15-m fog is quite low (8.5%), with an underestimation of 86.2% of fog-top height. That is, estimated thickness for 15-m fog is almost always underestimated, since the potential temperatures at the first and the second level do not converge to approximately the same value (less than 1.2 °C of difference). The same occurs for 30-m fog, although improving slightly the percentage of success (18.5%). However, for deeper fog, the percentage of success of correct estimations improves considerably, with a maximum of 82.9% of well estimated fog thickness for 140-m fog. That is, temperature convergence does not occur for shallow fog events, which are linked to strong thermal inversions and low levels of turbulence and the TC method is not valid.

However, the temperature convergence at the levels where the fog is established is observed for deeper fog, maintaining a considerable difference of temperature with the immediately upper level where the fog is not present. Nevertheless, a decrease in the hit (54.9%) is observed for 200-m fog, with an underestimation of 45.1% of fog. That is, the potential temperature at 200-m does not converge to the 2 m value in all the cases when the fog is observed

at the 200 m level. This result suggests that the upper layer of this thick fog is somehow decoupled from the conditions at lower layers.

Figure 5.7 shows the dispersion plot for the values of $\Delta\theta$ versus u_* for observed 200-m fog. Blue points indicate the cases associated with a correctly estimation of fog thickness with the TC method ($|\Delta\theta| < 1.2$ °C or $\Delta\theta > -1.2$ °C), while red points show the cases when the TC method underestimates the fog thickness due to a $|\Delta\theta| > 1.2$ °C (or $\Delta\theta < -1.2$ °C). In the latter cases, the differences in temperature between 200 m agl and 2 m agl are large and negative, or in other words, the thermal inversion is not broken up to the level of 200 m agl, even when the fog is present there. These cases are associated with less surface turbulence (u_*) than those when the 200-m fog is well estimated (blue points). The mean friction velocity for the correctly estimated 200-m fog events is 0.17 m s^{-1}, while it is 0.13 m s^{-1} for the incorrectly estimated ones (Figure 5.7).

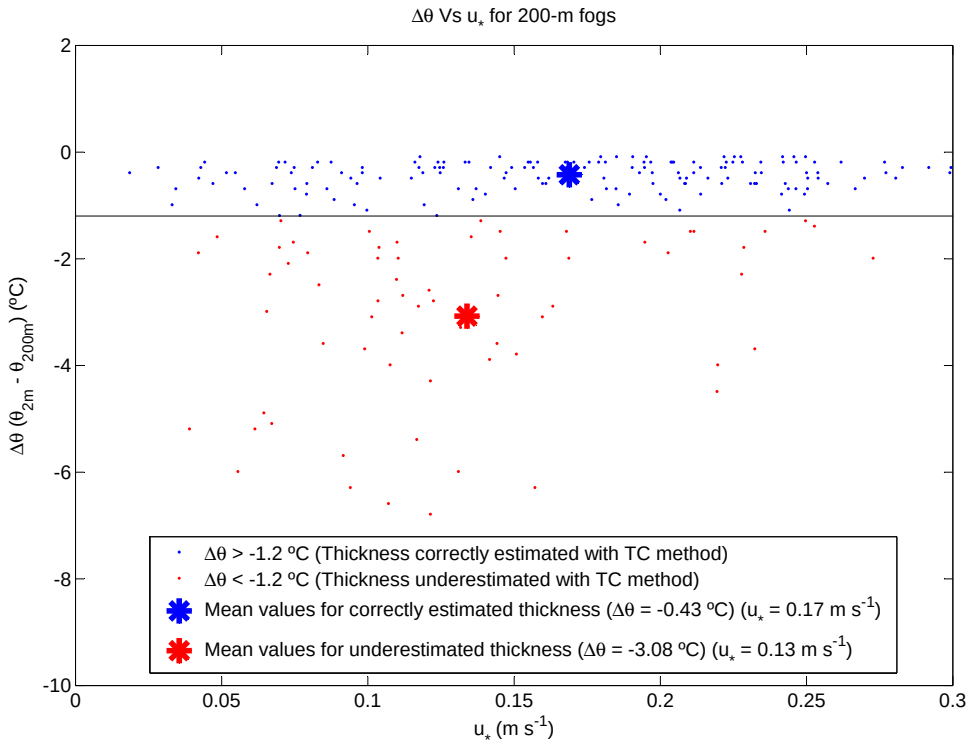

Figure 5.7: $\Delta\theta$ $(\theta_{2m} - \theta_{200m})$ versus u_* for 200-m fog. Blue points indicate $\Delta\theta > -1.2$ °C and red points $\Delta\theta < -1.2$ °C. The stars with the respective colors indicate their mean values for $\Delta\theta$ and u_*.

In the underestimated cases (red points in Figure 5.7), the visibility at 200 m agl is higher than at 2 m agl (not shown). That is, although the visibility is

< 1000 m, the reduction in visibility is not as large as at lower levels and the fog is less dense at the upper layers than below. However, for the correctly-estimated cases (blue points in Figure 5.7), the visibility is always lower at the fog top than at lower levels, as a result of the lower temperature corresponding to that height (in absolute values), leading to more condensation and thus, more LWC.

Figure 5.8 shows a conceptual picture of types of radiation fogs according to their thermal profile and analyses performed in previous paragraphs.

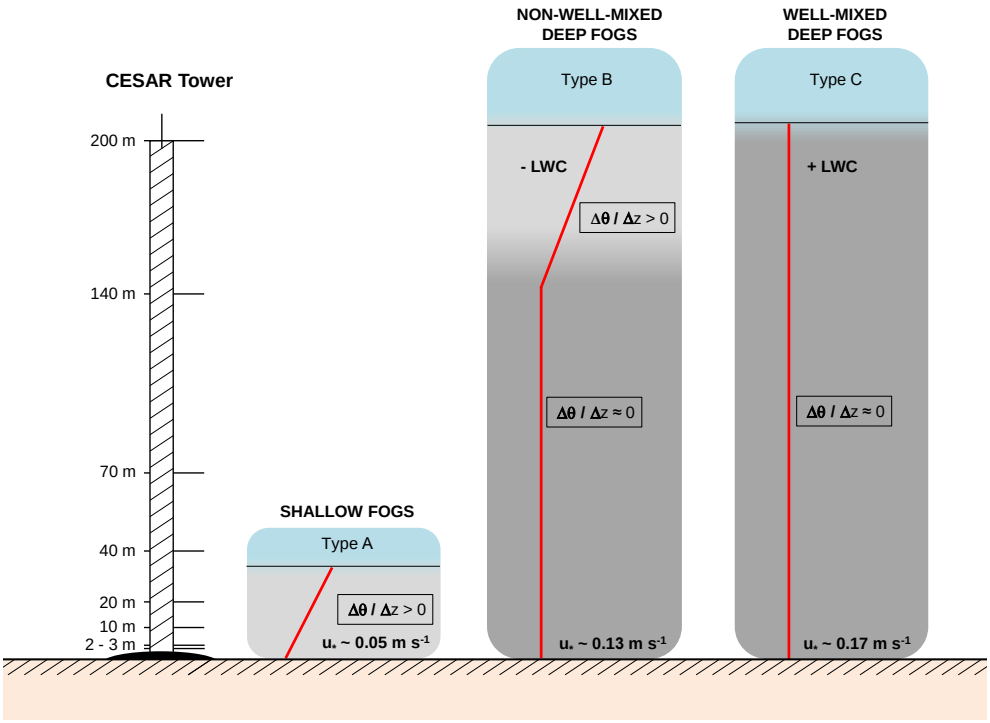

Figure 5.8: Conceptual picture of types of radiation fog according to their thermal vertical profile and results of Section 5.3.2.

The first one corresponds to shallow fog (type A), usually associated to surface-based thermal inversions, when the mean u_* is relatively low (~ 0.05 m s^{-1}) and not large enough to cause the homogenization of the fog layer, leading to a sub-adiabatic (stable) thermal profile. The other two cases correspond to deeper fog (~ 200 m depth), but they differ in the mean u_* measured at surface. The non-well-mixed deep fog (type B) is characterised by mean u_* values of around 0.13 m s^{-1}. In these cases, the fog is observed at the higher level (200 m), where the visibility is lower than 1000 m but larger than at lower layers. However, turbulent values are not strong enough to mix

the higher fog-layer and the stable thermal inversion is still present at these levels. Therefore, the temperature is larger at the top and the LWC is usually lower than at lower levels. However, during well-mixed deep fog (type C), the turbulent values measured at surface are relatively larger (~ 0.17 m s^{-1}), leading to an effective homogenisation of the fog layer even at the highest levels. Therefore, the temperature at the highest levels is lower and the LWC is higher, associated with more condensation.

5.3.3 *Evaluation of a case study at CESAR*

An analysis of observed and estimated fog thickness during a long-lasting fog event at CESAR is presented in this section. The case study corresponds to the fog formed during the afternoon of 19 November 2011 at CESAR and lasting until midday of 22 November 2011. This fog event has been chosen among all available cases because it is a long-lasting case with a gradual formation (dissipation) of the fog, slowly increasing (decreasing) its thickness and it also has a long mature stage of more than 24 hours. All these reasons make this case to be very appropriate to check the performance of the estimation of fog thickness through surface turbulent measurements (u_* and $\overline{w'\theta'_v}$) and from temperature measured at different heights (TC method or $|\Delta\theta|$). Note that this event was previously removed from the dataset used to obtain the results shown in the previous section in order to perform an independent verification of the skill of these methods.

Figure 5.9 (a) shows the comparison between observed real thickness (from visibility measurements at different heights, black line) and the estimated ones using the TC method (red dotted line), u_* (blue line, Equation 5.1), and a combination of u_* for shallow fog and $\overline{w'\theta'_v}$ for deeper fog (green dotted line, Equation 5.1 and Equation 5.3). In the latter case, u_* and Equation 5.1 have been used when $u_* < 0.061$ m s^{-1} (corresponding to fog of approximately less than 50 m depth), while $\overline{w'\theta'_v}$ and Equation 5.3 have been used when the friction velocity is above this threshold, using two different slopes depending on the buoyancy flux threshold indicated in Equation 5.3.

Regarding the u_*-based estimation (blue line in Figure 5.9 (a)) using the equation presented in Figure 5.2 (a) (Equation 5.1), the general evolution of fog thickness is well estimated, with a relatively good estimation when the fog is growing or dissipating (from above), following the behaviour of observed u_* (Figure 5.9 (c)). However, during the mature stage (from day 20 at 12:00 UTC to day 21 at 18:00 UTC approximately), this method tends to underestimate the fog thickness, which is most of the time constant (170 m) with some periods when the fog-top height is oscillating between 170

and 200 m agl (or more). In any case, this underestimation is sometimes within the uncertainty of observed fog events (170 ± 30 m). Besides this, the underestimation is quite constant, which suggest that correction factors could be added for thick fog (e.g. adding +40 m to the result obtained for fog thicker than approximately 100 m).

Green dotted line shows the estimation of fog thickness using u_* for non-well mixed fog and $\overline{w'\theta'_v}$ for convective fog or fog exceeding a critical value of u_*, as commented before. Hence, the green dotted line coincides with the blue line for shallow fog. However, for deeper fog, there is normally an overestimation, especially around midday, when the surface buoyancy flux is directly influenced by the heating of the ground caused by the part of the short wave radiation able to cross over the fog layer. However, this increase in the buoyancy flux (Figure 5.9 (d)) is not translated in a direct increase in fog thickness in the reality and in this particular case the $\overline{w'\theta'_v}$ - Z_{f-t} relation does not work satisfactorily during the daytime. However, during the mature stage and in nighttime conditions, the method provides a quite satisfactory estimation of the fog-top height (see for example from 18:00 UTC of day 20 to 06:00 UTC of day 21).

With respect to the temperature-based estimation (TC method) of fog thickness (red dotted line in Figure 5.9 (a)), the results are in general quite satisfactory, although the method underestimates the fog thickness when the fog is shallow, especially during the formation stage, when the vertical temperature profile is still stable and the inversion is not broken by the turbulent mixing within the fog (Figure 5.9 (b)). There is also an underestimation when the fog is fluctuating between two different levels, as happened for example around 06:00 UTC of day 20, when the fog thickness was oscillating between 55 and 105 m depth. In this case, it seems that the fog is not well established at the higher level and the temperature does not converge to the same value at that level. The same happens in the mature stage during the periods when the fog top is oscillating between 170 and 200 m agl (or more) (e.g. around 12:00 UTC of day 21). In these cases, the temperature at the highest level (200 m agl) is almost always considerably higher and it does not decrease to the values of lower layers (see Figure 5.9 (b)), meaning that although the visibility is less than 1000 m at 200 m agl, the upper layer is not completely well homogenised and the temperature remains higher, which would correspond to fog of type B in Figure 5.8.

The evaluation performed for this case study offers similar results than those from the statistical analysis provided in Section 5.3.1 and Section 5.3.2.

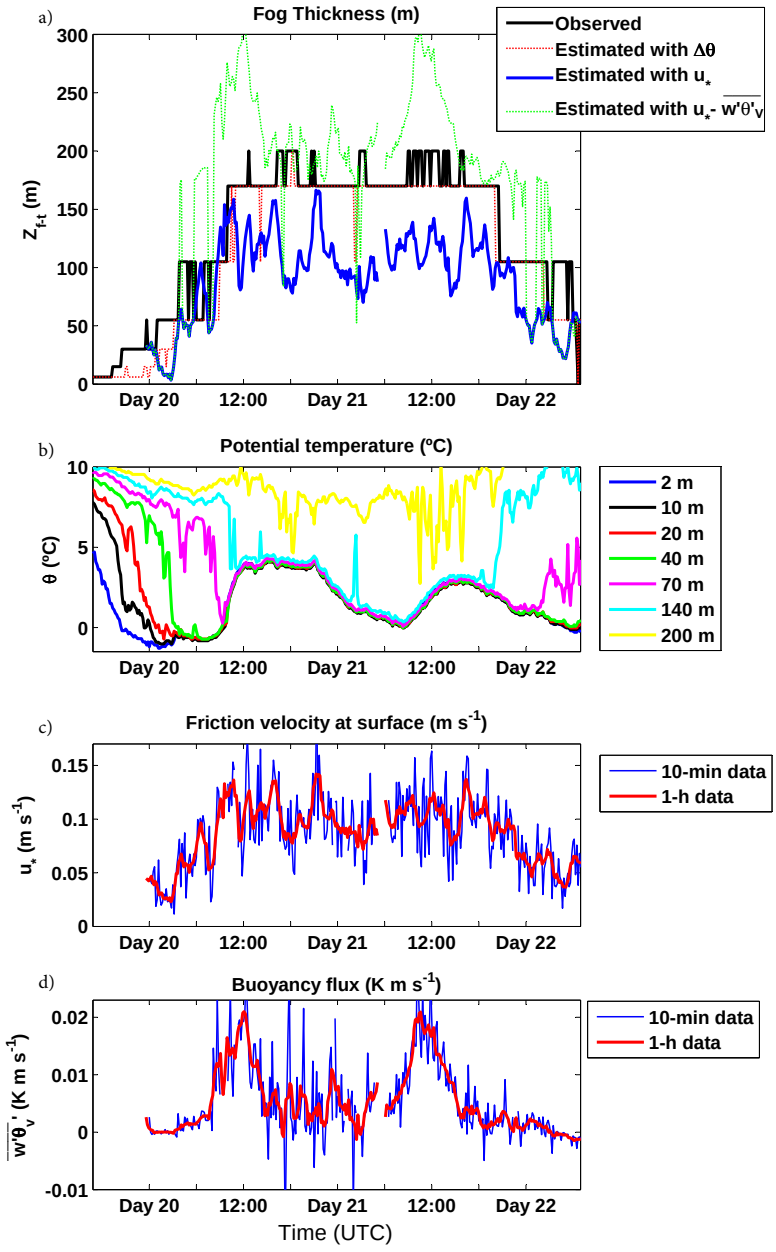

Figure 5.9: CESAR fog event. a) Comparison between real fog thickness (black line) and the estimated with temperature-convergence (TC) method (red dotted line), with friction velocity measurements and Equation 5.1 (blue line) and with u_* (Equation 5.1) for fog with $u_* < 0.061$ m s^{-1} and buoyancy flux and Equation 5.3 for fog with $u_* > 0.061$ m s^{-1} (green dotted line). b) Potential temperature (°C). c) Friction velocity (m s^{-1}). d) Buoyancy flux (K m s^{-1}).

5.4 SUMMARY AND CONCLUSIONS

The problem of having reliable information of fog thickness (fog-top height) is addressed in this study. On the one hand, a set of radiation (and cloud base lowering) fog events are used to correlate surface turbulence with fog thickness at two experimental sites (CESAR and CIBA). Fog thickness follows a linear correlation with surface friction velocity at both sites, with slight differences between sites. Therefore, linear equations are obtained for the estimation of fog-top height through surface friction velocity measurement for each site (Z_{f-t} = 1369 u_* - 28 at CESAR and Z_{f-t} = 1029 u_* - 30 at CIBA). These equations show high values of correlation coefficients (R^2 = 0.974 and 0.982 respectively). Additionally, the buoyancy flux measured at the surface is proposed for convectively active fog (exceeding an u_* threshold of approximately 0.07 m s^{-1}), since fog thickness also shows a significant correlation with this parameter. However, although a linear correlation is obtained, the error bars suggest this parameter to be noisier than u_* and it oscillates from large positive to slightly negative values. In addition, the evaluation of this method for a case study demonstrates how the use of the buoyancy flux usually overestimates the fog thickness during daytime, when the surface heat flux is larger due to the fraction of solar energy able to cross the fog layer and reach the surface.

On the other hand, the estimation of fog thickness through the temperature-convergence method is evaluated at CESAR. This method is based on the turbulent homogenization of well-mixed fog, which makes the potential temperature converge to approximately the same value at the heights where the fog layer is present. Thus, fog-top height is defined as the maximum height (z) where $|\Delta\theta| = \theta_{2m} - \theta_z$ is lower than 1.2 °C. It is shown how this method offers satisfactory results for deep fog (~ 100 m or more). However, the method is unsuccessful for shallow fog, since they are associated with surface-based thermal inversions and the turbulence within them is not enough to break the stability. Besides, it seems that the upper layer in very deep fog (~ 200 m) is somehow decoupled from the lower layers in some cases, associated with relatively low-moderate values of surface friction velocity (~ 0.13 m s^{-1}). In these cases, visibilities lower than 1000 m are observed at the top of the fog but the mixing from lower layers is not completely effective.

These results are tested with a long-lasting fog event observed at CESAR. The results suggest how these methods are valid options for estimating fog thickness in near-real time conditions during a complete fog cycle. However, the temperature-convergence method is not valid for shallow fog (especially during growing fog) and it tends to slightly underestimate fog thickness during periods when the fog is deeper. On the other hand, u_* is demonstrated as

a powerful parameter for the estimation of fog-top height if some corrections are applied during deeper-fog events.

The presented results can be useful when trying to estimate fog thickness from a unique sonic anemometer deployed at surface or a set of thermometers at different heights. However, further calibrations and studies at other sites are required to detect site-dependence and instruments-dependence issues.

PART II - GRAVITY WAVES

Oscillations are natural features of stable (calm) environments, but they can be dangerous if you cannot control their amplitude.

6

NEAR-MONOCHROMATIC DUCTED GRAVITY WAVES ASSOCIATED WITH A CONVECTIVE SYSTEM CLOSE TO THE PYRENEES

Near-monochromatic GWs associated with a mesoscale convective system (MCS) were detected during the BLLAST field campaign on 21 June 2011. These GWs are analysed using available instrumental data (e.g. an array of microbarometers, a microwave system Humidity And Temperature PROfiler (HATPRO) and an ultra-high-frequency (UHF) wind profiler). Pressure oscillations of up to 0.5 hPa were recorded after a pronounced pressure drop of 1.4 hPa, identified as the MCS wake low. Wavelet analysis and evaluated wave parameters confirm the occurrence of such GWs (period ~ 9 min, horizontal wavelength ~7 km), which propagated from southwest to northeast, i.e. in the same direction of propagation as the MCS. Observational evidence suggests the downdraughts associated with the rear-inflow jet at the wake low zone of the MCS as the most likely generator mechanism of the GWs. However, the complex orography and proximity of the Pyrenees to the field campaign could also play an important role. Wave propagation was possible through the ducting mechanism, favoured by the existence of a critical level in a wind-sheared environment around 2000 m agl. Wave-like motions related to the passage of the GWs were also observed in other atmospheric parameters close to the surface and within the lower troposphere. The effects of GWs on the surface fluxes have also been analysed through MRFD methods.

The content of this chapter has been published as:

ROMÁN-CASCÓN, C., YAGÜE, C., VIANA, S., SASTRE, M., MAQUEDA, G., LOTHON, M. & GÓMARA, I. (2015): Near-monochromatic ducted gravity waves associated with a convective system close to the Pyrenees. *Q. J. R. Meteorol. Soc.*, **141**, 1320-1332.
http://onlinelibrary.wiley.com/doi/10.1002/qj.2441/abstract

6.1 INTRODUCTION

The current scientific interest in GWs was previously introduced in Chapter 1. Regarding GWs associated with convective systems, several studies have shown that GWs can influence the formation and evolution of convective systems (e.g. Uccelini, 1975; Balachandran, 1980; Nicholls and Pielke, 2000) and produce widespread damage due to their associated wind gusts. These cases are specially important because they can be responsible for local and unexpected severe winds (Loehrer and Johnson, 1995; Bernardet and Cotton, 1998; Coleman and Knupp, 2009), which is a potential danger for aviation (Fujita and Caracena, 1977; Manasseh and Middleton, 1995; Miller, 1999, 2000).

Some of these GWs are associated with wake low zones of MCSs. A wake low is a relative surface pressure minimum observed at the rear part of a MCS during its mature or dissipation stage, near the back edge of the trailing stratiform precipitation region (figure 1 in Houze et al. (1989)). Together with the wake low, the thunderstorm surge and the thunderstorm high have also been identified as MCS features (Fujita, 1955; Johnson, 2001). The decrease in surface pressure associated with wake lows can be considerably important, reaching several hPa in a few minutes (Fujita, 1963; Schneider, 1990). The reasons for such a quick and intense pressure drop have been discussed over the years (Fujita, 1955, 1963; Pedgley, 1962; Williams, 1963; Johnson and Hamilton, 1988) and conclusions from these studies agree that the subsidence due to the descending rear-inflow jet at the rear part of MCSs causes an adiabatic warming that makes the surface pressure decrease (Johnson and Hamilton, 1988). This pressure drop and its subsequent increase have been observed in many squall lines, bow echoes or MCSs in general (Loehrer and Johnson, 1995; Johnson, 2001). Some of these studies have related observed GWs to wake lows. For instance, Bosart and Seimon (1988) analysed a case study of an intense GW related to a squall-line wake low, which caused strong fluctuations in pressure and intense wind gusts at the surface. Bauck (1992) also studied large pressure drops of 3 - 6 hPa associated with long-distance propagating GWs, which caused important vertical displacements and intense wind gusts.

However, the presence of clear and stable oscillations in the surface pressure records over a few wave cycles associated with these wake lows has been reported less frequently in the literature, mostly due to the lack of precise, high-resolution pressure data. This chapter presents a singular and comprehensive observational study of near-monochromatic and ducted GWs associated with the wake low of a MCS detected in a highly instrumented site near the Pyrenees. Among the measurements used, the combination of

data from three high-resolution microbarometers, an ultra-high frequency (UHF) wind profiler and a microwave system Humidity And Temperature PROfiler (HATPRO) radiometer allowed to perform a deep analysis and to offer substantiated hypotheses about the origin, propagation and effects of the GWs.

This chapter is laid out as follows: Section 6.2 explains in detail the BLLAST data used for the analysis. Results are provided in Section 6.3 and the main conclusions and a short summary are shown in Section 6.4.

6.2 DATA AND METHODOLOGY

Data used in this study have been obtained from different meteorological instruments deployed during the BLLAST field campaign.

One of the objectives of the field campaign was to learn more about the GWs that could develop during the evening transition to the nocturnal boundary layer. Therefore, fair-weather days were preferred for analysis, due to the better development of the convective boundary layer and a clear view of the evolution of the residual and stable nocturnal boundary layers that developed later. However, several rainy and stormy days occurred during the field campaign and this study focuses on one of them. Besides the instrumentation from the BLLAST field campaign, additional barometers located in the surroundings of Lannemezan (*Pic du Midi* observatory and *Tarbes-Lourdes-Pyrenees* Airport (LFBT)) were used to determine the horizontal propagation and generation of the analysed GWs.

The sites used to track the GW propagation have been renamed from A - E in this chapter, according to their distance from site A (Table 6.1). Note that site D corresponds to the *Pic du Midi* Observatory. This astronomical and meteorological observatory is situated approximately 25 km southwest from Site A at 2877 m asl at the *Pic du Midi*, which is a sharp mountain detached some kilometres to the north from the Pyrenees massif main line of the Spanish - French border, where the highest peaks are located (Figure 6.1).

A triangular array of three high-resolution PAROSCIENTIFIC microbarometers (Model 6000 - 16B; Cuxart et al. (2002)), separated by about 150 m and at 1 agl, was deployed at site A in Lannemezan, with the objective of studying gravity waves. The triangular configuration was used to characterize wave events by methods based on wavelet decompositions (Torrence and Compo, 1998; Terradellas et al., 2001; Viana et al., 2009, 2010, 2012), allowing the calculation of wave parameters (period, wavelength, phase velocity and direction of propagation) (see Section 2.2.1). A sampling rate of 2 Hz was used, which enabled a resolution of around 0.002 hPa.

Table 6.1: Information about sites of barometers used to track GW propagation.

Site	Original site	Location	Distance and direction from Site A	Time resolution / resolution
Site A	Microbarometer A	43°07′ 25.5″ N	Reference site	0.5 s/
	BLLAST	00°21′ 47.9″ E		0.002 hPa
Site B	Edge site	43°07′ 53.4″ N	1 km NNW	0.05 s (av 10 s)/
	BLLAST	00°21′ 35.2″ E		0.0001 hPa (LICOR)
Site C	Moor site	43°05′ 24.5″ N	4 km S	10 s (av 1 min)/
	BLLAST	00°21′ 42.6″ E		0.01 hPa
Site D	*Pic du Midi* Obs.	42°56′ 07.6″ N	25 km SW	1 min/
		00°08′ 24.2″ E		0.1 hPa
Site E	LFBT Airport	43°10′ 59.7″ N	30 km WNW	1 min/
		00°00′ 06.1″W		0.1 hPa

As described above, surface pressure measurements from other barometers placed at different locations (sites B, C and E) were also used. Although the available resolution, accuracy and sampling rate of these instruments were significantly lower than those for the microbarometers, they were quite useful to determine the extension and propagation of the GWs.

In order to determine the duct layer where the GWs were propagating, the vertical wavenumber (m) (see Section 6.3.3 and Equation 6.1) was calculated using wind measurements from an UHF wind profiler and temperature measurements from the HATPRO radiometer. The UHF wind profiler, a PCL1300 UHF profiler manufactured by Degreane Horizon, is a pulsed Doppler radar working with a transmitted frequency of 1274 MHz and a peak power of 2.5 kW. This instrument worked with a good temporal resolution (3.5 - 6 min) and offered two modes: the low mode and the high mode. The low mode was based on a 150 m pulse length and on 95 level gates spaced every 75 m, starting at 100 m from the radar. Although the high mode offers measurements at higher levels, the low mode data were used in this study for the calculation of the vertical wavenumber (m), due to the higher radial resolution and because the GWs detected in this work propagated mainly below 2000 m agl. Wind profiles from UHF measurements were compared with measurements from another UHF wind profiler located 5 km apart from the former. This comparison (not shown) served to provide additional quality control data. Both UHFs showed similar values, but with a coherent time lag between observations, which agreed with the storm direction and speed of propagation.

The HATPRO profiling passive microwave radiometer (Löhnert et al., 2009; Löhnert and Maier, 2012) is able to measure temperature and humidity with

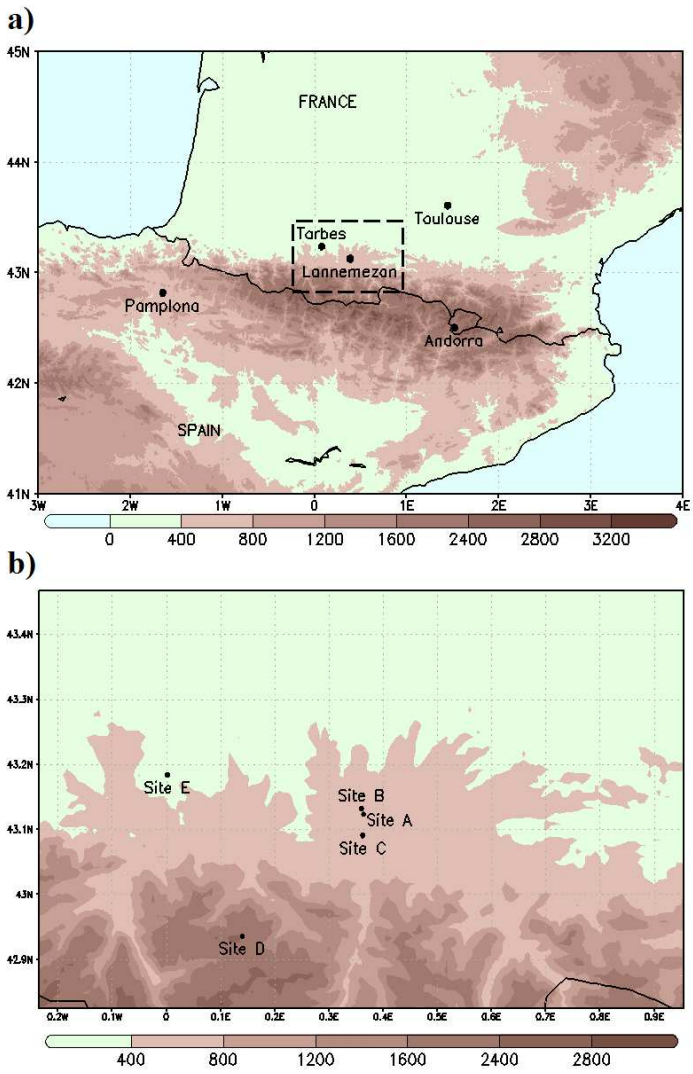

Figure 6.1: a) Geographical location of BLLAST site (Lannemezan) and surroundings. Land topography (in meters) is given in light green to dark red shadings. b) Zoomed area (dashed rectangle from (a)) with location of barometers used to track GWs propagation. Source: the Global Land One-km Base Elevation Project (GLOBE).

high temporal and spatial resolution. The instrument admits two different scanning modes: full troposphere and PBL profiling. Although the vertical resolution of the PBL profiling is higher, the full troposphere profiling mode has been used in this study, due to the higher temporal resolution (~ 2.5 min). The analysis of the MCS covers the period from 20:00 - 22:00 UTC on 21 June 2011, while the GWs were observed from 21:25 - 22:05 UTC. Quality control

flags for HATPRO radiometer data indicated unreliable measurements for periods from 20:00 - 21:00 UTC, due to high values of liquid water path (rain), which meant that these data could not be used. Rain was weaker from 21:00 to 21:30 UTC and the quality control flags indicated reduced quality data, which had to be used with caution. However, from 21:30 UTC onwards, the data showed the highest quality level and, since these data did not show appreciable differences from data from 21:00 to 21:30 UTC, data from 21:00 UTC onwards were used for calculation of the vertical wavenumber. Nevertheless, for the analysis of temperature oscillations related to the GW passage, only temperature fluctuations produced during the highest quality data period were taken into account.

Additional measurements from higher frequency instruments (Table 6.2) were used to detect oscillations in other meteorological parameters, to analyse the meteorological conditions near the surface and to perform MRFD (Howell and Mahrt, 1997; Viana et al., 2009) methods (see Section 2.2.1).

Table 6.2: Information about additional instruments located close to the surface.

Instrument	Model	Height (agl)	Freq.
Thermometers	*Campbell HMP45*	2, 15, 30, 45, 60 m	0.1 Hz
Anemometers	*Wind monitor Young 05103*	15 m	0.1 Hz
	Vector Instrument W2009	45 m	0.1 Hz
Sonic anemometers	*Campbell Csat3 3D*	45 m	10 Hz
	METEK USA 1 (MRFD)	2 m	20 Hz

6.3 RESULTS

6.3.1 *Mesoscale convective system overview*

The analysed GWs were associated with a MCS that crossed the experimental area from 20:00 - 22:00 UTC on 21 June 2011 (Figure 6.2 and Figure 6.3). Figure 6.2 (a and b) shows an overview of the convective activity during the afternoon over different regions over and around the Pyrenees, with several thunderstorms formed at the northern and southern sides of the mountains. Operational forecasters at the Spanish National Weather Service (AEMET) reported auspicious conditions for deep, severe and organized convection

over the northeast area of the Iberian Peninsula, due to the existence of a pre-frontal unstable line.

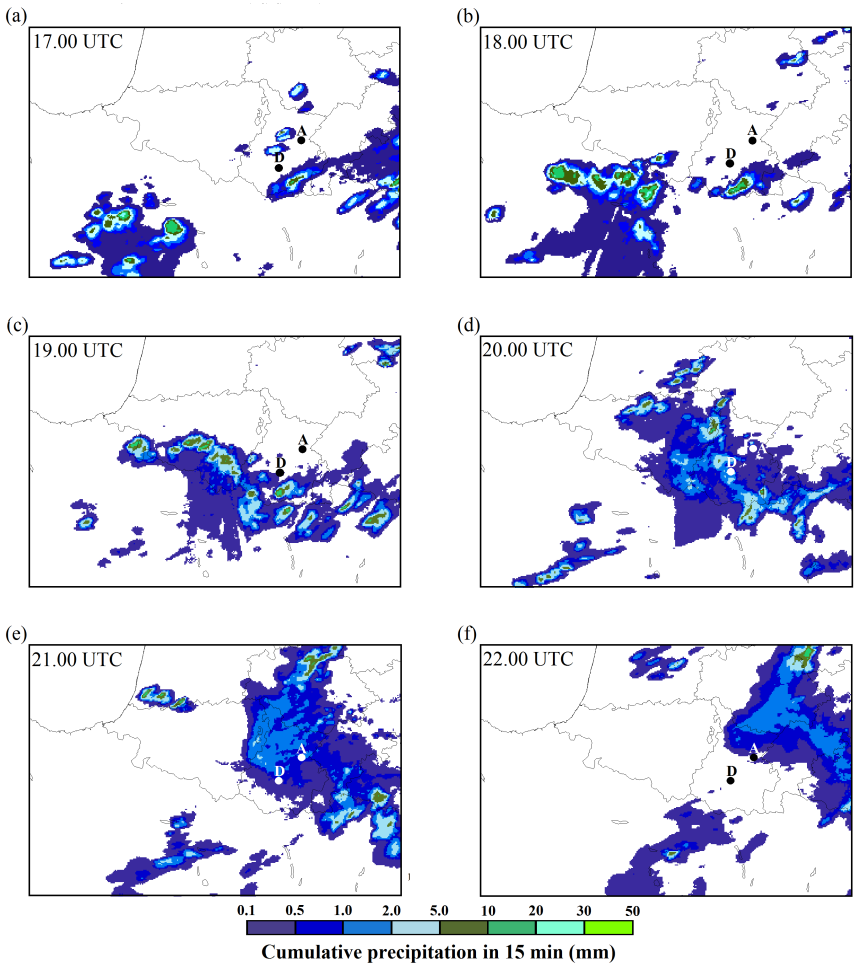

Figure 6.2: RADAR composites of cumulative precipitation (mm) over the 15 min preceding each hour between 17:00 and 22:00 UTC (a) - (f). Points indicate Sites A and D.

An extensive and organized convective system finally developed during the afternoon (Figure 6.2 (b and c) and Figure 6.3 (a and b)) very close to the Pyrenees. These figures show a well-defined convective line of more than 150 km composed of several individual thunderstorms that crossed the Pyrenees and caused intense precipitation over different areas. This MCS moved from southwest to northeast while weakening (see evolution of precipitation in Figure 6.2) and reached Lannemezan at 20:00 UTC.

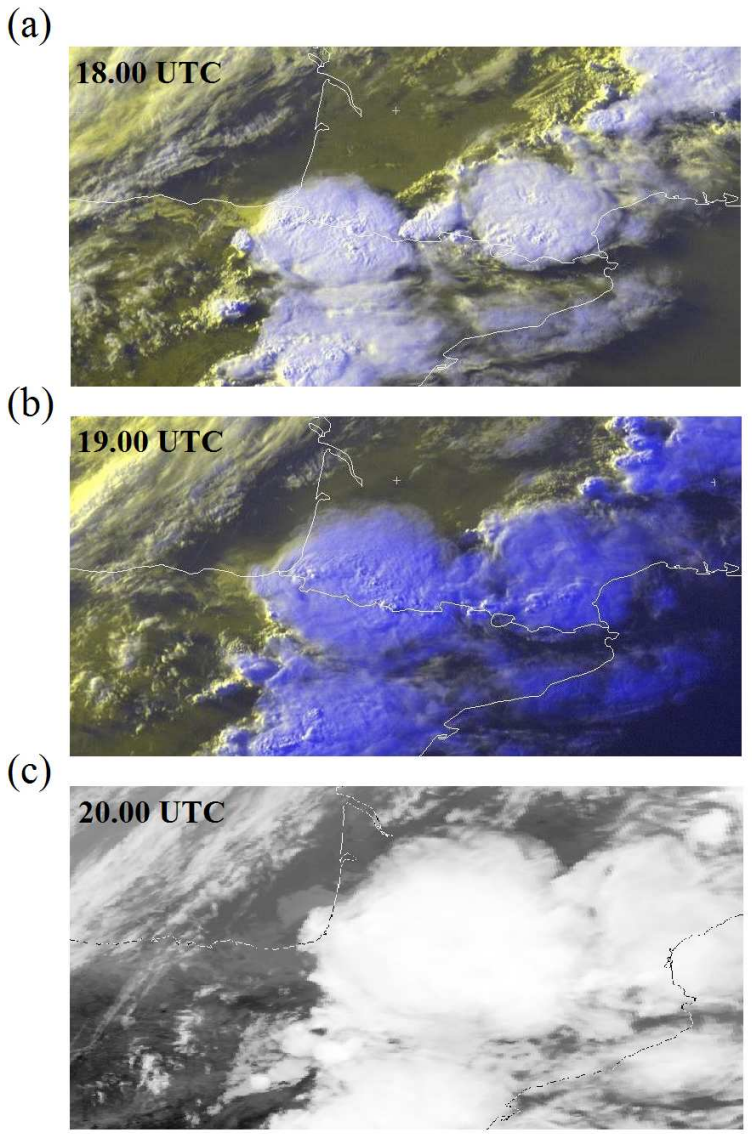

Figure 6.3: Satellite images at 18:00 UTC (a), 19:00 UTC (b) and 20:00 UTC (c) on 21 June 2011. Panels a and b are from visible satellite images of Meteosat RGB Segment 5. Panel c is from AVHRR Channel 4 (thermal) of the NOAA 16 satellite (Copyright NERC Satellite Receiving Station, Dundee University, Scotland, http://www.sat.dundee.ac.uk).

The rain-gauge at the experimental site reported a total precipitation of 5.9 mm from 20:15 - 21:30 UTC (see Figure 6.6 (b) later), although some drizzle was also reported until 22:00 UTC according to RADAR images and

flag indicators of the HATPRO radiometer. Although a detailed analysis of the MCS structure and processes is beyond the scope of this study*, the evolution in surface pressure observed at site A from 19:45 UTC onwards shown in Figure 6.4 (a, thick line) is consistent with the following processes associated with the typical structure of MCSs and squall lines:

1. The increase in surface pressure from 19:45 - 20:30 UTC has been identified as the thunderstorm high or mesohigh. This increase in pressure was caused by the cooling from evaporation of the rain during the former and more active part of the MCS.

2. The pressure drop at 21:05 UTC has been associated with the wake low at the rear part of the MCS, in a region of stratiform precipitation Figure 6.2 (e and f). This decrease in pressure was a consequence of the adiabatic warming (decrease in density) caused by downdraughts associated with the descending rear-inflow jet of the storm (Johnson and Hamilton, 1988). The decrease of rain rate at these times could also contribute to the pressure drop through the ceasing of evaporation (cooling) of the rain. The commented-on downdraughts were in turn favoured by the cooling effect, due to precipitation evaporation at higher levels (Lindzen, 1974; Raymond, 1975; Jewett et al., 2003), but since at that point there was not enough evaporative cooling to compensate for the adiabatic warming caused by the downdraughts, a net warming occurred and a rapid decrease was observed in the surface pressure records.

Figure 6.4 (a) also shows surface pressure (thin line) measured at the Pic du Midi Observatory (site D). The fact that surface pressure variations are not observed at site D, compared with site A, indicates that the main contributions were due to processes occurring below the height of the Pic du Midi Observatory. Nevertheless, part of the surface pressure drop due to the wake low was also slightly observed at site D at 20:50 UTC. This fact indicates that adiabatic warming could be produced not only below 2877 m asl, but also at higher levels.

*See figure 25 of Johnson and Hamilton (1988) and Johnson (2001) for more information about squall lines and MCS structures.

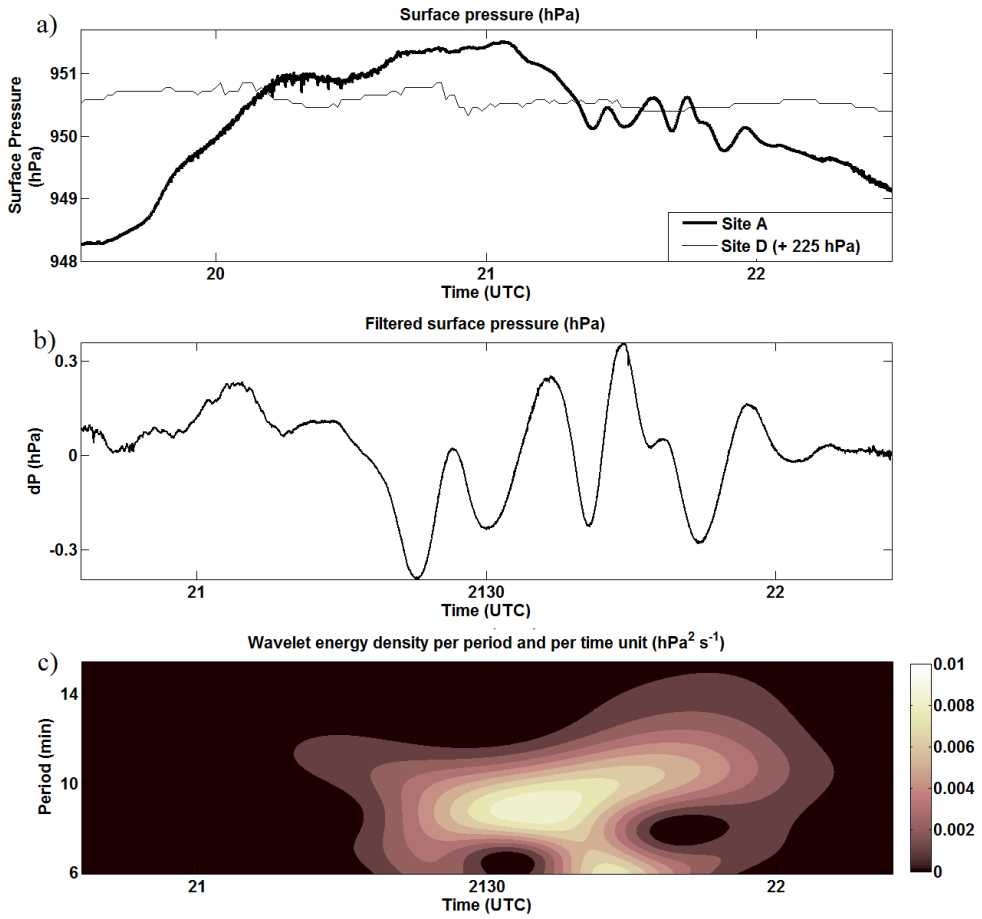

Figure 6.4: a) Surface pressure (hPa) measured by microbarometer A in Lannemezan (Site A, thick line) and by the barometer (+225 hPa) at the *Pic du Midi* Observatory (Site D, thin line) for 21 June 2011. b) Microbarometer A filtered pressure (hPa). c) Wavelet energy density per period and time unit ($hPa^2\ s^{-1}$).

6.3.2 *Gravity waves analysis*

The most interesting feature of this event, from our point of view, was observed in the surface pressure records of the microbarometers (Figure 6.4 (a), thick line). At 21:05 UTC, surface pressure from the three microbarometers showed a drop of 1.4 hPa in a few minutes, followed by several fluctuations of 0.4 - 0.5 hPa from 21:25 - 22:05 UTC. A 45-min Butterworth high-pass filter has been applied to the microbarometer data to remove the synoptic tendency and the daily cycle, so that only higher frequency fluctuations in

surface pressure are considered (Figure 6.4 (b)). Figure 6.4 (c) shows the wavelet energy per period and time unit: a clear energy increase is appreciated during the wave-like event, centred on periods of around 9 min. It is worth mentioning that most case studies of GWs related to convective activity described in the literature have longer periods (e.g. Lindzen, 1974; Uccelini, 1975; Alexander et al., 2000) than the GWs analysed here. Subsequently, wave parameters (Table 6.3) have been evaluated from the filtered surface pressure records using the exact location of the three microbarometers and phase differences analysis (Terradellas et al., 2001). This calculation has been done for the range of periods and times over which the wavelet analysis showed the strongest signal, i.e. from 21:30 - 21:45 UTC and for periods between 8 and 10 min. These parameters show a short range of values, which suggests a nearly monochromatic wave event. For the 9 min period, they indicate a wavelength of approximately 7 km, a phase speed of around 12.5 m s^{-1} and a direction of propagation of approximately 50°(from southwest to northeast). After calculating the direction of propagation, it seems reasonable to assume that these GWs were formed somewhere southwest from the microbarometer location (site A) and propagated in the storm's direction of movement.

Table 6.3: Wave parameters calculated from wavelet analysis.

Wave parameter	**Range of values from 21:30 UTC to 21:45 UTC**
Period	[7 - 11] min
Wavelength	[6500 - 8000] m
Phase speed	[12 - 14] m s^{-1}
Direction of propagation	[45 - 60] °

Data from several barometers located at different distances from site A have been analysed in order to track the GW propagation. Figure 6.5 (a) shows the filtered pressure from measurements of neighbouring barometers in Lannemezan and Figure 6.5 (b) shows the same at further locations (see Table 6.1 for locations). According to these data, it can be affirmed that the wave propagated for at least 5 km (presumably a greater distance) and was first detected at site C (at the southernmost barometer in Lannemezan), which proves that the GW propagation had a northward component of movement, in accordance with wavelet-derived parameters. Surface pressure from further locations (sites D and E) does not show apparent GW oscillations.

However, a decrease in surface pressure followed by an increase is clearly visible and could be an indicator of the passage of the wake low. This surface

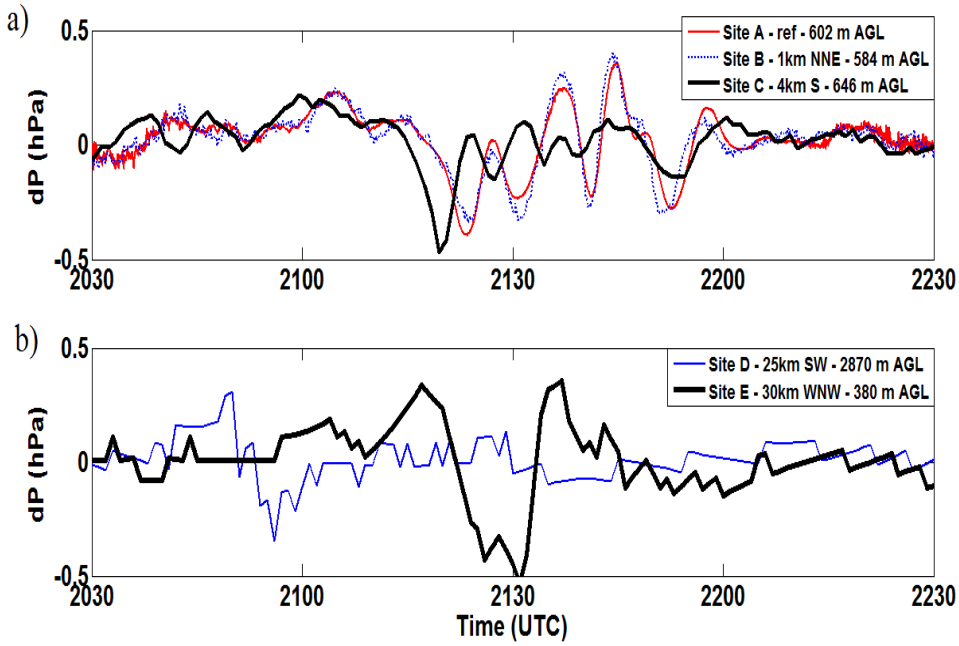

Figure 6.5: a) Filtered surface pressure (hPa) at nearby locations in Lannemezan: site A (thin red line), site B (dashed blue line) and site C (black thick line). b) Idem for further locations: site D (thin blue line) and site E (black thick line).

pressure drop was observed at site D approximately 25 min before than at site A and at site E 10 - 15 min later than at site A. According to the location of these instruments, these time lags amongst the observations agree relatively well with the speed of the storm (estimated to be approximately 15 m s^{-1} from RADAR images). It should be noted that site D corresponds to the *Pic du Midi* Observatory, situated at over 2800 m asl. Since GWs have been determined to propagate mainly below 2000 m agl (or 2600 m asl), as will be shown later, this could also be one of the reasons why these wave-like motions were not observed in the surface pressure records of the barometer at site D. Moreover, the fact that the wake low was observed at site E but not the GW oscillations suggests that not all directions from the source area were favourable for wave propagation.

It is therefore concluded that GWs were formed somewhere between 4 km (site C) and 25 km towards the southwest direction from site A. The 25 km limit has been imposed due to the lack of observation of GWs at site D and since there are mountains higher than the top height, where wave propagation was feasible from this limit towards the southwest. Vertical velocity measured by the UHF wind profiler (Figure 6.6 (a)) shows a region of strong

negative velocities from 21:00 - 21:30 UTC from the surface to approximately 2500 m agl and a more specific region of even stronger vertical velocities (-9 to -10 m s^{-1}) around 1500 - 2500 m agl from 21:15 - 21:25 UTC. Although it is hard to disentangle whether the UHF vertical velocities were caused by air downdraughts, the velocity of the raindrops or a combination of both effects, these stronger vertical velocities do not coincide with the maximum rain rates observed at the site according to the information provided by the rain-gauge (Figure 6.6 (b)) and RADAR images (Figure 6.2). Therefore, these negative vertical velocities can indicate downdraughts regions of the MCS and, as commented before, have been related to the surface pressure drop and proposed to be responsible for GW initiation.

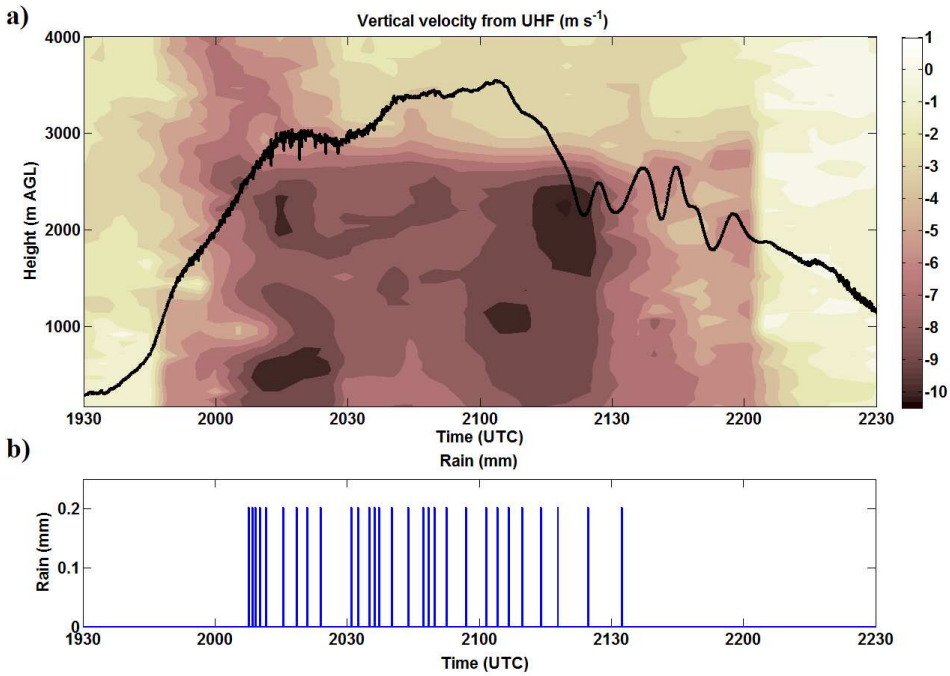

Figure 6.6: a) Vertical velocity (m s^{-1}) measured by the UHF wind profiler at site A. The surface pressure time series from microbarometer A is overlaid for reference (black line). b) Rain measured at site A (mm).

The association between GWs and wake lows has been previously documented in several studies and agrees quite well with the case study presented herein. However, it is difficult to point out whether the processes associated with the wake low zone of the MCS were the only ones involved in GW formation. The possible topographic effect of this mountainous area could play an important role in the final formation of the GWs. The *Pic*

du Midi is the closest high mountain of the Pyrenees to Lannemezan in the southwest direction, although it is detached from the main line of the highest peaks, which are around the France - Spain border. Since GWs were propagated in a layer below 2000 m agl and were not observed at site D, it can be concluded that the main mountain massif of the Pyrenees (located farther south from the *Pic du Midi*, see Figure 6.1) was not directly involved in GW formation. On the other hand, the GW formation could have been influenced by a combination of the effects of wake low downdraughts and the orography between *Pic du Midi* and Lannemezan, i.e. by the lee side of the *Pic du Midi*, by lower mountains between the *Pic du Midi* and Lannemezan or even by the southern border of the Plateau of Lannemezan. However, the specific role of the mountains is very difficult to determine with the available data. Specific numerical simulations with simplified 2D and 3D models or even with NWP models could add valuable information to this point.

6.3.3 *Wave ducting*

A mechanism that favours GW maintenance and propagation should exist when there is not a continuous source of energy. It is known as wave ducting and occurs when a reflecting layer at some height causes vertical wave reflection, thus allowing the horizontal propagation of the GWs trapped between two levels in a layer known as the duct layer (Lindzen and Tung, 1976). According to the wave-ducting theory, the properties of a wave duct can be obtained from the Taylor - Goldstein equation (Nappo, 2012):

$$\frac{d^2w'}{dz^2} + m^2 w' = 0 \ , \tag{6.1}$$

whence w' is the perturbation of the vertical velocity w, z is the height and m is the vertical wave number, defined by

$$m^2 = \frac{N^2}{c_i^2} + \frac{\overline{U}_{zz}}{c_i} - k_h^2 - \frac{1}{4H^2} \ . \tag{6.2}$$

Here, N^2 is the square of the Brunt - Väisälä frequency (Equation 1.2) , $c_i = c - U$, the intrinsic phase velocity (c) relative to the mean flow projected on the direction of wave propagation (U), U_{zz} is the second derivative with respect to height of the mean wind in the direction of propagation of the wave, k_h is the horizontal wavenumber (Equation 6.3):

$$k_h = \frac{2\pi}{\lambda} \ . \tag{6.3}$$

Where λ is the wavelength of the GWs and H is a height scale of the atmosphere, sufficiently large to neglect the fourth term on the right-hand of Equation 6.2.

The vertical wavenumber (m) will show real values in regions where the horizontal propagation of the wave is favoured and therefore positive values of m^2 will indicate a possible duct layer, while negative values will indicate regions where the waves become evanescent. Hatched areas in Figure 6.7 indicate negative values of m^2, while non-hatched areas denote positive values of m^2. These values have been calculated using quality-controlled temperature profiles from the HATPRO radiometer, wind from the UHF wind profiler and the values of wave parameters evaluated in Section 6.3.2 for k_h and c. The phase speed of the GWs has been assumed as constant (c = 12.5 m s^{-1}), as well as the horizontal wavenumber (k_h = 8.3 x 10 $^{-4}$ m, corresponding to a wavelength of 7500 m). The direction of propagation of the GWs (50°) was used for projecting the horizontal wind in this direction. Positive values of m^2 show a well-defined layer where wave propagation was possible, determined by an intense wind shear existing above approximately 2000 m agl (Figure 6.7), which served as an effective reflecting layer with a critical or steering level, i.e. a level wherein the wind speed of the main flow equals the phase speed of the GWs (Lindzen and Tung, 1976). In this case, the bottom layer of the wave duct was the ground.

Calculated values of m^2 are positive for the whole available vertical profile, also before the arrival of the pressure drop or wake low and prior to the record of the wave-like motions in surface pressure; however, it was just after the arrival of this wake low (after 21:15 UTC) that GWs were detected, coinciding with a confinement of the duct layer (where m^2 shows positive values) in the lowest atmospheric levels. Figure 6.7 also shows the horizontal wind speed for the event and it proves that the duct layer defined between the surface and approximately 2000 m agl was mainly determined by the wind profile, with an intense wind shear existing at the rear part of the MCS, just behind the wake low.

On the other hand, a further exploration of the filtered pressure records and wavelet analysis (Figure 6.4 (b and c)) shows a temporary decrease in the period (from 9 to 6 min) of the wave- like disturbances at 21:45 UTC, which coincides with a narrowing of the duct layer where the wave was able to travel (Figure 6.7). This narrowing was in turn conditioned by the position of the critical level found around 2000 m agl, which temporarily descended

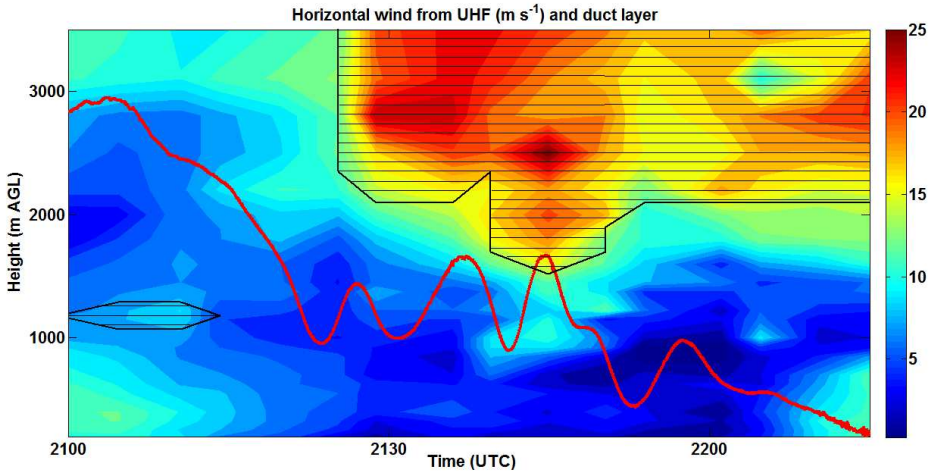

Figure 6.7: Wind speed (m s^{-1}) measured by the UHF wind profiler at site A. Hatched areas indicate negative m^2 values, while non-hatched areas indicate positive m^2 values, marking the duct layer. The surface pressure time series from microbarometer A is overlaid for reference (white line).

from 2000 to 1800 m agl approximately. This coincidence suggests that the thickness of the duct layer could have influenced the frequency of the GWs concerned.

6.3.4 *GW effects close to the surface and in the lower troposphere*

GWs perturb the environment where they propagate and cause oscillations in other meteorological parameters besides surface pressure. The relative phases and amplitudes of these parameters are described by polarization equations from linear wave theory (see for example Fritts and Nastrom, 1992; Nappo, 2012). In this case study, temperature and humidity oscillations associated with the passage of the GWs were observed in the lower troposphere (Figure 6.8). A certain phase lag is observed between these oscillations and surface pressure fluctuations, in agreement with the expected $\pi/2$ phase relationship from linear wave theory. However, due to the non-perfect monochromaticity of the GWs and the low time resolution of the HATPRO radiometer measurements, it is difficult to assess how closely this polarization relation is fulfilled.

The observed oscillations suggest that the air parcels were vertically narrowed (maxima of pressure) and spread (minima of pressure) alternately by the action of the GWs. The vertical narrowing of the layer caused displace-

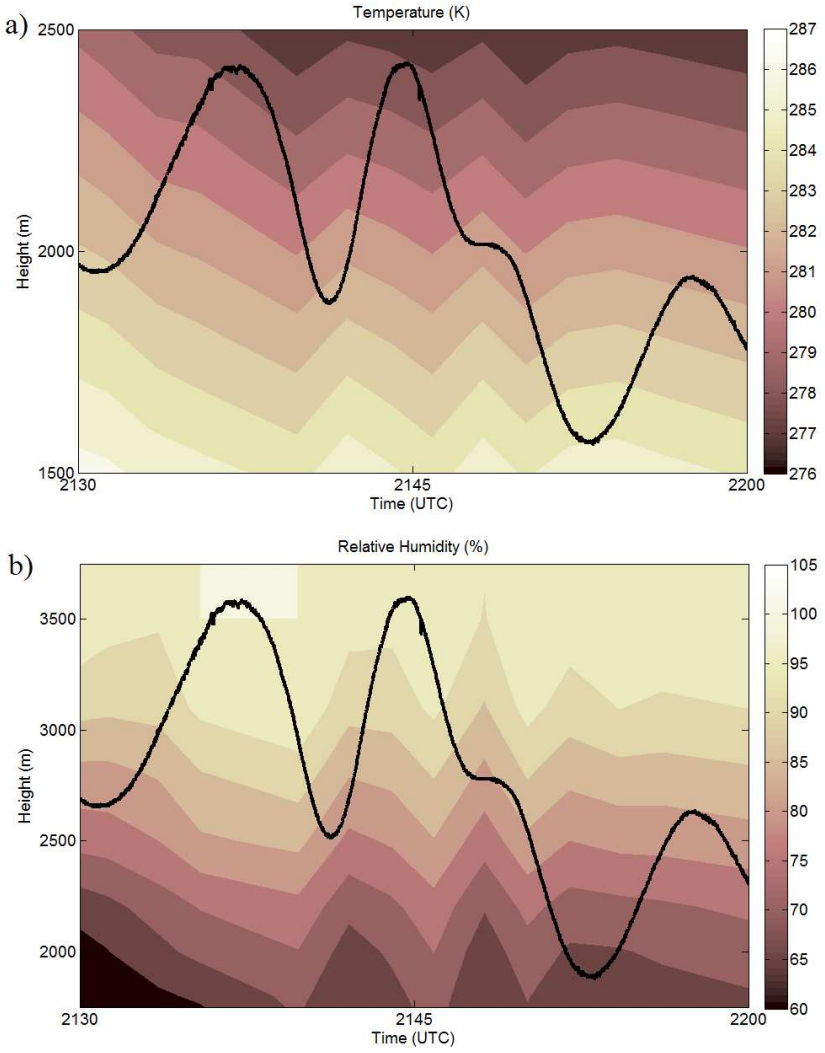

Figure 6.8: Temperature (K) (a) and relative humidity (%) (b) measured by the HATPRO radiometer. The surface pressure time series from microbarometer A is overlaid for reference (black line).

ments of upper air parcels (colder and with higher relative humidity) to lower layers and the spreading associated with minima of surface pressure caused the opposite effect. Near-saturation values of relative humidity indicate approximately the position of the cloud base; the oscillations detected in these records (around 3500 m agl) suggest that the GWs could shape and produce a wave-like cloud base. The effect of the GWs was also noted in wind measurements below 2000 m agl: this layer was characterized by light winds

and slight and alternating changes in wind direction (not shown). Higher frequency data from instruments at site A were used to check whether the oscillations in these meteorological parameters were also encountered near the surface. A combination of cooling produced by the evaporation of the rain water at the surface and radiative cooling during sunset most likely caused the formation of a surface-based temperature inversion from 20:00 UTC onwards (Figure 6.9).

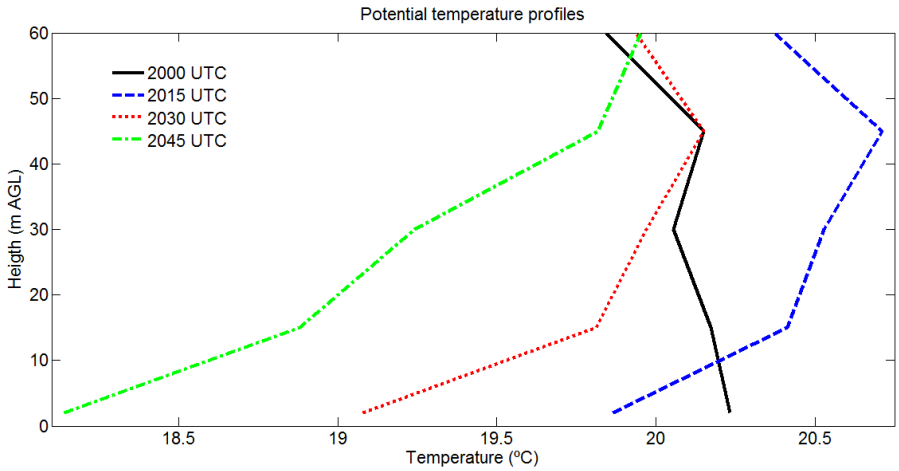

Figure 6.9: Potential temperature (°C) profiles from 60-m tower measurements at different times (20:00 UTC, solid black line; 20:15 UTC, dashed blue line; 20:30 UTC, dotted red line; 20:45 UTC, dash - dotted green line).

Later, the arrival of GWs to the site caused oscillations in wind speed, wind direction, temperature and vertical velocity measurements at different heights close to the surface. Figure 6.10 shows examples of the relationships found between surface pressure and other surface parameters at 45 m: (a) wind speed projected in the same direction of propagation as the GWs (50°), (b) wind direction, (c) temperature and (d) vertical velocity perturbation (Equation 6.4), where the mean of the vertical velocity has been calculated from 21:15 to 20:00 UTC:

$$w' = w - \overline{w} \ . \tag{6.4}$$

The observed oscillations in the wind speed projected in the same direction as the GWs have the same periodicity as the surface pressure records. This suggests that the effect of the GWs during narrowing (maxima in pressure) was to force the main flow to approach their own direction of propagation, as can also be seen in the changes in wind direction (closer to the

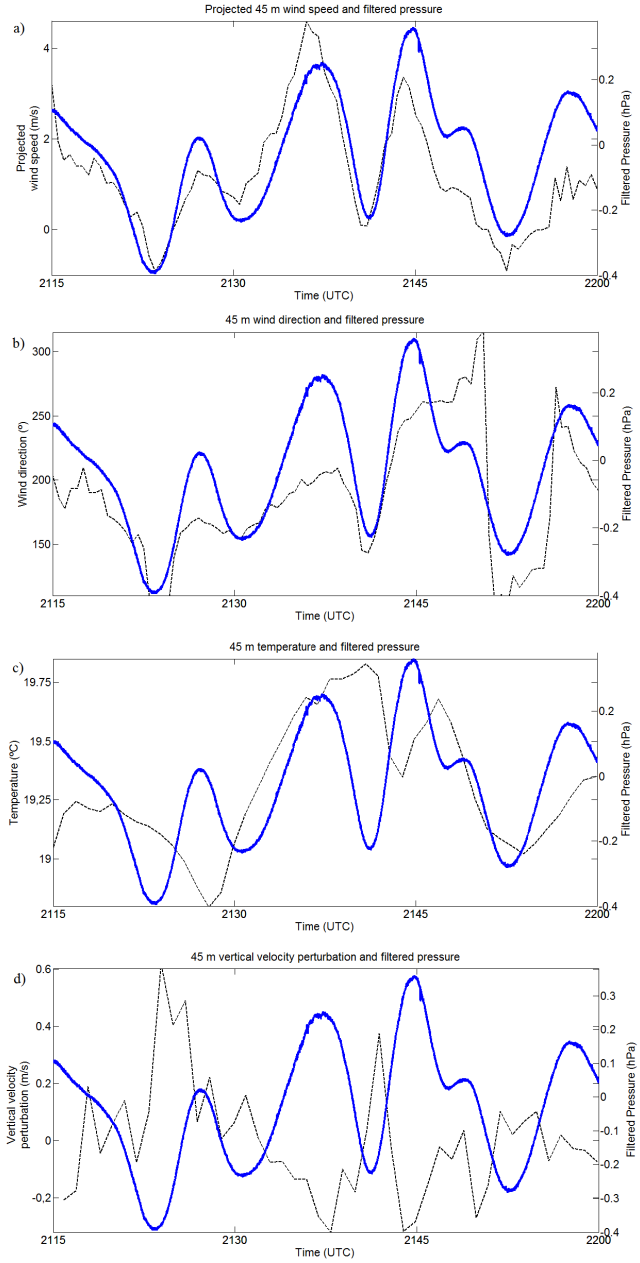

Figure 6.10: Time series of meteorological parameters at 45 m (dashed black line) and surface pressure (solid blue line) during the GW event. a) Wind speed projected in the same direction as GW propagation (m s^{-1}). b) Wind direction (°). c) Temperature (°C). d) Vertical velocity perturbation (m s^{-1}).

southwest during maxima). This relation between wind (projected in the direction of wave propagation) and pressure fluctuations can be obtained from the polarization equations (Equation 6.5; see Nappo (2012)):

$$\delta U = \frac{\delta p}{\rho_0 (c - U)} \ , \tag{6.5}$$

where ρ_0 is the air density. It can be observed that if phase speed (c) is larger than the main flow projected in the direction of wave propagation (U), oscillations in pressure and wind are expected to be in phase, as seen in Figure 6.10 (a) (a similar relationship was found in Viana et al. (2009)). Although some temperature oscillations near to the surface seem also to be related to the GW effect (Figure 6.10 (c)), these oscillations are more difficult to study further, since they are also affected by small changes in wind direction (local advection) and turbulence in highly heterogeneous terrain and not only by the vertical narrowing/spreading of the layer affected by GWs. Finally changes in the perturbation of the vertical velocity measured by a sonic anemometer at 45 m agl are also observed, as seen in other studies (Viana et al., 2009; Birch et al., 2013). Maxima in pressure correspond to minima in the vertical velocity measurements and vice versa.

Surface pressure records and oscillations observed in these parameters at other heights have also been compared (not shown) and in some cases they show similar agreements as for 45-m measurements. Although some of these relations agree qualitatively well with the aforementioned phase relationships obtained from the polarization equations (mainly the phase between pressure and wind), other phase relationships are not achieved, in accordance with the results obtained in Viana et al. (2009). As Nappo (2012) pointed out, turbulence in the surface layer affects wave perturbations. Although, for simplicity, linear theory is applied to these waves, gravity waves in the planetary boundary layer are seldom linear (Finnigan, 1988) and, consequently, the theoretical phase relationships are difficult to observe. In any case, a detailed analysis of the polarization equations is outside the scope of this study.

In addition, MRFD analysis (see Section 2.2.1) has been applied to high-frequency data from a sonic anemometer located at 2 m agl in order to study the effects caused by the propagation of GWs on the surface fluxes. The MRFD method (Howell and Mahrt, 1997) is applied when attempting to distinguish the contribution of the different temporal scales to the fluxes and it usually allows separation of turbulence from larger-scale contributions to the fluxes, such as gravity waves. Each vertical section of these figures shows

the MRFD analysis performed every 60 s, using time series of 820 s and gradually dividing these time series until time series of 0.1 s.

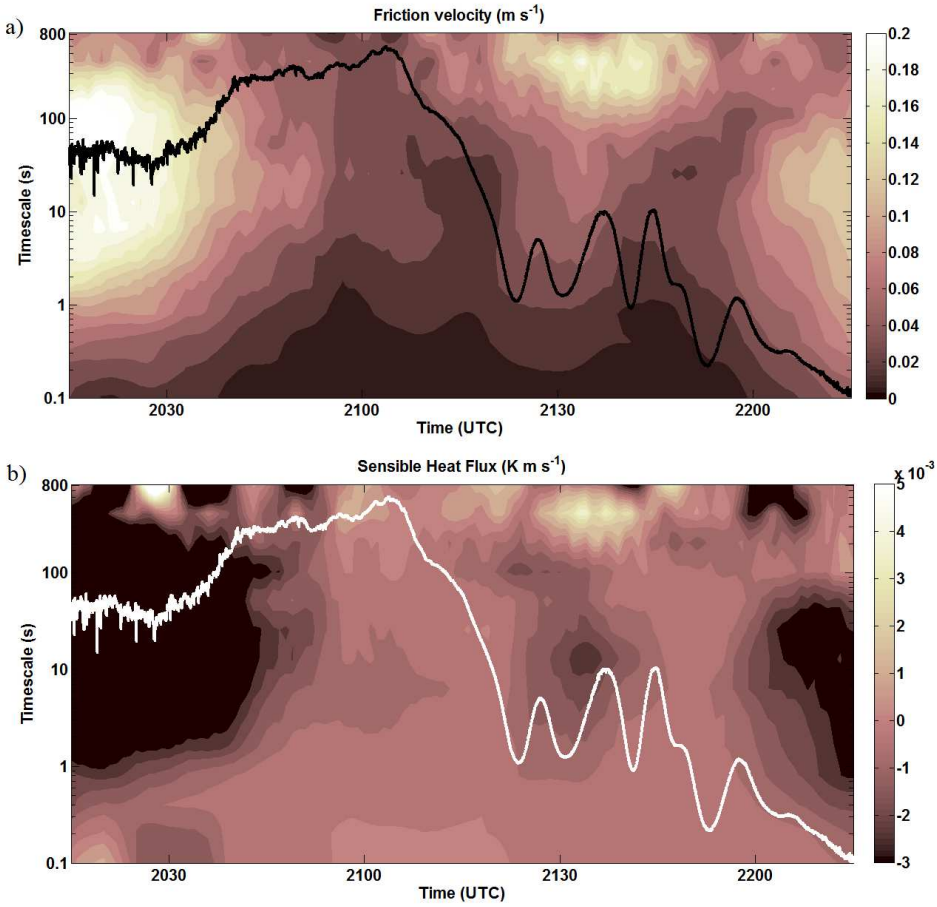

Figure 6.11: Multi-Resolution Flux Decomposition (MRFD) of (a) friction velocity (m s^{-1}) and (b) kinematic heat flux (K m s^{-1}) at 2 m agl. The surface pressure time series from microbarometer A is overlaid for reference (black line in (a) and white line in (b)).

High values of friction velocity are observed in Figure 6.11 (a) until 20:45 UTC, due to relatively high winds associated with the passage of the more active part of the MCS, with important contributions of scales between 1 and 300 s (turbulent). Afterwards, the turbulence decays significantly as a consequence of the decrease in wind speed and the stabilization of the layer. The surface-based thermal inversion formed caused an increase in the kinematic vertical heat flux (Figure 6.11 (b)) around 21:30 UTC. Although the turbulence remained relatively weak during GW propagation over the site, it in-

creased with the GW arrival at 21:20 UTC, probably due to the effect of the GWs generating turbulence by nonlinear effects and the oscillations in wind speed. In addition, an increase in the contribution to the friction velocity and heat flux occurred for temporal scales larger than 300 s during the wave event. These temporal scales coincide with the order of magnitude of the calculated period of the GWs (around 9 min). One should also note the positive values encountered for the vertical heat flux observed during the wave event, frequently known as counter-gradient fluxes when they are found in stable environments, since they indicate an upward heat flux. Counter-gradient fluxes have been associated with wave-breaking activity during stable conditions in the PBL (Nai-Ping et al., 1983; Yagüe and Redondo, 1995; Chimonas, 1999). In this case, these counter-gradient fluxes from higher temporal scales coincided with the GWs and coexisted with the co-gradient (positive vertical heat fluxes) turbulent heat fluxes from lower temporal scales.

6.4 SUMMARY AND CONCLUSIONS

Near-monochromatic GWs associated with a MCS were detected on 21 June 2011 during the BLLAST field campaign in Lannemezan (France). These GWs have been analysed in detail, taking advantage of the large amount of available data. The clearest manifestation of these GWs was observed in the surface pressure records measured by an array of three high- resolution microbarometers, showing clear sinusoidal oscillations of 0.4 - 0.5 hPa. Wavelet analysis has been performed and wave parameters have been evaluated, suggesting the occurrence of GWs propagating from southwest to northeast with a period of around 9 min, a wavelength of 7 km and a phase speed of around 12.5 m s^{-1}. These wave-like motions were preceded by a surface pressure drop of 1.4 hPa, which has been identified as the wake low of the MCS. The location of the pressure drop at the rear part of the MCS, the negative values of vertical velocity measured by the UHF wind profiler and the resemblance to the structure of many other documented MCSs support this wake low hypothesis. The downdraughts related to the wake low have been proposed to be the most likely mechanism responsible for GW initiation in a stably stratified atmosphere. GW tracking was performed with additional barometers placed at different locations and showed that not all directions were favourable for wave propagation. Although the orography between the *Pic du Midi* and Lannemezan could have played an important role in the final formation of GWs, this effect could not be analysed further due to the lack of measurements between the *Pic du Midi* and Lannemezan. The propagation of the GWs in the southwest - northeast direction was favoured by the exis-

tence of a duct layer defined by positive values of m^2 (vertical wavenumber) between the surface and 2000 m agl. The thickness of the duct layer was determined mainly by the wind profile, characterized by a wind sheared zone with a critical level around 2000 m agl. This critical level caused the vertical reflection of the GWs and permitted their horizontal propagation. The uncommon properties of these GWs compared with those usually associated with convection seemed to be possible in part because of the relatively low position of the wind shear and the critical level, i.e. these observations suggest some proportionality between the position of the critical level and the dimensions and properties of the GWs.

GW effects were also observed in the wind, temperature and humidity time series close to the surface and within the lower troposphere. The contributions of the different temporal scales to the surface fluxes (evaluated through MRFD analyses) were also affected by GW passage, which produced an increase in turbulence at certain moments, an important contribution to the fluxes from larger temporal scales and counter-gradient fluxes.

Although a detailed analysis was possible in this study, some questions still remain open, especially those concerning GW origin and the role of orography. Numerical simulations and the observational analysis of similar case studies at this site as well as at other locations not affected by mountains would add valuable information to these unresolved questions.

7

GRAVITY WAVES ASSOCIATED WITH DRAINAGE FLOWS AND THEIR INTERACTIONS WITH TURBULENCE

The interactions among several SBL processes occurring just after the evening transition of 2 July of 2011 have been analysed using data from instruments deployed over the area of Lannemezan (France) during the BLLAST field campaign. The near-calm situation of the afternoon was followed by the formation of local shallow drainage flows (SDFs) of less than 10 m meters depth at different locations. The SDF stage ended with the arrival of a stronger wind over a deeper layer more associated with the mountain-plain circulation, which caused mixing and destruction of the SDFs. Several gravity wave-related oscillations were also observed on different time series. Wavelet analyses and wave parameters were calculated from high resolution and accurate surface pressure data of an array of microbarometers. These waves propagated relatively long distances within the SBL. The effects of these phenomena on turbulent parameters (friction velocity and kinematic heat flux) have been studied through MRFD methods performed on high frequency data from sonic anemometers deployed at different heights and locations. With this method, the different timescales involved in each turbulent parameter were detected and separated from wave contributions, which becomes very important when choosing averaging-windows for surface flux computations using eddy covariance methods. The extensive instrumentation allowed to highlight in detail the peculiarities of the surface turbulent parameters in the SBL, where several of the noted processes were interacting and producing important variations in turbulence with height and between sites along the sloping terrain.

The content of this chapter has been published as:

ROMÁN-CASCÓN, C., YAGÜE, C., MAHRT, L., SASTRE, M., STEENEVELD, G. J., PARDYJAK, E., VAN DE BOER, A. & HARTOGENSIS, O. (2015): Interactions among drainage flows, gravity waves and turbulence: a BLLAST case study. *Atmos. Chem. Phys.*, **15**, 9031-9047.
http://www.atmos-chem-phys.net/15/9031/2015/acp-15-9031-2015.pdf

7.1 INTRODUCTION

As commented in Chapter 1, one of the reasons of the poor understanding of SBLs is the existence of the so-called submeso or submesoscale motions (Mahrt, 2009), which coexist with weak or very weak surface fluxes conditions (Mahrt et al., 2012). These motions (which include wave-like motions in the SBL) do not belong to the mesoscale neither to turbulent or micrometeorological scales. They are usually defined as submeso motions (Mahrt, 2014), comprising scales of less than 2 km, although this limit can be quite subjective. The separation (spectral gap) of these non-turbulent motions from turbulence is not always clear. Therefore, wrong estimations of surface turbulent fluxes are common in SBLs (Vickers and Mahrt, 2003; Voronovich and Kiely, 2007; Viana et al., 2009, 2012), especially over heterogeneous or complex terrain (Martínez et al., 2010; Seaman et al., 2012), where the interactions among local features and these phenomena complicate the analysis. The processes involved in the formation of these structures are hard to isolate and the appearance of these motions is often sporadic and unexpected in many cases.

Some small-scale gravity waves (GWs) and drainage flows can be included in the submeso motions; they can significantly change the stable and typical conditions of calm and clear nights through the generation of intermittent turbulence in the SBL (Nappo, 1991; Sun et al., 2002, 2004, 2012; Van de Wiel et al., 2003; Mahrt, 2011, 2014; Vindel and Yagüe, 2011). They can also change the vertical and horizontal gradients of scalars and consequently the turbulent fluxes observed near surface. The theoretical study of these phenomena has been demonstrated to be very complex (Stull, 1988; Sorbjan, 1989; Fernando and Weil, 2010; Mahrt, 2014; Sun et al., 2015b), and some approximations done with laboratory experiments (Hopfinger, 1987; Riley and Lelong, 2000; Ohya et al., 2008) do not include troublesome factors of the real atmosphere. Therefore, the understanding of these processes through the observational analysis of real case studies becomes very important, especially when high-quality micrometeorological data are available for this purpose.

On the other hand, drainage flows are thermal circulations generated by the differential cooling between surface air masses in sloped or complex terrain under low synoptic forcing, when local conditions gain importance (Whiteman, 2000; Monti et al., 2002; Soler et al., 2002, 2014; Adachi et al., 2004). They are also typical SBL motions and manifest as sudden changes in wind direction, a temperature drop (due to the cooler current) or increasing winds at certain heights, among other effects (Yagüe et al., 2006; Viana et al., 2010; Udina et al., 2013). Several field campaigns have recently increased

interest in these thermal circulations at different scales: e.g. METCRAX 2006 (Whiteman et al., 2008), COLPEX (Price et al., 2011), PCAPS (Lareau et al., 2013) or METCRAX II (Lehner et al., 2015b).

Drainage flow definitions include a wide range of possible spatial scales (Bossert and Cotton, 1994; Martínez et al., 2010). Katabatic and mountain-plain flows are mountain-scale phenomena across and along valleys respectively, while density currents are usually associated with relatively flat terrain. Mountain breezes or katabatic winds (Whiteman, 2000) have been studied in many zones of the world (e.g. Alps (Rotach et al., 2004; Nadeau et al., 2013) or Salt Lake Valley (Doran et al., 2002; Monti et al., 2002)). However, shallow drainage flows (SDFs) or density currents have been less studied (Mahrt et al., 2001; Soler et al., 2002; Udina et al., 2013; Oldroyd et al., 2014; Lehner et al., 2015a), in part because of their smaller scale, that often makes them more difficult to detect. Their proximity to the surface and their ability to change the surface conditions make them important and interesting phenomena worthy of analysis in SBL studies.

This chapter deals with an SBL case study characterized by SDFs generated at different locations just after the near-calm situation of the evening transition during the BLLAST field campaign. These SDFs are later broken up by the arrival of a larger-scale and deeper mountain-plain wind, causing mixing among different layers close to the surface. At the same time, several wave-like oscillations were detected in different time series, related to the passage of GWs. Although these phenomena are common in SBLs, it is not easy to find clear evidence of their existence given the fine horizontal and vertical resolutions required for such observations. Thus, only a few studies have reported in detail cases like the one here presented, as for example in Sun et al. (2015a).

In this work, the physical mechanisms behind these evening transition processes are elucidated, which was one of the goals of BLLAST campaign. Moreover, the analysis techniques employed to carry out this study have been shown to be appropriate for performing detailed studies of these local nocturnal-boundary-layer processes.

This chapter is divided as follows: Section 7.2 explains the features and location of the instrumentation and the techniques employed to carry out the study; Section 7.3 presents results in several subsections; Section 7.4 summarises this chapter and highlights the more important results and conclusions, while also making recommendations for future studies.

7.2 DATA AND METHODOLOGY

7.2.1 *BLLAST*

Data from the BLLAST (Lothon et al., 2014) campaign have been employed in this study. During this campaign, intense observational periods (IOPs) were identified as days with fair weather and weak synoptical forcing. On these days, additional measurements were performed: tethered balloons, aircrafts, unmanned aerial vehicles (UAVs) flights or extra soundings. A total of 12 IOPs resulted from the field campaign. This chapter focuses on a case study corresponding to the 2nd of July 2011 (IOP 10), specifically the period corresponding from approximately 18:00 UTC to 22:00 UTC. The observation of GWs, shallow flows and mountain-plain winds over these hours makes this day very interesting. Different sites with several research objectives and instrumentation were defined during the BLLAST field campaign around Lannemezan. Figure 7.1 shows an approximate location of the sites where instrumentation used in the present study was deployed.

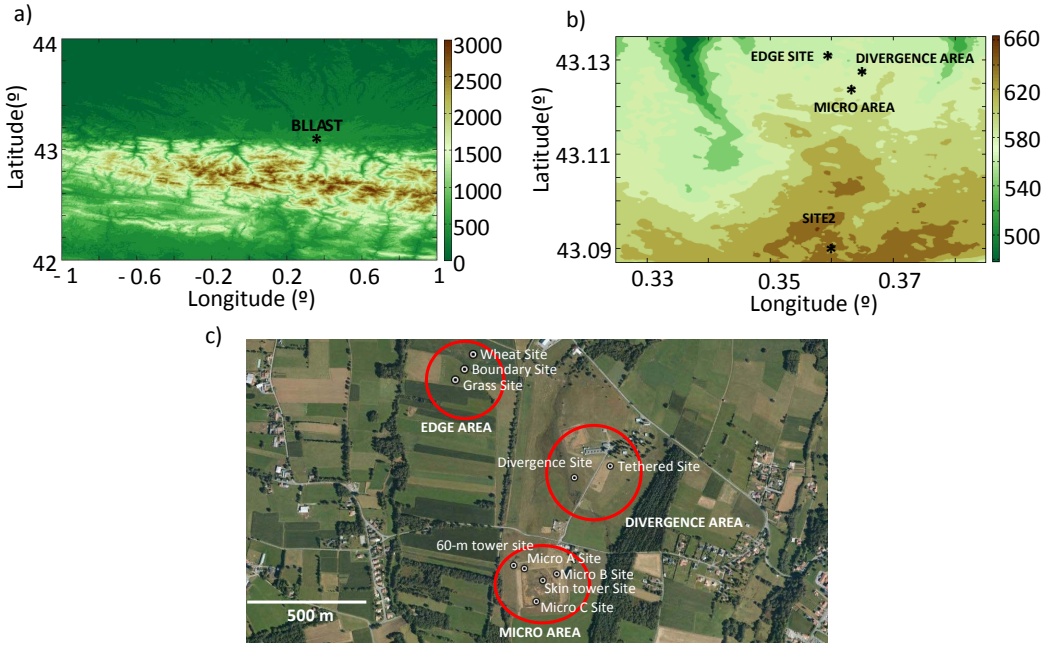

Figure 7.1: a) Topographic map of Pyrenees area around BLLAST (m asl). b) Topographic map of BLLAST area (m asl). c) Aerial view of BLLAST sites (except Area 2). NOTE - Figures a and b from *Routine ASTER Global Digital Elevation Model from NASA Land Processes Distributed Active Archive Center (LP DAAC)*. Figure c from *Google Earth.*

Table 7.1 is a summary with information about these sites and Table 7.2 specifies the instruments used.

Table 7.1: Characteristics of BLLAST sites considered in this study.

Super-Area	Area	Site	Location	Height asl
SUPER-AREA 1	Micro Area	Micro A Site	43°07′ 26,8″ N 00°21′ 46,9″ E	602 m
		Micro B Site	43°07′ 25,9″ N 00°21′ 53,1″ E	600 m
		Micro C Site	43°07′ 22,2″ N 00°21′ 49,2″ E	601 m
		Skin-tower Site	43°07′ 25,1″ N 00°21′ 50,4″ E	600 m
		60-m tower Site	43°07′ 27,1″ N 00°21′ 45,1″ E	602 m
	Divergence Area	Divergence Site	43°07′ 39,1″ N 00°21′ 56,3″ E	590 m
		Tethered Site	43°07′ 40,6″ N 00°22′ 03,1″ E	594 m
	Edge Area	Grass Site	43°07′ 52,5″ N 00°21′ 33,9″ E	582 m
		Wheat Site	43°07′ 56,1″ N 00°21′ 37,3″ E	582 m
		Boundary Site	43°07′ 54,1″ N 00°21′ 35,6″ E	582 m
SUPER-AREA 2	Area 2	Corn Site	43°05′ 25,1″ N 00°21′ 29,6″ E	646 m
		Moor Site	43°05′ 24,9 ″ N 00°21′ 42,6″ E	646 m

Table 7.2: Instrumentation used in each site.

Area	Site	Instruments
Micro Area	Micro A Site	Microbarometer PAROSCIENTIFIC
	Micro B Site	Microbarometer PAROSCIENTIFIC
	Micro C Site	Microbarometer PAROSCIENTIFIC
	Skin-tower Site	8-m tower Site (thermometers, wind vanes)
	60m-tower Site	60-m tower Site (thermometers, wind vanes)
Divergence Area	Divergence Site	8-m tower (thermocouples, sonic anemometers)
	Tethered Site	Tethered balloon (thermometers, wind vanes)
Edge Area	Grass Site	8-m tower (thermometers, sonic anemometers and P (LICOR))
	Wheat Site	8-m tower (thermometers, sonic anemometers)
	Boundary Site	Sonic anemometer
Area 2	Corn Site	Pressure data from LICOR barometer

Drainage flows were mainly investigated at the Divergence Site (additionally at the Micro and Edge Areas), while the GWs analysis from surface pressure records was mainly performed using high-resolution and accurate

data from an array of three microbarometers deployed at the Micro Area. Finally, the analysis of surface turbulent parameters was investigated using data from sonic anemometers installed at different heights on an 8-m tower at the Divergence Site and at the Edge Area, which in turn was composed of three different sites (Wheat Site, Grass Site and the border between these two sites, renamed Boundary Site in this study to avoid confusion).

7.2.2 *Methodology*

The physical processes studied in this work have been analysed through the combination of several techniques applied to measurements from different instruments. Initial comparisons were made among time series of atmospheric variables from instrumentation located at several heights and locations. It is instructive to compare the behaviour of these records among sites because they can sometimes suggest some very local processes happening at a certain site but not at another. Moreover, more complex techniques have been applied.

Firstly, phase differences and wavelet analyses (see Section 2.2.1) were performed on pressure data from an array of microbarometers in order to analyse the detected GWs. Subsequently, a comparison of the effects of SDFs, mountain-plain winds and GWs over surface turbulence have been performed using MRFD methods (see Section 2.2.1). The availability of several sonic anemometers at different sites and heights allowed to explore the spatio-temporal behaviour of turbulence in detail. MRFD is also used to evaluate the relevant turbulent scales and to separate them from larger scales.

Additionally, the WRF (see Section 2.2.2) model has been used as a complement for the determination of the origin of the wind observed at 20:30 UTC, since this question could not be resolved solely with the available observational data. In this study, the WRF-ARW version 3.5.1 of the model was used, with three two-way nested domains centred in Lannemezan (France) and a horizontal resolution of 9, 3 and 1 km respectively with 50 vertically distributed terrain following eta levels. The model was initialized at 00:00 UTC of 2nd July with NCEP-FNL operational global analysis data (1° resolution). It ran for 30 hours (6 hours of spin up) with a time step of 30 s. Yonsei University scheme was used for the PBL parameterization and MM5 similarity for the surface layer scheme. The Noah Land Surface Model was used with input land use and soil category data from USGS. RRTM and Dudhia schemes were selected for the representation of radiation (longwave and shortwave respectively) and the WRF Single-Moment 3-class parameterization was used for the microphysics.

7.3 RESULTS

7.3.1 *General analysis*

The 2nd of July of 2011 was characterized by a weak surface pressure gradient over the south of France, which led to the predominance of light northerly winds during the afternoon (mixed stage in Figure 7.2 (a)) and a near-calm period approximately one hour before astronomical sunset (19:40 UTC).

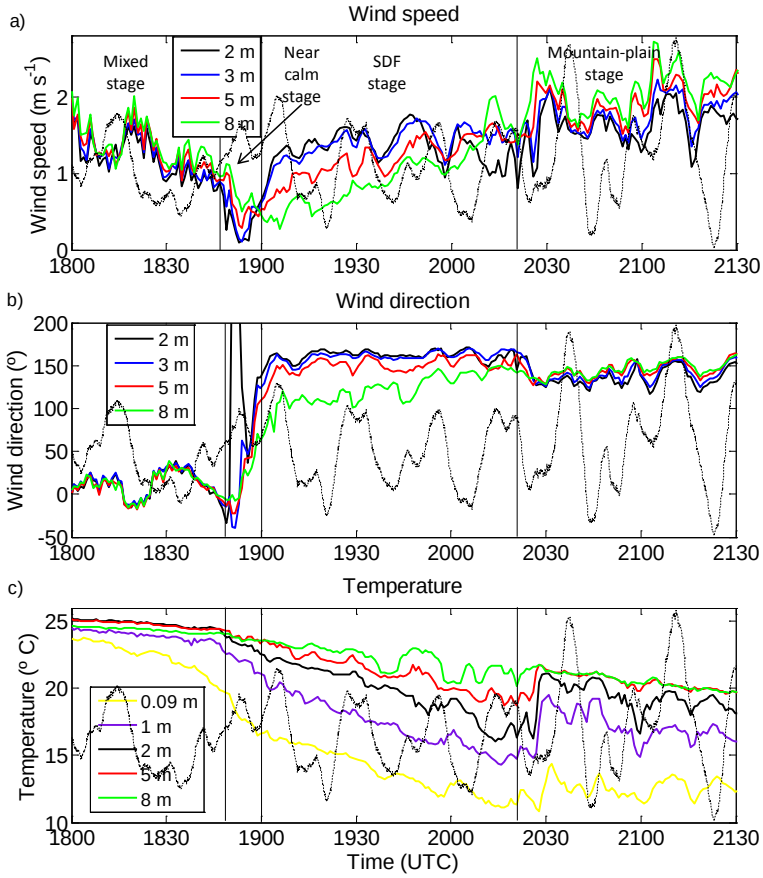

Figure 7.2: Time series from sonic anemometers and thermocouples measurements at the Divergence Site. a) Wind speed (m s^{-1}). (b) Wind direction (°). (c) Temperature (°C). Filtered surface pressure from Micro A is overlaid for reference (thin dotted black line.)

The wind speed decreased close to the surface around 18:55 UTC (Figure 7.2 (a), near-calm stage). This site will be the reference site for the SDF analysis due to the availability of six sonic anemometers from 0.8 m to 8 m agl. This situation of near-calm is propitious for the appearance of SDFs with

a markedly SSE-SE component in the BLLAST area*, which is the direction of most of the local slopes where the instrumentation of the field campaign were deployed. These density currents are caused by the differential cooling between near-surface air masses at different locations in sloped terrains. The sharp wind direction turning of this case study was well observed close to the surface around 18:55 UTC (Figure 7.2 (b)), while measurements at higher heights (more than 8 m agl, not shown) indicated a more gradual turning with time until 20:00 - 20:30 UTC. The wind direction veering near the surface was accompanied by a marked wind speed increase. Stronger winds were encountered at lower levels with maxima close to the surface (around 2-3 m agl) and wind intensity decreasing with height. This is the clear picture of a slight SDF blowing from more elevated terrains to lower elevations in a layer close to the ground. The onset of this SDF coincides with the establishment of a surface-based thermal inversion (Figure 7.2 (c)), although a more dramatic decrease in temperature is observed at the lowest levels approximately when the SDF arrives (18:40 - 19:00 UTC), as is expected when a cold density current appears. This decrease was especially noticeable at very low levels (below 1 m agl), which caused the enhancement of the temperature gradient between the ground and higher heights and the increase of stability close to the surface. The SDF was decoupled from the above flow by an upper low-wind layer and by the wind direction differences with height (blue line in Figure 7.3).

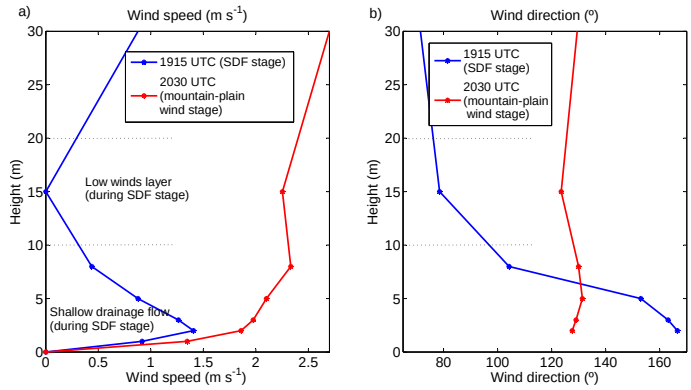

Figure 7.3: Wind speed (a) (m s^{-1}) and wind direction (b) (°) vertical profiles during SDF and mountain-plain wind. Measurements from Divergence 60-m tower sites.

* Up to four days of BLLAST field campaign showed SDFs after the near-calm period of the afternoon.

Nevertheless, surface heterogeneities and differences in local slopes between BLLAST sites led to differences in thickness and persistence of the SDFs from one location to another (Figure 7.4), even blocking its formation at some places (as Grass and Wheat Sites, both at the Edge Area) where these SDFs were poorly observed or lasted only for a few minutes.

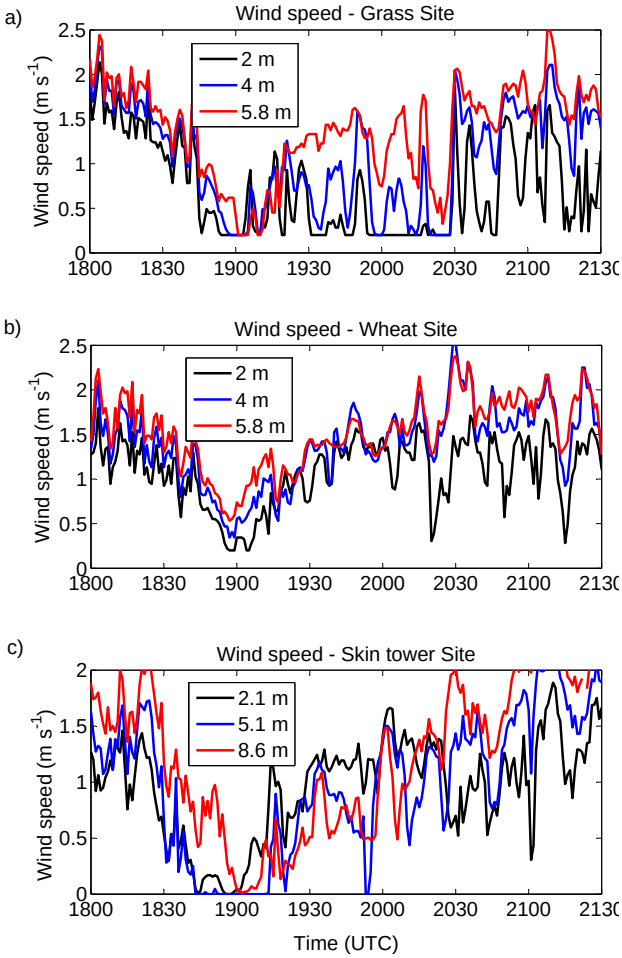

Figure 7.4: Wind speed (m s^{-1}) measured at different heights at the Grass Site (a), Wheat Site (b) and Skin tower Site (Micro Area) (c).

The SDF stage ended between 20:00 and 20:30 UTC with the arrival of a stronger and deeper wind from SE (Figure 7.2 (a) and red line in Figure 7.3, mountain-plain wind stage). This increase in wind was more noticeable at 45 and 60 m agl (not shown) and caused the breaking of the SDF and mixing (increase in temperature) at lower levels (Figure 7.2 (c)). The WRF model has been used to determine the origin and characteristics of this wind. Results

from this mesoscale model simulation indicate that the wind was originated in the southerly located Pyrenees mountains and channelled through the valleys (not shown). The depth of this wind is shown in Figure 7.5, where maximum in wind speed is observed around 80 m agl. This is a clear indicator of the relatively shallow nature of this flow (compared to winds more related to synoptic scales). Therefore, SDFs were disrupted by the arrival of another drainage flow, deeper, stronger and with different characteristics than the former. However, the WRF simulation was neither able to resolve the SDFs nor the GWs observed during these periods.

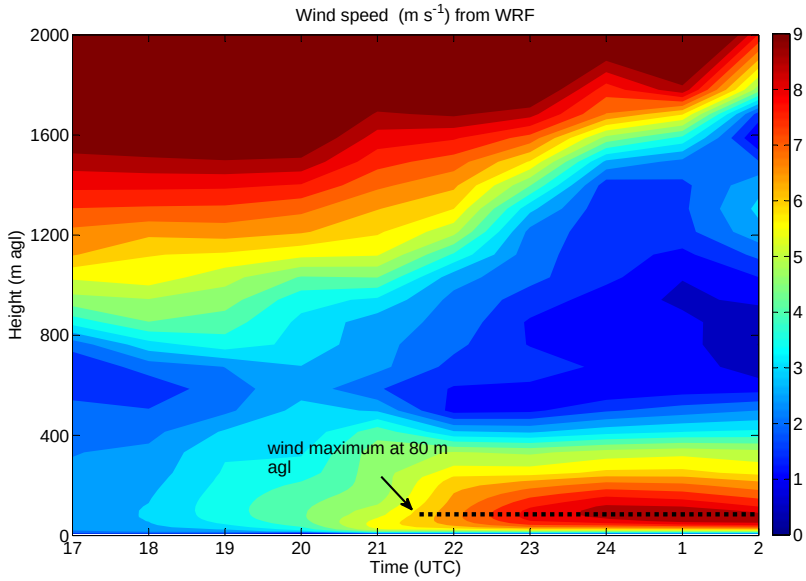

Figure 7.5: WRF wind speed (m s^{-1}) over Lannemezan from 17:00 UTC of 2nd July to 02:00 UTC of 3rd July from surface to 2000 m agl. The results indicate the appearance of the mountain-plain wind in the lowest meters.

7.3.2 *Pressure observations*

The previously described situation of decoupled layers in the lower PBL favours the formation of GWs generated by wind shear in a stable environment. The formation of the SBL around 18:00 UTC is characterized by an increase in the wave-like behaviour of the absolute and filtered pressure records from microbarometers (Figure 7.6 (a and b)). As commented in Section 2.2.1, periods greater than 45 minutes have been removed for the surface filtered pressure (Figure 7.6 (b)) using a high-pass Butterworth filter, in order to avoid the pressure tendency and the diurnal cycle.

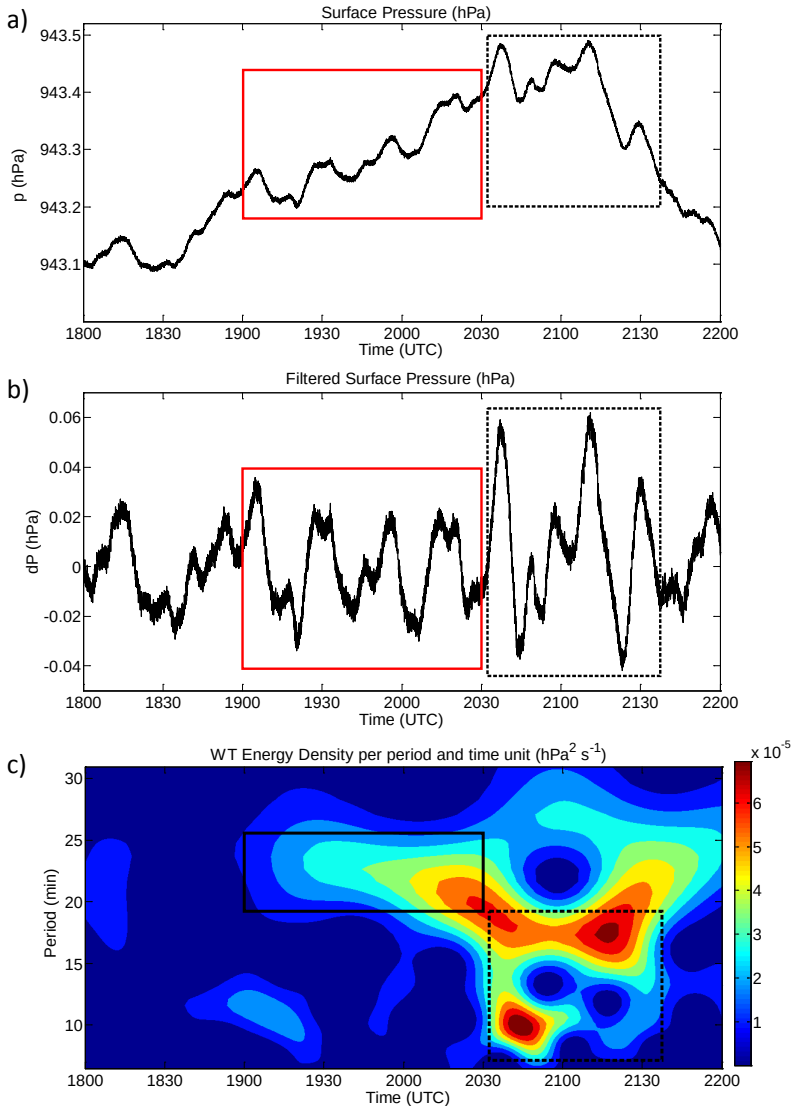

Figure 7.6: Absolute (a) and filtered (b) surface pressure (hPa) measured by microbarometer A. c) Morlet wavelet-based energy density (hPa^2 s^{-1}). Wave event 1 is indicated with red rectangles (black in c) and Wave event 2 with dashed black rectangles. Note: these figures are almost identical for microbarometers B and C.

Two different events can be isolated from the energy increases observed in the wavelet analysis (Figure 7.6 (c)). The first one corresponds to almost four cycles of 20-25 minutes of period observed during the SDF stage (from 19:00 UTC to 20:25 UTC approximately, red boxes in Figure 7.6 (a to b)). The second event is characterized by several oscillations of shorter periods with two notable cycles of greater amplitude from 20:30 UTC to 21:30 UTC, i.e.

after the destruction of the SDF by the arrival of the deeper wind (dashed black boxes in Figure 7.6 (a to b)). Wave parameters for these wave-like structures have been evaluated using phase differences analysis (see Section 2.2.1) and are shown in Table 7.3. Both events are analysed in depth in the next subsections.

a) Wave event 1 (SDF)

Wave parameters have been evaluated from phase differences analysis (see Section 2.2.1) (Terradellas et al., 2001; Viana et al., 2009). This evaluation indicates that values for the first part of Event 1 are not well defined (Table 7.3, from 19:25 to 20:00 UTC), meaning that these oscillations are not clear enough due to the superimposition of other structures and motions, which is a common feature of the real atmosphere. Only the third cycle (from 20:05 to 20:25 UTC) shows a shorter range of wave parameters (Table 7.3), indicating clearer wave structures with well-defined parameters: direction of propagation from W towards E, phase speed of around 18 m s^{-1} and approximate wavelength between 23 and 30 km.

Table 7.3: Gravity waves parameters evaluated from filtered surface pressure records of three microbarometers. Uncertainty is indicated inside brackets (range of values). Note how uncertainty is lower for wave event 2.

	Time (UTC)	**Period (min)**	**Wavelength (km)**	**Phase speed (m s^{-1})**	**Direction of propagation (°)**
Wave event 1	1925 - 2000	20 - 25	not well defined	not well defined	not well defined
	2005 - 2025	22 - 24	[23 - 30]	[17 - 19]	[80 - 90]
Wave event 2	2035 - 2055	10,5 - 12	[12 - 15]	[18 - 20]	[75 - 95]
	2105 - 2130	16 -21	[7 - 10]	[6 - 9]	[32 - 42]

On the other hand, all these oscillations (cycles) of surface pressure were also observed at Area 2 and at the Edge Area (Figure 7.7), which were located respectively at 3.8 km (to the south) and 1 km (to the north) from the Micro A Site. The resolution and accuracy of the barometers (LICOR barometers, except the microbarometers at Micro Site) located at these sites were not the most appropriate to apply phase differences analysis. However, they were used to confirm that these wave-like oscillations were not confined to one specific place and that they were not limited to local SDFs, only observed at some places. Additionally, terrain height variance among sites (up to 70 m of difference between Area 2 and Edge Area, see Table 7.1) and the existence of some buildings and forests between sites indicate that the propagation of

SDFs was perturbed, while the propagation of the wave-like motions in the pressure signals is clearly observed. With these outlines, the hypothesis that GWs are generated at the top or within the SDF is therefore discarded, while propagation of GWs in a deeper layer becomes more likely.

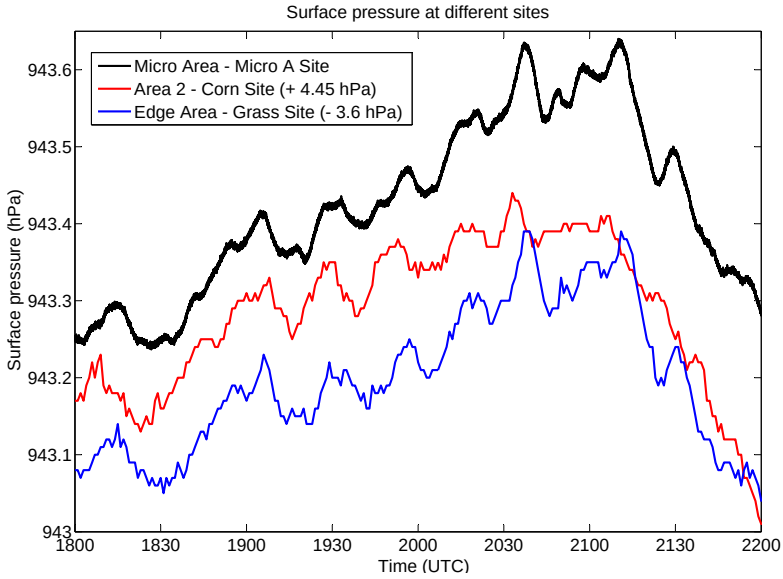

Figure 7.7: Absolute pressure (hPa) observed at three different sites of BLLAST: Micro A Site at Micro Area (black line), Corn Site at SS2 Area (red line, 3.8 km S from Micro A Site) and Grass Site at the Edge Area (blue line, 1 km NNW from Micro A Site). Note that 4.45 (3.6) hPa have been added (subtracted) to the original value at Corn site (Grass site) in order to compare the records.

Figure 7.8 (a and b) show vertical profiles of both wind speed and wind direction obtained from the combination of measurements from the descent of a tethered balloon from 19:52 UTC to 19:58 UTC and tower measurements at 19:55 UTC. These profiles indicate a relatively strong wind shear not only at very shallow levels (as seen before due to the SDF), but also up to 100 m agl, with winds blowing from S-SE at surface and from NE above 50 m agl. Note also the slight LLJ around 100 m agl. The Brunt-Väisälä frequency (N_{BV}, Equation 1.2) (Figure 7.8 (d)) has been calculated using temperature data from these sources (Figure 7.8 (c)) and it shows continuous stable conditions (SBL) up to approximately 200 m agl. This means that, theoretically, the GWs observed by the microbarometers could propagate from surface up to this height and are trapped in this layer.

It is difficult to explain the physical mechanism leading to the formation of the observed GWs with the available data, therefore, several hypotheses are offered. The first one is the intense wind shear (both in direction and

speed of the wind) between layers in the lowest atmosphere. The convergence of SDFs from S-SE and the previous NE winds or the interaction of these shallow flows with the complex orography in a region located more to the south are other hypotheses for the GWs generation. Besides this, other factors such as the LLJ developed at 100 m agl could also be involved on the GWs generation.

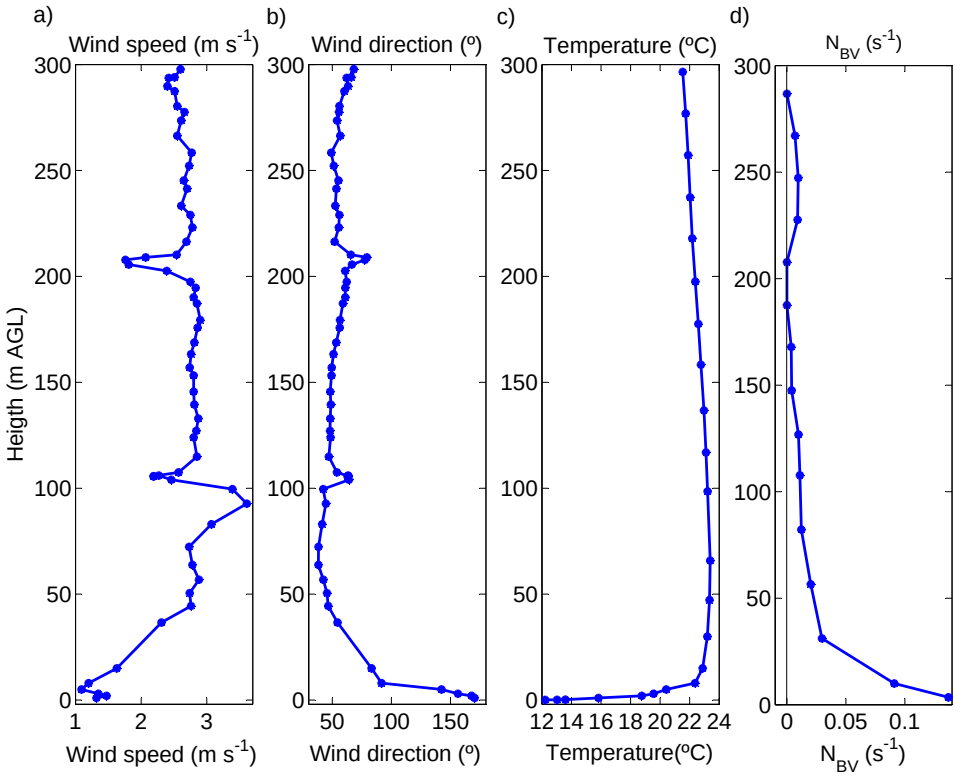

Figure 7.8: Vertical profiles considering combinations of measurements from 8-m tower measurements (from 1 m to 8 m agl), 60-m tower measurements (15 m agl) and the tethered balloon's descent measurements (from 30 m up to 300 m agl) approximately at 19:55 UTC. a) Wind speed (m s^{-1}). b) Wind direction (°). c) Temperature (°C). d) Brunt-Väisälä frequency (N_{BV}, Equation 1.2) (s^{-1}).

Wave-related oscillations in other surface parameters (wind speed, wind direction and temperature) were also observed at all the locations (see Figure 7.2 and Figure 7.4), which indicate the effect of the GWs by alternating horizontal divergence and convergence patterns. Although the agreement between surface pressure and other parameters oscillations is quite good in some cases, linear polarization equations have been not applied to these records because of the existent difficulties when trying to isolate 'clean' records in a real atmosphere like the case presented here. These difficulties

have also been reported in other works (e.g. Nappo, 2012; Mahrt, 2014; Sun et al., 2015b).

b) Wave event 2 (mountain-plain wind)

Evaluated parameters for the second wave event show differences compared to the first one. In this case, the event is characterized by values with little variation (Table 7.3), especially for the two noteworthy oscillations which caused the highest energy signal observed in the wavelet energy analysis. This indicates a clear propagation and an absence of perturbations from other motions. These surface pressure oscillations were also observed at sites separated more than 4 km (Figure 7.7), which also gives an idea of their horizontal propagation.

The higher amplitudes observed in the surface pressure compared to wave event 1 could be due to changes in the depth of the duct layer or stable layer where the GWs were propagating (see comment in the discussion journal, Román-Cascón et al. (2015e) or the case study presented in Chapter 6). That is, the Brunt-Väisälä frequency vertical profile at this stage is likely different than the one shown in Figure 7.8 (d) (at 19:55 UTC), but this fact could not be checked due to the unavailability of tethered balloon or radio-sounding data after 20:00 UTC.

The oscillations observed in surface pressure from 20:35 UTC onwards are related to oscillations in other parameters, such as wind speed (Figure 7.2 (a)), wind direction (Figure 7.2 (b)) or temperature (Figure 7.2 (c)). The wind during this stage is characterised by a wave-like behaviour related to the passage of the GWs, as is observed when compared to filtered surface pressure records (dotted black line in Figure 7.2). Although the oscillations in wind speed have approximately the same period as the oscillations in pressure, the agreement between maxima and minima of both variables is not constant, while the turning of wind due to the GWs is more obvious. In this case, maxima in surface pressure coincides with turnings of wind to the south and minima in pressure with turnings to the east direction. These oscillations have an approximate amplitude of 30-45°. Regarding temperature close to the surface, oscillations of several degrees of amplitude were also observed at different heights and sites (see for example Figure 7.2 (c) at the Divergence site). These oscillations are again moderately correlated to surface pressure, as in wave event 1. The variations in temperature and wind caused by the GWs at some levels led to a complex evolution of the gradients of these parameters with height, which in turn becomes very important for the surface fluxes and turbulence close to the surface, analysed in the next section.

7.3.3 *Surface turbulence: height differences*

The dependence of turbulent parameters on height has been analysed using sonic anemometers at three heights (0.80, 2 and 8 m agl) installed in an 8-m tower at the Divergence Site. Large differences were observed in wind and temperature records between near-ground and upper levels (Figure 7.2) due to the microscale and local behaviour of the SDFs observed at some locations. The turbulent parameters were affected by these differences and the general evolution shows several peculiarities which are analysed hereinafter through MRFD techniques.

For a clearer interpretation of the following figures, one must keep in mind that the x-axis shows the time in UTC and vertical axis indicates temporal scales (logarithmic), while the colour bar shows the magnitude of the friction velocity or kinematic heat flux. Therefore, colours indicate the contribution of different temporal scales to the total value of each turbulent parameter.

a) Friction velocity

A wide range of temporal scales contributed to the friction velocity (Figure 7.9) during the mixed stage (until 18:30 UTC approximately). However, the smallest scales (below 1 s) were more predominant at 0.8 m agl than at 8 m agl, due to the effect of the surface ground generating very small eddies. Moreover, larger scale eddies (from 10 s to 800 s) were more relevant at 2 and 8 m agl.

The near-calm stage was especially noticeable at the lowest level (0.8 m agl), where a decrease for timescales below 200 s is clearly observed (around 18:45 UTC), as a consequence of the decrease in wind and stabilization of the layers very close to the ground. There is still an observed peak for contributions from larger scales (more than 300 s), which is probably the result of larger eddies from the residual layer still present above.

The formation of the SDF after the near-calm stage (around 19:00 UTC) enhanced the turbulence very close to the surface (0.8 m agl). However, friction velocity values remained very low for almost all scales at 2 m agl (SDF maximum of wind), while some turbulence is observed at 8 m agl. This indicates the generation of turbulence by the SDF very close to the ground and above the shallow flow, but not in the middle of the flow (see also comment on Román-Cascón et al. (2015e), discussion stage of the paper associated with this chapter). This is the result of the SDF wind profile (Figure 7.3), with maximum around 2-3 m agl and with wind speed shear vanishing right at this maximum.

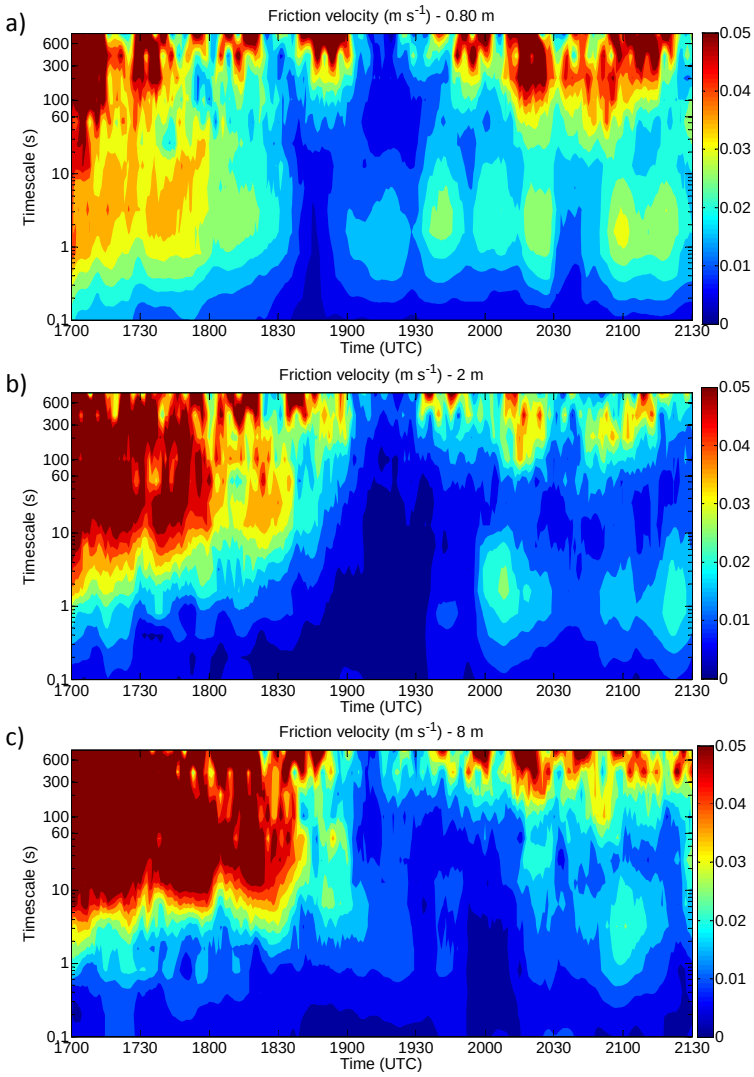

Figure 7.9: Multi-resolution flux decomposition (MRFD) of the friction velocity (m s^{-1}) at 0.8 m agl (a), 2 m agl (b) and 8 m agl (c) at the Divergence Site.

A wave-like pattern is also observed in the evolution at this stage, i.e. the friction velocity MRFD analysis shows alternating increases and decreases for scales between 0.5 and 20 s, especially at 0.8 m agl (Figure 7.9 (a)). This pattern is associated with the GW-related oscillations seen in the wind speed time series.

The SDF wind shear from 2 to 8 m agl disappeared around 20:00 UTC, when wind speed at all levels converged to the same value. This is trans-

lated to an increase in the friction velocity at 2 m agl, where the minimum was observed during the previous SDF stage. The decrease in wind shear above 2 m agl also caused an observed decrease in turbulence at 8 m agl around 20:00 UTC. Later on, the arrival of the mountain-plain wind caused the complete destruction of the SDF and the wind shear at low levels decreased considerably. In this case, the mountain-plain wind generated turbulence more effectively at all levels, without the clear minimum observed in the SDF stage.

Contributions to the friction velocity from larger scales are also observed from 19:30 UTC onwards, associated with the wave event 1. In this case, contributions from 60 to 800 s are separated from smaller scale turbulence (around 2 s) by the spectral gap at 20-60 s approximately. That is, the absence of a continuous signal in the MRFD indicates that these contributions to the friction velocity are due to different mechanisms. Since wave scales are not supposed to contribute significantly to the turbulent mixing, these scales should not be included in a total flux calculation and an averaging window of no more than 20-60 s should be used during this period. However, there is still an open question about the possibility that some of these contributions to the friction velocity from scales between 60 to 800 s are in fact also turbulence, but are generated by the GWs themselves, in which case they should be included in a total turbulent flux calculation. In any case, the conclusions obtained from this case study and from this data set should not be applied to other data sets, due to the complexity of the studied event and local features (see comment of scientific discussion in Román-Cascón et al. (2015d)).

b) Kinematic heat flux

Kinematic heat flux at different heights (Figure 7.10) changes from upwards to downwards at different times. This change happens first at the lower level and then more than half an hour later at 8 m agl, as result of the progressive stabilization of the layers upwards from the surface. After this moment (and already with negative fluxes), there is an increase in the negative fluxes observed at 18:15 UTC, especially at 0.8 and 2 m agl and of scales between 1 and 100 s (green colours in Figure 7.10 (a and b)), as a consequence of the increase in the temperature gradient of the low levels. Later on, the kinematic heat flux magnitude decreases again (yellow colours in Figure 7.10), which is directly related to the strong decrease in wind speed during the near-calm period.

The SDF stage is characterized by an increase in the contribution of small scales (around 1 s) to the surface kinematic heat flux very close to the ground

(at 0.80 m agl, green and blue colours in Figure 7.10 (a) from 19:00 UTC to 20:00 UTC) due to the SDF-related increase in friction velocity seen in the previous section. However, at 2 and 8 m agl, this stage is characterized by very low kinematic heat fluxes (near 0, orange colours) because both temperature and wind gradients are smaller at these heights.

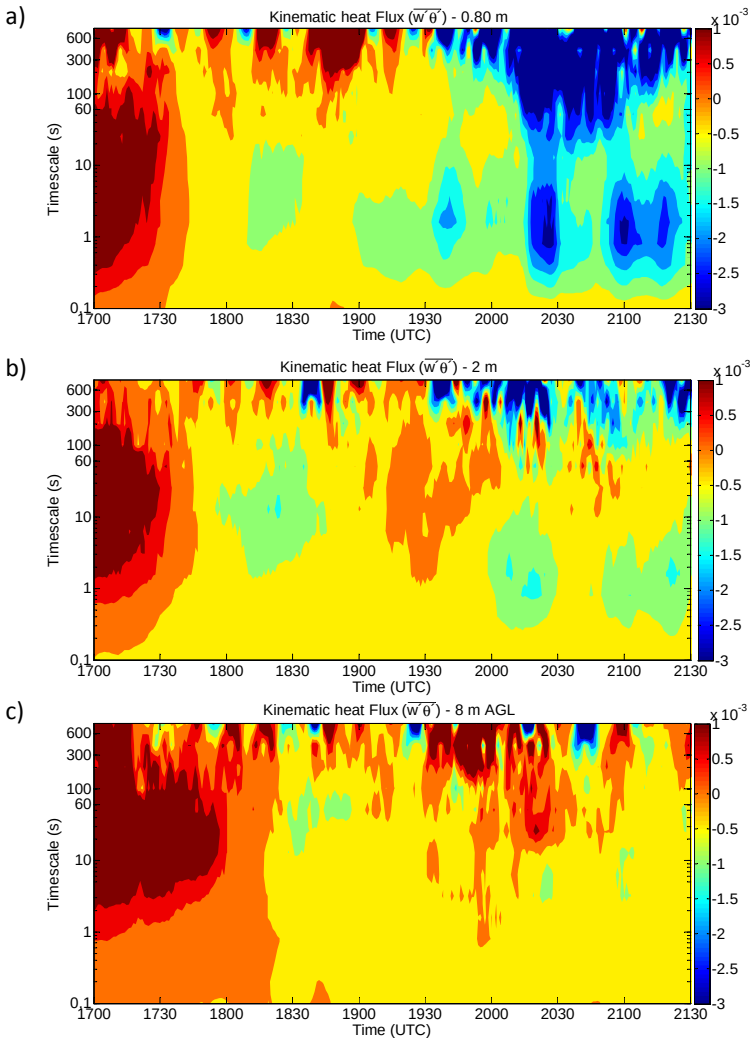

Figure 7.10: Multi-resolution flux Decomposition (MRFD) of kinematic heat flux (K m s^{-1}) at 0.8 m agl (a), 2 m agl (b) and 8 m agl (c) at the Divergence Site.

Considering the height of 0.8 m agl (Figure 7.10 (a)), it should be noted that the temporal scales (around 1 s) contributing to the turbulence in this SDF period are smaller when compared to the scales observed before the

arrival of the density current. The mean wind speed at 0.8 m agl (not shown) was of approximately 1 m s^{-1} from 18:00 UTC to 18:30 UTC and of 1.5 m s^{-1} during the SDF stage (19:00 UTC to 20:30 UTC). If the frozen eddies hypothesis of Taylor (Stull, 1988) is applied to convert temporal scales to length scales for both periods, approximate eddy sizes of 5 m and 1.5 m are obtained respectively. In fact, the turbulence generated near surface due to the SDF is observed only in the lowest levels, but not at higher levels, while during the period previous to the near-calm situation (18:00 UTC to 18:30 UTC), this increase in turbulence was also observed at 2 m agl and up to 5 m agl (not shown). The same can be concluded from friction velocity MRFD (Figure 7.9) and it is indicative of the small eddies generated by the SDF by friction with the ground compared to the predominant eddies during low-winds-stable situations (period previous to the near-calm situation).

Finally, the arrival of the mountain-plain wind causes an increase in temperature at all levels except 8 m agl (Figure 7.2 (c)), meaning that the wind is causing mixing among the lowest levels and breaking the SDF. That is, air from aloft is brought to lower levels and therefore the temperature increases, but this increase is progressive with height; it takes place sooner and it is more pronounced at higher heights, enhancing the temperature gradient between levels located very close to the ground. This fact and the increase in wind lead to an enhancement of the negative surface kinematic heat fluxes at 0.8 m agl (blue colours in Figure 7.10 (a)) at 20:15 UTC. However, the mixing at the highest level (8 m agl) causes the homogenization of the layer and therefore the heat flux does not increase (Figure 7.10 (c)) at 8 m agl. Later on, several increases and decreases in the heat flux are observed (especially at 0.80 m agl), corresponding to the wave-like behaviour of this period. As seen in the friction velocity MRFD, the turbulent scales are well separated from non-turbulent motions by a spectral gap around 10 s. Again, the selection of a higher averaging window could cause an overestimation of the fluxes, since large scales could be associated with GWs.

7.3.4 *Surface turbulence: site differences*

The difficulties estimating surface fluxes over heterogeneous terrain are well known, especially during very stable situations. In this section the evolution of turbulent parameters is compared through MRFD performed over measurements of three nearby sonic anemometers located at the so-called Edge Area. These instruments were strategically deployed on different land use sites and separated around 60 m among them, allowing to analyse the effect of the different roughness lengths and land use over surface turbulence.

These sonic anemometers were installed at 2 m agl over grass (10 cm height approximately), wheat (80 cm height approximately) and over the border between them. This border (boundary site) was composed by denser vegetation (harder) and a small ditch (see van de Boer et al. (2014) and comment on Román-Cascón et al. (2015d) for more information and figures about the Edge Area).

a) Friction velocity

The near-calm period is observed at all the places some minutes before 19:00 UTC but with slight differences in the starting time (Figure 7.11). The SDF was not effectively formed at the Edge Area (see Figure 7.4 (a and b)), and therefore, a clear related increase in surface turbulence was neither observed at the Grass Site, nor at the Wheat Site. However, certain increase in turbulence is observed at the boundary between these places (Figure 7.11 (c) from 19:00 to 19:45 UTC) and reveals the turbulence enhancement effect of this border.

The wind records at the Grass Site were clearly characterized by a wave-like behaviour during this stage with a maximum observed at the lowest levels (less than 5 m agl) around 19:30 UTC, which indicates an attempt of settling of some SDF (see Figure 7.4 (a)). This increase in wind does not cause a direct increase in mechanical turbulence at the Grass Site (Figure 7.11 (a)), but it does it over the Boundary Site (Figure 7.11 (c)). This increase is possibly a consequence of the crash between a shallow flow from SE (from Grass Site) and the denser and higher vegetation at the Boundary Site. Beyond this point (at the Wheat Site) this increase is again not observed, except for very small scales (below 1 s). This fact is contrary to the processes observed at the Grass Site, where these small contributions were almost suppressed from 18:30 to 20:15 UTC, as a result of very small winds observed at the Grass Site during this period. These low winds observed at the Grass Site could be in turn affected by the maize field located upwind (to the south, see comment on Román-Cascón et al. (2015c) in the discussion stage of the paper associated to this chapter).

With the arrival of the mountain-plain wind around 20:15 UTC, the turbulence slightly increases at the Grass and Wheat Site, while there is a marked increase at the Boundary Site (Figure 7.11 (c)), highlighting again the important effect of this obstacle between both places generating turbulence. In this stage, the very small-scale turbulence increase was observed at both sites, although it is more noticeable at the Wheat Site. The important increase in wind observed at the Grass Site some minutes before 20:30 UTC (Figure 7.4 (a)) is the cause of this enhancement observed in the friction velocity MRFD.

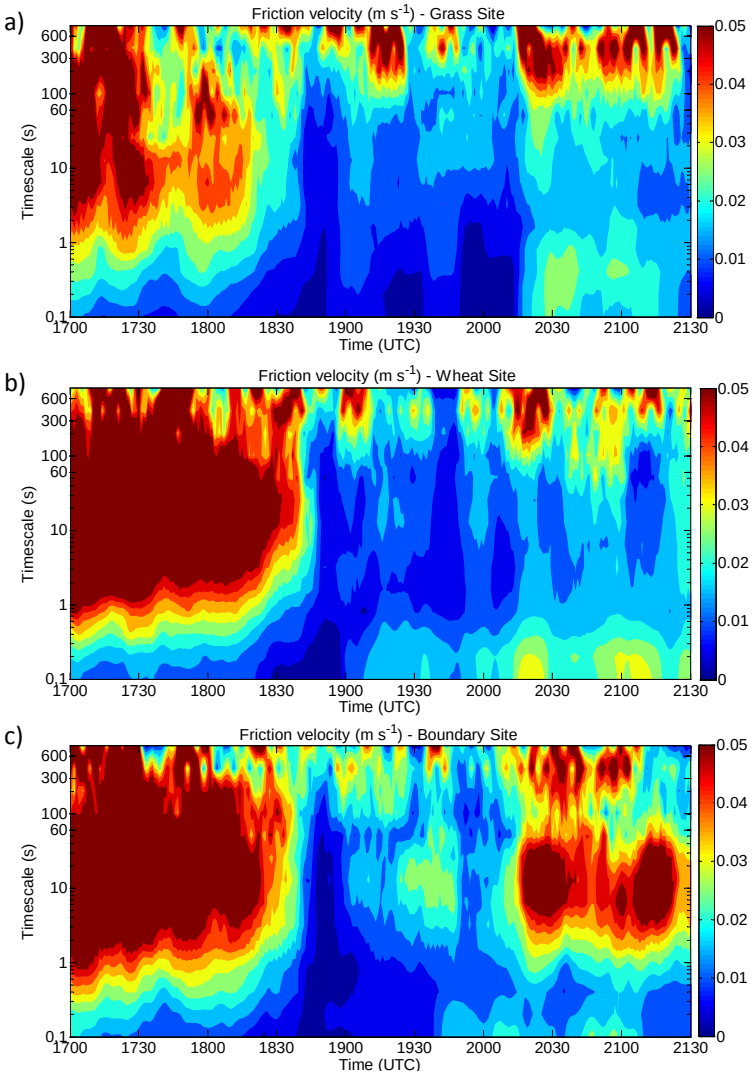

Figure 7.11: Multi-resolution flux decomposition (MRFD) of the friction velocity (m s^{-1}) at Grass (a), Wheat (b) and Boundary (c) Sites (located at Edge Area and at 2 m agl).

However, reasons for the specific scale-contributions in this case are difficult to determine and are probably related to the roughness length of the different surfaces. It seems that unlike in the SDF stage, the grass roughness is acting efficiently in the generation of turbulence, mainly because of the important increase in wind speed observed at 2 m agl at 20:25 UTC (Figure 7.4 (a)), where the wind changes radically with the arrival of the mountain-plain wind.

Finally, the effects of the observed GWs are also present at all the sites, with important large-scale contributions for scales higher than 100 s and especially for scales of the order of minutes, as seen also before at the Divergence Site (Figure 7.9). However, the GWs effects are not only observed over these large-scale contributions; there is a clear wave-like behaviour in turbulent scales (intermittent turbulence) during the whole period, with maximum followed by minimum contributions for all the involved scales. This is the result of the alternating horizontal divergence and convergence patterns of the SBL caused by the waves. That is, the oscillations observed in temperature and wind profiles at different heights are causing alternating increases and decreases in the temperature and wind gradients, which is consequently translated into these changes in surface fluxes.

b) Kinematic heat flux

Large differences have also been found among surface kinematic heat fluxes analysed at these three nearby but different places (Figure 7.12). It is interesting to note that the kinematic heat flux changes from upward to downward considerably later at the Wheat Site than at the other sites. The wheat was drier in this season and therefore the daytime convection is more intensive and the decay takes longer. Consequently, the increase in negative surface kinematic fluxes due to the stabilization of the layer around 18:00 UTC at the other sites is not observed at the Wheat Site. The characteristics of the wheat canopy could also play a role limiting the effect of the radiative cooling by the wheat itself.

The near-calm period just before 19:00 UTC is well observed at all sites, especially at the Grass Site, where the diffusion of heat was almost completely suppressed for all scales. Later on, during the SDF stage, there is a tendency toward very small kinematic heat fluxes over wheat and grass surfaces (yellow colours), while an increase in the negative heat fluxes is observed at the edge between the sites (Boundary Site, Figure 7.12 (c)), as also seen and explained in the previous section (greater friction velocity).

The consequences of the arrival of the mountain-plain wind are also very different depending on the site. Contrary to expected, a reduction of the surface fluxes is observed when the wind increases, and only small scales are contributing to diffuse the heat downward at the Grass Site (yellow colour below 3 s versus orange colour for contributions between 3 to 60 s, from 20:15 UTC onwards). Although the mechanical turbulence slightly increased at this time (Figure 7.11 at 20:15 UTC), the kinematic heat flux drop was probably caused by the mixing that occurred at higher levels, leading to a reduction of the temperature gradient. In contrast, the effect of the mountain-

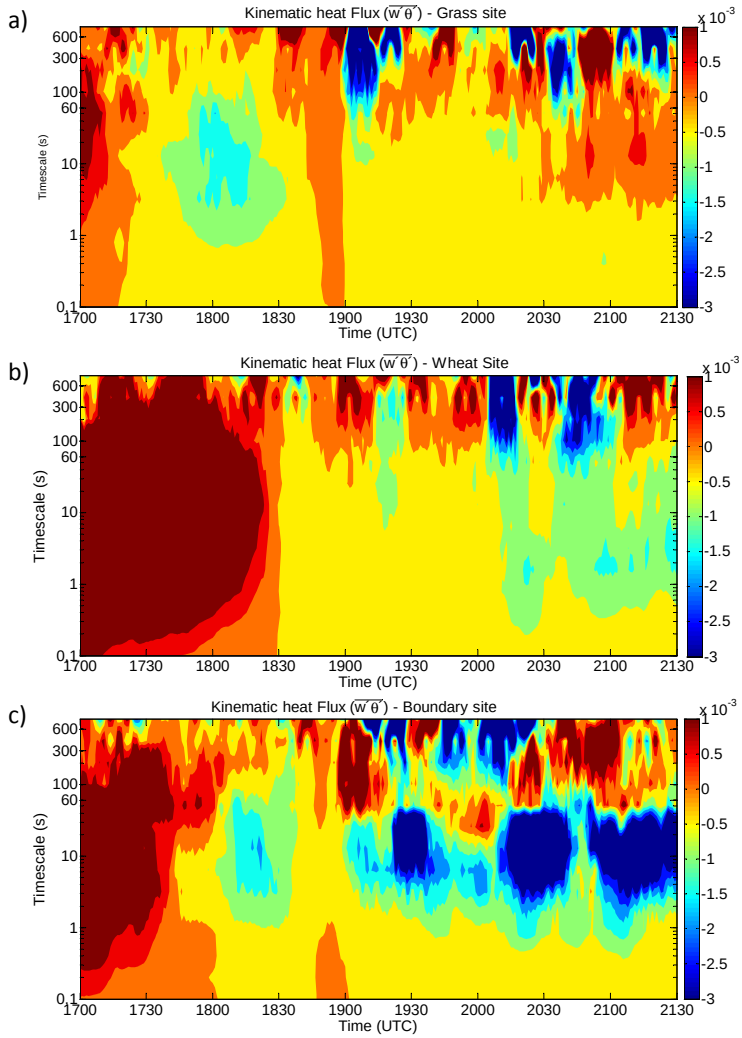

Figure 7.12: Multi-resolution flux decomposition (MRFD) of kinematic heat flux (K m s^{-1}) at Grass (a), Wheat (b) and Boundary (c) Sites (located at Edge Area and at 2 m agl).

plain wind over the Wheat site was to cause the enhancement of the negative kinematic heat fluxes, the explanation of which is hard to determine, since the temperature gradient behaviour was similar at the Grass Site (not shown).

The gap between turbulent and larger scales is very well-defined at these sites during the whole period. There are clear alternations between positive and negative values (red and blue colours) of large scales, which is

a distinctive characteristic of GWs (Viana et al., 2009, 2010). The spectral gap is especially well marked at the Boundary Site (Figure 7.12 (c)), where a change from negative (turbulence) to positive contributions (probably related to waves) is observed around 60 s from 19:00 UTC onwards. In this case, an inappropriate choice of the averaging interval when using eddy covariance methods to estimate turbulent parameters could lead to an important underestimation or even be the cause of the counter-gradient fluxes found sometimes in SBLs.

7.4 SUMMARY AND CONCLUSIONS

Several stable-boundary-layer processes occurring along the afternoon and evening transition during the 2nd of July 2011 (IOP 10) of the BLLAST field campaign have been analysed in detail taking advantage of the large amount of accurate and high frequency instrumentation deployed over the area of Lannemezan (France).

Shallow drainage flows (SDFs) were formed just after the near-calm period of the afternoon at different locations due to small local slopes. The formation of these density currents led to untypical wind profiles, with maxima in wind speed around 2-3 m agl, decreasing winds with height and marked changes in wind direction among different levels. These SDFs (not observed at all the sites due to heterogeneities of the area) were eroded by the arrival of a mountain-plain wind. This deeper wind was more associated with the scale of the Pyrenees and caused partial mixing and the establishment of new wind and temperature profiles.

Time series of pressure, wind and temperature showed a wave-like pattern during the SDFs stage and during the mountain-plain wind. The availability of precise and high-frequency data of surface pressure from an array of microbarometers allowed to evaluate wave parameters, which indicated a shorter (more precise) range of values for gravity waves (GWs) parameters during the mountain-plain wind, with smaller wavelengths and phase speeds. These GWs were observed at different locations, indicating a non-local character and a clear propagation. Tethered balloons and tower measurements indicated stable stratification at least up to 200 m agl, wind direction changing with height and even a weak LLJ around 100 m agl. This wind shear or even the LLJ effects are proposed to be involved in the generation of these GWs, which in any case were trapped within the SBL. However, the effect of the nearby hilly terrain could also be important.

Finally, the effects of these different processes on the surface turbulent parameters (friction velocity and kinematic sensible heat flux) have been

studied in detail using MRFD techniques from sonic anemometers data at different heights and sites. The microscale and shallow nature of some of these processes is underscored by the differences found at several heights. The selection of the height of the sensor could lead to underestimations of surface fluxes or turbulent parameters when density currents are present in very shallow layers, specially if sonic anemometers are located at the SDF wind-maximum height (minimum in turbulence). The dependence of these turbulent parameters on the land-use and terrain is also highlighted through the comparison among the MRFD at the grass, wheat and at the boundary between both sites.

MRFD is shown to be a powerful tool to determine the averaging-window needed to compute turbulent parameters or fluxes from the spectral gap observed between turbulent and larger-scale motions, as done in Nappo et al. (2008) or Durden et al. (2013), where GWs scales are removed from the flux computation in order to avoid overestimation of fluxes. Otherwise, possibly wrong estimations of momentum (overestimation) and heat (overestimation, underestimation or even false counter-gradient) turbulent fluxes can be assumed. However, there is still an open question about the possible overlapping between wave scales and wave-generated turbulence (separated by a spectral gap from turbulence of smaller scales created by other mechanisms). In this case, part of these larger scales should be definitely included (Vercauteren and Klein, 2014), since their turbulent behaviour would contribute to the diffusion of scalars. These considerations must be taken into account, especially when analysing SBLs over heterogeneous terrain and during the evaluation of numerical models performance with field measurements.

CONCLUDING REMARKS

Things in life are normally oscillating and sometimes foggy. Both can be dissipated by adding more turbulence (energy).

8

CONCLUSIONS AND FUTURE WORK

This last chapter presents the most relevant conclusions obtained from this thesis and their applicability. Besides, a point-by-point listing of the specific conclusions obtained after every chapter of results is provided, in order to facilitate the reading of these findings. Possible future work points are also provided for each issue.

8.1 GENERAL CONCLUSIONS AND APPLICABILITY

The main objective of this thesis was to gain knowledge about two SBL phenomena (gravity waves and radiation fog), with special emphasis on their interactions with turbulence. Thus, some new helpful insights for the physical understanding and forecasting of these phenomena have been provided:

- It has been shown how the numerical forecasting of radiation fog with the WRF model can be improved through the specific selection of physical parameterizations, obtaining successful predictions, although some deficiencies of the model have also been highlighted. Radiation-fog forecasting through statistical methods (M14) is also a valid alternative, specially for nowcasting with observations. These results are expected to be useful for NWP modellers and operational forecasters that try to improve the forecast of this phenomenon. The differences between shallow and deep radiation fog are also shown in terms of their different vertical profiles of temperature and through their distinct values of surface turbulence. Thus, the fog-top height can be estimated from surface turbulent measurements. This result opens a new way for the estimation of this variable with a sonic anemometer deployed at surface, which could be operationally implemented, for example at airports or at the World Meteorological Organization (WMO) stations.

- The observational analysis of two case studies of GWs has served to understand how these phenomena can be formed and propagated in the atmosphere. In one of the cases, the ducting mechanism was described and the features of the GWs were associated to the thickness of the duct layer, while the GWs formation was linked to the wake low located at the rear part of a MCS. The other case study showed how drainage flows of different scales governed the structure and evolution of the SBL during the evening transition at the BLLAST site, while at the same time GWs appear to coexist with them and propagate in the whole SBL. It is expected that the descriptions provided in this thesis will serve to improve the representation of these processes in NWP models. The analysed GWs influenced notably the turbulence at different heights and sites. These structures were clearly separated from small-scale turbulence by a spectral gap, which should be taken into account when calculating surface fluxes. However, there is still an open question about the diffusive or non-diffusive character of the structures linked to GWs, whose time scales are lower than the GWs ones but higher than those of the turbulent motions.

8.2 SPECIFIC CONCLUSIONS AND FUTURE WORK

This section allows the reader to have a quick point-by-point look of the specific conclusions obtained after each chapter of results.

Chapter 3 - WRF sensitivity experiments (Román-Cascón et al., 2012).

- *OBJECTIVE:*

  - To determine the ability of the WRF model simulating radiation fog under different physical options of the model.

- *CONCLUSIONS:*

  - The results depended on the analysed case study (the physical parameterizations do not behaved equal for shallow or deep fogs).

  - The model normally overestimates the nocturnal surface temperature. However, the mixing ratio is also overestimated in many cases, leading to a successful prediction of fog (combination of errors leading to correct relative humidity values).

  - The model normally overestimates the fog vertical extension.

  - Sensitivity experiments to physical parameterizations:

    - PBL: MYNN and QNSE provide better results for fog modelling.
    - Gravity-settling option: it produces shallower fog (more realistic).
    - Surface-layer: no-significant influence.
    - Microphysic: Lin et al. and Goddard improve fog forecasting.
    - Land-surface: RUC improves the results for shallow fog.

- *FUTURE WORK:*

  - To focus on the technical configuration of the model (horizontal resolution, number of domains, nesting or not, spin-up, etc.).

  - To perform experiments including data assimilation.

Chapter 4 - Forecasting radiation fog (Román-Cascón et al., 2015a).

- *OBJECTIVES:*

  - To evaluate and extend the M14 method at two contrasting sites.

  - To evaluate the ability of WRF simulating radiation fog.

  - To develop a radiation-fog climatology for the studied sites.

- *CONCLUSIONS:*

  - The results of applying M14 at CESAR and CIBA were quite satisfactory, especially for nowcasting using observations.

  - The threshold values of the key-variables for fog formation can be modified to improve the hit-rate (H-R) or false-alarm rate (F-A), depending on the purposes of the forecaster.

  - The use of WRF model output as predictors for the M14 method does not provide satisfactory performance indicators.

  - The WRF model was able to simulate radiation fog at the expense of sophisticated physical options and high resolution, although the results were highly sensitive to the spin-up time:

    – Long and adequate spin-up times are required to let the model to get in balance with the initial conditions.

    – The downscaling from a coarser model is contraindicated and the use of data assimilation encouraged, as well as the use of higher and lower resolution models with similar physics and dynamics. This could avoid the spurious waves formed during the spin-up.

  - CESAR: radiation-fog events are distributed throughout the whole year, they form soon after sunset and are not persistent.

  - CIBA: radiation-fog events occur mainly during late-autumn/winter. They form later in the night in general (after strong nocturnal surface cooling) and they are more persistent than at CESAR.

- *FUTURE WORK:*

  - To apply M14 method in near-real time and continuous mode at CIBA or CESAR with relatively simple programs (work in progress).

  - To use a similar statistical approach, but with neural networks, using the information of more variables (work in progress).

  - To use data assimilation or higher and lower resolution models with similar physics and dynamics.

Chapter 5 - Estimating fog-top height (Román-Cascón et al., 2015f).

- *OBJECTIVES:*

  - To provide new methods for the estimation of fog-top height through surface turbulent measurements.

  - To evaluate the skill of the estimation of fog-top height through vertical profiles of temperature (TC method).

- *CONCLUSIONS:*

  - Fog thickness can be estimated with a unique sonic anemometer deployed at surface, since it follows a linear correlation with surface friction velocity and buoyancy flux (for convectively active fog).

  - The use of $\overline{w'\theta'_v}$ overestimates the fog thickness during daytime.

  - TC method offers satisfactory results for deep fog ($\sim$ 100 m or more), but it is unsuccessful for shallow and some very deep fog events.

  - The upper layer in very deep fog ($\sim$ 200 m) is somehow decoupled from the lower layers in some cases associated with relatively low-moderate values of surface friction velocity. Thus, the TC method tends to slightly underestimate fog thickness during these cases.

- *FUTURE WORK:*

  - Further calibrations and studies at other sites are required to detect site/instrument dependences and to contrast the equations obtained for the estimation of fog-top height based on turbulent measurements.

  - The characterization of the turbulence at different heights within fog would add valuable information for the understanding of its life cycle.

Chapter 6 - GWs associated with a MCS (Román-Cascón et al., 2015g).

- *OBJECTIVES:*

  - To analyse observationally near-monochromatic oscillations detected in surface pressure records.

- *CONCLUSIONS:*

  - The detected GWs were preceded by a surface pressure drop, identified as the MCS wake low.

  - The wave parameters presented a short range of values, indicating near-monochromatic GWs.

  - The downdraughts related to the wake low are proposed to be the most likely mechanism generator of GWs, although the complex orography of the area could also play an important role.

  - The GWs were propagated horizontally and they were ducted in a layer between ground and 2000 m agl. This height was determined by a wind sheared zone with a critical level.

  - The observations suggest some proportionality between the position of the critical level (thickness of the duct layer) and the dimensions and parameters of the GWs.

  - Associated wave-like oscillations were also detected in the wind, temperature and humidity time series close to the surface and within the lower troposphere.

  - The GWs passage produced an increase in turbulence, flux-contribution from larger temporal scales and counter-gradient heat fluxes.

- *FUTURE WORK:*

  - To analyse similar case studies in sites with availability of similar instrumentation. Thus, the duct layer can be determined and we could obtain a better understanding of its relation with the GWs features.

  - To determine whether events with these features are only observed close to mountainous areas or if they can be associated with MCS formed over flat terrain. This can provide information about the role of the mountains in such events.

  - To carry out ideal simulations with numerical models (with controlled orography) specially developed for the representation of these type of GWs, in order to gain knowledge about the formation mechanisms.

Chapter 7 - GWs related to drainage flows (Román-Cascón et al., 2015b).

- *OBJECTIVES:*

  - To analyse in detail the interactions between evening transition processes and turbulence in the SBL.

- *CONCLUSIONS:*

  - Local SDFs form at BLLAST site due to small slopes.The mountain-plain wind is more associated with the scale of the Pyrenees and arrive later, causing mixing at the lowest levels.

  - The GWs were observed at different locations, indicating a non-local character and a clear propagation. They were trapped in the SBL but it was not possible to specify the formation mechanisms.

  - The selection of the height of the sensor could lead to underestimations of surface fluxes when density currents are present in very shallow layers, especially if sonic anemometers are located at the SDF wind-maximum height (minimum in turbulence). These turbulent parameters are also highly variable in a heterogeneous area such as BLLAST.

  - Possibly wrong estimations of momentum (overestimation) and heat (overestimation, underestimation or even false counter-gradient) turbulent fluxes can be assumed if the averaging-window for flux computation is not correctly determined from the spectral gap.

  - Structures with temporal scales lower than those of the GWs usually appear associated with the GWs (sometimes manifested as counter-gradient buoyancy fluxes). These scales are separated from the turbulent ones by a well-defined spectral gap. There is still an open question about the diffusive or non-diffusive character of these structures. Thus, it is not clear if they should be included in a total flux computation.

- *FUTURE WORK:*

  - In my opinion, it is crucial to know if the GW-related structures (larger than turbulence but lower than GWs scales) are turbulent and diffusive or coherent and non-diffusive for a correct estimation of surface fluxes in SBLs. To study this, further analyses should be done over cases like the one presented in this thesis.

  - To extend the study for the BLLAST area in order to find a general pattern in the generation of GWs during similar weak-synoptic conditions and to focus on the vertical velocity-surface pressure correlation to better understand the wave-turbulence interactions.

Adachi, A., Clark, W. L., Hartten, L. M., Gage, K. S., and Kobayashi, T.: An observational study of a shallow gravity current triggered by katabatic flow, Ann. Geophys., 22, 3937–3950, doi:10.5194/angeo-22-3937-2004, 2004.

Agam, N. and Berliner, P.: Dew formation and water vapor adsorption in semi-arid environments - a review, J. Arid Environ., 65, 572–590, 2006.

Alexander, M. J., Beres, J. H., and Pfister, L.: Tropical stratospheric gravity wave activity and relationships to clouds, J. Geophys. Res.-Atmos. (1984–2012), 105, 22 299–22 309, 2000.

Andreae, M. and Rosenfeld, D.: Aerosol–cloud–precipitation interactions. Part 1. The nature and sources of cloud-active aerosols, Earth-Sci. Rev., 89, 13–41, 2008.

Andrén, A.: Evaluation of a turbulence closure scheme suitable for air-pollution applications, J. Appl. Meteorol., 29, 224–239, 1990.

Arya, P. S.: Introduction to micrometeorology, International Geophysics Series. Academic Press, London, 420pp, 2001.

Azevedo, J. and Morgan, D.: Fog precipitation in coastal California forests, Ecology, 55(5), 1135–1141, 1974.

Baklanov, A. A., Grimmond, S., Mahura, A., and Athanassiadou, M.: Meteorological and Air Quality Models for Urban Areas, Springer Berlin Heidelberg, 2009.

Baklanov, A. A., Grisogono, B., Bornstein, R., Mahrt, L., Zilitinkevich, S. S., Taylor, P., Larsen, S. E., Rotach, M. W., and Fernando, H.: The nature, theory, and modeling of atmospheric planetary boundary layers, Bull. Am. Meteorol. Soc., 92, 123–128, 2011.

Balachandran, N. K.: Gravity waves from thunderstorms, Mon. Weather Rev., 108, 804–816, 1980.

Bari, D., Bergot, T., and El Khlifi, M.: Numerical study of a coastal fog event over Casablanca, Morocco, Q. J. R. Meteorol. Soc., 141, 1894–1905, doi:10.1002/qj.2494, 2015.

Barnes, L. R., Schultz, D. M., Gruntfest, E. C., Hayden, M. H., and Benight, C. C.: Corrigendum: False alarm rate or false alarm ratio?, Wea. Forecasting, 24, 1452–1454, 2009.

Bartok, J., Bott, A., and Gera, M.: Fog prediction for road traffic safety in a coastal desert region, Boundary-Layer Meteorol., 145, 485–506, 2012.

Bauck, B. H.: An unusually strong gravity wave over western Washington, Wea. Forecasting., 7, 389–397, 1992.

Beljaars, A. C. and Bosveld, F. C.: Cabauw data for the validation of land surface parameterization schemes, J. Clim., 10, 1172–1193, 1997.

Belušić, D. and Mahrt, L.: Is geometry more universal than physics in atmospheric boundary layer flow?, J. Geophys. Res-Atmos. (1984–2012), 117, 2012.

Belušić, D. and Mahrt, L.: Estimation of length scales from mesoscale networks, Tellus, A, 60, 706–715, doi:10.1111/j.1600-0870.2008.00328.x, 2008.

Bendix, J., Thies, B., Cermak, J., and Nauß, T.: Ground fog detection from space based on MODIS daytime data-a feasibility study, Wea. Forecasting, 20, 989–1005, 2005.

Bergot, T. and Guedalia, D.: Numerical forecasting of radiation fog. Part I: Numerical model and sensitivity tests, Mon. Weather Rev., 122, 1218–1230, 1994.

Bergot, T., Terradellas, E., Cuxart, J., Mira, A., Liechti, O., Mueller, M., and Nielsen, N. W.: Intercomparison of single-column numerical models for the prediction of radiation fog, J. Appl. Meteorol. Climatol., 46, 504–521, 2007.

Bernardet, L. R. and Cotton, W. R.: Multiscale evolution of a derecho-producing mesoscale convective system, Mon. Weather Rev., 126, 2991–3015, 1998.

Betts, A. K.: Diurnal cycle, in: Enclyclopedia of Atmospheric Sciences, Academic Press. London., 2001.

Betts, A. K.: Radiative scaling of the nocturnal boundary layer and the diurnal temperature range, J. Geophys. Res-Atmos. (1984–2012), 111, 2006.

Birch, C., Parker, D., O'Leary, A., Marsham, J., Taylor, C., Harris, P., and Lister, G.: Impact of soil moisture and convectively generated waves on the initiation of a West African mesoscale convective system, Q. J. R. Meteorol. Soc., 139, 1712–1730, 2013.

Blay-Carreras, E., Pardyjak, E. R., Pino, D., Hoch, S. W., Cuxart, J., Martínez, D., and Reuder, J.: Lifted temperature minimum during the atmospheric evening transition, Atmos. Chem. Phys., 15, 6981–6991, doi:10.5194/acp-15-6981-2015, 2015.

Bocchieri, J. R., Crisci, R. L., Glahn, H. R., Lewis, F., and Globokar, F. T.: Recent developments in automated prediction of ceiling and visibility, J. Appl. Meteorol., 13, 277–288, 1974.

Boers, R., Baltink, H. K., Hemink, H., Bosveld, F., and Moerman, M.: Ground-based observations and modeling of the visibility and radar reflectivity in a radiation fog layer, J. Atmos. Oceanic Technol., 30, 288–300, 2013.

Bosart, L. F. and Seimon, A.: A case study of an unusually intense atmospheric gravity wave, Mon. Weather Rev., 116, 1857–1886, 1988.

Bossert, J. E. and Cotton, W. R.: Regional-scale flows in mountainous terrain. Part 1: A numerical and observational comparison, Mon. Weather Rev., 122, 1449–1471, doi: 10.1175/1520-0493(1994)122<1449:RSFIMT>2.0.CO;2, 1994.

Boutle, I., Finnenkoetter, A., Lock, A., and Wells, H.: The London Model: forecasting fog at 333 m resolution, Quarterly Journal of the Royal Meteorological Society, doi:10.1002/qj.2656.

Brenguier, J.-L., Pawlowska, H., Schüller, L., Preusker, R., Fischer, J., and Fouquart, Y.: Radiative properties of boundary layer clouds: Droplet effective radius versus number concentration, J. Atmos. Sci., 57, 803–821, 2000.

Carlson, T. N. and Boland, F. E.: Analysis of urban-rural canopy using a surface heat flux/temperature model, J. Appl. Meteorol., 17, 998–1013, 1978.

Carpenter, J. R., Tedford, E. W., Heifetz, E., and Lawrence, G. A.: Instability in stratified shear flow: Review of a physical interpretation based on interacting waves, Appl. Mech. Rev., 64, 060 801, 2013.

Cermak, J. and Bendix, J.: Detecting ground fog from space–a microphysics-based approach, Int. J. Remote Sens., 32, 3345–3371, 2011.

Chagnon, J. M. and Gray, S. L.: Analysis of convectively-generated gravity waves in mesoscale model simulations and wind-profiler observations, Q. J. R. Meteorol. Soc., 134, 663–676, 2008.

Chen, F. and Dudhia, J.: Coupling an advanced land surface-hydrology model with the Penn State-NCAR MM5 modeling system. Part I: Model implementation and sensitivity, Mon. Weather Rev., 129, 569–585, 2001.

Chimonas, G.: Steps, waves and turbulence in the stably stratified planetary boundary layer, Boundary-Layer Meteorol., 90, 397–421, 1999.

Coleman, T. A. and Knupp, K. R.: Factors affecting surface wind speeds in gravity waves and wake lows, Wea. Forecasting, 24, 1664–1679, 2009.

Cuxart, J.: Nocturnal basin low-level jets: an integrated study, Acta Geophys., 56, 100–113, doi:10.2478/s11600-007-0042-2, 2008.

Cuxart, J. and Jiménez, M.: Deep radiation fog in a wide closed valley: Study by numerical modeling and remote sensing, Pure Appl. Geophys., 169, 911–926, 2012.

Cuxart, J., Yagüe, C., Morales, G., Terradellas, E., Orbe, J., Calvo, J., Fernández, A., Soler, M., Infante, C., Buenestado, P., Espinalt, A., Joergensen, H., Rees, J., Vilà, J., Redondo, J., Cantalapiedra, I., and Conangla, L.: Stable atmospheric boundary-layer experiment in Spain (SABLES 98): a report, Boundary-Layer Meteorol., 96, 337–370, 2000.

Cuxart, J., Morales, G., Terradellas, E., and Yagüe, C.: Study of coherent structures and estimation of the pressure transport terms for the nocturnal stable boundary layer, Boundary-Layer Meteorol., 105, 305–328, doi:10.1023/A:1019974021434, 2002.

Dabas, A., Remy, S., and Bergot, T.: Use of a sodar to improve the forecast of fogs and low clouds on airports, Pure Appl. Geophys., 169, 769–781, 2012.

Daubechies, I.: Ten lectures on wavelets, vol. 61, Society for Industrial and Applied Mathematics (SIAM). Capital City Press. Philadelphia. 354 pp., 1992.

Davy, R. and Esau, I.: Global climate models' bias in surface temperature trends and variability, Environ. Res. Lett., 9, 114 024, doi:10.1088/1748-9326/9/11/114024, 2014.

Dawson, T. E.: Fog in the California redwood forest: ecosystem inputs and use by plants, Oecologia, 117, 476–485, 1998.

De Rooy, W. C. and Kok, K.: A combined physical-statistical approach for the downscaling of model wind speed, Wea. Forecasting, 19, 485–495, 2004.

DOC/NOAA: Surface weather observations and reports, Federal Meteorological Handbook No. 1, 94 pp, Available from Department of Commerce, NOAA, Office of the Federal Coordinator for Meteorological Services and Supporting Research, 8455 Colesville Road, Suite 1500, Silver Spring, MD, 20910., 1995.

Doran, J. C., Fast, J. D., and Horel, J.: The VTMX 2000 campaign, Bull. Am. Meteorol. Soc., 83, 537–551, doi:10.1175/1520-0477(2002)083<0537:TVC>2.3.CO;2, 2002.

Doyle, J. D. and Durran, D. R.: The Dynamics of Mountain-Wave-Induced Rotors, J. Atmos. Sci., 59, 186–201, doi:10.1175/1520-0469(2002)059<0186:TDOMWI>2.0.CO;2, 2002.

Dudhia, J.: Numerical study of convection observed during the winter monsoon experiment using a mesoscale two-dimensional model, J. Atmos. Sci., 46, 3077–3107, 1989.

Dupont, J.-C., Haeffelin, M., Protat, A., Bouniol, D., Boyouk, N., and Morille, Y.: Stratus–fog formation and dissipation: a 6-day case study, Boundary-Layer Meteorol., 143, 207–225, 2012.

Durden, D., Nappo, C., Leclerc, M., Duarte, H., Zhang, G., Parker, M., and Kurzeja, R.: On the impact of wave-like disturbances on turbulent fluxes and turbulence statistics in nighttime conditions: a case study, Biogeosciences, 10, 8433–8443, 2013.

Duynkerke, P. G.: Observation of a quasi-periodic oscillation due to gravity waves in a shallow radiation fog, Q. J. R. Meteorol. Soc., 117, 1207–1224, 1991.

Einaudi, F. and Finnigan, J. J.: Wave-turbulence dynamics in the stably stratified boundary layer, J. Atmos. Sci., 50, 1841–1864, doi:10.1175/1520-0469(1993)050<1841:WTDITS>2.0.CO;2, 1993.

Einaudi, F., Bedard, A. J. J., and Finnigan, J. J.: A climatology of gravity waves and other coherent disturbances at the Boulder Atmospheric Observatory during March-April 1984, J. Atmos. Sci., 46, 303–329, 1989.

Ellrod, G. P.: Advances in the detection and analysis of fog at night using GOES multispectral infrared imagery, Wea. Forecasting, 10, 606–619, 1995.

Fabbian, D., de Dear, R., and Lellyett, S.: Application of artificial neural network forecasts to predict fog at Canberra International Airport, Wea. Forecasting, 22, 372–381, 2007.

Fernando, H. and Weil, J. C.: Whither the stable boundary layer?, Bull. Am. Meteorol. Soc., 91, 1475–1484, doi:10.1175/2010BAMS2770.1, 2010.

Fernando, H., Pardyjak, E., Sabatino, S. D., Chow, F., Wekker, S. D., Hoch, S., Hacker, J., Pace, J., Pratt, T., Pu, Z., Steenburgh, W., Whiteman, C., Wang, Y., Zajic, D., Balsley, B., Dimitrova, R., Emmitt, G., Higgins, C., Hunt, J., Knievel, J., Lawrence, D., Liu, Y., Nadeau, D., Kit, E., Blomquist, B., Conry., P., Coppersmith, R., Creegan, E., Felton, M., Grachev, A., Gunawardena, N., Hang, C., Hocut, C., Huynh, G., Jeglum, M., Jensen, D., Kulandaivelu, V., Lehner, M., Leo, L., Liberzon, D., Massey, J., McEnerney, K., Pal, S., Price, T., Sghiatti, M., Silver, Z., Thompson, M., Zhang, H., and Zsedrovits, T.: THE MATERHORN - Unraveling the Intricacies of Mountain Weather, Bull. Am. Meteorol. Soc., e-view, doi:http://dx.doi.org/10.1175/BAMS-D-13-00131.1, 2015.

Finnigan, J.: Kinetic energy transfer between internal gravity waves and turbulence, J. Atmos. Sci., 45, 486–505, 1988.

Foken, T.: The energy balance closure problem: an overview, Ecol. Appl., 18, 1351–1367, 2008.

Fritts, D. C. and Alexander, M. J.: Gravity wave dynamics and effects in the middle atmosphere, Rev. Geophys., 41, 2003.

Fritts, D. C. and Nastrom, G. D.: Sources of mesoscale variability of gravity waves. Part II: Frontal, convective, and jet stream excitation, J. Atmos. Sci., 49, 111–127, 1992.

Fu, G., Li, P., Crompton, J. G., Guo, J., Gao, S., and Zhang, S.: An observational and modeling study of a sea fog event over the Yellow Sea on 1 August 2003, Meteorol. Atmos. Phys., 107, 149–159, 2010.

Fujita, T. T.: Results of detailed synoptic studies of squall lines, Tellus, 7, 405–436, 1955.

Fujita, T. T.: Analytical mesometeorology: A review, Severe Local Storms, Meteor. Monogr, 5, 77–125, 1963.

Fujita, T. T. and Caracena, F.: An analysis of three weather-related aircraft accidents, Bull. Am. Meteorol. Soc., 58, 1164–1181, 1977.

Garratt, J. R.: The atmospheric boundary layer, Cambridge university press, 1994.

Guedalia, D. and Bergot, T.: Numerical forecasting of radiation fog. Part II: A comparison of model simulation with several observed fog events, Mon. Weather Rev., 122, 1231–1246, 1994.

Gultepe, I., Tardif, R., Michaelides, S., Cermak, J., Bott, A., Bendix, J., Müller, M., Pagowski, M., Hansen, B., Ellrod, G., Jacobs, W., Toth, G., and Cober, S.: Fog research: A review of past achievements and future perspectives, Pure Appl. Geophys., 164, 1121–1159, 2007.

Gultepe, I., Hansen, B., Cober, S., Pearson, G., Milbrandt, J., Platnick, S., Taylor, P., Gordon, M., and Oakley, J.: The fog remote sensing and modeling field project, Bull. Am. Meteorol. Soc., 90, 341–359, 2009.

Gupta, K. S. and Sunil, T.: Thunderstorm generated wave disturbance in the atmospheric boundary layer-a case study, J. Atmos. Sol.-Terr. Phys., 63, 1585–1592, 2001.

Gurka, J. J.: The role of inward mixing in the dissipation of fog and stratus, Mon. Weather Rev., 106, 1633–1635, 1978.

Haar, A.: Zur Theorie der orthogonalen Funktionensysteme (On the theory of orthogonal function systems), Math. Ann., 69, 331–371, 1910.

Haeffelin, M., Barthès, L., Bock, O., Boitel, C., Bony, S., Bouniol, D., Chepfer, H., Chiriaco, M., Cuesta, J., Delanoë, J., Drobinski, P., Dufresne, J.-L., Flamant, C., Grall, M., Hodzic, A., Hourdin, F., Lapouge, F., Lemaitre, Y., Mathieu, A., Morille, Y., Naud, C., Noël, V., OHirok, B., Pelon, J., Pietras, C., Protat, A., Romand, B., Scialom, G., and Vautard, R.: SIRTA, a ground-based atmospheric observatory for cloud and aerosol research, Ann. Geophys., 23, 253–275, 2005.

Haeffelin, M., Bergot, T., Elias, T., Tardif, R., Carrer, D., Chazette, P., Colomb, M., Drobinski, P., Dupont, E., Dupont, J., Gomes, L., Musson-Genon, L., Pietras, C., Plana-Fattori, A., Protat, A., Rangognio, J., Raut, J.-C., Rémy, S., Richard, D., Sciare, J., and Zhang, X.: PARISFOG: shedding new light on fog physical processes, Bull. Am. Meteorol. Soc., 91, 767–783, 2010.

Hoch, S. W.: Radiative flux divergence in the surface boundary layer: A study based on observations at Summit, Greenland., Ph.D. thesis, ETH, 2006.

Hogan, R. J., Ferro, C. A., Jolliffe, I. T., and Stephenson, D. B.: Equitability revisited: Why the "equitable threat score" is not equitable, Wea. Forecasting, 25, 710–726, 2010.

Holton, J. R.: The influence of gravity wave breaking on the general circulation of the middle atmosphere, J. Atmos. Sci., 40, 2497–2507, 1983.

Holtslag, A. A. M., Svensson, G., Baas, P., Basu, S., Beare, B., Beljaars, A. C. M., Bosveld, F., Cuxart, J., Lindvall, J., Steeneveld, G. J., Tjernström, M., and Van de Wiel, B.: Stable atmospheric boundary layers and diurnal cycles: challenges for weather and climate models, Bull. Am. Meteorol. Soc., 94, 1691–1706, 2013.

Hong, S.-Y. and Lim, J.-O. J.: The WRF Single-Moment 6-Class Microphysics Scheme (WSM6), J. Korean Meteor. Soc., 42, 129–151, 2006.

Hong, S.-Y., Dudhia, J., and Chen, S.-H.: A Revised Approach to Ice Microphysical Processes for the Bulk Parameterization of Clouds and Precipitation, Mon. Weather Rev., 132, 103–120, 2004.

Hong, S.-Y., Noh, Y., and Dudhia, J.: A new vertical diffusion package with an explicit treatment of entrainment processes, Mon. Weather Rev., 134, 2318–2341, 2006.

Hopfinger, E.: Turbulence in stratified fluids: a review, J. Geophys. Res., 92, 5287–5303, doi: 10.1029/JC092iC05p05287., 1987.

Houze, J. R. A., Biggerstaff, M., Rutledge, S., and Smull, B.: Interpretation of Doppler weather radar displays of midlatitude mesoscale convective systems, Bull. Am. Meteorol. Soc., 70, 608–619, 1989.

Howell, J. and Mahrt, L.: Multiresolution flux decomposition, Boundary-Layer Meteorol., 83, 117–137, doi:10.1023/A:1000210427798, 1997.

Janjić, Z. I.: Nonsingular implementation of the Mellor–Yamada level 2.5 scheme in the NCEP Meso model, NCEP office note, 437, 61, 2002.

Jewett, B. F., Ramamurthy, M. K., and Rauber, R. M.: Origin, evolution, and finescale structure of the St. Valentine's Day mesoscale gravity wave observed during STORM-FEST. Part III: Gravity wave genesis and the role of evaporation, Mon. Weather Rev., 131, 617–633, 2003.

Johnson, R. H.: Surface mesohighs and mesolows, Bull. Am. Meteorol. Soc., 82, 13–31, 2001.

Johnson, R. H. and Hamilton, P. J.: The relationship of surface pressure features to the precipitation and airflow structure of an intense midlatitude squall line, Mon. Weather Rev., 116, 1444–1473, 1988.

Katata, G., Nagai, H., Kajino, M., Ueda, H., and Hozumi, Y.: Numerical study of fog deposition on vegetation for atmosphere–land interactions in semi-arid and arid regions, Agr. Forest. Meteorol., 150, 340–353, 2010.

Katata, G., Kajino, M., Hiraki, T., Aikawa, M., Kobayashi, T., and Nagai, H.: A method for simple and accurate estimation of fog deposition in a mountain forest using a meteorological model, J. Geophys. Res.-Atmos. (1984–2012), 116, 2011.

Kim, C. K., Stuefer, M., Schmitt, C. G., Heymsfield, A., and Thompson, G.: Numerical modeling of ice fog in interior Alaska using the weather research and forecasting model, Pure Appl. Geophys., 171, 1963–1982, 2014.

Kim, Y. J. and Hong, S. Y.: Interaction between the orography-induced gravity wave drag and boundary layer processes in a global atmospheric model, Geophys. Res. Lett., 36, 19–23, doi:10.1029/2008GL037146, 2009.

Kleczek, M. A., Steeneveld, G. J., and Holtslag, A. A. M.: Evaluation of the weather research and forecasting mesoscale model for GABLS3: impact of boundary-layer schemes, boundary conditions and spin-up, Boundary-Layer Meteorol., 152, 213–243, 2014.

Klemm, O., Schemenauer, R. S., Lummerich, A., Cereceda, P., Marzol, V., Corell, D., van Heerden, J., Reinhard, D., Gherezghiher, T., Olivier, J., Osses, P., Sarsour, J., Frost, E., J, E. M., Valiente, J. A., and Fessehaye, G.: Fog as a fresh-water resource: overview and perspectives, Ambio, 41, 221–234, 2012.

Knupp, K.: Observational analysis of a gust front to bore to solitary wave transition within an evolving nocturnal boundary layer, J. Atmos. Sci., 63, 2016–2035, 2006.

Koračin, D., Lewis, J., Thompson, W. T., Dorman, C. E., and Businger, J. A.: Transition of stratus into fog along the California coast: Observations and modeling, J. Atmos. Sci., 58, 1714–1731, 2001.

Kunkel, B. A.: Parameterization of droplet terminal velocity and extinction coefficient in fog models, J. Clim. Appl. Meteorol., 23, 34–41, 1984.

Lane, T. P. and Reeder, M. J.: Convectively generated gravity waves and their effect on the cloud environment, J. Atmos. Sci., 58, 2427–2440, 2001.

Lapworth, A.: Observations of the site dependency of the morning wind and the role of gravity waves in the transitions, Q. J. R. Meteorol. Soc., doi:10.1002/qj.2340, 2014.

Lareau, N. P., Crosman, E., Whiteman, C. D., Horel, J. D., Hoch, S. W., Brown, W. O., and Horst, T. W.: The persistent cold-air pool study, Bull. Am. Meteorol. Soc., 94, 51–63, 2013.

Leduc, M. and Laprise, R.: Regional climate model sensitivity to domain size, Clim. Dyn., 32, 833–854, 2009.

Leduc, M., Laprise, R., Moretti-Poisson, M., and Morin, J.-P.: Sensitivity to domain size of mid-latitude summer simulations with a regional climate model, Clim. Dyn., 37, 343–356, 2011.

Lehner, M., Whiteman, C., Hoch, S., Jensen, D., Pardyjak, E., Leo, L., Di Sabatino, S., and Fernando, H.: A case study of the nocturnal boundary-layer evolution on a slope at the foot of a desert mountain, J. Appl. Meteorol. Climatol., doi:10.1175/JAMC-D-14-0223.1,inpress, 2015a.

Lehner, M., Whiteman, C. D., Hoch, S. W., Crosman, E. T., Jeglum, M. E., Cherukuru, N. W., Calhoun, R., Adler, B., Kalthoff, N., Rotunno, R., Horst, T., Semmer, S., Brown, W., Oncley, S., Vogt, R., Grudzielanek, M., Cermak, J., Fonteyne, N., Bernhofer, C., and Pitacco, A.: The METCRAX II field experiment-A study of downslope windstorm-type flows in Arizona's Meteor Crater, Bull. Am. Meteorol. Soc., 2015b.

Li, J. and Nozaki, H.: Application of wavelet cross-correlation analysis to a plane turbulent jet., JSME Int. J. Ser. B, Fluids and thermal engineering, 40, 58–66, 1997.

Lin, Y.-L., Farley, R., and Orville, H.: Bulk parameterization of the snow field in a cloud model, J. Climate Appl. Meteor., 22, 1065–1092, 1983.

Lindzen, R. and Tung, K.: Banded convective activity and ducted gravity waves, Mon. Weather Rev., 104, 1602–1617, 1976.

Lindzen, R. S.: Wave-CISK in the tropics, J. Atmos. Sci., 31, 156–179, 1974.

Liu, D., Yang, J., Niu, S., and Li, Z.: On the evolution and structure of a radiation fog event in Nanjing, Adv. Atmos. Sci., 28, 223–237, 2011.

Loehrer, S. M. and Johnson, R. H.: Surface pressure and precipitation life cycle characteristics of PRE-STORM mesoscale convective systems, Mon. Weather Rev., 123, 600–621, 1995.

Löhnert, U. and Maier, O.: Operational profiling of temperature using ground-based microwave radiometry at Payerne: prospects and challenges, Atmos. Meas. Tech., 5, 1121–1134, 2012.

Löhnert, U., Turner, D., and Crewell, S.: Ground-based temperature and humidity profiling using spectral infrared and microwave observations. Part I: Simulated retrieval performance in clear-sky conditions, J. Appl. Meteorol. Climatol., 48, 1017–1032, 2009.

Lothon, M., Lohou, F., Pino, D., Couvreux, F., Pardyjak, E., Reuder, J., Vilà-Guerau de Arellano, J., Durand, P., Hartogensis, O., Legain, D., Augustin, P., Gioli, B., Faloona, I., Yagüe, C., Alexander, D. C., Angevine, W. M., Bargain, E., Barrié, J., Bazile, E., Bezombes, Y., Blay-Carreras, E., van de Boer, A., Boichard, J. L., Bourdon, A., Butet, A., Campistron, B., de Coster, O., Cuxart, J., Dabas, A., Darbieu, C., Deboudt, K., Delbarre, H., Derrien, S., Flament, P., Fourmentin, M., Garai, A., Gibert, F., Graf, A., Groebner, J., Guichard, F., Jimenez Cortes, M. A., Jonassen, M., van den Kroonenberg, A., Lenschow, D. H., Magliulo, V., Martin, S., Martinez, D., Mastrorillo, L., Moene, A. F., Molinos, F., Moulin, E., Pietersen, H. P., Piguet, B., Pique, E., Román-Cascón, C., Rufin-Soler, C., Saïd, F., Sastre-Marugán, M., Seity, Y., Steeneveld, G. J., Toscano, P., Traullé, O., Tzanos, D., Wacker, S., Wildmann, N., and Zaldei, A.: The BLLAST field experiment: Boundary-layer late afternoon and sunset turbulence, Atmos. Chem. Phys., 14, 10 931–10 960, 2014.

Luo, Z. and Fritts, D. C.: Gravity-wave excitation by geostrophic adjustment of the jet stream. Part II: Three-dimensional forcing, J. Atmos. Sci., 50, 104–115, 1993.

Mahrt, L.: Weak-wind mesoscale meandering in the nocturnal boundary layer, Environ. Fluid Mech., 7, 331–347, 2007.

Mahrt, L.: Characteristics of submeso winds in the stable boundary layer, Boundary-Layer Meteorol., 130, 1–14, doi:10.1007/s10546-008-9336-4, 2009.

Mahrt, L.: Surface wind direction variability, J. Appl. Meteorol. Climatol., 50, 144–152, doi:10.1175/2010JAMC2560.1, 2011.

Mahrt, L.: Stably Stratified Atmospheric Boundary Layers, Annu. Rev. Fluid Mech., 46, 23–45, doi:10.1146/annurev-fluid-010313-141354, 2014.

Mahrt, L., Vickers, D., Nakamura, R., Soler, M. R., Sun, J., Burns, S., and Lenschow, D. H.: Shallow drainage flows, Boundary-Layer Meteorol., 101, 243–260, doi:10.1023/A:1019273314378, 2001.

Mahrt, L., Richardson, S., Seaman, N., and Stauffer, D.: Turbulence in the nocturnal boundary layer with light and variable winds, Q. J. R. Meteorol. Soc., 138, 1430–1439, doi:10.1002/qj.1884, 2012.

Manasseh, R. and Middleton, J. H.: Boundary layer oscillations from thunderstorms at Sydney Airport, Mon. Weather Rev., 123, 1166–1177, 1995.

Martínez, D., Jiménez, M. A., Cuxart, J., and Mahrt, L.: Heterogeneous Nocturnal Cooling in a Large Basin Under Very Stable Conditions, Boundary-Layer Meteorol., 137, 97–113, doi:10.1007/s10546-010-9522-z, 2010.

Mellor, G. L. and Yamada, T.: Development of a turbulence closure model for geophysical fluid problems, Rev. Geophys. and space physics, 20, 851–875, 1982.

Mensbrugghe, V.: The formation of fog and of clouds, translated from Ciel et Terre, Symons's Monthly Meteor. Magazine, 27, 40–41, 1892.

Menut, L., Mailler, S., Dupont, J.-C., Haeffelin, M., and Elias, T.: Predictability of the meteorological conditions favourable to radiative fog formation during the 2011 ParisFog Campaign, Boundary-Layer Meteorol., 150, 277–297, 2014.

Merrill, J. T. and Grant, J. R.: A gravity wave-critical level encounter observed in the atmosphere, J. Geophys. Res.-Oceans (1978–2012), 84, 6315–6320, 1979.

Meyers, S., Kelly, B., and O'Brien, J.: An introduction to wavelet analysis in oceanography and meteorology: With application to the dispersion of Yanai waves., Mon. Weather Rev., 121, 2858–2866, 1993.

Miller, D. W.: Thunderstorm induced gravity waves as a potential hazard to commercial aircraft, in: American Meteorological Society 79th Annual Conference, 10 - 15 January 1999, Wyndham Anatole Hotel, Dallas, TX, edited by Society, A. M., Boston, MA., 1999.

Miller, D. W.: Exploring the possibility of a low altitude gravity wave encounter as the cause of a general aviation accident near Norman Oklahoma on December 6, 1998, in: Ninth Conference on Aviation, Range, and Aerospace Meteorology, 20th Conference on Severe Local Storms, 11 - 15 September 2000, Radisson Twin Towers Hotel, Orlando FL., edited by American Meteorological Society, Boston, MA., 2000.

Miller, S., Keim, B., Talbot, R., and Mao, H.: Sea breeze: Structure, forecasting, and impacts, Rev. Geophys., 41, 2003.

Mlawer, E. J., Taubman, S. J., Brown, P. D., Iacono, M. J., and Clough, S. A.: Radiative transfer for inhomogeneous atmospheres: RRTM, a validated correlated-k model for the longwave, J. Geophys. Res.-Atmos. (1984–2012), 102, 16 663–16 682, 1997.

Moene, A. F. and van Dam, J. C.: Transport in the Atmosphere-Vegetation-Soil Continuum, Cambridge University Press, 2014.

Monin, A. and Obukhov, A.: Basic laws of turbulent mixing in the surface layer of the atmosphere, Contrib. Geophys. Inst. Acad. Sci. USSR, 151, 163–187, 1954.

Monserrat, S. and Thorpe, A. J.: Use of ducting theory in an observed case of gravity waves, J. Atmos. Sci., 53, 1724–1736, 1996.

Monti, P., Fernando, H. J. S., Princevac, M., Chan, W. C., Kowalewski, T. A., and Pardyjak, E. R.: Observations of Flow and Turbulence in the Nocturnal Boundary Layer over a Slope, J. Atmos. Sci., 59, 2513–2534, doi:10.1175/1520-0469(2002)059<2513:OOFATI>2.0.CO;2, 2002.

Müller, M., Masbou, M., and Bott, A.: Three-dimensional fog forecasting in complex terrain, Q. J. R. Meteorol. Soc., 136, 2189–2202, 2010.

Nadeau, D. F., Pardyjak, E. R., Higgins, C. W., Huwald, H., and Parlange, M. B.: Flow during the evening transition over steep Alpine slopes, Q. J. R. Meteorol. Soc., 139, 607–624, doi: 10.1002/qj.1985, 2013.

Nai-Ping, L., Neff, W., and Kaimal, J.: Wave and turbulence structure in a disturbed nocturnal inversion, Boundary-Layer Meteorol., 26, 141–155, 1983.

Nakanishi, M.: Large-eddy simulation of radiation fog, Boundary-Layer Meteorol., 94, 461–493, 2000.

Nakanishi, M. and Niino, H.: An improved Mellor–Yamada level-3 model with condensation physics: Its design and verification, Boundary-Layer Meteorol., 112, 1–31, 2004.

Nappo, C., Miller, D., and Hiscox, A.: Wave-modified flux and plume dispersion in the stable boundary layer, Boundary-Layer Meteorol., 129, 211–223, 2008.

Nappo, C. J.: Sporadic breakdown of stability in the PBL over simple and complex terrain, Boundary-Layer Meteorol., 54, 69–87, doi:10.1007/BF00119413, 1991.

Nappo, C. J.: An introduction to atmospheric gravity waves (2nd ed.), vol. 102, Academic Press, 2012.

Nastrom, G. D. and Fritts, D. C.: Sources of mesoscale variability of gravity waves. Part I: Topographic excitation, J. Atmos. Sci., 49, 101–110, 1992.

NCEP: Mesoscale & Microscale Meteorology Division. Weather Research & Forecasting ARW Version 3 Modeling System User's Guide, 2011.

Nicholls, M. E. and Pielke, R. A.: Thermally induced compression waves and gravity waves generated by convective storms, J. Atmos. Sci., 57, 3251–3271, 2000.

Nilsson, E. O., Sahlée, E., and Rutgersson, A.: Turbulent momentum flux characterization using extended multiresolution analysis, Q. J. R. Meteorol. Soc., 140, 1715–1728, 2014.

Ohya, Y., Nakamura, R., and Uchida, T.: Intermittent bursting of turbulence in a stable boundary layer with low-level jet, Boundary-Layer Meteorol., 126, 349–363, doi: 10.1007/s10546-007-9245-y, 2008.

Oldroyd, H. J., Katul, G., Pardyjak, E. R., and Parlange, M. B.: Momentum balance of katabatic flow on steep slopes covered with short vegetation, Geophys. Res. Lett., 41, 4761–4768, doi: DOI:10.1002/2014GL060313, 2014.

Pagowski, M., Gultepe, I., and King, P.: Analysis and modeling of an extremely dense fog event in southern Ontario, Pure Appl. Geophys., 43, 3–16, 2004.

Pan, H.-L. and Mahrt, L.: Interaction between soil hydrology and boundary-layer development, Boundary-Layer Meteorol., 38, 185–202, 1987.

Pasini, A., Pelino, V., and Potestà, S.: A neural network model for visibility nowcasting from surface observations: Results and sensitivity to physical input variables, J. Geophys. Res.: Atmospheres (1984–2012)., 106, 14 951–14 959, 2001.

Payra, S. and Mohan, M.: Multirule Based Diagnostic Approach for the Fog Predictions Using WRF Modelling Tool, Adv. Meteorol., 2014, 2014.

Pedgley, D. E.: A meso-synoptic analysis of the thunderstorms on 28 August, 1958, HM Stationery Office, 1962.

Porson, A., Price, J., Lock, A., and Clark, P.: Radiation fog. Part II: Large-eddy simulations in very stable conditions, Boundary-Layer Meteorol., 139, 193–224, 2011.

Prabha, T. and Hoogenboom, G.: Evaluation of the weather research and forecasting model for two frost events, Comput. Electron. Agric., 64, 234–247, 2008.

Price, J.: Radiation fog. Part I: observations of stability and drop size distributions, Boundary-Layer Meteorol., 139, 167–191, 2011.

Price, J., Vosper, S., Brown, A., Ross, A., Clark, P., Davies, F., Horlacher, V., Claxton, B., McGregor, J., Hoare, J., Jemmet-Smith, B., and Sheridan, P.: COLPEX: field and numerical studies over a region of small hills, Bull. Am. Meteorol. Soc., 92, 1636–1650, 2011.

Price, J., Porson, A., and Lock, A.: An Observational Case Study of Persistent Fog and Comparison with an Ensemble Forecast Model, Boundary-Layer Meteorol., pp. 1–27, 2015.

Ralph, F., Venkateswaran, V., and Crochet, M.: Observations of a mesoscale ducted gravity wave, J. Atmos. Sci., 50, 3277–3291, 1993.

Ralph, F. M., Neiman, P. J., Keller, T. L., Levinson, D., and Fedor, L.: Observations, Simulations, and Analysis of Nonstationary Trapped Lee Waves, J. Atmos. Sci., 54, 1308–1333, doi:10.1175/1520-0469(1997)054<1308:OSAAON>2.0.CO;2, 1997.

Raymond, D. J.: A model for predicting the movement of continuously propagating convective storms, J. Atmos. Sci., 32, 1308–1317, 1975.

Rees, J. and Mobbs, S.: Studies of internal gravity waves at Halley Base, Antarctica, using wind observations., Q. J. R. Meteorol. Soc., 114, 939–966, 1988.

Rémy, S. and Bergot, T.: Assessing the impact of observations on a local numerical fog prediction system, Q. J. R. Meteorol. Soc., 135, 1248–1265, 2009.

Rémy, S. and Bergot, T.: Ensemble Kalman filter data assimilation in a 1D numerical model used for fog forecasting, Mon. Weather Rev., 138, 1792–1810, 2010.

Rémy, S., Pannekoucke, O., Bergot, T., and Baehr, C.: Adaptation of a particle filtering method for data assimilation in a 1D numerical model used for fog forecasting, Q. J. R. Meteorol. Soc., 138, 536–551, 2012.

Reudenbach, C. and Bendix, J.: Experiments with a straightforward model for the spatial forecast of fog/low stratus clearance based on multi-source data, Meteorol. Appl., 5, 205–216, 1998.

Riley, J. J. and Lelong, M.-P.: Fluid motions in the presence of strong stable stratification, Annu. Rev. Fluid Mech., 32, 613–657, doi:10.1146/annurev.fluid.32.1.613, 2000.

Roach, W., Brown, R., Caughey, S., Garland, J., and Readings, C.: The physics of radiation fog: I–a field study, Q. J. R. Meteorol. Soc., 102, 313–333, 1976.

Román-Cascón, C., Yagüe, C., Sastre, M., Maqueda, G., Salamanca, F., and Viana, S.: Observations and WRF simulations of fog events at the Spanish Northern Plateau, Adv. Sci. Res., 8, 11–18, 2012.

Román-Cascón, C., Steeneveld, G., Yagüe, C., Sastre, M., Arrillaga, J.-A., and Maqueda, G.: Forecasting radiation fog at climatologically contrasting sites: evaluation of statistical methods and WRF, Submitted to Q. J. R. Meteorol. Soc., QJ-15-0176, 2015a.

Román-Cascón, C., Yagüe, C., Mahrt, L., Sastre, M., Steeneveld, G. J., Pardyjak, E., van de Boer, A., and Hartogensis, O.: Interactions among drainage flows, gravity waves and turbulence: a BLLAST case study, Atmos. Chem. Phys., 15, 9031–9047, 2015b.

Román-Cascón, C., Yagüe, C., Mahrt, L., Sastre, M., Steeneveld, G. J., Pardyjak, E., van de Boer, A., and Hartogensis, O.: Comment, Atmos. Chem. Phys. Discuss., 15, C3759–C3759, 2015c.

Román-Cascón, C., Yagüe, C., Mahrt, L., Sastre, M., Steeneveld, G. J., Pardyjak, E., van de Boer, A., and Hartogensis, O.: Comment, Atmos. Chem. Phys. Discuss., 15, C3760–C3760, 2015d.

Román-Cascón, C., Yagüe, C., Mahrt, L., Sastre, M., Steeneveld, G. J., Pardyjak, E., van de Boer, A., and Hartogensis, O.: Comment, Atmos. Chem. Phys. Discuss., 15, C3761–C3761, 2015e.

Román-Cascón, C., Yagüe, C., Steeneveld, G., Sastre, M., Arrillaga, J.-A., and Maqueda, G.: Estimating fog-top height through near-surface micrometeorological measurements., Submitted to Atmos. Res., ATMOSRES-D-15-00532, 2015f.

Román-Cascón, C., Yagüe, C., Viana, S., Sastre, M., Maqueda, G., Lothon, M., and Gómara, I.: Near monochromatic ducted gravity waves associated with a convective sytem close to the Pyrenées, Q. J. R. Meteorol. Soc., 141, 1320–1332, doi:10.1002/qj.2441, 2015g.

Rotach, M. W., Calanca, P., Graziani, G., Gurtz, J., Steyn, D. G., Vogt, R., Andretta, M., Christen, A., Cieslik, S., Connolly, R., De Wekker, S. F. J., Galmarini, S., Kadygrov, E. N., Kadygrov, V., Miller, E., Neininger, B., Rucker, M., Van Gorsel, E., Weber, H., Weiss, A., and Zappa, M.: Turbulence structure and exchange processes in an Alpine Valley: The Riviera Project, Bull. Am. Meteorol. Soc., 85, 1367–1385, doi:10.1175/BAMS-85-9-1367, 2004.

Ryerson, W. R. and Hacker, J. P.: The Potential for Mesoscale Visibility Predictions with a Multimodel Ensemble, Wea. Forecasting, 29, 543–562, 2014.

San José, R., Casanova, J., Viloria, R., and Casanova, L.: Evaluation of the turbulent parameters of the unstable surface boundary layer outside Businger's range, Atmos. Environ., 19, 1555–1561, 1985.

Sastre, M., Yagüe, C., Román-Cascón, C., Maqueda, G., Salamanca, F., and Viana, S.: Evening transitions of the atmospheric boundary layer: characterization, case studies and WRF simulations, Adv. Sci. Res., 8, 39–44, doi:10.5194/asr-8-39-2012, 2012.

Sastre, M., Yagüe, C., Román-Cascón, C., and Maqueda, G.: Atmospheric Boundary-Layer Evening Transitions: A Comparison Between Two Different Experimental Sites, Boundary-Layer Meteorol., pp. 1–25, doi:10.1007/s10546-015-0065-1, 2015.

Schemenauer, R. S. and Cereceda, P.: A proposed standard fog collector for use in high-elevation regions, J. Appl. Meteorol., 33, 1313–1322, 1994.

Scherrer, S. C. and Appenzeller, C.: Fog and low stratus over the Swiss Plateau - a climatological study, Int. J. Climatol., 34, 678–686, 2014.

Schneider, R. S.: Large-amplitude mesoscale wave disturbances within the intense Midwest extratropical cyclone of 15 December 1987, Wea. Forecasting., 5, 533–558, 1990.

Seaman, N. L., Gaudet, B. J., Stauffer, D. R., Mahrt, L., Richardson, S. J., Zielonka, J. R., and Wyngaard, J. C.: Numerical Prediction of Submesoscale Flow in the Nocturnal Stable Boundary Layer over Complex Terrain, Mon. Weather Rev., 140, 956–977, doi:10.1175/MWR-D-11-00061.1, 2012.

Seity, Y., Brousseau, P., Malardel, S., Hello, G., Bénard, P., Bouttier, F., Lac, C., and Masson, V.: The AROME-France convective-scale operational model, Mon. Weather Rev., 139, 976–991, 2011.

Serafimovich, A., Hoffmann, P., Peters, D., and Lehmann, V.: Investigation of inertia-gravity waves in the upper troposphere/lower stratosphere over Northern Germany observed with collocated VHF/UHF radars, Atmos. Chem. Phys., 5, 295–310, 2005.

Shi, C., Wang, L., Zhang, H., Zhang, S., Deng, X., Li, Y., and Qiu, M.: Fog simulations based on multi-model system: a feasibility study, Pure Appl. Geophys., 169, 941–960, 2012.

Shin, H. H. and Hong, S.-Y.: Intercomparison of planetary boundary-layer parametrizations in the WRF model for a single day from CASES-99, Boundary-Layer Meteorol., 139, 261–281, 2011.

Sisterson, D. L. and Frenzen, P.: Nocturnal boundary-layer wind maxima and the problem of wind power assessment., Environ. Sci. Technol., 12, 218–221, 1978.

Skamarock, W., Klemp, J., Dudhia, J., Gill, D., Barker, D., Duda, M., Huang, X.-Y., Wang, W., and Powers, J.: A Description of the Advanced Research WRF Version 3, Tech. Rep., p. 113, doi:10.5065/D6DZ069T, 2008.

Smedman, A.-S., Tjernström, M., and Högström, U.: Analysis of the turbulence structure of a marine low-level jet, Boundary-Layer Meteorol., 66, 105–126, 1993.

Smedman, A.-S., Bergström, H., and Högström, U.: Spectra, variances and length scales in a marine stable boundary layer dominated by a low level jet, Boundary-Layer Meteorol., 76, 211–232, doi:10.1007/BF00709352, 1995.

Smirnova, T., Brown, J., and Benjamin, S.: Performance of different soil model configurations in simulating ground surface temperature and surface fluxes., Mon. Weather Rev., 125, 1870–1884, 1997.

Smirnova, T., Brown, J., Benjamin, S., and Kim, D.: Parameterization of cold season processes in the MAPS land-surface scheme., J. Geophys. Res., 105D, 4077–4086, 2000.

Snyder, R. and Melo-Abreu, J.: Frost Protection: Fundamentals, Practice and Economics, 1., Food and Agricultural Organization of the United Nations, Rome. ISSN 1684-8241., 1, 2005.

Soler, M., Infante, C., Buenestado, P., and Mahrt, L.: Observations of nocturnal drainage flows in a shallow gully, Boundary-Layer Meteorol., 105, 253–273, doi:10.1023/A:1019910622806, 2002.

Soler, M. R., Udina, M., and Ferreres, E.: Observational and Numerical Simulation Study of a Sequence of Eight Atmospheric Density Currents in Northern Spain, Boundary-Layer Meteorol., 153, 195–216, doi:10.1007/s10546-014-9942-2, 2014.

Sorbjan, Z.: Structure of the Atmospheric Boundary Layer, Prentice Hall, Englewood Cliffs. 317 pp., New Jersey, 1989.

Steeneveld, G. J.: Current challenges in understanding and forecasting stable boundary layers over land and ice, Front. Environ. Sci., 2, 41, 2014.

Steeneveld, G. J., Wokke, M., Groot Zwaaftink, C., Pijlman, S., Heusinkveld, B., Jacobs, A., and Holtslag, A. A. M.: Observations of the radiation divergence in the surface layer and its implication for its parameterization in numerical weather prediction models, J. Geophys. Res.-Atmos. (1984–2012), 115, 2010.

Steeneveld, G. J., Ronda, R. J., and Holtslag, A. A.: The Challenge of Forecasting the Onset and Development of Radiation Fog Using Mesoscale Atmospheric Models, Boundary-Layer Meteorol., 154, 265–289, 2015.

Stolaki, S., Pytharoulis, I., and Karacostas, T.: A study of fog characteristics using a coupled WRF–COBEL model over Thessaloniki airport, Greece, Pure Appl. Geophys., 169, 961–981, 2012.

Storm, B., Dudhia, J., Basu, S., Swift, A., and Giammanco, I.: Evaluation of the weather research and forecasting model on forecasting low-level jets: Implications for wind energy, Wind Energy, 12, 81–90, 2009.

Stull, R. B.: An Introduction to Boundary Layer Meteorology, Kluwer Academic Publisher. 666 pp., 1988.

Sukoriansky, S., Galperin, B., and Perov, V.: Application of a new spectral theory of stably stratified turbulence to the atmospheric boundary layer over sea ice, Boundary-Layer Meteorol., 117, 231–257, 2005.

Sukoriansky, S., Dikovskaya, N., and Galperin, B.: Transport of momentum and scalar in turbulent flows with anisotropic dispersive waves, Geophys. Res. Lett., 36, 3–7, doi:10.1029/2009GL038632, 2009.

Sun, J., Burns, S. P., Lenschow, D. H., Banta, R., Newsom, R., Coulter, R., Frasier, S., Ince, T., Nappo, C., Cuxart, J., Blumen, W., Lee, X., and Hu, X. Z.: Intermittent turbulence associated with a density current passage in the stable boundary layer, Boundary-Layer Meteorol., 105, 199–219, doi:10.1023/A:1019969131774, 2002.

Sun, J., Lenschow, D. H., Burns, S. P., Miller, D., and Skelly, B.: Turbulence in Nocturnal Boundary Layers, Boundary-Layer Meteorol., 110, 255–279, 2004.

Sun, J., Mahrt, L., Banta, R. M., and Pichugina, Y. L.: Turbulence Regimes and Turbulence Intermittency in the Stable Boundary Layer during CASES-99, J. Atmos. Sci., 69, 338–351, doi:10.1175/JAS-D-11-082.1, 2012.

Sun, J., Mahrt, L., Nappo, C., and Lenschow, D. H.: Wind and temperature oscillations generated by wave–turbulence interactions in the stably stratified boundary layer, J. Atmos. Sci., 72, 1484–1503, 2015a.

Sun, J., Nappo, C. J., Mahrt, L., Belusic, D., Grisogono, B., Stauffer, D. R., Pulido, M., Staquet, C., Jiang, Q., Pouquet, A., Yagüe, C., Galperin, B., Smith, R. B., Finnigan, J. J., Mayor, S. D., Svensson, G., Grachev, A. A., and Neff, W. D.: Review of Wave-Turbulence Interactions in the Stable Atmospheric Boundary Layer, Rev. Geophys., 53, doi:10.1002/2015RG000487, 2015b.

Syed, F. S., Körnich, H., and Tjernström, M.: On the fog variability over south Asia, Clim. Dyn., 39, 2993–3005, 2012.

Tanaka, H., Honma, S., Nishi, M., Igarashi, T., Teramoto, S., Nishio, F., and Abe, S.: Acid fog and hospital visits for asthma: an epidemiological study, Eur. Respir. J., 11, 1301–1306, 1998.

Tang, Y. M., Capon, R., Forbes, R., and Clark, P.: Fog prediction using a very high resolution numerical weather prediction model forced with a single profile, Meteorol. Appl., 16, 129–141, 2009.

Tao, W.-K. and Simpson, J.: The Goddard cumulus ensemble model. Part I: Model description., Terr. Atmos. Oceanic Sci., 4, 35–72, 1983.

Tardif, R.: The impact of vertical resolution in the explicit numerical forecasting of radiation fog: A case study, Pure Appl. Geophys., 164, 1221–1240, 2007.

Tardif, R. and Rasmussen, R. M.: Event-based climatology and typology of fog in the New York City region, J. Appl. Meteorol. Climatol., 46, 1141–1168, 2007.

Terradellas, E., Morales, G., Cuxart, J., and Yagüe, C.: Wavelet methods: application to the study of the stable atmospheric boundary layer under non-stationary conditions, Dynam. Atmos. Oceans, 34, 225–244, 2001.

Torrence, C. and Compo, G. P.: A Practical Guide to Wavelet Analysis, Bull. Am. Meteorol. Soc., 79, 61–78, doi:10.1175/1520-0477(1998)079<0061:APGTWA>2.0.CO;2, 1998.

Twonisvi, S. and Wojciechowski, T.: Observations of the Geographical Variation of Cloud Nuclei, J. Atmos. Sci., 26, 684–688, 1969.

Uccelini, L. W.: A case study of apparent gravity wave initiation of severe convective storms, Mon. Weather Rev., 103, 497–513, 1975.

Udina, M., Soler, M. R., Viana, S., and Yagüe, C.: Model simulation of gravity waves triggered by a density current, Q. J. R. Meteorol. Soc., 139, 701–714, doi:10.1002/qj.2004, 2013.

van de Boer, A., Moene, A. F., Graf, A., Schüttemeyer, D., and Simmer, C.: Detection of Entrainment Influences on Surface-Layer Measurements and Extension of Monin-Obukhov Similarity Theory, Boundary-Layer Meteorol., 152, 19–44, doi:10.1007/s10546-014-9920-8, 2014.

Van de Wiel, B., Moene, A. F., Hartogensis, O. K., De Bruin, H. A. R., and Holtslag, A. A. A.: Intermittent Turbulence in the Stable Boundary Layer over Land. Part III: A Classification for Observations during CASES-99, J. Atmos. Sci., 60, 2509–2522, doi: 10.1175/1520-0469(2003)060<2509:ITITSB>2.0.CO;2, 2003.

Van de Wiel, B., Moene, A. F., Steeneveld, G., Baas, P., Bosveld, F., and Holtslag, A.: A conceptual view on inertial oscillations and nocturnal low-level jets, J. Atmos. Sci., 67, 2679–2689, 2010.

Van de Wiel, B., Moene, A. F., and Jonker, H.: The cessation of continuous turbulence as precursor of the very stable nocturnal boundary layer, J. Atmos. Sci., 69, 3097–3115, 2012.

van den Kroonenberg, A. and Bange, J.: Turbulent flux calculation in the polar stable boundary layer: Multiresolution flux decomposition and wavelet analysis, J. Geophys. Res. Atmos., 112, 1–12, doi:10.1029/2006JD007819, 2007.

Van der Velde, I., Steeneveld, G. J., Wichers Schreur, B., and Holtslag, A. A. M.: Modeling and forecasting the onset and duration of severe radiation fog under frost conditions, Mon. Weather Rev., 138, 4237–4253, 2010.

Vercauteren, N. and Klein, R.: A clustering method to characterize intermittent bursts of turbulence and submeso motions interaction in the stable boundary layer., J. Atmos. Sci., doi:http://dx.DOI.org/10.1175/JAS-D-14-0115.1, 2014.

Viana, S.: Estudio de los procesos físicos que tienen lugar en la capa límite atmosférica nocturna a partir de campañas experimentales de campo., Ph.D. thesis, Universidad Complutense de Madrid, 2011.

Viana, S., Yagüe, C., and Maqueda, G.: Propagation and effects of a mesoscale gravity wave over a weakly-stratified nocturnal boundary layer during the SABLES2006 field campaign, Boundary-Layer Meteorol., 133, 165–188, doi:10.1007/s10546-009-9420-4, 2009.

Viana, S., Terradellas, E., and Yagüe, C.: Analysis of Gravity Waves Generated at the Top of a Drainage Flow, J. Atmos. Sci., 67, 3949–3966, doi:10.1175/2010JAS3508.1, 2010.

Viana, S., Yagüe, C., and Maqueda, G.: Vertical structure of the stable boundary layer detected by RASS-SODAR and in-situ measurements in SABLES 2006 field campaign, Acta Geophys., 60, 1261–1286, doi:10.2478/s11600-011-0072-7, 2012.

Vickers, D. and Mahrt, L.: The cospectral gap and turbulent flux calculations, J. Atmos. Ocean. Technol., 20, 660–672, doi:10.1175/1520-0426(2003)20<660:TCGATF>2.0.CO;2, 2003.

Vilà-Guerau de Arellano, J., van Heerwaarden, C. C., van Stratum, B. J., and van den Dries, K.: Atmospheric boundary layer: Integrating air chemistry and land interactions, Cambridge University Press, 2015.

Vindel, J., Yagüe, C., and Redondo, J.: Structure function analysis and intermittency in the atmospheric boundary layer, Nonlin. Processes Geophys., 15, 915–929, 2008.

Vindel, J. M. and Yagüe, C.: Intermittency of Turbulence in the Atmospheric Boundary Layer: Scaling Exponents and Stratification Influence, Boundary-Layer Meteorol., 140, 73–85, doi: 10.1007/s10546-011-9597-1, 2011.

Voronovich, V. and Kiely, G.: On the gap in the spectra of surface-layer atmospheric turbulence, Boundary-Layer Meteorol., 122, 67–83, doi:10.1007/s10546-006-9108-y, 2007.

Wang, W., Barker, D., Bray, J., Bruyere, C., Duda, M., Dudhia, J., Gill, D., and Michalakes, J.: User's Guide for Advanced Research WRF (ARW) Modeling System Version 3, 2011.

Warner, T. T., Peterson, R. A., and Treadon, R. E.: A tutorial on lateral boundary conditions as a basic and potentially serious limitation to regional numerical weather prediction, Bull. Am. Meteorol. Soc., 78, 2599–2617, 1997.

Welch, R. M. and Wielicki, B. A.: The stratocumulus nature of fog, J. Clim. Appl. Meteorol., 25, 101–111, 1986.

Whiteman, C.: Mountain Meteorology: Fundamentals and Applications, Oxford University Press. 355 pp., New Jork, 2000.

Whiteman, C. D., Hoch, S. W., Hahnenberger, M., Muschinski, A., Hohreiter, V., Behn, M., Cheon, Y., Zhong, S., Yao, W., Fritts, D., Clements, C., Horst, T., Brown, W., and SP, O.: METCRAX 2006: Meteorological experiments in Arizona's Meteor crater, Bull. Am. Meteorol. Soc., 89, 1665–1680, 2008.

Willett, H. C.: Fog and haze, their causes, distribution, and forecasting, Mon. Weather Rev., 1928.

Williams, D. T.: The thunderstorm wake of May 4, 1961, US Weather Bureau, 1963.

WMO, No. 182. TP. 91. Geneva (Secretariat of the World Meteorological Organization) 1966. Pp. xvi, . S. f. .: International meteorological vocabulary., Q. J. R. Meteorol. Soc., 93, doi: 10.1002/qj.49709339524, 1967.

Wyngaard, J. C.: Turbulence in the Atmosphere, Cambridge University Press, 2010.

Yagüe, C. and Cano, J.: Eddy transfer processes in the atmospheric boundary layer, Atmos. Environ., 28, 1275–1289, 1994.

Yagüe, C. and Redondo, J. M.: A case study of turbulent parameters during the Antarctic winter, Antarct. Sci., 7, 421–433, 1995.

Yagüe, C., Viana, S., Maqueda, G., and Redondo, J. M.: Influence of stability on the flux-profile relationships for wind speed, Φ m, and temperature, Φ h, for the stable atmospheric boundary layer, Nonlin. Processes Geophys., 13, 185–203, 2006.

Yagüe, C., Viana, S., Maqueda, G., Morales, G., Sastre, M., Ramos, D., and Vindel, J. M.: CIBA2008, an experimental campaign on the atmospheric boundary layer: preliminary nocturnal results, Física de la Tierra, 21, 13–26, 2009.

Zhou, B. and Ferrier, B. S.: Asymptotic analysis of equilibrium in radiation fog, J. Appl. Meteorol. Clim., 47, 1704–1722, 2008.

Zilitinkevich, S.: Non-local turbulent transport pollution dispersion aspects of coherent structure of convective flows, Air Pollution III, Air pollution theory and simulation (H Power, N Moussiopoulos, CA Brebbia, eds) Computational Mechanics Publ. Southampton, Boston, 1, 53–60, 1995.

LIST OF ACRONYMS

agl above ground level
asl above sea level
BLLAST Boundary-Layer Late Afternoon and Sunset Turbulence
CBL convective boundary layer
cbl cloud base lowering
CCN cloud condensation nuclei
CESAR Cabauw Experimental Site for Atmospheric Research
CIBA Research Site for the Lower Atmophere *(Centro de Investigación de la Baja Atmósfera)*
ECMWF European Centre for Medium-range Weather Forecasts
F-A false-alarm
GSS Gilbert skill score
GW gravity wave
HATPRO Humidity And Temperature PROfiler
H-R hit rate
IOP intensive observational period
LEVD Valladolid-Villanubla airport (ICAO code)
LFBT Tarbes-Lourdes-Pyrenees airport (ICAO code)
LWC liquid water content
NCEP National Centre for Environmental Prediction
NWP numerical weather prediction
M14 Menut et al. (2014)
MCS mesoscale convective system
MRFD multi-resolution flux decomposition
MYNN Mellor-Yamada Nakanishi and Niino
MYJ Mellor-Yamada-Janjic
PBL planetary boundary layer
QNSE Quasi-Normal Scale Elimination
RH relative humidity
RRTM Rapid Radiative Transfer Model
SBL stable boundary layer
SDF shallow drainage flow
SL surface layer
UHF ultra-high frequency
UTC Coordinated Universal Time
WRF Weather Research and Forecasting
WT wavelet transform

PUBLICATIONS

The main contents of this thesis have been published in the following articles:

- **Román-Cascón, C.**, Yagüe, C., Sastre, M., Maqueda, G., Salamanca, F. & Viana, S. (2012): Observations and WRF simulations of fog events at the Spanish Northern Plateau. *Adv. Sci. Res.*, **8(1)**, 11-18.
  http://www.adv-sci-res.net/8/11/2012/asr-8-11-2012.html
- **Román-Cascón, C.**, Yagüe, C., Viana, S., Sastre, M., Maqueda, G., Lothon, M. & Gómara, I. (2015): Near-monochromatic ducted gravity waves associated with a convective system close to the Pyrenees. *Q. J. R. Meteorol. Soc.*, **141**, 1320-1332.
  http://onlinelibrary.wiley.com/doi/10.1002/qj.2441/abstract
- **Román-Cascón, C.**, Yagüe, C., Mahrt, L., Sastre, M., Steeneveld, G. J., Pardyjak, E., van de Boer, A. & Hartogensis, O. (2015): Interactions among drainage flows, gravity waves and turbulence: a BLLAST case study. *Atmos. Chem. Phys.*, **15**, 9031-9047.
  http://www.atmos-chem-phys.net/15/9031/2015/acp-15-9031-2015.pdf
- **Román-Cascón, C.**, Steeneveld, G. J., Yagüe, C., Sastre, M., Arrillaga, J. A. & Maqueda, G. (2015): Forecasting radiation fog at climatologically contrasting sites: evaluation of statistical methods and WRF. Under revision in *Q. J. R. Meteorol. Soc.*, QJ-15-0176.
- **Román-Cascón, C.**, Yagüe, C., Steeneveld, G. J., Sastre, M., Arrillaga, J. A. & Maqueda, G. (2015): Estimating fog-top height through near-surface micrometeorological measurements. Under review in *Atm. Res.*, ATMOSRES-D-15-00532.

Other publications (not included in this Thesis):

- **Sastre, M.**, Yagüe, C., Román-Cascón, C., Maqueda, G., Salamanca, F. & Viana, S. (2012): Evening transitions of the atmospheric boundary layer: characterization, case studies and WRF simulations. *Adv. Sci. Res.*, **8(1)**, 39-44.
  http://www.adv-sci-res.net/8/39/2012/asr-8-39-2012.html
- **Lothon, M.**, Lohou, F., Pino, D., Couvreux, F., Pardyjak, E. R., Reuder, J., ..., Román-Cascón, C., ..., & Molinos, F. (2014): The BLLAST field experiment: Boundary-Layer Late Afternoon and Sunset Turbulence. *Atmos. Chem. Phys.*, **14(20)**, 10931-10960.
  http://www.atmos-chem-phys.net/14/10931/2014/acp-14-10931-2014.pdf
- **Sastre, M.**, Yagüe, C., Román-Cascón, C. & Maqueda, G. (2015): Atmospheric boundary-layer evening transitions: a comparison between two different experimental sites. *Boundary-Layer Meteorol.*, 1-25.
  http://link.springer.com/article/10.1007/s10546-015-0065-1?wt_mc=email.event.1.SEM.ArticleAuthorOnlineFirst